System Modeling, Design, and Control of the Mars Oxygen In-Situ Resource Utilization Experiment (MOXIE) and Implications for Atmospheric ISRU Processing Plants

By

Forrest Edward Meyen

B.S. Mechanical Engineering
B.S. Biological Engineering
University of Missouri, 2011

S.M. Aerospace Engineering
Massachusetts Institute of Technology, 2013

SUBMITTED TO THE DEPARTMENT OF AERONAUTICS AND ASTRONAUTICS
IN PARTIAL FULFILLMENT OF THE REQUIREMENTS FOR THE DEGREE OF

DOCTOR OF PHILOSOPHY IN AERONAUTICS AND ASTRONAUTICS

AT THE

MASSACHUSETTS INSTITUTE OF TECHNOLOGY

May 2017

Signature of Author .... Signature redacted ....
Forrest E. Meyen
Department of Aeronautics and Astronautics
May 18, 2017

Accepted by .... Signature redacted ....
Youssef M. Marzouk
Associate Professor of Aeronautics and Astronautics
Chair, Graduate Program Committee

System Modeling, Design, and Control of the Mars Oxygen In-Situ Resource Utilization Experiment (MOXIE) and Implications for Atmospheric ISRU Processing Plants

By

Forrest Edward Meyen

DOCTOR OF PHILOSOPHY IN AERONAUTICS AND ASTRONAUTICS
AT THE
MASSACHUSETTS INSTITUTE OF TECHNOLOGY

Signature redacted

Certified by: . ...
Jeffrey A. Hoffman
Professor of the Practice
Department of Aeronautics and Astronautics
Thesis Committee Chair

Signature redacted

Certified by: ....
Bilge Yildiz
Associate Professor of Nuclear Science and Engineering
Associate Professor of Materials Science and Engineering
Department of Nuclear Science and Engineering
Thesis Committee Member

Certified by: . Signature redacted ....
Joseph Hartvigsen
Senior Engineer, MOXIE Science Team Member
Ceramatec Inc.
Thesis Committee Member

System Modeling, Design, and Control of the Mars Oxygen In-Situ Resource Utilization Experiment (MOXIE) and Implications for Atmospheric ISRU Processing Plants

by

Forrest Edward Meyen

Submitted to the Department of Aeronautics and Astronautics on
May 18, 2017 in Partial Fulfillment of the Requirements for the Degree of
Doctor of Philosophy in Aeronautics and Astronautics

Abstract

As humankind expands its footprint in the solar system, it is increasingly important to make use of Earth independent resources to make these missions sustainable and economically feasible. In-Situ Resource Utilization (ISRU), the science of using space resources to support exploration missions, unlocks potential destinations by significantly reducing the mass to be launched from Earth. Mars is considered a promising location with significant indigenous resources. The carbon dioxide that comprises nearly 96% of the Martian atmosphere can be utilized to produce oxygen for propulsion and life support systems.

The Mars Oxygen ISRU Experiment (MOXIE) is a payload being developed by NASA for the Mars 2020 mission. MOXIE will demonstrate oxygen production at a rate of at least 6 grams per hour from the Martian atmosphere by using solid oxide electrolysis (SOXE) technology. Individual SOXE cells form a 10-cell SOXE stack. The stack consists of two 5-cell groups to generate oxygen and carbon monoxide molecules from a CO_2 electrolysis reaction. MOXIE is the first step to creating an oxygen processing plant that might enable a human expedition to Mars in the 2030s through the production of the oxygen needed for the propellant for a Mars Ascent Vehicle (MAV).

MOXIE will be the first demonstration of ISRU on another planet. The goal of this program is to learn what technological advancements are needed for development of larger scale ISRU systems to support human spaceflight missions. This thesis studies solid oxide electrolysis based atmospheric ISRU systems from a controls and system performance perspective. The purpose is to use the results of this analysis to inform MOXIE operation and the design of a full-scale ISRU system for Mars.

A novel, tunable grey electrochemical model is developed from experimental characterization and used to predict oxygen production and safe operational limits for MOXIE. This model is then incorporated into the first multi-domain physical system model of a solid oxide electrolysis system implemented in Simscape. This model, named SimSitu, is used to test MOXIE control interactions and performance. A new control system, The Safe Margin Active Reduction Tracking (SMART) controller is proposed to safely maximize oxygen production from MOXIE. A strategy for characterizing and selecting space flight SOXE stacks based on discoveries from experimental results is also proposed. The models and lessons learned from MOXIE are then applied to make scaling estimates and recommendations for a full-scale ISRU system.

Thesis Supervisor:
Jeffrey A. Hoffman, Professor of the Practice in Aeronautics and Astronautics

Acknowledgements

I have been blessed to work on MOXIE as the topic of my doctoral research. Participating in the creation of a Mars-bound experiment taught me much more than modeling and control approaches to solid oxide electrolysis. Teamwork, communication, and politics are as central to a space mission as technological knowhow. People make space exploration happen, and similarly, people made this thesis and my entire doctoral journey at MIT possible. I would like to acknowledge the people who helped me during my time at MIT.

My advisor, Professor Jeffrey Hoffman, was my unwavering supporter throughout the years. You helped me navigate the doctoral process and navigate our canoe to the best fishing spots. Thank you for welcoming me to the MOXIE team. I am honored to have been your student.

My other committee members, Joseph Hartvigsen and Professor Bilge Yildiz were instrumental to the success of this research. Thank you Joe for hosting me at Ceramatec during my experiments. I greatly enjoyed the time I spent in Utah.

Thank you to the MOXIE PI and thesis reader, Michael Hecht. I learned a lot from you about the flight mission process. I also enjoyed your company during our adventures to JPL, conferences, and serving as co-Grand Marshals of the Moxie soda parade.

Thank you to Koorosh Araghi for being an official reader of my thesis. Also thanks to those who gave me feedback on chapters and presentations including Jerry Sanders, Carl Guernsey, Don Rapp, and Gerald Voecks.

MIT staff work the scenes to make everything possible. Thanks to Liz Zotos, Beth Marois, Quentin Alexander, Todd Billings, and Mark Belanger. I also appreciate the hard work of my undergraduate students who helped with the research, Maya Nasr, Sean Parks and Andrew DeNucci. Best wishes to Eric Hinterman who will move the research forward for his graduate degree.

Thanks to everyone at the Man Vehicle Laboratory, Graduate Association of Aeronautics and Astronautics, and MIT Emergency Medical Services for being there for non-academic diversions such as trips to the Muddy, sailing, IM sports, ski trips, 5 HST formals and trips to all parts of the globe. We have made so many great memories. I will miss all my students at Next House, who have added a new dimension of adventure to my time here. Thanks to the MIT Summer Research Program, especially Christopher Jones and Monica Orta for introducing met to MIT and encouraging me to achieve my dreams.

My parents read every word of my thesis, thanks for your support.

Thanks to my wife Rachel for joining me on this journey. I could not have done this without your love and encouragement.

I acknowledge my funding sources, including the National Science Foundation Graduate Research Fellowship Program, which funded 3 of the years I have been at MIT. Thanks to Aero/Astro Unified Engineering TA for covering my funding until the MOXIE budget came through. MOXIE was supported by NASA through the Human Exploration and Operations Mission Directorate (HEOMD), Space Technology Mission Directorate (STMD), and the Science Mission Directorate (SMD).

Table of Contents

List of Abbreviations

ASR	Area Specific Resistance [Ω-cm^2] represents SOXE cell resistance
ASR_{app}	Approximate Area Specific Resistance [Ω-cm^2] low accuracy measurement used as a historical development benchmark, calculated with only 1 sample point
ASR_{lin}	Linear Area Specific Resistance [Ω-cm^2] accurate for normal SOXE operation in the linear region of i-V curve. Changes with flow condition and temperature.
ASR_{int}	Intrinsic Area Specific Resistance [Ω-cm^2] (or ASR_{cc}) a conversion corrected ASR term. Reflects the portion of ASR, attributed to cell ohmic and other minor cell resistances. Changes with temperature.
CAC	Carbon Dioxide Acquisition System
CAS	Characterization and Analysis Sensors
CBE	Current Best Estimate
CDR	Critical Design Review
CFY	Chromium-Iron-Yttrium
CSA	Ceramatec Stack Assembly (identifier for experimental SOXE stacks)
DRM	Design Reference Mission
DSN	Deep Space Network
ELEX	Electronics
ERV	Earth Return Vehicle
FPGA	Field-Programmable Gate Array
GC	Gas Chromatograph
GSE	Ground Support Equipment
HLLV	Heavy Lift Launch Vehicle
HMO	High Mars Orbit
IMLEO	Initial Mass to Low Earth Orbit
I	Current [A]
i	Current density [A/cm^2]
ISRU	In-Situ Resource Utilization
JPL	Jet Propulsion Laboratory
JSA	JPL Stack Assembly (identifier for experimental SOXE stacks)
LMO	Low Mars Orbit
LSM	Lanthanum Strontium Manganite
MAV	Mars Ascent Vehicle
MCS	Monitor and Control System
MEDA	Mars Environmental Dynamics Analyzer
MIT	Massachusetts Institute of Technology
MOXIE	Mars Oxygen Institute Resource Utilization Experiment
mT	Metric Ton (1,000 kg)

NASA	National Aeronautics and Space Administration
PDR	Preliminary Design Review
PID	Proportional Integral Derivative
RAMP	Rover Avionics Mounting Panel
RCE	Rover Compute Element
RCT	Run Control Table
RTG	Radioisotope Thermoelectric Generator
RWGS	Reverse Water Gas Shift
S/cm	Siemen/cm (unit of ionic conductivity)
sccm	Standard Cubic Centimeters per Minute
SOFC	Solid Oxide Fuel Cell
Sol	Day on Mars (duration is 24.66 Earth hours)
SOE	Solid Oxide Electrolysis (refers to the physical process)
SOFC	Solid Oxide Fuel Cell
SOXE	Solid Oxide Electrolysis (refers to MOXIE SOE Device)
STPA	System Theoretic Process Analysis
TPTO	Two Phase To Orbit
T/W_o	Thrust to weight (in Earth g's)
V	Voltage [V]
V_{add}	Additional voltage [V] intercept when calculating ASR_{lin}
V_{act}	Activation potential [V]
VFCD	Viscous Flow Control Device
YSZ	Yttria-Stabilized Zirconia

List of Figures

List of Tables

1. Introduction

1.1 Problem statement and objectives

As humankind expands its footprint in the solar system, it is increasingly important to use the resources existing throughout our solar system to make exploration economically feasible and sustainable. In-Situ Resource Utilization (ISRU), the science of using space resources to support exploration missions, unlocks travel to more destinations by significantly reducing the mass required to be launched from Earth (Drake 2009). Carbon dioxide is an example of an in-situ resource that comprises nearly 96% of the Martian atmosphere (Mahaffy, Webster et al. 2013) and can be used as a source of oxygen for propellant and life support systems (Ash, Dowler et al. 1978). To develop the technology needed for Martian ISRU, NASA is developing the Mars Oxygen ISRU Experiment (MOXIE) as a payload aboard the Mars 2020 rover (Hartvigsen, Elangovan et al. 2015, Rapp, Hoffman et al. 2015, Meyen, Hecht et al. 2016). MOXIE will produce oxygen from the Martian atmosphere using a process called solid oxide electrolysis. MOXIE is about 0.5% of the scale of an oxygen processing plant that could enable a human expedition to Mars in the 2030s through the production of the oxygen needed for the propellant of a Mars Ascent Vehicle (Rapp, Hoffman et al. 2015).

1.1.1 Problem statement

In space mission architecture design, initial mass to low Earth orbit (IMLEO) is often used as a first order measure of cost (Drake 2009). Therefore, extreme diligence is put into minimizing the mass of all components used to support a space mission. The reduction of the propellant mass required for space missions has the potential to dramatically reduce costs because propellant mass comprises most of a launch vehicle's mass. ISRU allows the production of propellant from space-based resources so that it no longer consumes valuable launch vehicle mass on Earth. For this reason, NASA is pursuing ISRU technology as a "cross-cutting" technology needed for the sustainable exploration of Mars (Drake 2009).

A manned trip to Mars has a massive potential to benefit from ISRU technology. Oxygen that could be extracted from the Martian atmosphere would comprise 78% of the mass of a LOX/Methane type rocket for a Mars Ascent Vehicle (MAV) that could be used to leave the surface of Mars. This represents an estimated 22.7-29.3 mT of oxygen (Polsgrove, Thomas et al. 2015, Rapp, Hoffman et al. 2015) that would otherwise need to be launched from Earth and landed on Mars. ISRU enables the reduction of Initial Mass to Low Earth Orbit (IMLEO) by up to 336 mT (Rapp, Hoffman et al. 2015). Oxygen ISRU production could save nearly 3 SLS launches at a 130 metric ton capacity (United States Senate 2010) and billions of dollars (Strickland 2013).

The Viking Mars landers of the 1970s greatly enhanced our understanding of the atmospheric composition of Mars. (Nier and McElroy 1977, Soffen 1977). This data enabled Ash, Dowler et al. (1978) from the NASA Jet Propulsion laboratory to develop the first concepts of Martian ISRU in their study "Feasibility of rocket propellant production on Mars." Since then, the need for ISRU to support Mars missions has been cited in reports including the "Pioneering the Space Frontier" report by the National Commission on Space (Paine 1986), the "Mars Direct Architecture" (Zubrin, Baker et al. 1991), the first NASA Design Reference Mission (Hoffman and Kaplan 1997), and the latest NASA Design Reference Mission 5 (Drake 2009). In addition to these mission architecture studies, numerous other studies have been conducted to develop the required technologies for Martian ISRU with a focus on ISRU products derived from the Martian atmosphere (Richter 1981, Frisbee, French Jr et al. 1987, Ramohalli, Dowler et al. 1987, Ramohalli, Lawton et al. 1989, Sridhar, Iacomini et al. 2004). NASA DRM 5 expanded Mars ISRU architecture evaluation to include regolith water processing options in light of an improved understanding of Martian regolith water content. Sanders, Paz et al. (2015) presented an extended summary of the current state of the art of Mars ISRU studies. Most of these systems consist of processing Martian resources such as atmospheric CO_2 for a carbon and oxygen source, and water trapped in regolith for a hydrogen and oxygen source. Other critical buffer gases for the life support systems such as nitrogen can be extracted from the atmosphere, adding greater redundancy to the life support system.

The specifics of implementing a robust and sustainable ISRU plant to support human Mars missions are still debated. No ISRU technology has yet to be tested during any space mission (Sanders and Larson 2011). Several technologies have been identified and evaluated at a high level in ISRU system design studies, as well as demonstrated on Earth through analogue field tests (Sanders and Larson 2011). Potential technology options include atmospheric oxygen production only, production of oxygen and methane (or other hydrocarbons) using atmospheric oxygen and a hydrogen source, and processing of regolith water to produce hydrogen and oxygen. Most proposed ISRU systems make use of the products of multiple chemical processes which may include CO_2 electrolysis, water electrolysis, the reverse water gas shift (RWGS), Sabatier reaction, Bosch reaction, steam reforming, and methane reformation (Sanders, Paz et al. 2015).

Only one other ISRU system, the Mars ISPP Precursor (MIP), has undergone the rigor of preparing for a flight mission (Kaplan, Baird et al. 2000), and no ISRU plant has ever been flown in space. Thus, the information we have about these systems is missing many of the "unknown unknowns" that are discovered during a mission. Details such as safe operation and control of ISRU systems, ISRU reactor performance, and the impact of mission constraints on mass and energy requirements can only be explored as part of such a challenge. The Mars Oxygen In-Situ Resource Utilization Experiment (MOXIE) presents an unprecedented opportunity to evaluate systems engineering methodologies for the development of an ISRU plant, to learn more about its feasibility and operation, and to thoroughly evaluate solid oxide electrolysis technology.

1.1.2 Objectives

This thesis contributes to the design of the MOXIE payload. Additionally, it uses the development of MOXIE to gain the scientific understanding to size the design of a human mission scale ISRU system to a level of detail and accuracy beyond what has been achievable before the existence of an ISRU flight project to the scale of MOXIE.

This thesis explores different levels of scale and abstraction, both in modeling and control design. The MOXIE payload development is used to create and verify models. The resulting analysis contributes to the design of MOXIE. The ultimate objective is to achieve the greatest understanding possible for the design and operation of an ISRU plant sized to enable a human mission to Mars. Each level of scale strengthens the next. System engineering methodologies inform the system model and control design. The system models feed parameters to the solid oxide electrolysis model. All levels provide new insights into the development of an ISRU system that can create the propellants needed to return astronauts to the Earth from the surface of Mars.

Modeling solid oxide electrolysis

At the smallest scale, this thesis develops electrochemical models to calculate the flow of oxygen ions though the solid oxide electrolyzer. The performance of each cell depends on applied voltages, temperatures, gas compositions, degradation rates, and design. Cathode materials and operating voltages affect degradation risk. Individual cells comprise a solid oxide electrolysis stack, which informs the system production rate, power consumption, and mass of the SOXE, the heart of the MOXIE ISRU system. The SOXE development process has made significant technological advances during the MOXIE program. Data derived from the testing and characterization of these cells informs models that create the best understanding to date of what can be expected for ISRU supporting a crewed Mars mission.

Differentiating features of the Mars bound SOXE unit compared to Earth based systems include chromium-iron-yttrium (CFY) interconnects, specialized glass seals, and a mechanical clamping system. All components are designed to harden the SOXE against the tough conditions of Mars's comparatively low pressure and low temperature environment, and to overcome the pressure differential between the interior of the stack and Mars ambient conditions. These additions affect estimates for the mass required for a full-scale ISRU plant. Furthermore, the MOXIE program has enabled significant development of cell materials to improve robustness and performance - developments that improve scale performance estimates.

SimSitu, a multi-domain physical modeling framework for ISRU systems

SOXE stack power, inlet gas feed, and cell temperatures are supported by the larger ISRU plant system. These systems include a scroll pump, heaters, power supplies, mechanical support, sensors, and control systems that are not detailed in the SOXE model alone.

To understand the system in a holistic and integrated manner, this thesis develops a multi-domain, physical model of the MOXIE system. The goal is to capture the system dynamics and interactions as a tool for testing control concepts and component interactions. Multi-domain physical modeling enables the system model to be decomposed by electrical, pneumatic, thermal, and control domains. The result is a modular model where each domain can be independently tuned and verified. The SOXE models mentioned above are included in this multi-domain physical model.

System trades for an extensible Mars atmospheric ISRU processing plant

Insights from the experimental characterization, physical system model, and control system development are used to create an extensible system model of a solid oxide electrolysis based, atmospheric ISRU plant to support a human Mars exploration mission. This model shows the impact of trades between designed plant flow, required SOXE cell count, system mass, and power. The results are intended to be used by ISRU system designers to highlight considerations in design of a system for a crewed mission.

1.2 Research questions

The specific research questions that are addressed in this thesis are:

1. What is the expected performance of solid oxide electrolysis cells for CO_2 electrolysis on Mars? How do operational range limits and degradation affect system performance? What time scale is important for modeling SOXE effects on a systems level?

As part of the discovery process, the following Hypotheses are presented:

> Hypothesis 1: *SOXE cell-to-cell variation observed in stacks is caused by variability in material processing. A modeling approach that characterizes current-voltage trends and shifts these values with respect to a characterized ASR for each cell can be used to accurately describe the full envelope performance of a stack.*
>
> Hypothesis 2: *SOXE cells can be represented accurately by the approximate ASR equations that represent the ASR as the slope of a linear, current density – voltage (i-V) curve with an intercept of the open circuit voltage (OCV). This equation is assumed to be valid if little to no activation potential is observed.*

2. Given the understanding of system components, hazards, and interactions, how should the MOXIE system be controlled and operated?

3. What are the mass and power requirements of a human mission ISRU system, given recent MOXIE developments in the understanding of solid oxide electrolysis performance and degradation and compressor performance? What design recommendations can be derived from the development of MOXIE?

1.3 Research approach

Given the recent developments in the understanding of ISRU systems and technological advances derived from the MOXIE program, the proposed thesis will seek to answer the research questions by using these research approaches:

> Research approach 1 is to apply grey modeling to the solid oxide electrolysis process to predict the effects of SOXE performance and SOXE degradation on atmospheric ISRU system design and control.
>
> Research approach 2 is to apply a multi-domain physical modeling (SimSitu) approach from the field of model-based systems engineering to understand control interactions during ISRU system design and development.
>
> Research approach 3 is to apply the results from SimSitu, knowledge from electrochemical characterization, and a selected system control scheme to assess trades for crewed Mars mission ISRU system design.

1.4 Thesis contributions

This thesis contributes to the fields of ISRU, system development, and modeling of solid oxide electrolysis cells. Below is a summary of these contributions.

1. A novel, tunable grey SOXE model to predict oxygen production performance
    a. This model is developed and verified with testing at a range of stack operating parameters
    b. The model is tunable to a specific stack after a shortened characterization process
    c. The model is verified by comparing outputs from stack characterization data
2. A multi-domain physical model, called SimSitu, which can be used to test control schemes for MOXIE and full scale atmospheric ISRU systems
    a. Framework for multi-domain model of ISRU systems
    b. Model components are validated through component characterization data
    c. Alternative control concepts are demonstrated

3. Creation of the Safe Margin Active Reduction Tracking (SMART) control algorithm for control of solid oxide electrolysis systems
4. The first atmospheric ISRU system mass and power estimates based on data derived from the development of MOXIE, a Mars-bound ISRU experiment. This data will be published for use by others for studying ISRU architecture design trades
   a. Standard set of mission requirements to base production requirements
   b. Maximum achievable performance of a scale system

1.5 Description of thesis chapters

This thesis is organized into 7 chapters. Chapter 1 is the thesis introduction, including the problem statement, research questions, objectives, and approach. Chapter 2 describes the background of ISRU for the support of Mars missions. This chapter also details types of ISRU methods for Mars, describes solid oxide electrolysis, and summarizes the MOXIE system. Next, Chapter 3 establishes a SOXE modeling framework. The models presented in this chapter are primarily "white" physics-based models that do not require major MOXIE-specific characterization of the SOXE cells to implement. Chapter 4 describes the experimental process to collect empirical characterization data from the SOXE cells. Chapter 4 publishes the results of these characterization experiments, which are used to develop a "grey" SOXE model in chapter 5. Chapter 5 describes the SimSitu multi-domain physical system model and verifies these components, analyzes SOXE control methods using System Theoretic Process Analysis (STPA), and demonstrates system control response. Chapter 6 covers the extensibility of MOXIE and scaling the system to a human Mars mission. The results are derived from SimSitu assuming ideal performance and the SMART control developed in chapter 5. The thesis concludes with chapter 7, providing recommendations for MOXIE and suggestions for future work.

2. Background

In-situ resource utilization (ISRU) refers to methods and technologies for harvesting resources on-site to use in space exploration activities. ISRU methodologies are dependent on the types of resources at the point of interest. Mars has several valuable resources that can be used to support Mars missions. The atmosphere is a combination of CO_2, Ar, N_2, CO, H_2O, and other gases. The Martian regolith contains various elements including a water content that varies depending on location. Potential ISRU products include rocket fuel and oxidizer, life support gases, buffer gases for life support, fuel for exploration vehicles, and materials for habitat and infrastructure construction.

The Mars environmental data from the Viking missions (Soffen 1977) created an understanding of potential ISRU resources on Mars. This enabled Ash, Dowler et al. (1978) to conduct the first comprehensive study into the feasibility of Mars ISRU. In this study, Ash, Dowler et al. (1978) identified atmospheric CO_2 as the most promising resource to exploit for ISRU. Regolith water was also identified. Even though the water content was uncertain at the time, the primary architecture presented included its use.

The concept of ISRU eventually made it into official policy direction with the 1986 "Pioneering the Space Frontier" report of the National Commission on Space. This report called for NASA's augmented technology program to include "vigorous development" of ISRU technologies, including propellant production, to reduce the cost of exploration of the inner Solar System (Paine 1986). The exploitation of Martian resources was specifically noted. "In principal, oxygen, hydrogen, water, nitrogen, fertilizer, and methane, as well as other compounds, could all be extracted from the atmosphere of Mars."

Zubrin, Baker et al. (1991) presented the case for pursuing an ISRU first strategy for a manned mission to Mars when describing their "Mars Direct" approach. They argued that the development of ISRU technology was more mature than nearly everything else in development at the time for a Mars mission. Strategies that proposed bringing everything to Mars on the first mission and then working ISRU into future missions for sustainability would be an example of waste by developing one technology (the non-ISRU approach) while also building the hardware to make the first approach obsolete.

Drake (2009) presented a clear endorsement of ISRU technology for Mars missions for DRM 5.0. The findings are summarized in Table 1 below.

Table 1 – ISRU recommendation summary from NASA DRM 5.0 (Drake 2009)

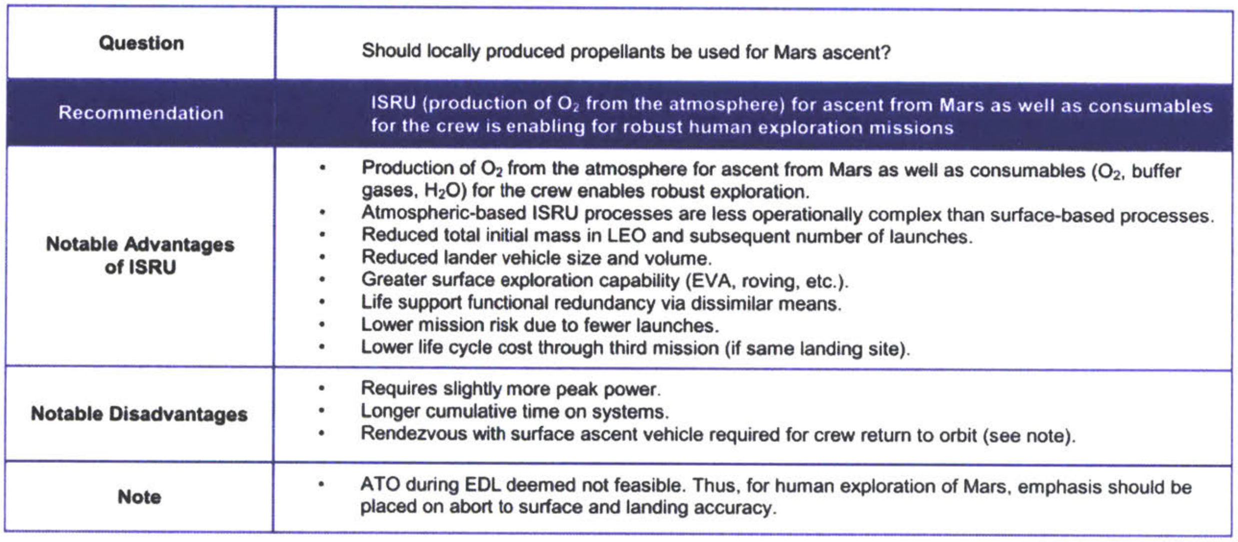

Question	Should locally produced propellants be used for Mars ascent?
Recommendation	ISRU (production of O_2 from the atmosphere) for ascent from Mars as well as consumables for the crew is enabling for robust human exploration missions
Notable Advantages of ISRU	• Production of O_2 from the atmosphere for ascent from Mars as well as consumables (O_2, buffer gases, H_2O) for the crew enables robust exploration. • Atmospheric-based ISRU processes are less operationally complex than surface-based processes. • Reduced total initial mass in LEO and subsequent number of launches. • Reduced lander vehicle size and volume. • Greater surface exploration capability (EVA, roving, etc.). • Life support functional redundancy via dissimilar means. • Lower mission risk due to fewer launches. • Lower life cycle cost through third mission (if same landing site).
Notable Disadvantages	• Requires slightly more peak power. • Longer cumulative time on systems. • Rendezvous with surface ascent vehicle required for crew return to orbit (see note).
Note	• ATO during EDL deemed not feasible. Thus, for human exploration of Mars, emphasis should be placed on abort to surface and landing accuracy.

The following background describes the history of Mars ISRU systems including early concepts and architectures. Next, solid oxide electrolysis and some of the related work studying solid oxide electrolysis for ISRU is described. Finally, a baseline description of MOXIE is presented to motivate the rest of the thesis.

2.1 ISRU for Mars system architectures: origins and early concepts

Ash, Dowler et al. (1978) planned a 400-day, 2-man surface mission using a conjunction-class trajectory. The ISRU system and return vehicle would be launched one trajectory opportunity ahead of the astronauts, allowing for 693 days of propellant production. With the estimated dry landed mass of 4200 kg, the ISRU system was required to produce 13,850 kg of total propellant at a rate of 20 kg per day.

Oxygen was to be the oxidizer. H_2, CO, CH_4, C_3H_8, C_4H_{10}, and CH_3OH were considered for fuels. CH_4 was favored because of its ease of production compared to the more complex hydrocarbons and preferred over H_2 because of its higher liquefaction temperature.

The described propellant production method was a water electrolysis reaction (Equation (2.1) below) to produce hydrogen and oxygen. The hydrogen feeds a Sabatier reaction (Equation (2.2) below) with atmospheric carbon dioxide to produce methane. Excess water produced by the Sabatier reaction can be recycled to provide some of the water in the electrolysis reaction.

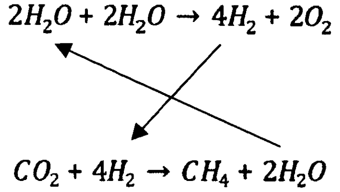

$$2H_2O + 2H_2O \rightarrow 4H_2 + 2O_2 \tag{2.1}$$

$$CO_2 + 4H_2 \rightarrow CH_4 + 2H_2O \tag{2.2}$$

Water can be recovered from the Sabatier reaction for use in the electrolysis reaction. The oxygen produced from electrolysis is stored for use as an oxidizer.

Water was to be extracted by using autonomous rovers to excavate regolith to feed batch-processing evaporators. The carbon dioxide collection system selected was a cryocooler because of concerns about the high-power consumption of vacuum pumps and the difficulty of filtering out Martian dust at 6.6 mbar with a small, tolerable pressure drop. A schematic of the entire system scaled for a Mars sample return mission can be seen in Figure 1.

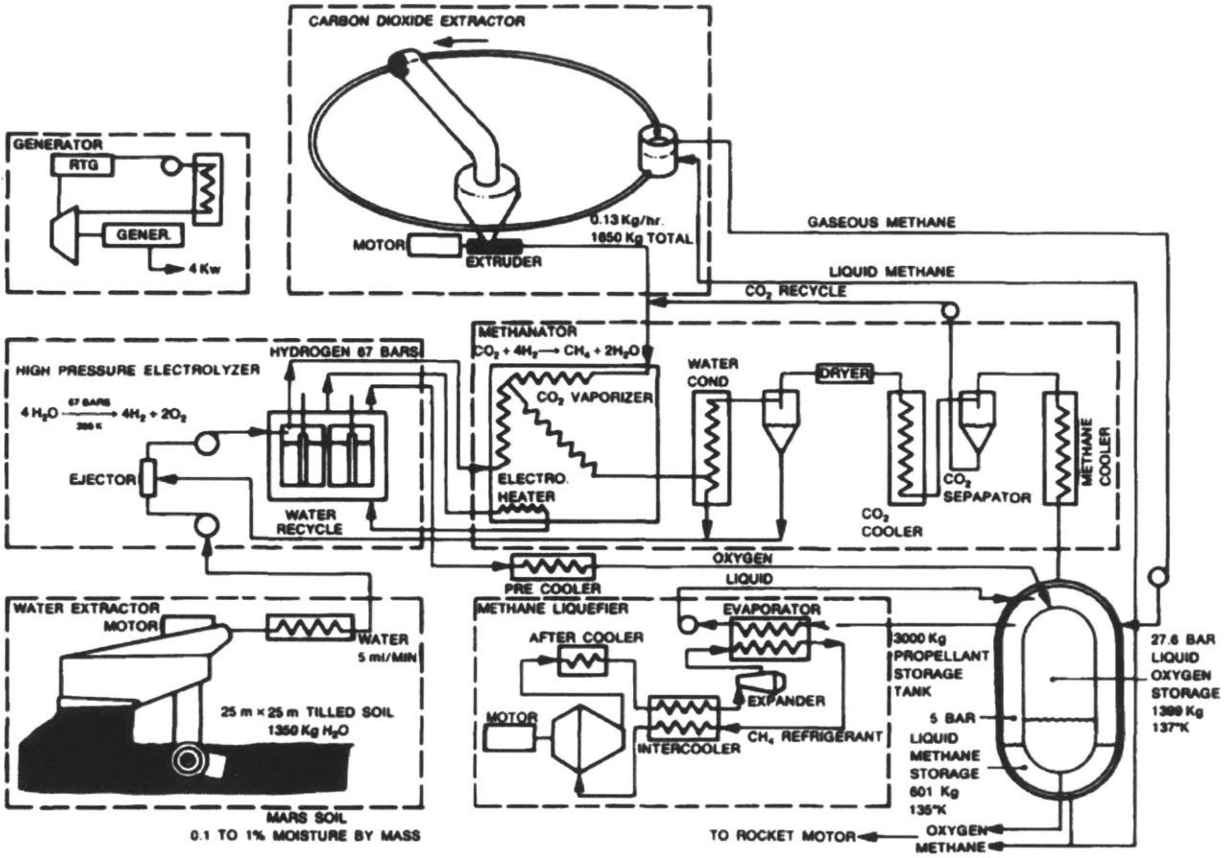

Figure 1 – Schematic of a Martian refueling station for a Mars sample return mission (Ash, Dowler et al. 1978)

Ash, Dowler et al. (1978) concluded that ISRU for Mars appears feasible and could reduce landed mass by over 50%. Their seminal paper spurred many other studies exploring ISRU for both a Mars sample return and human Mars missions.

Ramohalli, Lawton et al. (1989) expanded on the work of Ash, Dowler et al. (1978) and explored the use of ISRU for a Mars sample return mission. The ISRU architectures described to support the sample return architecture in this paper were originally developed by Frisbee, French Jr et al. (1987). The ISRU designs included an atmospheric-only based O_2 production plant that supplies O_2 to combust with CH_4 propellant brought from Earth. Ramohalli, Lawton et al. (1989) discussed three variants of the O_2 production-only ISRU systems. All three systems would use solid oxide electrolysis (Equation (2.3) below) to extract CO_2 from the atmosphere.

$$2CO_2 \rightarrow 2CO + O_2 \tag{2.3}$$

The variants were largely similar except for a few components. Option 1 used compressors to achieve an inlet cell pressure of 28 mbar. A solid oxide electrolysis cell was used to produce oxygen. A second compressor and two radiators were described to compress and cool the product O_2 for use in liquefaction tanks. Figure 2 is a schematic of option 1 with spare compressors, cells, and refrigeration units.

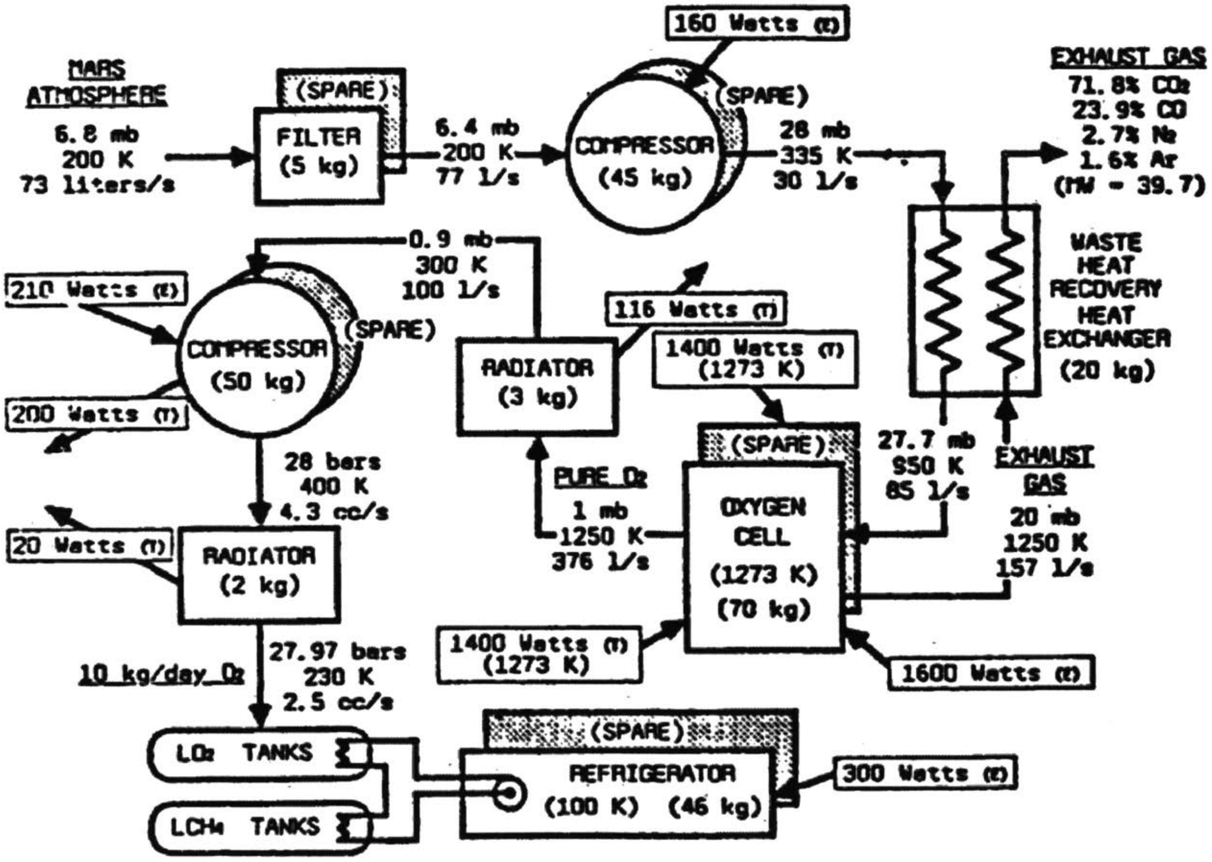

Figure 2 – Option 1 ISRU system with deal compressors (Ramohalli, Lawton et al. 1989)

Option 2 was distinguished from option 1 in that the first CO_2 compressor was replaced with a CO_2 adsorption pump. The solid oxide electrolysis (SOE) unit input pressure was increased to 1 bar. An improved electrolysis cell consumes 936 W compared to the 1600 W of option 1. An improved refrigerator was also selected.

The design for option 3 sought to eliminate the need for rotating machinery all together. Both pumps were replaced with adsorption type pumps. CO_2 would be delivered to the SOE cell and the effluent O_2 electrochemically compressed to an outlet pressure of 4 bar before entering the radiator and second adsorption compressor. For additional electrochemical compression, the authors proposed replacing the second adsorption compressor with another electrolytic cell.

Ramohalli, Lawton et al. (1989) evaluated these ISRU system options by ranking the developmental risk factors for each of the system components. Risk was assessed from a 1-5 scale. The highest risk included the SOE cell (4) because of risks of seal and membrane durability and challenges to achieving adequate current density, and the CO_2 Compressor (4) because of degradation under continual operation. The secondary CO_2 compressor was also rated a 4 because of the challenges associated with compressing from 1 mbar to 28 bar. The filters were rated as a risk factor 3 for the compressor based option. The outlook for the filters was improved to a 2 with the CO_2 adsorption pump architecture because of the potential to blow dust off the filters. All adsorption pumps were ranked 3 for risk, although O_2 adsorption pumps were less developed than CO_2 adsorption pumps.

2.1.1 Evolution of ISRU mission architectures for Mars

The Mars Direct mission architecture was described by Zubrin, Baker et al. (1991) as a Mars mission designed with "simplicity, robustness, and cost effectiveness" in mind. The cornerstone of this architecture is the use of ISRU technology to reduce costs and increase mission reliability. Mars Direct improves on the reliability of the Mars architecture described by Ash, Dowler et al. (1978) by producing O_2 at a faster rate so that the Earth return vehicle (an alternative to the Mars Ascent Vehicle or MAV described by other authors) could be fully fueled before the manned mission departs Earth.

Mars Direct takes an approach similar to Ash, Dowler et al. (1978) in creating methane using the Sabatier reaction (Equation (2.1) above) while coupling that reaction with water electrolysis (Equation (2.2) above). The primary difference is that Mars Direct does not depend on the processing of Martian regolith to extract water. Rather, 6 mT of hydrogen are transported from

Earth to the surface of Mars. The hydrogen is then reacted catalytically (Sabatier) with atmospheric CO_2 to produce 24 mT of methane and is stored. Water produced from the Sabatier process is electrolyzed to create 48 mT of O_2. Because the proper mixing ratio of oxygen to methane is 3.5:1 (to achieve an ideal specific impulse of 373s) a CO_2 electrolysis process is also conducted to produce an additional 36 mT of oxygen from the Mars atmosphere (Zubrin, Baker et al. 1991). From the original 6 mT of hydrogen brought from Earth, 108 mT of propellant is synthesized. Of that, 11 mT is allocated to power CH_2/LOX surface vehicles.

Zubrin, Baker et al. (1991) identified CO_2 acquisition as the rate-limiting step in synthesizing CH_4 through the Sabatier process. Mechanical compressors were considered sufficient, but liquefaction of CO_2 was suggested after partial mechanical compression to reject inert compounds such as Ar and N_2. The energy cost to compress and liquefy CO_2 from the Martian atmosphere was calculated to be 0.08 kWe-hr/kg.

A key component of the Mars Direct mission is the continual pre-positioning of assets for the sustainability of future missions. The first launch would contain the ISRU system, and the second launch would not proceed until the Earth Return Vehicle (ERV) was fueled. The second launch would include two 40 ton Heavy Lift Launch Vehicles (HLLVs), one as a crewed landing platform and one as a second ISRU plant to be pre-positioned for the next mission. The second ISRU plant could be repositioned to land near the current crew if the crew lands outside of range of the pre-positioned ISRU plant. This strategy is an early variation of the "abort to surface" contingency that is adopted for future NASA Design Reference (DRM) missions such as DRM 5.0 by Drake (2009).

2.1.2 NASA Design Reference Missions

The NASA Design Reference Missions (DRM) represent NASA's best strategies for a Mars mission at the time of their publication. The NASA DRM's began in the late 1980's as a series of NASA case studies. These were followed by a 90-day study for human exploration to the Moon and Mars (Cohen 1989), The first design reference mission (DRM 1) was presented by Weaver, Duke et al. (1993). Subsequent NASA DRMs made improvements on the previous ones based on new analysis and technologies. Notable follow-ons described below include NASA DRM 3 (Hoffman and Kaplan 1997), which explored the use of an ISRU processing plant for ascent propellant and NASA DRM 5.0 (Drake, Hoffman et al. 2010) which expanded the feasibility analysis of ISRU for a Mars mission by including it in one of the study's 5 "decision packages."

NASA Design Reference Mission 3

NASA DRM 3 (Hoffman and Kaplan 1997) included two redundant ISRU processing plants. The first was to be delivered before the first manned missions and the second before the follow-up manned mission. Each system is required to produce enough oxygen for two Mars Ascent Vehicle (MAV) missions. Only the first produces backup life support gases. As in the Mars Direct architecture, the manned mission is not sent until the MAV is fueled. For the first mission, all water produced from the Sabatier process is stored for life support. All the oxygen for the MAV is produced through carbon dioxide electrolysis by means of solid oxide electrolysis (SOE).

The ISRU system depends on the Sabatier reaction to convert carbon dioxide and hydrogen at high temperatures to produce methane and water and is similar to the systems described by Ash, Dowler et al. (1978) and Zubrin, Baker et al. (1991). At the time of the publication, the amount of indigenous water on Mars was less certain so it was suggested that a supply of hydrogen be brought from Earth (also similar to Mars Direct (Zubrin, Baker et al. 1991)). The ISRU system described combines the Sabatier process, water electrolysis, carbon dioxide electrolysis, and buffer gas absorption to achieve ISRU system goals.

The ISRU system is designed to produce 20.2 mT of oxygen per MAV and 5.8 mT of methane. Backup requirements of the first ISRU system for redundant life support include the production of 4.5 mT of oxygen for breathing, 20.2 mT of oxygen for fuel, and 3.9 mT of N_2 and Ar for buffer gases. Solid oxide electrolysis is used to boost the combined Sabatier/water electrolysis system's 2:1 oxygen to methane production ratio to an appropriate oxidizer to fuel ration of 3.5 to 1 (Hoffman and Kaplan 1997). Figure 3 is a diagram of the ISRU system described in DRM 3.

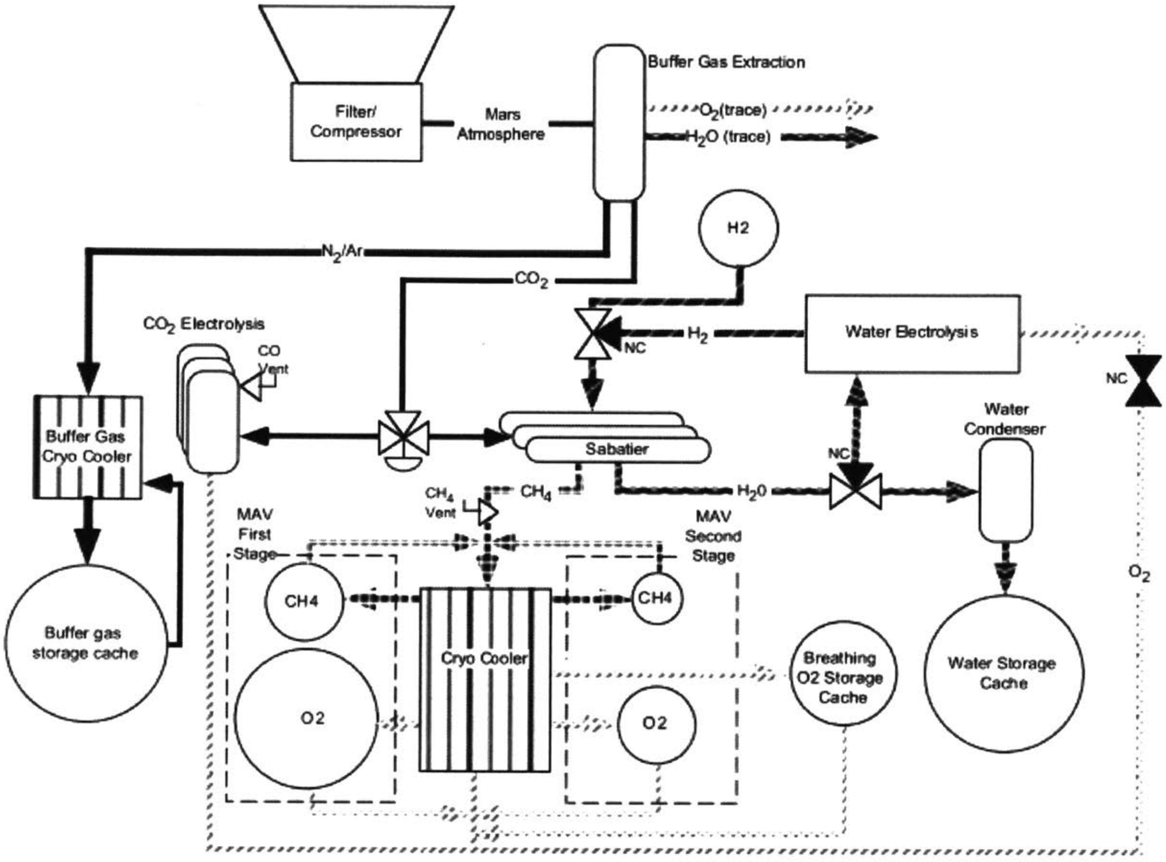

Figure 3 – First ISRU plan to arrive on Mars as presented in the Design Reference Mission (Hoffman and Kaplan 1997)

The second ISRU plant is smaller than the first because it is not producing backup consumables for the crew. A comparison of the mass and power requirements for the first and second ISRU plants can be seen in Table 2 and Table 3 below.

Table 2 - Mass and power estimates for the first ISRU plant (Hoffman and Kaplan 1997)

Plant Component	Production Rate (per day)	Component Mass (kg)	Component Power (kWe)
Compressor	269.7 kg	716	4.09
CO_2 Electrolysis	53.2 kg	2128	63.31
Sabatier	22.9 kg	504	1.15
H_2O Electrolysis	27.8 kg	778	0.00
Buffer Gas Extraction	8.7 kg	23	0.13
Cryogenic Coolers	84.8 kg	653	3.59

Table 3 – Mass and power estimates for the second ISRU plant (Hoffman and Kaplan 1997)

Plant Component	Production Rate (per day)	Component Mass (kg)	Component Power (kWe)
Compressor	87.8 kg atm	233	1.33
CO_2 Electrolysis	18.5 kg O_2	740	22.00
Sabatier	12.4 kg CH_4	272	0.62
H_2O Electrolysis	27.8 kg H_2O	778	5.79
Cryogenic Coolers	30.8 kg	238	2.3

NASA Design Reference Mission 5.0

The NASA DRM 5.0 Architecture (Drake 2009) represents one of the more recent manned Mars mission architectures. It was updated by an addendum in 2009 (Mars Architecture Steering Group 2009) and a second addendum in 2014 (Drake and Watts 2014). DRM 5 is centered on 6 crewmembers making a 6-month outward journey with an 18-month surface stay and a 6-month transit back to Earth. ISRU assets are pre-deployed and a Mars Ascent Vehicle (MAV) is tested and confirmed full before the crew departs Earth. A diagram of the proposed architecture is shown in Figure 4 below.

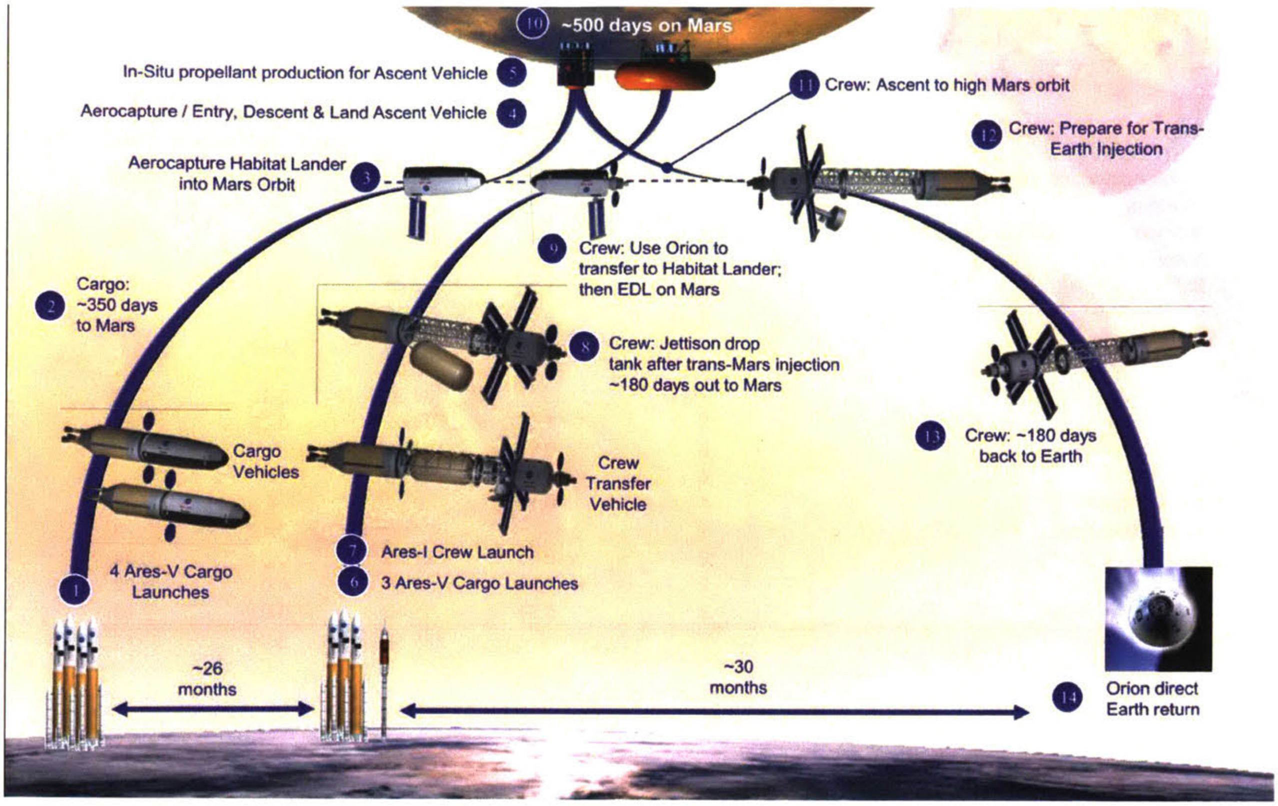

Figure 4 – Mars DRM 5.0 Architecture (Drake, Hoffman et al. 2010)

DRM 5.0 departs from many of the previous architectures in that only 400 kg of hydrogen is transported to Mars for creating water for life support. CH_4 fuel is brought from Earth to be used as fuel. The oxidizer is created using solid oxide electrolysis. N_2 and Ar processing is used to create a supply of buffer gases for the life support systems. Cryocoolers liquefy the O_2 and CH_4 for storage.

The mass power and volume estimates of the selected ISRU system are shown below. In the final architecture, two redundant systems are sent to the surface. Table 4 below describes the mass, power, and volume requirements for each of these systems.

Table 4 – ISRU system mass for DRM 5 (Drake 2009)

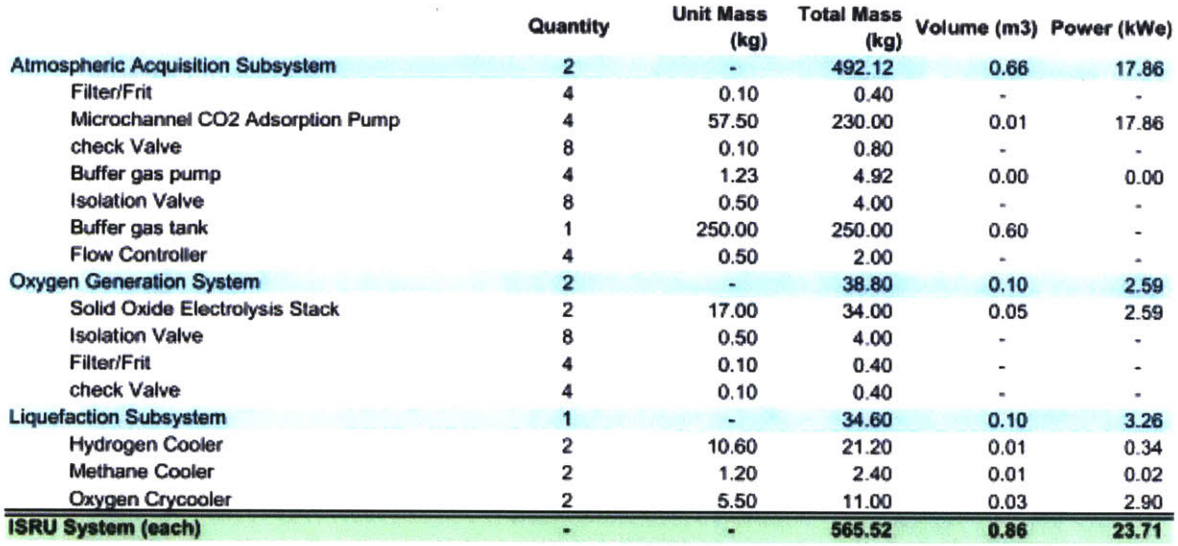

	Quantity	Unit Mass (kg)	Total Mass (kg)	Volume (m3)	Power (kWe)
Atmospheric Acquisition Subsystem	2	-	492.12	0.66	17.86
Filter/Frit	4	0.10	0.40	-	-
Microchannel CO2 Adsorption Pump	4	57.50	230.00	0.01	17.86
check Valve	8	0.10	0.80	-	-
Buffer gas pump	4	1.23	4.92	0.00	0.00
Isolation Valve	8	0.50	4.00	-	-
Buffer gas tank	1	250.00	250.00	0.60	-
Flow Controller	4	0.50	2.00	-	-
Oxygen Generation System	2	-	38.80	0.10	2.59
Solid Oxide Electrolysis Stack	2	17.00	34.00	0.05	2.59
Isolation Valve	8	0.50	4.00	-	-
Filter/Frit	4	0.10	0.40	-	-
check Valve	4	0.10	0.40	-	-
Liquefaction Subsystem	1	-	34.60	0.10	3.26
Hydrogen Cooler	2	10.60	21.20	0.01	0.34
Methane Cooler	2	1.20	2.40	0.01	0.02
Oxygen Crycooler	2	5.50	11.00	0.03	2.90
ISRU System (each)	**-**	**-**	**565.52**	**0.86**	**23.71**

To reach a conclusion that this was the best architecture at the time, Drake (2009) considered three ISRU options:

1. Atmospheric based O_2 production using solid oxide electrolysis. Bringing CH_4 from Earth to use as fuel
2. Atmospheric based O_2 and CH_4 production by the Sabatier process. Bringing Earth H_2
3. Regolith extraction of H_2O to produce O_2 and CH_4 with Sabatier and water electrolysis, evaluated at a regolith water concentration of 3% and 8%

Each system was evaluated for the delivered mass, volume, and power consumption. A plot comparing all systems is depicted in Figure 5 below.

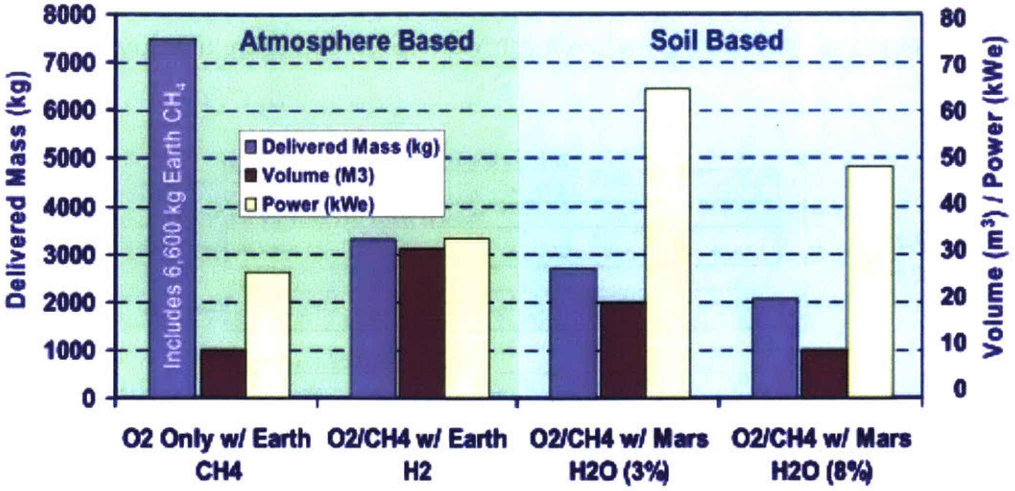

Figure 5 – Trade study of mass, volume, and power requirements of ISRU systems (Drake 2009)

Drake (2009) identified power as a limiting factor for ISRU. The regolith-based systems were the lowest mass and highest power options for ISRU. In locations where the regolith water concentration is 8%, the required power is greatly reduced. This suggests that regolith water based ISRU architectures may be more appealing at sites with certainty of high water concentration.

The systems that included the production of CH_4 from Earth H_2 and Mars CO_2 had significantly higher volume to transport H_2 but were lower mass than the O_2 only approach with Earth CH_4. The O_2 production with Earth based CH_4 ISRU system was ultimately selected because of the balance of mass savings with a low power requirement and total volume required.

2.2 Summary of the types of Martian ISRU identified

The previous summary of the evolution of ISRU strategies shows that the best approach to ISRU for Mars has evolved based on our knowledge of the planet and the progression of ISRU processing technologies. Almost all strategies make use of the production of O_2 for oxidizer, which comprises over 3/4ths of the propellant mass of a Mars Ascent Vehicle. Sanders, Paz et al. (2015) created a summary of the potential processing methods for Mars ISRU in Figure 6 below.

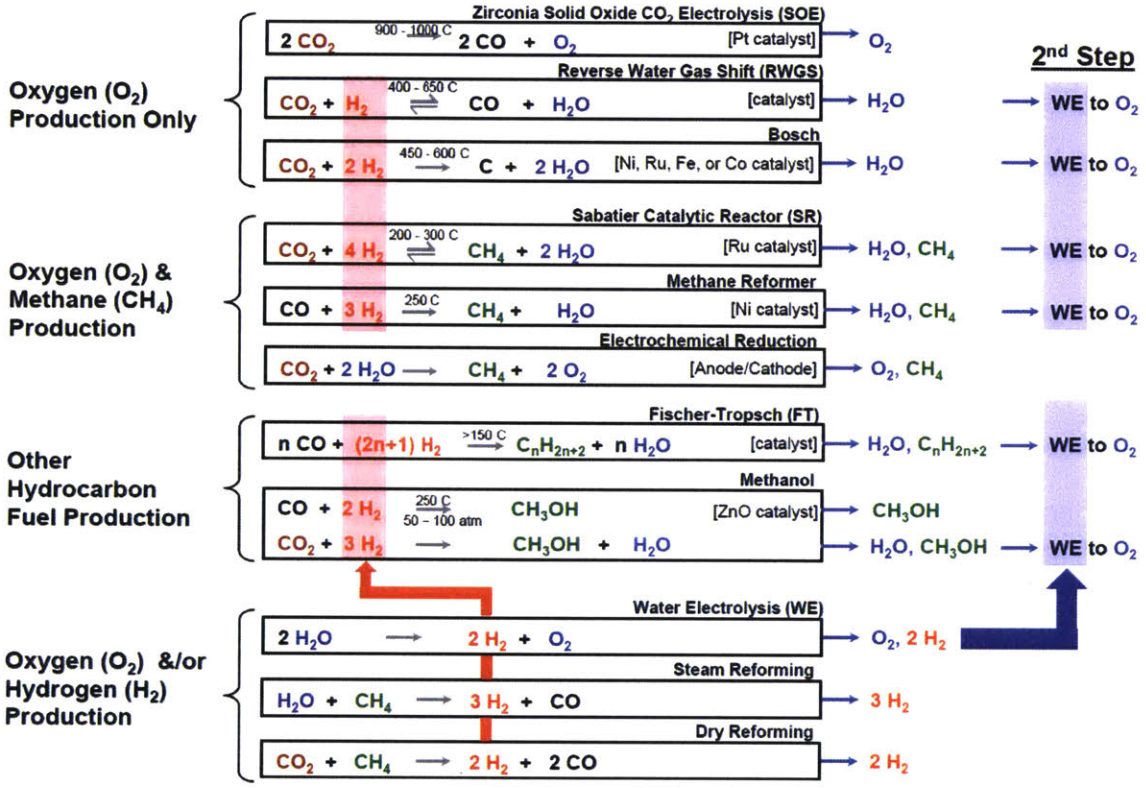

Figure 6 – The chemistry of Mars ISRU (Sanders, Paz et al. 2015)

The processes that can directly produce O_2 include solid oxide electrolysis, water electrolysis, and electrochemical reduction. Of those, only solid oxide electrolysis can produce O_2 from the Martian atmosphere alone. Water electrolysis is used after most of the other processes to produce O_2 from the water produced in those reactions. It should be noted that while the solid oxide electrolysis process shown details the production of O_2 alone, if enough water can be supplied to the process, solid oxide electrolysis could produce syngas in addition to O_2. Syngas is a combination of H_2, CO, and CO_2 that can be used to produce hydrocarbon fuels or as an intermediate process to produce ammonia, fertilizer, and even plastic precursors.

2.3 What is solid oxide electrolysis?

The simplicity and portability of an atmospheric processing ISRU system made it an obvious choice as an ISRU payload aboard the Mars 2020 rover. Wherever the rover might travel, in-situ resources will be available. The key technology that enables the extraction of O_2 from atmospheric CO_2 is solid oxide electrolysis.

In 1899, Walther Nernst discovered that oxygen can be conducted ionically through stabilized zirconia (Nernst 1899). This phenomenon has been applied to both the development of solid oxide fuel cells and solid oxide electrolysis cells. MOXIE produces O_2 through the process of high temperature CO_2 electrolysis through the application of a voltage across a yttria stabilized zirconia (YSZ) membrane. The net chemical reaction is:

$$2CO_2 \rightarrow 2CO + O_2 \qquad (2.4)$$

The solid oxide electrolysis cell (SOEC) and supporting system is referred to as the SOXE subsystem of the MOXIE instrument. A SOXE cell consists of a porous anode and porous cathode, separated by a zirconia ceramic electrolyte. The cathode includes catalytic sites that promote the reaction. Figure 7 below details the process.

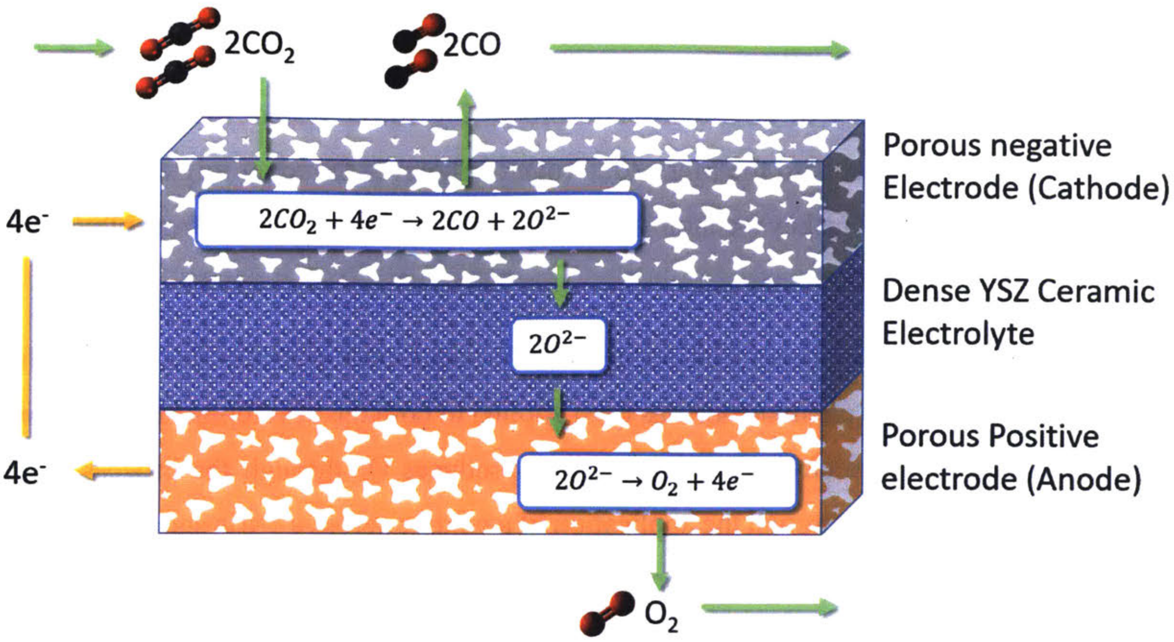

Figure 7 – Reactions across a SOXE cell (Meyen, Hoffman et al. 2015)

As the CO_2 flows through the porous cathode, the CO_2 contacts catalytic sites while an electronic potential is applied. The CO_2 is reduced to CO and an O^{2-} ion.

$$2CO_2 + 4e^- \rightarrow 2CO + 2O^{2-} \tag{2.5}$$

The potential drives the charged O^{2-} ions through the yttria-stabilized zirconia (YSZ) electrolyte. Once in the positive electrode material, two O^{2-} ions are oxidized per O_2 molecule formed.

$$2O^{2-} \rightarrow O_2 + 4e^- \tag{2.6}$$

2.4 Solid oxide electrolysis developments for Mars exploration

2.4.1 Early Mars SOE technology developments

Solid oxide electrolysis (SOE) is a technology that has been pursued since the late 1980s to support ISRU missions. These studies had goals such as improving cell performance, cell characterization, and process control. Much of this work was conducted at NASA's Jet Propulsion Laboratory. Richter (1981) studied the development and modeling of solid oxide electrolysis for supporting a Mars sample return mission. He proposed a thermodynamic and electrochemical model of a solid oxide electrolysis system and investigated operating parameters (flow rate, current density, and voltage) over a range of temperatures and pressures. The solid oxide electrolysis cell studied consisted of 8% yttria stabilized zirconia.

Colvin, Schallhorn et al. (1992), from NASA's JPL, developed a tubular solid oxide electrolysis test bed for testing SOE technology from a control standpoint. Control parameters used were the applied electrolyte potential, operating temperature, and CO_2 inlet flow rate. These control variables were used to study the effects on O_2 production rates and were cast considering the cell Nernst efficiency and system efficiency.

The testing environment was bound by operational hazards zones. These limits included a maximum voltage of 2.24 VDC to avoid driving bound oxygen from the zirconia lattice structure. The temperature was also bound below 1150 °C to avoid a phase change in the zirconia (Colvin, Schallhorn et al. 1992). The characterization test matrix was defined by varying cell temperature, applied cell potential, and CO_2 flow rates. Cell temperature was varied from 800 to 1100 °C in 0.25-degree increments. Cell potentials were tested from 0.6 to 2 VDC in 0.1 increments, with a CO_2 flow rate from 38-1475 sccm (approximately 4-174 g/hr CO_2). The study observed a second order dependence based on cell potential and oxygen dependence. A weak dependence was observed for cell production rate and flow rate.

Extensive modeling and testing of solid oxide electrolysis cells was conducted by K. R. Sridhar at the University Arizona in the late 1990s and early 2000s. Sridhar developed estimates of mass and power consumption for a Mars sample return ISRU system (Sridhar 1995), investigated co-electrolysis of H_2O and CO_2 for use in ISRU (Sridhar, Iacomini et al. 2004), explored the use of electrolysis to produce life support consumables (Sridhar, Finn et al. 2000), and characterized and molded the performance of a tubular solid oxide electrolysis cell (Sridhar and Vaniman 1997). Sridhar also provided the SOE cell for the Mars ISPP Precursor Mission (Kaplan, Baird et al. 2000).

2.4.2 The Mars ISPP Precursor (MIP)

The Mars In-situ Propellant Production (ISPP) Precursor (MIP) Flight Demonstration was an SOE ISRU payload selected in 1997 to fly aboard the Mars Surveyor craft that was planned to launch in 2001. After the crash of the Mars Polar Lander in 1999, NASA decided to cancel the Surveyor lander. The development of MIP continued and publications on its design contributed to our knowledge of assembling flight-like ISRU systems. MIP also set a precedent for embedding acronyms in acronyms when naming ISRU technology flight demonstrations.

MIP was slightly larger in volume than MOXIE with dimension of 40 x 24 x 25 cm (15.7 x 9.4 x 9.8 inches) vs. MOXIE 23.9 x 23.9 x 30.9 cm (9.4 x 9.4 x 12.2 inches) but about half as dense, weighing 8.5 kg (18.7 lbm) vs. MOXIE which will weigh about 15 kg. Part of the volume of MIP was occupied by additional experiments, including the Mars Array Technology Experiment (MATE) to test advanced solar cells on Mars, the Dust Accumulation and Repulsion Test (DART) to investigate dust properties and settling on the solar arrays, and the Mars Thermal Environment and Radiator Characterization (MTERC), a device that would measure night sky temperature and test radiator performance. (Kaplan, Baird et al. 2000)

MIP used a Zeolite adsorption compressor as part of a subsystem called the Mars Atmospheric Acquisition and Compression (MAAC.) This system was designed to adsorb CO_2 from the atmosphere over a 65-hour period when the system is near nighttime ambient temperatures of about 200 K (Kaplan, Baird et al. 2000). After saturation, the bed is heated to 450 °C and 4.5 grams of CO_2 is expelled over a 6-hour period. The delivery goals were a pressure of 440 +/1 52 Torr at a flow rate of 3.0 +/- 0.5 sccm. This is a mass flow rate of about 0.75 g/hr and average rate of 0.063 g/hr when considering adsorption time. These gases were fed to the Oxygen Generator Subsystem (OGS) for oxygen extraction. The OGS consisted of a solid oxide electrolysis cell operated at 750 C (1023 K). The goal for production rate was 0.5 sccm of O_2. The OGS was designed to be operated 10 times over 90 sols (Kaplan, Baird et al. 2000).

2.5 The Mars Oxygen ISRU Experiment (MOXIE)

The primary goal of MOXIE is to be a pathfinder mission for future similar ISRU technologies. The ability to use oxygen already present on Mars in the form of atmospheric CO_2 is a revolutionary technology. It will enable a completely new class of sustainable missions by reducing the amount of material that needs to be brought on a mission.

The potential uses for this oxygen production technology are:

1. Produce oxidizer for a return trip from Mars
2. Produce oxidizer for use with surface vehicle fuels
3. Generate oxygen for life support systems
4. Scrub CO_2 from life support systems
5. Concentrate O_2 for life support systems

Application 1 is the primary motivator for MOXIE, as the propellant to return from Mars has the largest mass requirement of any of the applications. Recent estimates state that 29.3 mT of oxygen need to be produced to return astronauts from the Mars surface to a staging orbit around Mars. ISRU can harvest the oxygen already on Mars, resulting in a 29% reduction in landed mass, and effectively reduce the initial mass required in Low Earth Orbit (LEO) by 336 mT. (Rapp, Hoffman et al. 2015). Integrating a full scale MOXIE-like system into future mission designs would save nearly 3 SLS launches per mission at the SLS designed capacity of 130 metric tons (United States Senate 2010). The final launch cost could be as high as 5 billion dollars per launch depending on the launch frequency (Strickland 2013). Use of an ISRU system could potentially save tens of billions of dollars.

2.5.1 MOXIE system overview

MOXIE consists of 3 major subsystems:

1. Carbon dioxide Acquisition and Compression (CAC)
2. Solid Oxide Electrolysis (SOXE)
3. Process Monitoring and Control (PMC)

Sub-system 1 includes a Mars atmosphere intake, a filter for dust mitigation, and a scroll compressor. Sub-system 2 is the solid oxide electrolysis unit (SOXE) and includes an inlet gas pre-heater, 10 solid oxide electrolysis cells (wired in series as two 5-cell stacks), two cell heaters, insulation, mechanical stack compression, and outlet gas heat exchangers. Sub-system 3, the monitoring and control system, includes the sensors, electronics, and gas characterization unit. A simplified depiction of the MOXIE components is shown in Figure 8.

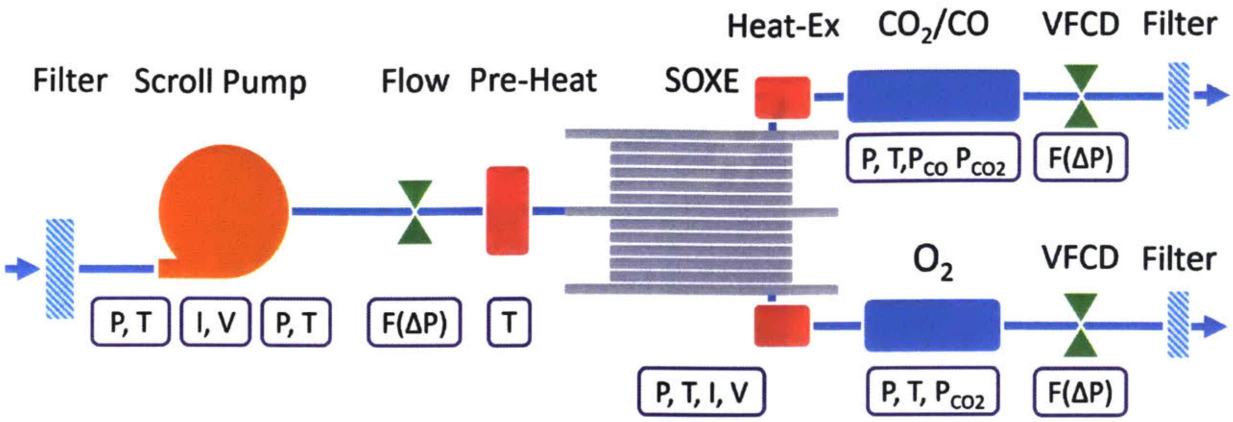

Figure 8 – Simplified MOXIE system diagram

MOXIE is enclosed in a case that is 23.9 x 23.9 x 30.9 cm (9.4 x 9.4 x 12.2 inches) and will weigh about 15 kg (33 lbs). A mechanical structure serves as a mounting point for various components. One side of the enclosure is dedicated for gas exchange tubing ports, called the inlet panel. The sensors are mounted together on a sensor panel located on an adjacent wall. Across from the sensor panel is the ELX (Electronics) Box that holds the MOXIE FPGA, cabling, and controllers. The SOXE assembly and the scroll pump are mounted to the floor panel that is connected to the RAMP (Rover Avionics Mounting Panel). Figure 9 is a solid model representation of MOXIE.

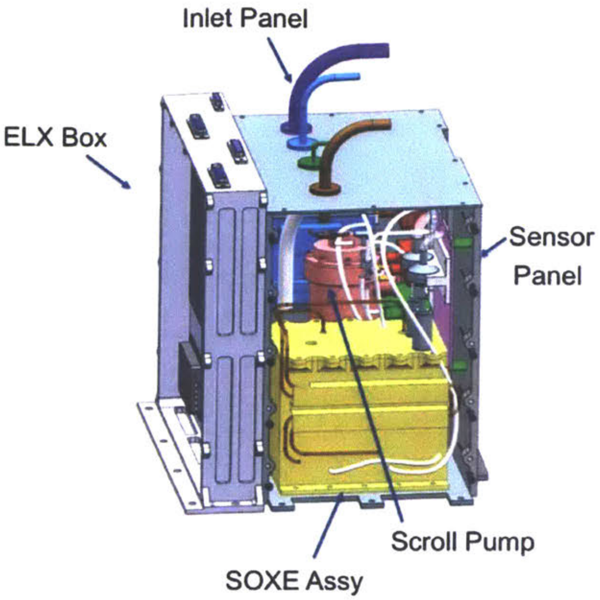

Figure 9 – Solid model representation of the MOXIE design

2.5.2 Carbon dioxide Acquisition and Compression (CAC)

Martian atmosphere is drawn through a dust filter by the MOXIE scroll pump (Figure 10), a mechanical pump that volumetrically compresses the Mars atmosphere and forces it into the system. Viscous flow control devices (VFCDs) restrict the flow through MOXIE to create additional back pressure. The combined pump and VFCD restrictions are used to generate a pressure of 1 Earth atmosphere at a total compression ratio of about 100.

Figure 10 – A CAD rendering of the MOXIE scroll pump design

There is uncertainty in the final location of the Mars 2020 landing site. Atmospheric pressure on Mars varies by altitude and season, with an average pressure of 636 Pa at mean radius (Williams 2015). Lower inlet pressures increase the energy required to deliver compressed CO_2 to the SOXE. Reduction of the inlet pressure reduces the flow rate because less fluid mass is captured in the volume of the scrolls. A small decrease in volumetric efficiency is also observed because of a larger delta P across the pump. The pump inlet is on the outside edge of the scroll. Air is compressed and expelled at the center of the pump's radius. Pump inlet temperature is also important in defining the density of the gas that enters the pump. The Mars atmosphere travels through an inlet tube before reaching the pump, resulting in a temperature rise above Mars ambient.

Figure 11 – A scroll pump consists of a fixed and rotating set of involutes. PTFE seals at the face of each scroll help seal the pump and reduce leakage

The initial design for the scroll pump driven MOXIE architecture included a small volume, or "plenum," to help buffer the SOXE from pressure spikes from the rotating pump. The plenum has been replaced with a check valve to reduce back flow as the exit of the pump opens to force gas into the downstream system. Characterization of the pump design will improve the models of pump volumetric efficiency for different pressure ratios. A crucial advantage of this type of pump is that it enables a one-step system with on-demand pressure. A challenge with this type of pump is that, over time the tip seals may wear and reduce volumetric efficiency.

A secondary option for the CAC system that was originally planned was to use cryopumps that would freeze CO_2 out of the Martian atmosphere. This system required two steps, an acquisition period where dry ice is collected, and a pressure stage where the dry ice is sublimated and stored to generate pressure to feed into the SOXE. The cryogenic system operates in a batch approach, where dry ice can be accumulated over a long period. The CO_2 is stored as a high pressure gas until an electrolysis run is initialized. This batch method has a lower peak power than the scroll pump method but uses more power per combined collection and electrolysis cycle (Rapp, Hoffman et al. 2015). The mechanical pump was considered an "advanced technology option" (ATO) in the MOXIE proposal because of a perceived technology gap. NASA DRM 5 described mechanical pumps as not feasible because of high power draw and mass, and the study recommended that cryocooler or micro-channel adsorption pump technology should be advanced instead (Drake 2009). Other studies have deemed mechanical pumps sufficient (Zubrin, Baker et al. 1991).

2.5.3 Solid oxide electrolysis stack (SOXE)

The oxygen generating chemical reaction takes place inside the solid oxygen electrolysis (SOXE) stack. The base unit of the SOXE is a cell. Each cell contains an oxygen permeable electrolyte sandwiched between a cathode and an anode. Gas flow is directed over the cells by means of CFY interconnects, metal plates with flow channels, and current collectors that contact the anode and cathode. Atmospheric gas flows over the cathode where the reduction reaction takes place. Oxygen ions transport through the electrolyte and form O_2 in the anode. Multiple SOXE cells are placed in a SOXE "stack" configuration. A stack is a group of cells connected through interconnects held together by a compression fixture and glass seals. The cells in the stack are connected in series and a voltage is applied across the stack. The current through each cell in the stack is the same, but the voltage drop varies across each cell depending on the electrochemical resistance of that cell. As elaborated later, all the current is ionically transmitted through each cell so the production rate of each cell in a stack is the same. Figure 12 shows the final SOXE stack design.

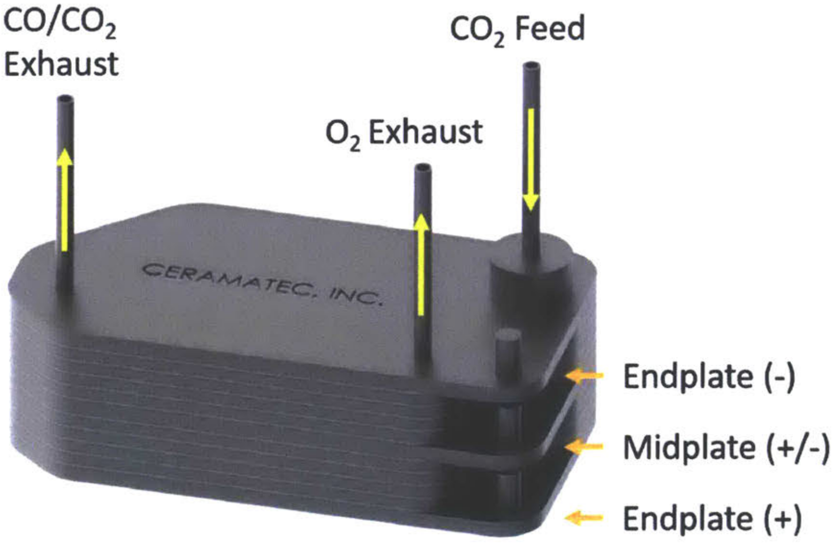

Figure 12 – The 10 cell SOXE stack design. A center voltage midplate electrically separates the two 5 cell groups for added redundancy

The final stack design includes two electrically independent groups of 5 cells each. The original design included a stack with two 11-cell groups for a total of 22 cells. The selection for the reduced number of cells was primarily driven by available power supplies and a desire to reduce thermal mass.

2.5.4 Process Monitoring and Control (PMC)

The process monitoring and control system characterizes the states of the inlet gas, pump performance, state of the electrochemical process, and the outlet gas composition. Figure 8 above identifies the system sensors and their locations are outlined in purple. Pressure and temperature measurements are taken at the exit of the inlet filter to characterize the gas stream entering the scroll pump. The controlled processes include:

1. The scroll pump speed (which can be used to adjust system pressure or flow)
2. SOXE inlet gas heater temperature
3. SOXE temperature
4. SOXE voltage (which can be used to adjust SOXE current)
5. Outlet gas composition analysis sensors (CAS) temperature

Process and control overview

A field programmable gate array (FPGA) with an embedded microprocessor implements the MOXIE process control and sensing elements. MOXIE is initialized from a boot command from the rover. In this state, MOXIE waits for a second command to select the run program. Several programs can be selected depending on the type of experimental run that is desired. Each program consists of several states that progress to the next state after an allocated amount of time. Each state determines control loops that are active and the behavior needed to achieve the goals of that state.

A standard run program consists of the following states: idle, preheat, flow through, electrolysis, cool down, and then a return to idle. During initial idle, the pressure and temperature sensors take readings while the SOXE, scroll compressor, heater systems, and compositional analysis sensors remain powered off. The initial pressure readings are used to provide an initial pressure baseline and for sensor calibration.

After the idle time needed to collect baseline readings has passed, the SOXE preheat state begins. The preheat mode executes proportional-integral-derivative (PID) control for a SOXE heater ramp profile. The set point of the PID temperature controller increases over several time-based steps to approximate a 10 °C per minute ramp to an operating temperature of 800 °C (1073 K.) The SOXE preheat temperature profile can be designed to avoid thermal expansion rates that could damage the SOXE. During preheat, the CO_2 and CO sensors are activated to warm up.

The composition and analysis sensors (CAS) are a part of the MCS that analyzes the gas composition of the MOXIE outlet gases. This is comprised of a CO sensor, a CO_2 sensor on the cathode exhaust, and CO_2 and O_2 sensors on the oxygen exhaust. The CAS sensor can perform mass balance checks, verify production requirements, and potentially trigger fault responses if needed. These sensors perform better when thermally controlled so they have a dedicated heater. The heater controller for the CAS takes advantage of having shorter time constants and saves power by initializing after the SOXE has completed a portion of its heating cycle. At the end of the heating profile, there is a short dwell period to allow the temperature to stabilize.

Once the heating dwell period is complete, the electrolysis state begins. This state is broken into several steps. The first step initializes the pump seconds before the next step that applies a voltage to the SOXE stack. The short delay in voltage is meant to align with the actual arrival of flow to the stack. The goal is to avoid the condition of flow through a hot stack, which could result in an oxidation degradation mechanism, and to avoid applying stack voltage to a stack with no flow, which could result in a coking degradation mechanism.

In the standard run program, the actual O_2 generating process, electrolysis, is conducted for 30-120 minutes depending on available power. During this process, several parameters are being controlled with closed PI controllers. The scroll compressor outlet pressure set point is controlled by pressure sensor feedback.

The electrolysis process in the SOXE is controlled by voltages applied across the stack. A starting voltage is adjusted by a PI controller responding to stack current feedback current (which directly correlates to O_2 production rate) and a current goal set point. Additional voltage control feedback for advanced controls may include inlet pressure, flow rate, system temperatures, and calculated utilization. Voltage is adjusted to reach the maximum safe production rate.

Inlet pressure, pump rotations per minute (RPM) gain, and stack temperatures are fixed variables during the electrolysis process and are controlled to match desired set points such as 1 atm, 2800 rpm, and 1073K. The baseline pump controls command a starting RPM value that is adjusted by a PI controller acting on the error between a pressure set point and sensor. Advanced controls may adjust RPM based on flow rate because flow directly correlates with MOXE safe operating parameters.

After a production run, the system enters a cool down state. In this mode, the heaters, including the SOXE heaters, are turned off. The cooling time constant of the SOXE greater than 10 °C per minute eliminates the necessity for a heater controlled cooling profile for safe cooling.

The final idle phase begins after a set period passes (the estimated time for the system temperatures to reach nominal). The pressure and temperature readings is taken during final idle can be used for calibration purposes. MOXIE completes transmitting all telemetry commands to the rover and waits for a power off command.

2.6 Chapter summary and conclusion

This chapter provided the justification and background for the Mars Oxygen ISRU Experiment. It began with a brief history of ISRU architectures developed to support Mars missions. Different types of ISRU methods proposed for Mars were discussed. The operating principles of the technology best suited for atmospheric ISRU on Mars, solid oxide electrolysis, was explained. Next, some early developments of solid oxide electrolysis for Mars were discussed and the design of the MIPP flight demonstration was summarized. The chapter ended with a baseline description of MOXIE and its system components.

ISRU technology has long been envisioned as an enabling technology for sustainable space exploration. Leighton and Murray (1966) proposed that the polar ice caps of Mars are primarily CO_2 and Mars has a CO_2 atmosphere. The Viking landers directly measured the CO_2 atmosphere on Mars and sparked the idea of oxygen extraction on Mars for propellant production. Many architecture studies have been developed to help understand the benefits of implementing ISRU technology but no such technologies have yet been tested or proven on another planet. MOXIE is an opportunity to demonstrate that extraterrestrial oxygen production is feasible and reliable. The data derived from MOXIE and flight program developments enable this thesis to assess this technology, implementation, and controls to a new level of realism.

3. Thermodynamic Modeling of Solid Oxide Electrolysis

3.1 Motivation

The enabling technology for MOXIE is solid oxide electrolysis (SOE). This chemical process occurs in 10 SOE cells that are electrically linked in series to form a unit called the SOXE. The SOXE produces oxygen by drawing power from the MOXIE electronics, thermal energy from the SOXE heaters, and CO_2 from the scroll pump. The relationship between flow (rate and composition), temperature, voltage, and current determine the oxygen production rate. In addition, the relationship between these parameters determines if the SOXE is at risk of degradation from mechanisms such as cathode oxidation and carbon deposition (coking). The system control authority is limited for each state variable. The scroll pump flow rate is constrained by the pump design and the Mars ambient pressure and temperature. Power to MOXIE is limited by two 10-amp switches that link MOXIE to the rover power systems. SOXE power is limited to 4 A by a DC/DC power converter. SOXE thermal uniformity reduced by environmental conditions and constraints on the SOXE heater and insulation design. Furthermore, the MOXIE flight instrument will not have individually instrumented SOXE cells to measure cell voltage, so individual cell performance must be derived. Limitations are the nature of all space flight vehicles. The need to know more than what can be sensed, and to establish safe operating strategies, validate command sequences, and interpret mission data, are the motivation for the development of this SOXE model.

3.2 Introduction to modeling approach

The SOXE is based on technologies developed for solid oxide fuel cells (SOFCs). Solid oxide fuel cells are used to efficiently convert fuels to electricity, a common fuel being methane, but CO and O_2 can also serve as fuel and oxidizer. The SOXE is essentially a SOFC operating in reverse. The extensive modeling efforts for SOFCs bolster the more limited SOE modeling landscape.

Within SOFCs, several strategies have been implemented to create cell and stack models. These are typically grouped by dimensionality and type. Dimensionality ranges from 0D lumped parameter models to full 3D models of the cells and stack. As dimensionality increases, so does fidelity and complexity for similar modeling resolution. 3D model types are typically appropriate for detailed design, while 0D or 1D models are used to represent plant models for control systems.

The model dimensionality most valuable in answering the questions in this thesis are 0D plant models, though individual model components have additional dimensionality to aid in understanding the impact of component scaling.

The modeling types include a spectrum from "white" physics-based models that require no empirical characterization inputs from the system being modeled, to "black" empirical models that rely purely on the empirical characterization of the performance of a cell or stack. Most published research is in one of these types of modeling. "grey" models are based on both physical principles and empirical characterization data. Figure 13 shows an example of each type of model and describes some of their characteristics.

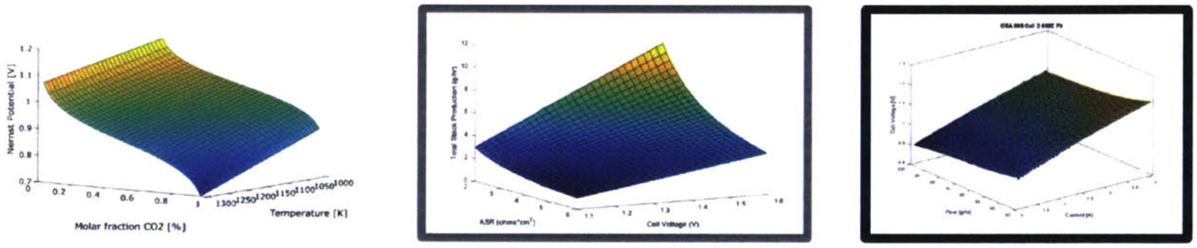

$$V_{ocv} = \frac{-\Delta G_f}{4F} + \frac{RT}{4F}\ln\left[\frac{(P^0_{CO})^2 P^0_{O_2}}{(P^0_{CO_2})^2}\right]$$

White Models

- Physics based models of the electrochemical processes
- Does not account for some losses in the actual device
- Only option without hardware and experimentation
- White Models include:
  - CO_2 to CO Nernst potential and OCV
  - CO to C Nernst potential
  - Thermal neutral voltage and heat generation

$$ASR_{imp} = \frac{((V_{op} - (V_{act} + V_{ocv}))/N_{cells}}{I/A}$$

Grey Models

- Combines physics based modeling and characterization of test units
- Can be tuned to model system well in expected constraints
- Gives the most insight when encountering "Unknown Unknowns"
- Grey Models include:
  - I-V relationships with given ASR
  - Temperature dependence of ASR
  - Flow dependent fits

$$V = a + bI + cF + dIF + eI^2 + gF^2$$

Black Models

- System characterized by input-output functions
- Great for simulating specific unit responses when parameters are inside the characterized range
- Validity breaks down outside tested range
- Black Models include:
  - Regression fits to experimental data
  - Machine learning

Figure 13 – Survey of modeling approaches

White models include thermodynamic equations that must be satisfied for a reaction. These are good predictors of performance in perfect systems where all parameters in each equation are understood and well distributed. White model equations include the reaction Nernst potentials, cell open circuit voltage, mass and energy balance, and heat generated or consumed by the electrochemical reaction. White models alone can be used to get a general sense of system performance and ideal energy costs. White models are also critically important for understanding SOXE behavior and interpreting the results of characterization data. Black models are useful when characterizing a specific SOXE unit that will be used, especially in the case where it will only be operated within the range of characterization. A black model could be created through fitting of the characterization data or machine learning. A negative aspect of this model type is that it is descriptive, not predictive. Black models provide little to no insight into why a system performs in a particular way. As demonstrated when analyzing the results of experimentation in Chapter 4, the black model approach described the data well, but the grey model provided insights into why cell-to-cell SOXE variation was occurring. The capability to aid in the interpretation of the results from real systems is the primary advantage of a grey model. Grey models incorporate empirical characterization terms, such as area specific resistance (ASR) and activation potential, to describe the I-V relationship in combination with white model components such as Nernst potentials. Grey model synthesis requires more effort than black model generation but grey models advance the understanding of the system and can provide valid representation outside of the characterized performance range.

3.3 White models for solid oxide electrolysis

Research objective 1 is to apply grey modeling to the solid oxide electrolysis process to predict the effects of SOXE performance on atmospheric ISRU system design and control. This approach focuses on accuracy and efficiency by implementing a 0 D model that is enhanced by higher dimensionality when advantageous. This section focuses on the development of the white model of the SOXE and establishes the thermodynamic and electrochemical basis for the grey model.

3.3.1 Electrochemistry for SOXE

An individual SOXE cell includes an oxygen-permeable yttria-stabilized zirconia like (YSZ) ceramic electrolyte between two porous electrodes, a cathode and anode. Each electrode has a chemical composition designed to catalyze the appropriate reaction. The cathode is comprised of Nickel and Cerium Oxide (Ni CeO_2) and the anode is a Lanthanum Strontium Manganite (LSM) perovskite.

In the SOXE, Mars atmospheric gas flows into the cathode guided by flow channels in CFY metal interconnect plates. The interconnects also serve as current collectors that provide a conduction path for electrons to reach the cathode for the reduction reaction, and to conduct electrons away from the anode after oxidation. The cathode reduction reaction takes place at the three-phase boundary, a place in the cathode where the gaseous, electronic, and ionic components of the electrochemical reaction come together. The steps in the electrochemical process are illustrated in Figure 14.

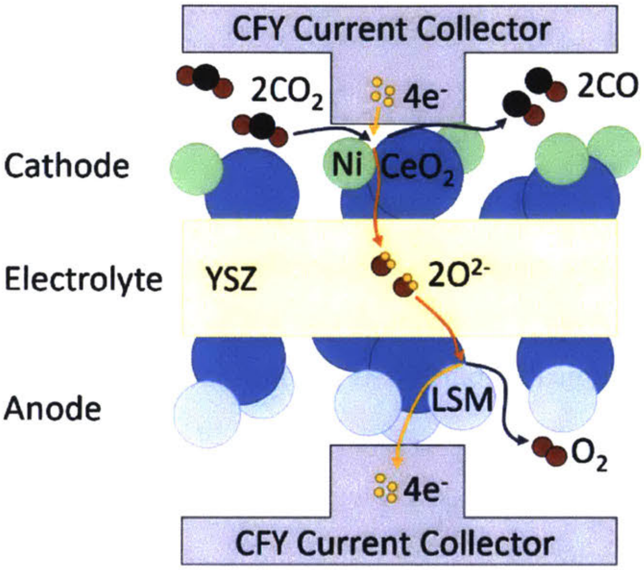

Figure 14 – The electrochemical reaction occurs at the three phase boundary, where gaseous (blue arrow), electronic (yellow arrow), and ionic (orange arrow) phases are present

At the cathode three-phase boundary, two CO_2 molecules are reduced to two CO molecules and two negatively charged O^{2-} atoms:

$$2CO_2 + 4e^- \rightarrow 2CO + 2O^{2-} \tag{3.1}$$

The electrical potential applied to the cell drives the charged O^{2-} ions through the YSZ electrolyte. Once the ions exit the electrolyte and enter the perovskite anode, two O^{2-} ions are oxidized to form an O_2 molecule:

$$2O^{2-} \rightarrow O_2 + 4e^- \qquad (3.2)$$

The YSZ electrolyte is ionically but not electrically conductive. The current efficiency or Faraday efficiency (η_F) is the ratio of ionic current transfer over total current transfer (Nehrir and Wang 2009) and can be described by the following relation:

$$\eta_F = \frac{I_{ion}}{I_{tot}} = 1 - \frac{I_{para}}{I_{tot}} \qquad (3.3)$$

Where I_{ion} is the ionic current in amps, I_{para} is the parasitic or electronic current, and I_{tot} is the total current transfer. Experiments using YSZ electrolyte for solid oxide electrolysis of CO_2 have shown that practically all current is ionically transferred (Sridhar and Vaniman 1997). Therefore, it can be assumed that for the SOXE:

$$\eta_F = 1 \qquad (3.4)$$

This property of the electrolyte used in the SOXE enables MOXIE to perform real time monitoring of oxygen production rates. Because all electrons are ionically transferred with an oxygen ion, and four electrons are transferred per molecule of O_2, the molar production rate can be calculated from the cell current measurement:

$$\dot{n}_{O_2}\left[\frac{mol}{s}\right] = \frac{I}{4F} \qquad (3.5)$$

Where $\dot{n}_{O_2}$ is the molar flow rate of oxygen in moles per second, I is the stack current in amps, and F is Faraday's constant, 96,485 Coulombs per mole of electrons. MOXIE O_2 production is measured on the order of grams per hour. Converting time and the molar mass of oxygen yields:

$$\dot{m}_{O_2}\left[\frac{g}{hr}\right] = \frac{I}{3.3503} \tag{3.6}$$

This is the relationship between measured current and oxygen production for a single cell in the SOXE stack. In the configuration for MOXIE, all cells are electrically connected in series so each cell conducts the same current. Production rate in each cell in a stack is the same, while voltages may vary per cell depending on differences in production. Total stack oxygen production is calculated by multiplying Equation (3.6) by the number of cells in the SOXE stack.

The YSZ electrolyte must also be at elevated temperatures to permit oxygen ion transport. Much research has been conducted on improving electrolyte materials to improve transport properties at lower temperatures (Wachsman and Lee 2011). Higher operating temperatures drive down all resistances for the reaction. The MOXIE design reference temperature for the SOXE is 1073K. The resistance of the electrolyte to oxygen ion transport decreases at higher operating temperatures, a design parameter that must be balanced with an increased rate of long-term degradation, and additional energy required to warm the stack before operation. The heat consumption and production of the electrochemical reactions and elevated risks of long-term degradation mechanisms must be considered when determining the operating temperature and voltage.

3.3.2 Relating flow rate to utilization

MOXIE has a good measurement of current, which has a direct correlation to O_2 production. Therefore, we can calculate the utilization from flow rate and stoichiometry after subtracting about 5% for inert atmospheric mixed gases (N_2 and Ar). Equation (3.7) is the reaction mass balance.

$$2\left(44\left[\frac{g\ CO_2}{mol}\right]\right) = 2\left(28\left[\frac{g\ CO}{mol}\right]\right) + 32\left[\frac{g\ O_2}{mol}\right] \tag{3.7}$$

The ratio of CO_2 consumed per gram of O_2 produced is:

$$\frac{88}{32} = 2.75 \ \frac{grams\ CO_2\ cons.}{grams\ O_2\ gen.} \tag{3.8}$$

Therefore, the utilization can be calculated by:

$$U_{CO_2} = \frac{\dot{m}_{CO_{2_{cons}}}}{\dot{m}_{CO_{2_{in}}}} = \frac{\left(2.75 * \dot{m}_{O_{2_{out}}}\right)}{\dot{m}_{CO_{2_{in}}}} \tag{3.9}$$

CO_2 utilization is an important parameter for monitoring the MOXIE system. Low utilizations signal that the system flow rate is more than what the cell is processing. In the event of low CO_2 utilization, energy is being wasted by compressing excess CO_2 in the acquisition process. If the utilization is high, it signals that the system is at higher risk for degradation processes such as carbon deposition on the SOXE cathode.

3.3.3 Thermal neutral voltage

The thermal neutral voltage is the voltage where all energy necessary for the reaction is provided electrically. At this point, the reaction is neither endothermic nor exothermic. The voltages exceeding the thermal neutral voltage result in a net exothermic reaction. The thermal neutral voltage can be calculated by:

$$V_{tn} = \frac{\Delta H_f}{4F} \tag{3.10}$$

Where ΔH_f is the enthalpy of reaction and $4F$ is the charge transferred in the reaction as written in Equation (3.11). In a temperature range from 800 K to 1400 K, the thermal neutral voltage can be calculated by second order polynomial fit of the temperature dependent enthalpy of reaction divided by 4F:

$$V_{tn} = -8.655(10^{-9})T^2 - 1.496(10^{-6})T + 1.475 \quad (3.11)$$

Evaluating the thermal neutral voltage at the SOXE reference operating temperature 1073 K (800 C) yields V_{tn} = 1.463 V.

3.3.4 The open circuit voltage and Nernst potential

The open circuit voltage (OCV) is a special case of the Nernst potential. The OCV is the potential across the cell when no current is passing through the cell. With no current, other potential losses such as ohmic losses are not present. The OCV can be calculated from the Nernst potential equation which depends on the composition of products and reactants on either side of the cell. The Nernst potential for solid oxide electrolysis can be represented as done by Hartvigsen, Elangovan et al. (2015), and Ni (2010):

$$V_{Nernst} = E = E_0 + \frac{RT}{2F}\ln\left[\frac{P^0_{CO}(P^0_{O_2})^{\frac{1}{2}}}{P^0_{CO_2}}\right] \quad (3.12)$$

Where P^0_{CO} and $P^0_{CO_2}$ are the partial pressures of CO and CO_2 at the cathode, and $P^0_{O_2}$is the partial pressure of O_2 at the anode. R is the universal gas constant, T is the operating temperature and F is Faraday's constant. The factor 2 is the number of electrons transferred per oxygen ion. E_0 is the equilibrium potential (or free energy potential) at standard pressure. This relation was based on the reaction in Equation (3.13) below.

$$CO_2 \rightarrow CO + \frac{1}{2}O_2 \quad (3.13)$$

For consistency in this thesis, it has been rewritten here for the chemical balance described in Equations (3.1) and (3.2):

$$V_{Nernst} = V_{rev} + \frac{RT}{4F}\ln\left[\frac{(P^0_{CO})^2 P^0_{O_2}}{(P^0_{CO_2})^2}\right] \tag{3.14}$$

The reversible voltage, V_{rev}, can be calculated from thermodynamic tables and evaluated at any operating temperature:

$$V_{rev} = \frac{-\Delta G_f^o}{4F} \tag{3.15}$$

ΔG_f° is the standard free energy of reaction. V_{rev} can be linearly approximated over a temperature range from 800 K to 1400 K:

$$V_{rev} = 1.4629 - 4.4924(10^{-4})T \tag{3.16}$$

Where T is the temperature of the cell in Kelvin. The OCV equation ultimately simplifies to Equation (3.17), which is dependent on the partial pressures of CO, O_2, CO_2 and the temperature of the gasses supplied to the SOXE.

$$V_{ocv} = 1.4629 - \left(4.4924(10^{-4}) - 2.1543(10^{-5})ln\left[\frac{(P^0_{CO})^2 P^0_{O_2}}{(P^0_{CO_2})^2}\right]\right)T \tag{3.17}$$

At the reference operating temperature of 1073K, $V_{rev} = 0.9809$. Equation (3.17) models the open circuit voltage as a function of partial pressures. This is important because the partial pressures of the products and reactants change as the gases flow across the stack and a portion of the CO_2 is reduced. The equation is undefined when $P_{co} = 0$. For a 1% CO concentration, Vocv = 0.7684. Figure 15 displays the results of this model for the Nernst potential as a function of molar fraction CO_2 to CO and temperature. The pressure of O_2 effluent on the anode is assumed to be 1 Earth atmosphere as controlled by restrictions on gas flow exiting MOXIE. The incoming gases are assumed to be pressurized to 1 Earth atmosphere by the MOXIE scroll pump.

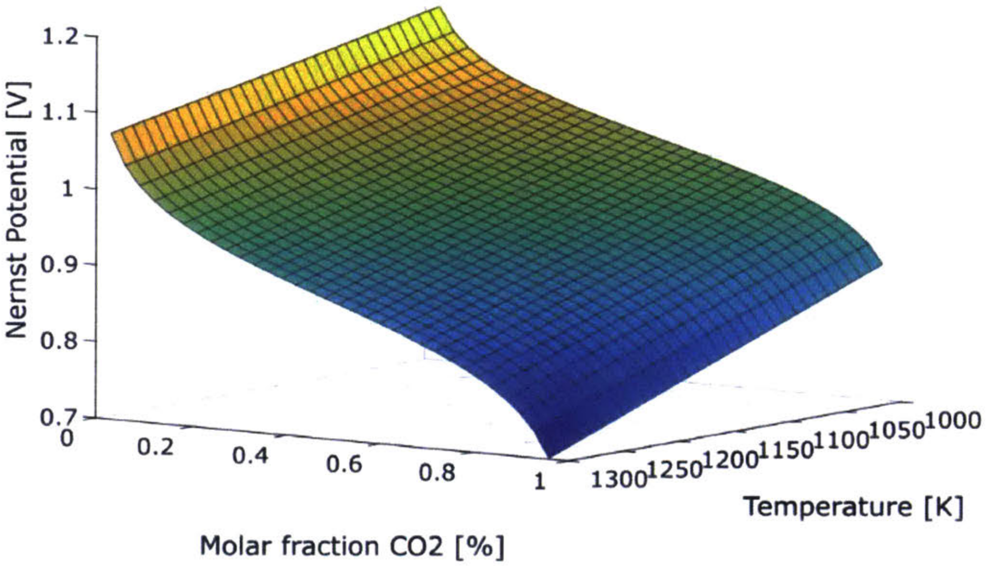

Figure 15 – The Nernst potential as a function of molar fraction CO_2 to CO and temperature.

Figure 15 depicts the Nernst potential as a function of molar fraction of CO_2 with respect to CO, and the operating temperature. The Nernst potential decreases with higher temperature and with higher concentration of CO_2 with respect to CO. Section 3.4.1 on page 66 below describes the impact of the Nernst potential on the cell current and oxygen production.

3.3.5 1D calculation of CO_2 - CO Nernst potential

The reactant gas composition flowing over the catalytic sites of the cathode changes as the gas flows longitudinally through the cathode. At the entrance to the cell, the gas is the composition of the Martian atmosphere, approximately 96% CO_2 with only trace amounts of CO. The Ni Ceria used in the SOXE cells is susceptible to oxidation (CO_2 rich) environment. This typically occurs near the upstream portions of the SOXE cells where less of the incoming gases have been electrolyzed. To increase the CO concentration in the inlet during operation, recirculation of a portion of the effluent gas is implemented on MOXIE. Figure 16 represents the baseline case for the Nernst potential without recirculation. The Nernst potential is calculated from a CO_2 utilization of 1% to define the equation with an upper bound of the example reaction at 50% utilization.

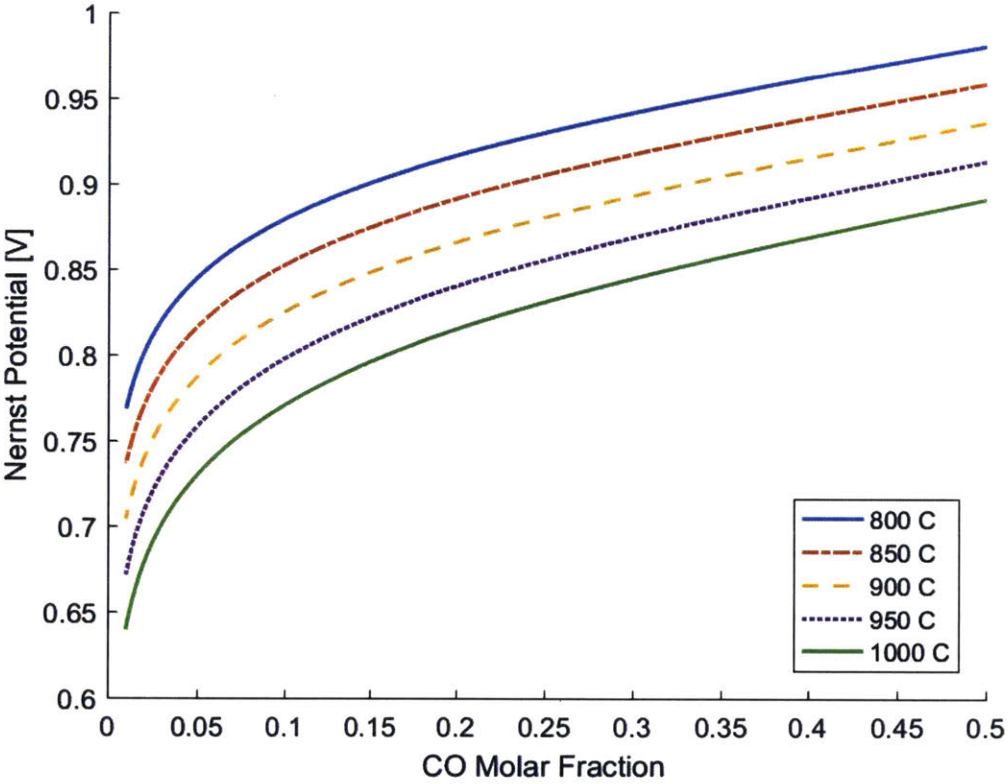

Figure 16 – Nernst potential as a function of CO to CO_2 molar fraction. CO molar fraction increases across the stack as the CO_2 flowing through is consumed

In order to derive a better approximation of the Nernst potential for modeling the bulk properties of the SOXE as a component of the MOXIE system, a calculation of the Nernst potential is derived. This approximation accounts for the high molar fraction of CO_2 as it enters the cell and proceeds to the targeted 50% utilization. This equation calculates the average Nernst potential over the length of the cell assuming a uniform longitudinal increase in molar CO fraction (a simplifying assumption for the whole cell. The actual active area changes near the cell entrance and exit and reactant consumption rates may also change):

$$V_{Nernst,Ave} = \frac{1}{x_{co,out} - x_{co,in}} \int_{x_{co.in}}^{x_{co,out}} \left(E_0 + \frac{RT}{4F} ln \left[\frac{(P_c * x_{co})^2 P^0_{O_2}}{(P_c * (1 - x_{co}))^2} \right] \right) dx_{co} \tag{3.18}$$

Where x is the local CO_2 utilization (the molar ration of CO to CO_2) in the stream, P_c is the total pressure over the cathode. When the partial pressures are represented in terms of utilization and cathode pressure, the cathode pressure term is eliminated. This has important operational implications that are discussed in chapter 5. The integral captures the Nernst potential changes longitudinally over the length of the cell as more CO_2 is converted to CO given the simplifying assumption that the rate of CO_2 consumption is constant across the length of the cell. Integrating and combining Equations (3.17) and (3.18) yields:

$$\frac{1}{x_{co,out} - x_{co,in}} * \left[1.4629 * x_{co} - 4.4924(10^{-4})T * x_{co} + 2.1543(10^{-5})T * \left(x_{co} \ln\left(\frac{P_{O_2} * x_{co}^2}{(x_{co} - 1)^2} \right) + 2\ln(1 - x_{co}) \right) \right]_{x_{co\,in}}^{x_{co,out}} \tag{3.19}$$

The applied voltage is constant throughout the cell and is laterally uniform. x_{in} is specified as 1% to avoid an undefined potential at the inlet stream. Integrating the Nernst potential from a CO_2 utilization of 1% to a rate 50% at 1073 K (800 C) and operating at 1 atmosphere yields an average Nernst potential of:

$$\overline{V}_{Nernst} = 0.9208V \tag{3.20}$$

This is an average value for this case at an estimated utilization. The Nernst potential captures one component of the required potential to drive the reaction across the SOXE. The total required potential across the SOXE can be accounted for as:

$$V = V_{Nernst} + \eta_{ohm} + \eta_{act,c} + \eta_{act,a} + \eta_{conc,c} + \eta_{conc,a} \tag{3.21}$$

Where η_{ohmic} is the ohmic resistance potential loss consisting of ionic and electric losses, $\eta_{act,c}$ and $\eta_{act,a}$ are the cathode and activation potential losses, and $\eta_{conc,c}$ and $\eta_{conc,a}$ are the cathode and anode concentration potential loses. Several models have been developed to quantify some or all of these losses for solid oxide electrolysis (Sridhar and Vaniman 1997, Ni, Leung et al. 2006, Nehrir and Wang 2009, Ni 2010). These models require in-depth characterization of the SOXE parameters, and often borrow models from other fields that may or may not be valid for high temperature solid oxide electrolysis. To capture the losses significant to the SOXE, this thesis integrates the above white model equations with experimental characterization data to create a grey model. The grey model approach is described below.

3.4 Framework for grey modeling

3.4.1 Parametrizing electrochemical dynamics as area specific resistance

Area specific resistance (ASR) is a parameter that represents the slope of the linear region current-voltage relationship for a cell on a per unit area basis. It is useful for quantifying cell performance and predicting cell voltages or currents. ASR is simple to derive experimentally but is more complex to model and predict before testing. Factors that influence it include electrode kinetics, gas diffusion, and local variations in flow, temperature, and current density. By incorporating these terms into ASR we reduce key parameters down to a variation of Ohm's law. The units are typically Ω-cm^2. ASR is described this way in (Ebbesen and Mogensen 2009) and is used to help quantify performance in testing data.

$$ASR_{app} = \frac{(V_{op} - V_{ocv})}{i_{den}} \tag{3.22}$$

Where V_{op} is the operating voltage and V_{ocv} is the open circuit voltage (the CO_2 - CO Nernst potential at the cell inlet), and i_{den} is the current density in amps per cm^2. The current density is calculated by dividing the current through a cell by the active area of each cell in MOXIE, which is 22.74 cm^2. This equation represents the ASR well when V_{ocv} is the same as the intercept of the linear fit of the i-V curve for a cell. Equation (3.22) is a good approximation for CO_2 electrolysis with steam. This approximation is called ASR_{app} for "Approximate ASR." and is calculated using a single current density-voltage data point. The characterization tests conducted in Chapter 4 demonstrate that for dry electrolysis, the i-V curve shows an additional potential (V_{add}), comprised of a Nernst contribution and activation potential that appears as an offset in intercept of the i-V fit above the open circuit voltage. To appropriately model ASR we can include this additional potential term as shown in Equation (3.23) below. This equation is useful for predicting the current for a given voltage for a cell with a characterized ASR_{lin}

$$ASR_{lin} = \frac{(V_{op} - (V_{add} + V_{ocv}))}{i_{den}} \tag{3.23}$$

In the linear portion of the i-V curve, and for most of MOXIE operation, ASR_{lin} and ASR are deemed equivalent. Historic values that ignore the effects of activation or additional potentials will be reference ASR_{app} and will be used to compare SOXE stack performance because it is the metric used for reference early on in the MOXIE program before the additional potential term was identified and quantified. A third ASR term is derived in Chapter 5 called the intrinsic ASR (conversion corrected ASR). This is the slope of the i-V curve after subtracting out the effects of CO_2 utilization and adjusting for activation potential. It represents current dependent losses through the cell. Intrinsic ASR is a useful term because it is constant across all flow rates.

One of the major challenges of CO_2 electrolysis of the Martian atmosphere for the MOXIE experiment is that the electrolysis process is done without the benefit of any moisture added to the process stream. In the presence of water vapor, the reaction is called co-electrolysis. With water, an additional reaction can take place that will enable the production of syngas, which improves efficiency and could be used for fuel production:

$$H_2O + CO_2 \rightarrow H_2 + CO + O_2 \tag{3.24}$$

Completion of this reaction requires the reverse water gas shift (RWGS) reaction:

$$CO_2 + H_2 \rightarrow CO + H_2O \tag{3.25}$$

It is more favorable than dry CO_2 electrolysis and would likely decrease ASR. In these conditions $ASR_{app} = ASR_{lin}$ as activation potential is minimal. Results from SOEC stacks in an Idaho National Lab study published by Stoots, O'Brien et al. (2008) shows dry CO_2 electrolysis with an approximate ASR of 3.84 Ω-cm^2 while results for H_2O co-electrolysis were around 1.38 Ω-cm^2 (Stoots, O'Brien et al. 2008). This 64% ASR reduction by incorporating H_2O co-electrolysis demonstrates great promise for a solid oxide electrolysis ISRU system on Mars that can leverage both the local water and ambient carbon dioxide. Ceramatec has made significant improvements in the performance of the dry electrolysis cells of MOXIE. Chapter 4 details results of ASR_{app} often reaching extraordinary low values of 1.3 Ω-cm^2 for dry CO_2 electrolysis. H_2O co-electrolysis may be able to improve that value even more.

3.4.2 Relating SOXE models to system performance

A major challenge of SOXE development and design is achieving a low ASR value. A low ASR is desirable because it allows a stack to have higher current (and therefore, production rate) at the same voltage. The implications are that lower ASR values result in higher production for the same power. Additionally, degradation processes such as the electrolysis of CO to C are more favorable at higher voltages. For a given operating point (defined by utilization, temperature, and pressure), Figure 17 demonstrates the importance of ASR on SOXE stack performance for a given cell voltage.

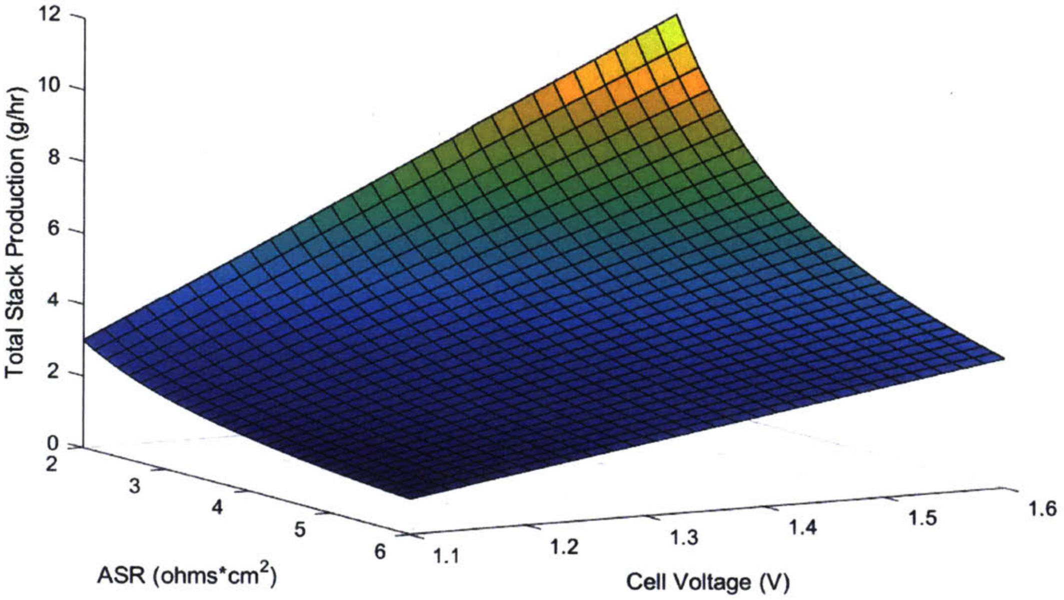

Figure 17 – Oxygen production rate and operating voltage for a 5 cell SOXE stack operating at 1073K

Figure 17 shows that to maximize production the cell can be operated at a higher voltage. However, a high ASR cannot always be compensated for by applying a higher voltage across the stack. In solid oxide electrolysis of CO_2, operating at high voltages increases the risk of a degradation process called coking. Coking is a process in which the cathode is fouled by carbon deposition which reduces the performance of the reaction. This risk increases as cell potential and utilizations increase. One mechanism in which coke can form is the Boudouard reaction. (Bove and Ubertini 2008):

$$2CO(g) \leftrightarrow CO_2(g) + C(s) \tag{3.26}$$

The coking threshold in the MOXIE SOXE cells is characterized in Chapter 4.

Alternately, production can be increased at the same operating voltage by lowering the ASR of the stack. Most ASR improvement needs to be accomplished in the cell design, production processes, and operational practices. ASRs for SOECs with YSZ electrolytes generally improve (lower resistance) as operating temperature increases. For example, YSZ electrolyte doped with 8 mol-% yttria (Y_2O_3) has an ionic conductivity of 0.1 S/cm (Siemens per centimeter) at 1273 K (1,000 °C) but falls to 0.03 S/cm at 1073 K (800 °C) (Bove and Ubertini 2008). The model above assumes a constant temperature and a fixed ASR. Chapter 4 presents the results of thermal performance characterization data for MOXIE flight-like stacks. From these data, an enhanced model is derived for how ASR varies with temperature and other test conditions.

It is important to note that MOXIE is power and operation-time constrained. Higher MOXIE operation temperatures require more time and power and more time to cool back to nominal. A human-scale ISRU system would perform a single heat cycle and hold an elevated temperature for the duration of the mission. In this situation, the increased heater power and increase of some material degradation modes at a higher operation temperature would need to be weighed against a lower coking risk, lower ASR, and greater electrical efficiency. See Chapter 7 for a more in-depth discussion of these trades.

3.4.3 Relevant time scales for dynamic modeling components

Several approaches exist for the modeling of the solid oxide electrolysis process. For the purposes of determining the level of detail to model the SOXE for the system model, we can look at time scales relative to the time scales that the MOXIE system can both sense and respond. MOXIE has a sensor sample rate of 1 Hz. Any dynamic response with a time scale below 1 second will be difficult for MOXIE to sense, and any response with a time scale less than a few seconds will be difficult to actuate upon effectively. Gemmen and Johnson (2005) completed a study in which they looked at the modeling time scales for planar solid oxide fuel cells. Their results are shown in Table 5 below.

Table 5 – Characteristic transient time scales of a planar SOFC (Gemmen and Johnson 2005)

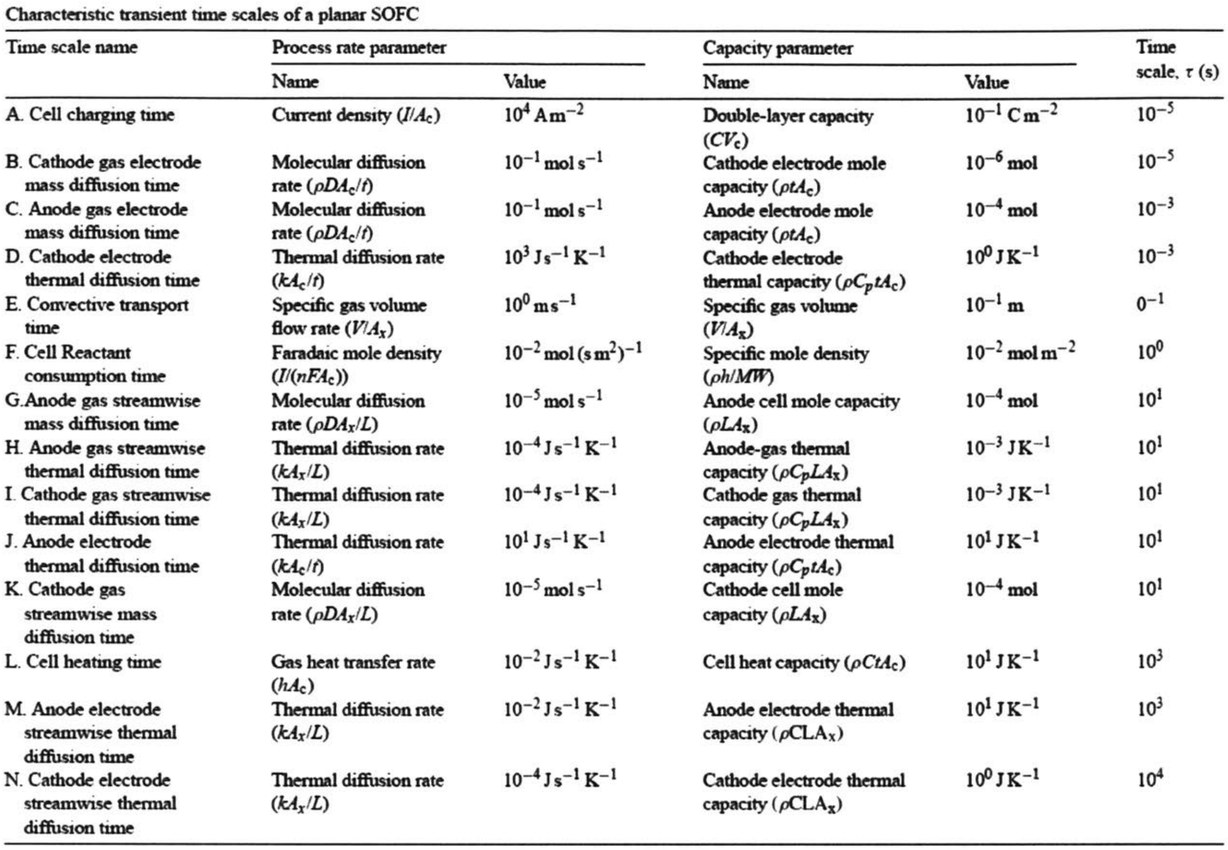

Characteristic transient time scales of a planar SOFC

Time scale name	Process rate parameter		Capacity parameter		Time scale, τ (s)
	Name	Value	Name	Value	
A. Cell charging time	Current density (I/A_c)	$10^4\ \mathrm{A\,m^{-2}}$	Double-layer capacity (CV_c)	$10^{-1}\ \mathrm{C\,m^{-2}}$	10^{-5}
B. Cathode gas electrode mass diffusion time	Molecular diffusion rate ($\rho DA_c/t$)	$10^{-1}\ \mathrm{mol\,s^{-1}}$	Cathode electrode mole capacity (ρtA_c)	$10^{-6}\ \mathrm{mol}$	10^{-5}
C. Anode gas electrode mass diffusion time	Molecular diffusion rate ($\rho DA_c/t$)	$10^{-1}\ \mathrm{mol\,s^{-1}}$	Anode electrode mole capacity (ρtA_c)	$10^{-4}\ \mathrm{mol}$	10^{-3}
D. Cathode electrode thermal diffusion time	Thermal diffusion rate (kA_c/t)	$10^3\ \mathrm{J\,s^{-1}\,K^{-1}}$	Cathode electrode thermal capacity ($\rho C_p tA_c$)	$10^0\ \mathrm{J\,K^{-1}}$	10^{-3}
E. Convective transport time	Specific gas volume flow rate (V/A_x)	$10^0\ \mathrm{m\,s^{-1}}$	Specific gas volume (V/A_x)	$10^{-1}\ \mathrm{m}$	0^{-1}
F. Cell Reactant consumption time	Faradaic mole density ($I/(nFA_c)$)	$10^{-2}\ \mathrm{mol\,(s\,m^2)^{-1}}$	Specific mole density ($\rho h/MW$)	$10^{-2}\ \mathrm{mol\,m^{-2}}$	10^0
G. Anode gas streamwise mass diffusion time	Molecular diffusion rate ($\rho DA_x/L$)	$10^{-5}\ \mathrm{mol\,s^{-1}}$	Anode cell mole capacity (ρLA_x)	$10^{-4}\ \mathrm{mol}$	10^1
H. Anode gas streamwise thermal diffusion time	Thermal diffusion rate (kA_x/L)	$10^{-4}\ \mathrm{J\,s^{-1}\,K^{-1}}$	Anode-gas thermal capacity ($\rho C_p LA_x$)	$10^{-3}\ \mathrm{J\,K^{-1}}$	10^1
I. Cathode gas streamwise thermal diffusion time	Thermal diffusion rate (kA_x/L)	$10^{-4}\ \mathrm{J\,s^{-1}\,K^{-1}}$	Cathode gas thermal capacity ($\rho C_p LA_x$)	$10^{-3}\ \mathrm{J\,K^{-1}}$	10^1
J. Anode electrode thermal diffusion time	Thermal diffusion rate (kA_c/t)	$10^1\ \mathrm{J\,s^{-1}\,K^{-1}}$	Anode electrode thermal capacity ($\rho C_p tA_c$)	$10^1\ \mathrm{J\,K^{-1}}$	10^1
K. Cathode gas streamwise mass diffusion time	Molecular diffusion rate ($\rho DA_x/L$)	$10^{-5}\ \mathrm{mol\,s^{-1}}$	Cathode cell mole capacity (ρLA_x)	$10^{-4}\ \mathrm{mol}$	10^1
L. Cell heating time	Gas heat transfer rate (hA_c)	$10^{-2}\ \mathrm{J\,s^{-1}\,K^{-1}}$	Cell heat capacity (ρCtA_c)	$10^1\ \mathrm{J\,K^{-1}}$	10^3
M. Anode electrode streamwise thermal diffusion time	Thermal diffusion rate (kA_x/L)	$10^{-2}\ \mathrm{J\,s^{-1}\,K^{-1}}$	Anode electrode thermal capacity (ρCLA_x)	$10^1\ \mathrm{J\,K^{-1}}$	10^3
N. Cathode electrode streamwise thermal diffusion time	Thermal diffusion rate (kA_x/L)	$10^{-4}\ \mathrm{J\,s^{-1}\,K^{-1}}$	Cathode electrode thermal capacity (ρCLA_x)	$10^0\ \mathrm{J\,K^{-1}}$	10^4

Of these dynamic components, cell reactant consumption occurs in seconds. Most thermal diffusion rates are 10 seconds or higher, as well as anode gas streamwise mass diffusion time. Cell heating and anode streamwise thermal diffusion occur on a magnitude of 1,000 seconds, while cathode electrode streamwise thermal diffusion is about 10,000 seconds. This data indicates that the cell dynamics near MOXIE's range of sensing are primarily thermally based. The design of the model will reflect this with a thermal mass driven component.

3.4.3.1 Thermal relations to electrolyte conductivity

Richter (1981) presented the total voltage required for the extraction of oxygen from the cell in the form:

$$V_T = E + E_0 + i(R_s + R_z) \tag{3.27}$$

Where E is the electrical potential determined by the partial pressure ratio of oxygen across the membrane, E_o is the overpotential of CO_2 independent of current flow, i is the current density in A/cm^2 and R_s is the combined resistances of the electrodes, including the thickness, current path, electrode density and contact resistances. R_z is the resistance (area specific resistance) of the solid oxide electrolyte. Both R_s and R_z are in terms of $\Omega*cm^2$ and when combined are the total ASR for the cell. The electrical resistance of the electrolyte R_z is more readily broken out and characterized for temperature dependence:

$$R_z = \frac{t}{\sigma_z} \tag{3.28}$$

Where t is the thickness of the electrolyte and σ_z is the conductivity $(\Omega\text{-cm})^{-1}$. Electrolyte thickness is an example of a system design variable that must be carefully considered as a balance between electrochemical performance and structural stability. Resistance decreases with thickness, but so does the strength of the electrode. This has led to the consideration of different cell designs that are structurally supported by the cathode material to minimize electrolyte thickness. The MOXIE SOXE is an electrolyte supported cell.

Strickler and Carlson (1965) characterized the conductivity of several zirconia ceramics. The temperature dependence is represented as:

$$\sigma = A_c e^{\frac{-E_a}{kT}} \tag{3.29}$$

Where A_c is a pre-exponential term for the fit, E_a is the activation energy, k is the Boltzmann constant ($8.617065 * 10^{-5}$ eV/K), and T is the absolute temperature. For 8% YSZ, it was found that $E_a = 0.738$ and $A_c = 86.2$ (Strickler and Carlson 1965).

3.4.3.2 Reaction conditions and heat generation

Heat flow in and out of the stack can be calculated based on the operating parameters. This section establishes the thermodynamic linkages between other parts of the system.

As discussed earlier, the thermal neutral voltage described in Equation (3.10) is the voltage at which operating the reaction does not generate or consume heat. Above V_{tn} the reaction is exothermic and below V_{tn} the reaction is endothermic. The heat generated per cell during the reaction can be quantified by:

$$\dot{Q}_{gen} = I(V_{op} - V_{tn}) \tag{3.30}$$

If the stack is operated below the thermal neutral voltage, additional heat will need to be supplied to make up for the endothermic reaction. Operation at thermal neutral voltage requires some heat addition by the SOXE heaters to maintain steady operating temperature, as some heat is lost through the SOXE insulation and to pre-heating the gas entering the SOXE.

The system model described in Chapter 5 balances this heat transfer with other heat transfer in and out of the system. Reaction heat generated and consumed has little effect on the model when operating near thermal neutral voltage but may have some impact on heater power requirements when operating at operational limits. For the SOXE system, a majority of heat is lost through the insulation (about 70 W) and pre-heating gases (about 24 W).

3.4.4 Acquiring test data for enhanced grey model

The SOXE stack model is considered a grey model because it combines thermodynamic (white model) and black box characterization parameters. The black parameters relied upon include ASR, activation potential, and other corrections that are identified in Chapter 4. In the simplified model presented in this chapter, an estimated ASR value was used to represent the resistances of the cell, including the concentration, activation, and ohmic resistances. To enhance the reliability of the grey model, cell ASR must be mapped through the expected operating range and characterized for degradation effects. ASR dependence on the temperature, flow rates, and operating voltage must be determined in addition to the activation potential.

3.5 Chapter summary and conclusion

Chapter 3 established the modeling framework for the SOXE cells of MOXIE. First, white models were developed to calculate key thermodynamic variables of the SOE reaction. The white model equations include the reaction stoichiometry, relation between measured current and oxygen production, thermal neutral voltage, open circuit voltage, Nernst potential, and reaction heat generation. Second, grey models were created that will accept characterization data to model the I-V curve for different operating conditions. Parameters that will be experimentally determined include ASR_{app}, ASR_{lin}, activation potential, thermal ASR fits, and flow ASR fits. Experimentation will also help determine the relationship between operational conditions and degradation limits. Chapter 4 will discuss the procedure for these characterization experiments and report the results of the characterization of 3 SOXE stacks.

4. SOXE Experimental Characterization

Three experiments were conducted to characterize the performance and safe operational ranges of three flight-like SOXE stacks. The SOXE stacks tested were Ceramatec Stack Assemblies (CSA) 003R, CSA 004, and CSA 005. These experiments investigated the performance and limits of each stack with slightly different operational procedures. First, this chapter describes the motivation, background, and hypotheses for these experiments. Next, the general experimental setup and equipment used in all three experiments are described. Then, experiment-specific setup, procedures, and results are detailed. The chapter concludes with a comparison of the data from each experiment, hypothesis evaluation, and a discussion of the impact of the experimental results on the SOXE modeling approach.

4.1 Motivation

Chapter 3 introduced the white model approach for modeling the SOXE cells. This included several equations derived from thermodynamic principles that hold true for the operation of an ideal SOXE cell. Parameters such as Nernst potentials, thermal neutral voltage, and enthalpy of formation are directly calculated for a defined reaction at measureable state variables including pressure, voltage, and mass flow rate. A flight SOXE is an imperfect, complex chemical plant with many possible simultaneous reactions. Furthermore, the SOXE does not operate under ideal, perfectly distributed conditions. Flow, temperature, and currents are distributed unevenly across the cell area. Additional temperature and flow variation exists between cells in a stack. Imperfect conditions require grey models to achieve an accurate model of SOXE performance at a system level. Grey models are white models enhanced with characterization data from the operation of the system. Grey model parameters include area specific resistance (ASR) and activation potential. These terms can be adjusted with established relations such as the Arrhenius equation to model temperature dependence, and design specific fits such as those based on flow conditions in a particular SOXE design.

4.2 Objectives

These experiments were designed to derive the grey SOXE model terms. The ultimate goal was to develop a SOXE model that is accurate across many different cells and easily adjusted to account for cell-to-cell variation. The model requires accuracy to predict the I-V relationship for various flow conditions and temperatures that the SOXE may encounter. A clear understanding of the SOXE operational limits and their relationships to degradation factors is also required. The experimental objectives were:

Objective 1: to characterize SOXE performance under a range of operating conditions to derive terms needed to implement the grey models

Objective 2: to understand how operational conditions affect the risk factors for degradation.

4.3 Background

Operational mapping is completed by creating a test matrix that spans the range of possible cell flow rates and temperatures, and then performing I-V steps through that range. The current steps are adjusted at each flow rate in order to map to different cell utilizations so that a similar number of steps can be achieved at each flow level. A description of the test plan used for the operational window is in Section 4.6.2, Operational window testing.

4.3.1 Cell degradation mechanisms

Understanding SOXE degradation mechanisms is important for extracting the most scientific value from MOXIE and the highest resource value from an extensible ISRU system. There are two types of degradation mechanisms, defined here as long-term and short-term degradation. Long-term degradation mechanisms happen over time scales from hours to months of operation, while short-term mechanisms occur over the span of seconds. Long-term degradation mechanisms include:

1. Coarsening of the cathode
2. Anode poisoning by chromium
3. Cation inter-diffusion in the perovskite

4. Interconnect oxidation and scale growth

The long-term degradation mechanisms listed above relate to the chemical stability of the SOXE cell materials and supporting structures. The degradation rates of these mechanisms usually increase with higher operating temperatures. Mitigation strategies could include lowering the operating temperature, adjustments to material design, or designing the SOXE cells with excess production capacity to account for a predictable decrease in performance over time. Given the nature of long-term degradation, the performance decline is neither quick nor catastrophic. A human-scale ISRU plant would run for about 14 months to manufacture oxygen for a return trip (Drake 2009). Additional time of operation may be required to support a multi-mission Mars base. For these reasons, long-term degradation must be well understood and factored into the design of a manned Mars mission. These mechanisms will have less impact on MOXIE, as it is only designed to run for 15 cycles. For each MOXIE cycle, the stack will be operating in electrolysis mode for 15-110 minutes (Johnson 2017), amounting to a maximum total electrolysis time of 27.5 hours.

Compared to a human-scale mission that may only turn on once, MOXIE will undergo many start-up and shut-down cycles. This puts MOXIE in the unique position to help understand and retire risk associated with repeated start-up and shut downs, as well as operation with different control parameters. Because of the frequent cycling and potential to experience changes in operating conditions, short-term SOXE degradation mechanisms pose the greatest risk to the MOXIE. Primary short-term degradation mechanisms include:

1. Oxidation of the nickel cathode
2. Carbon deposition on the cathode
3. Thermal cycling induced degradation (seal and electrical contact damage)

Two of these degradation mechanisms are the result of chemical reactions that are possible at opposite ends of the CO_2 utilization spectrum. Oxidation of the nickel cathode occurs when there is insufficient CO in the flow stream to prevent oxidation by CO_2, and coking occurs when the ratio of CO to CO_2 is too high, allowing CO molecules to be reduced. Figure 18 shows how it is possible for both the oxidation risk conditions and coking conditions to occur simultaneously in the same SOXE cell.

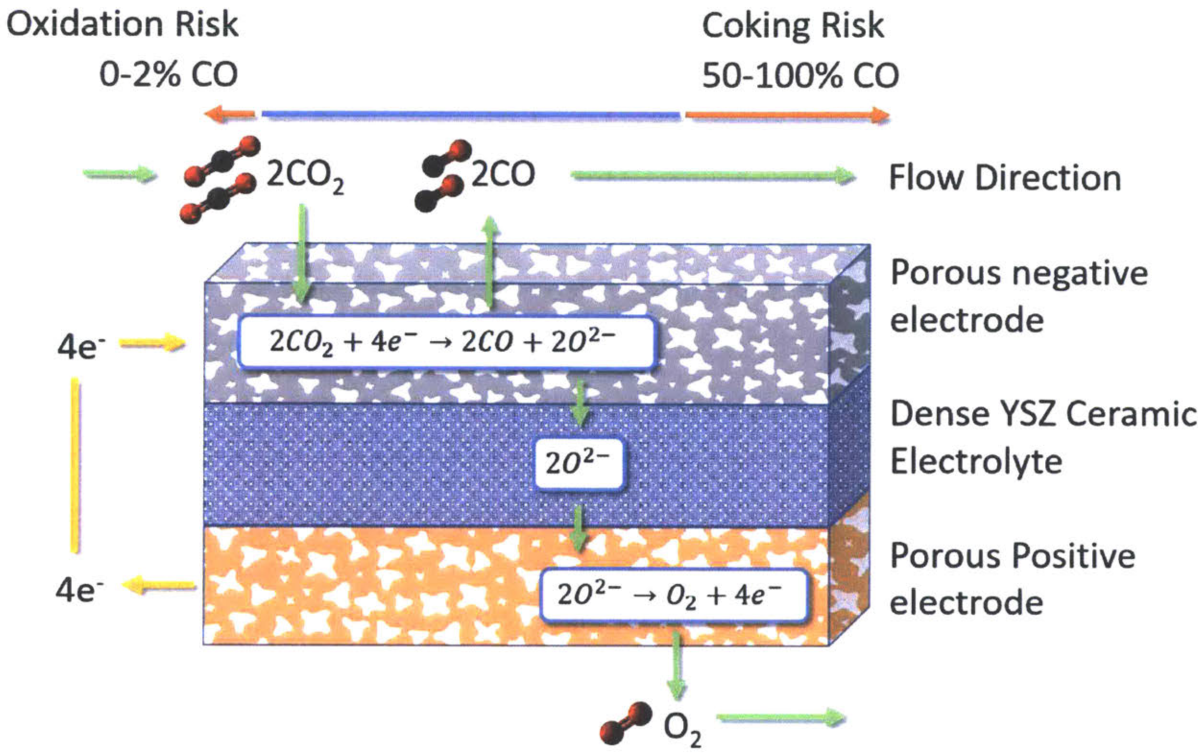

Figure 18 – A cell cross-section including lateral regions of oxidation and coking risk (adapted from Meyen, Hecht et al. (2016))

Without effluent flow recirculation, CO_2 entering the cell has almost no CO content, putting the cathode at risk for oxidation. As the gas flows across the active length of the cell, CO_2 is consumed and the flow composition becomes favorable to CO_2 electrolysis. At the end of the length of the cell, CO_2 is depleted until electrolysis of CO is possible and could result in carbon deposition on the cathode.

4.3.1.1 Oxidation

The solid oxide electrolysis (SOE) cells used in the SOXE have a nickel-based catalyst to facilitate the electrolysis of CO_2. A drawback of using nickel as a catalyst is that under certain thermodynamic conditions, the nickel can oxidize, reducing its effectiveness. This reaction is shown in Equation (4.1) below:

$$Ni + \frac{1}{2}O_2 \leftrightarrow NiO \tag{4.1}$$

The Equation (4.1) chemical equilibrium interacts with the chemical equilibrium of Equation (4.2):

$$CO + \frac{1}{2}O_2 \leftrightarrow CO_2 \tag{4.2}$$

At 800 °C with 0.55% mol fraction CO or greater, the O_2 potential thermodynamically favors Equation (4.2) and cathode oxidation is no longer likely (Hartvigsen 2016). Introducing just a small amount of CO into the incoming stream can be an effective mitigation strategy for the cathode oxidation risk. This will be accomplished on MOXIE by recirculating a fraction of the SOXE effluent, containing CO, back to the SOXE inlet. During operation, this strategy will keep the inlet CO concentration above 0.55%. Upon SOXE start up, there will only be a few seconds before recirculation begins to mitigate the risk of oxidation.

There is the potential to risk nickel oxidation of the entire stack depending on the control process design. Oxidation can occur when there is CO_2 in a hot SOXE with CO_2 flow and no current applied. The hot SOXE makes production of O_2 favorable from the supply of CO_2. In this situation, there is no applied potential to drive oxygen ions away from the Ni and through the YSZ as oxygen forms. This operational state has important control system implications described in Chapter 5.

4.3.1.2 Coking

Coking is a process where the electrolyzer produces carbon that forms on the cathode of the SOXE. It occurs when the CO is reduced to carbon. Coking can form by means of the Boudouard reaction shown in Equation (4.3) below:

$$2CO(g) \leftrightarrow CO_2(g) + C(s) \tag{4.3}$$

Coking can reduce the effectiveness of the cathode by fouling its porous surface and blocking the catalytic sites. In extreme cases, carbon deposition can occlude the flow channels within a SOXE cell. Figure 19 below shows a comparison of two SOXE cells from stack CSA 003R that were intentionally driven into the coking regime. The cell on the left (Cell 7) shows no apparent coke formation while the cell on the right shows significant coke formation.

Figure 19 – CSA 003R SOXE cell cathode without signs of coking (left) and with significant coking (right)

The amount of coke on cell 8 is so significant that it may have partially blocked some of the flow channels through the cell. Restricted airflow to parts of the cell may further increase the apparent CO_2 utilizations in those areas and promote additional coking. Carbon formation affects the function of the entire cell by increasing the resistance across the cell. The result is an increase in the voltage to maintain a current through the entire stack, or a diminishing current flow through a stack under constant voltage operation. Ultimately, the resistance can grow so high that the entire stack can no longer effectively generate oxygen.

The primary way to avoid coking is to understand the system sufficiently to only operate under conditions that are not thermodynamically favorable to carbon formation. If coking is not avoidable, a potential mitigation strategy is to design a control system that could monitor any upward drift in voltage during constant current operation that may indicate coking. Once degradation is recognized, the system should leave the hazardous operational conditions by reducing the current. The stack can be "parked" at open circuit voltage or a lower current (and higher utilization %) to recover some of the damage. If the stack has independently controlled cells or the ability to bypass a cell, a current path can be provided to bypass the damaged cell. Our SOXE flight system will not have the ability to bypass individual cells but could potentially bypass one of the two, electronically coupled, five-cell groups.

Coke formation is thermodynamically possible when the operating voltage is above the CO reduction potential. This potential is calculated as the Nernst potential for CO-C based on the temperature and partial pressures of the reactants and products as shown in Equation (4.4):

$$V_{CO \to C_s} = \frac{\left(\Delta G^{\circ}_{f,CO_2} + RTln\left(\frac{(PO_2)^{\frac{1}{2}}}{(PCO)} \right) \right)}{2F} \tag{4.4}$$

where the Gibbs free energy of formation follows the temperature dependent linear fit:

$$\Delta G^{\circ}_{f,CO_2} = 1.118(10^5) + 88.5 * T \tag{4.5}$$

where T is the temperature in Kelvin. This fit is based on a fit derived by Hartvigsen, Elangovan et al. (2015). The relation has a Pearson correlation coefficient (r-value) of 0.9999 and is valid between 1043 K (770 °C) and 1103 K (830 °C). Equation (4.4) is plotted in Figure 20 to illustrate CO reduction potential trends with respect to mole fraction and temperature. The pressure used to generate Figure 20 is 0.868 atm to reflect the pressure in Salt Lake City, UT where the characterization of these experiments was conducted.

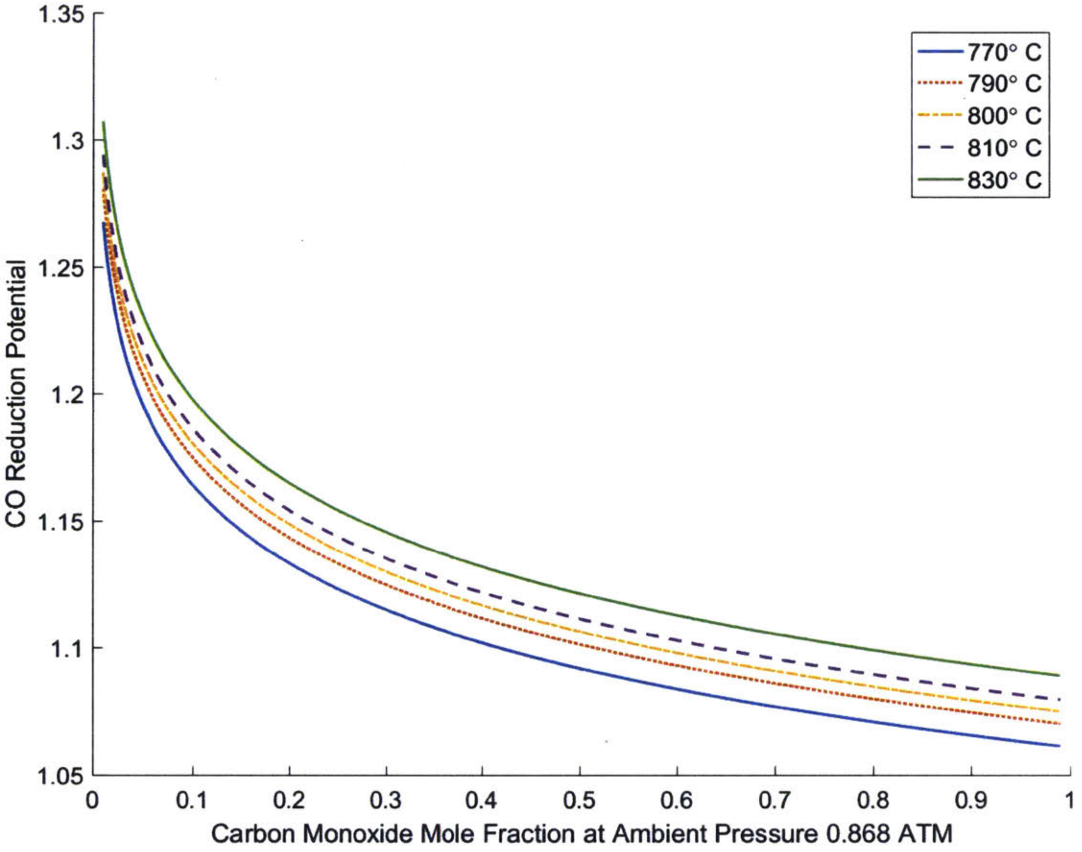

Figure 20 – CO Nernst potential as a function of mole fraction

The CO Nernst potential increases at lower CO mole fractions and higher temperatures. Because the safe zone for a cell is below this line, MOXIE can safely operate at higher voltages when the temperature is higher and the CO_2 utilization is lower.

Operating at a voltage below the CO Nernst potential should be safe with respect to coking degradation. However, this voltage cannot be exceeded for an individual cell. Overall stack voltage measurements alone cannot ensure that every cell is operating in a safe region. The voltage available for this reaction is slightly less than what is measured by the voltage tabs of the SOXE due to losses between the sensors and reaction sites. Additional uncertainty is introduced by the uncertainty of temperature and local CO mole fractions in the cathode.

CO_2 reduction still occurs at voltages above the CO Nernst potential. As long as the CO_2 Nernst potential is below the CO Nernst potential, it is favorable to electrolyze CO_2 before CO. Chapter

3 described the CO_2 Nernst potential for the reaction. The Nernst potentials for CO_2 reduction and CO reduction vary based on the partial pressures of CO_2 and CO. As more CO_2 is consumed to produce CO, the relative partial pressures of these gases change. At higher utilizations, the CO reduction potential decreases and the CO_2 reduction potential increases. The point where the potentials are equivalent is called the Boudouard boundary. Figure 21 shows where the thermodynamic equilibrium point for these two reactions occurs.

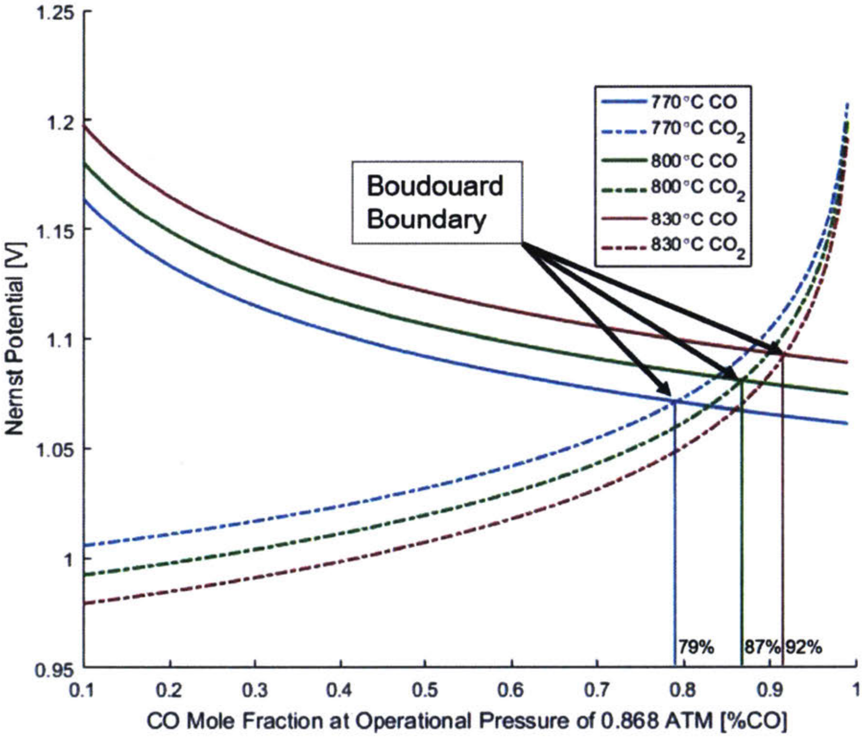

Figure 21 – The Boudouard boundary occurs where the CO_2-CO and CO-C Nerst potentials cross

At 800°C and 0.868 atm (the ambient pressure for the Ceramatec tests), the Nernst potentials for CO_2 and CO reduction are equal when the utilization is above 87%. For the same pressure at 770°C the utilization at the Boudouard boundary is 79%. Any utilization above this will most likely result in coke formation. The left image of Figure 22 shows the Boudouard boundary plotted for varying pressures and temperatures. By calculating the Boudouard boundary, an a priori maximum utilization percent for SOXE operation can be determined.

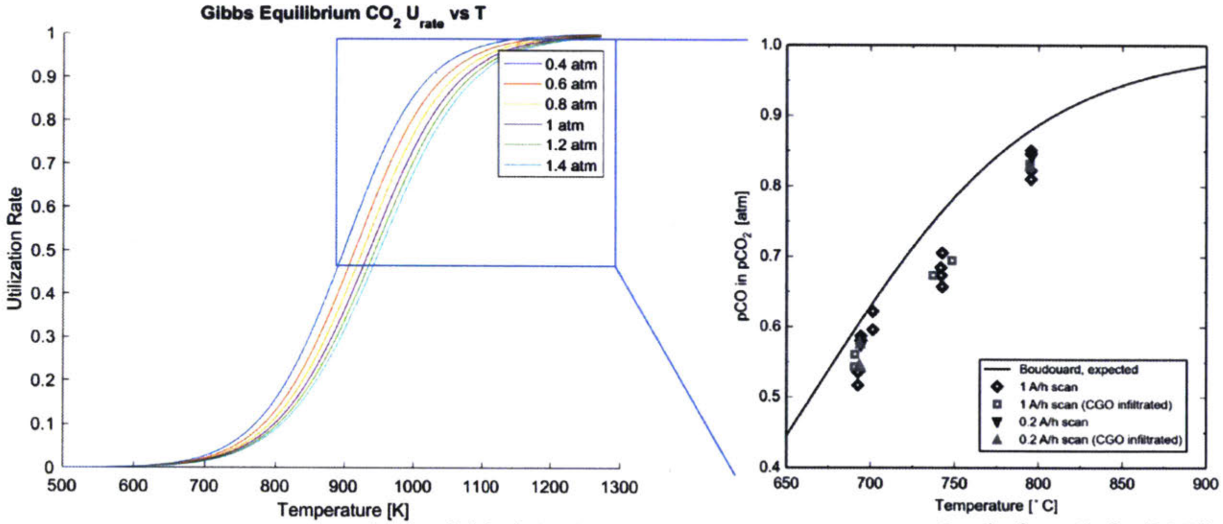

Based on calculations by Hartvigsen

Results from Skafte (2015)

Figure 22 – Calculated Boudard limit for coke formation (Hartvigsen, Elangovan et al. 2015)(left) and coking limits from Skafte (2015) (right)

The actual level at which coking occurs is slightly below that boundary. The right image shows work by Skafte (2015) that compared the actual coking thresholds of a SOE cell to the Boudouard boundary. As stated above, it is possible to form carbon at any operating condition above the CO Nernst potential. Coking becomes the more favorable reaction above the Boudouard limit. Experiments 1 and 2 investigate the coking boundary and its relation to the Boudouard limit by increasing the stack current until cell degradation is observed. The operational mapping of CSA 005 in experiment 3 stays clear of any potential coking by monitoring all cells and ending the I-V sweeps before any cell exceeds the CO Nernst potential.

4.4 Hypotheses

Two hypotheses were evaluated as part of the experimental testing. The results of these will be used to inform flight stack characterization and grey model development.

4.4.1 Hypothesis I

Hypothesis I: *The cell-to-cell variation observed in SOXE stacks is caused by variability in material processing. A modeling approach that characterizes current-voltage trends and shifts these values with respect to a characterized ASR for each cell can be used to describe accurately the full envelope performance of a stack.*

From prior experience with these SOXE stack designs, it is known that there is some cell-to-cell variability. The worst performing SOXE cell is the one that determines the boundary of operation to avoid cell coking. The flight stacks will not undergo a pre-flight characterization to the same extent of the experiments in this chapter. Additionally, the flight stack will only have voltage leads across each 5-cell group. Therefore, understanding cell-to-cell variation is the key. The importance of Hypothesis I is that it will determine how the final flight stacks are characterized. If the variation in cell ASR is primarily due to variation in material composition and processing steps, then it may be possible to establish the baseline for the performance of each cell at one flow and current condition and then extrapolate the performance at other conditions based on repeatable relationships observed in other SOXE stacks. The baseline plan for the flight SOXE characterization test is to observe the performance at a temperature of 800°C and 100 g/hr (98% CO_2 2% CO) over several current steps. If the cell-to-cell variation is caused by some other factor, a different baseline characterization range may be more suitable.

Data collected from Experiment 3, the characterization of CSA 005, will be used to test this hypothesis. Results from Experiments 1 and 2 (using stacks CSA 003R and CSA 004) are used to supplement these conclusions but are not considered as reliable because of the cell damage that may have occurred to these stacks due to the nature of their testing procedures.

4.4.2 Hypothesis II (additional potential)

Hypothesis II: *SOXE cells can be represented accurately by the approximate ASR equations that represent the ASR as the slope of the I-V curve with an intercept of the open circuit voltage (OCV). This equation is valid because little to no additional potential (activation or otherwise) is observed.*

$$ASR_{app} = \frac{(V_{op} - V_{ocv})}{i_{den}} \tag{4.6}$$

Alternately, if the additional potential is observed, it is predicted that the I-V relationship will more closely follow this form:

$$ASR_{lin} = \frac{(V_{op} - (V_{add} + V_{ocv}))}{i_{den}} \tag{4.7}$$

Where ASR_{lin} is the best fit ASR in the linear region of the i-V curve, and V_{add} is an additional voltage which may be comprised of an activation potential or other loss. SOXE is unique from most research on terrestrial SOE applications in that the cells process dry CO_2. As described in Chapter 3, dry electrolysis is less thermodynamically favorable than CO_2 co-electrolysis with steam. This hypothesis assumes that the difference between dry and steam co-electrolysis does not manifest as a significant activation potential. For these reasons, the standard for comparing SOXE cell performance during the development of MOXIE has been to use Equation (3.22), without considering the activation potential term.

Evaluating Hypothesis II is important for the operation of the MOXIE control system. ASR describes the characteristics of the I-V curve. The most accurate relations must be established to predict expected current and voltages during operation. The ASR equations also influence the PI gains for control models and the results of sensitivity analysis. When developing models of extensible systems, an accurate representation of ASR for dry CO_2 electrolysis will improve the accuracy of system trades and models.

Evidence to support Hypothesis II was derived from Experiment 4, the characterization of SOXE stack activation energy. Additional data on activation energies for each cell is supported by data from Experiments 1, 2, and 3.

4.5 Experimental setup and test equipment

The SOXE characterization lab used in these experiments is located at Ceramatec Inc. in Salt Lake City, Utah. The test facility includes four independent test rigs. Each test rig uses five Alicat mass flow controllers for the supply gases. Available feed gas lines are CO_2, CO, H_2, N_2, and Air. In these experiments, only CO_2, CO, and H_2 supply gases were used. The gases mix in tubing along the path to the temperature-controlled kiln where the SOXE stack is installed. Figure 23 below shows the layout of the four SOXE test rigs. One set of flow controllers is shown in the image on the right.

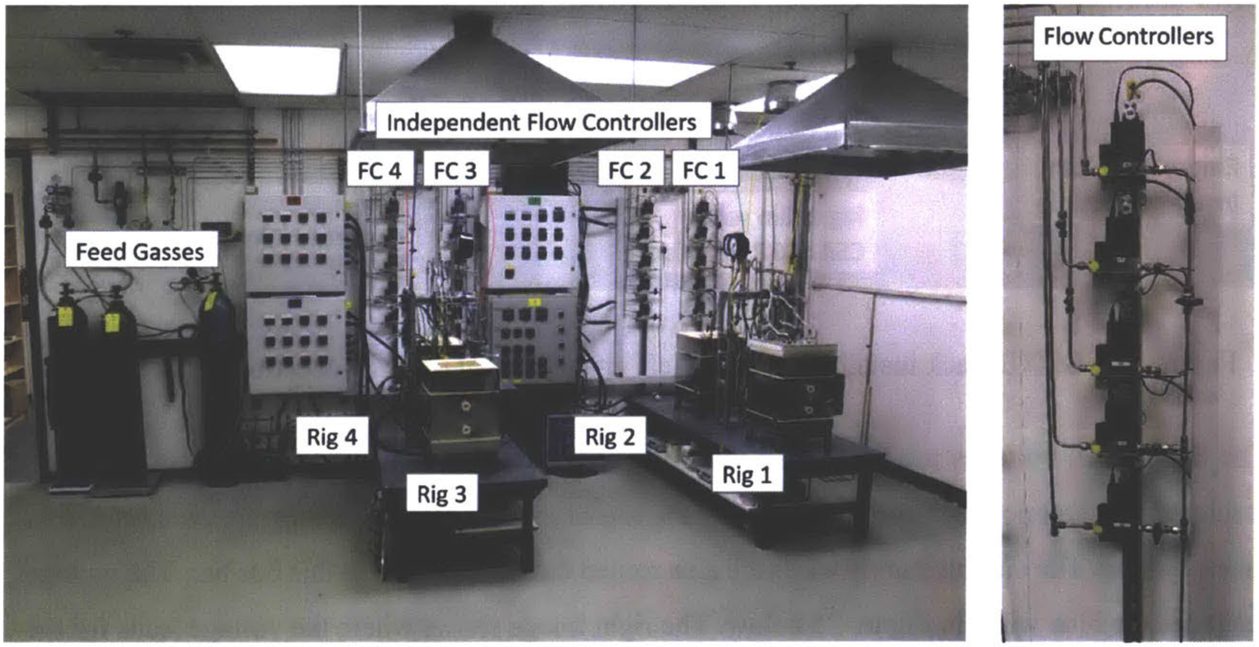

Figure 23 – Experimental test cells consists of 4 independent test rigs (left) with independent mass flow controllers (FC) for each type of gas (right)

The SOXE is secured to the removable lid of each kiln. The left image of Figure 24 below shows the Rig 2 kiln with lid removed and the Rig 1 kiln with a SOXE secured under the lid and installed in the kiln. The gas tubing and electrical connections pass through the top of the kiln. Three, 1/8 inch Inconel (an austenitic nickel-chromium based alloy) tubes are routed through the lid to the stack within the hot zone of the kiln. The first tube provides the feed gases (usually a CO_2 and CO mixture), the second tube exhausts cathode CO_2/CO effluent gases, and the third tube connects to the cell anode to exhaust the O_2 effluent. Depicted in the right image of Figure 24 is the location of the inlet and outlet tubes, stack current leads, and voltage probes.

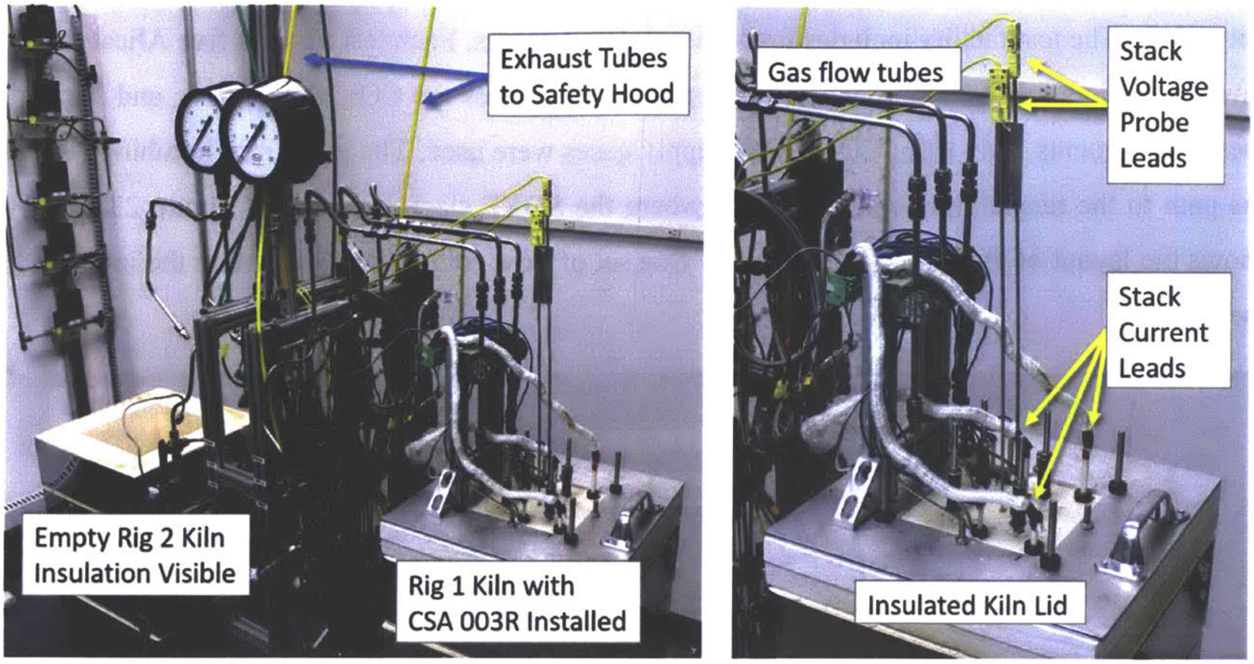

Figure 24 – SOXE stack installed in Rig 1 (left image) Detail of lid connection (right image)

The SOXE cell voltages are monitored by thin wire leads welded to each cell. These leads are insulated by ceramic tubes and routed out of the top of the kiln lid where they are connected to a green bus bar. The current supply wires are also routed through the kiln to this bus bar. The voltage leads are the blue wires in Figure 25 below. The right image shows where the voltage leads for the cells, endplates, midplate, and power supplies connect to the bus bar.

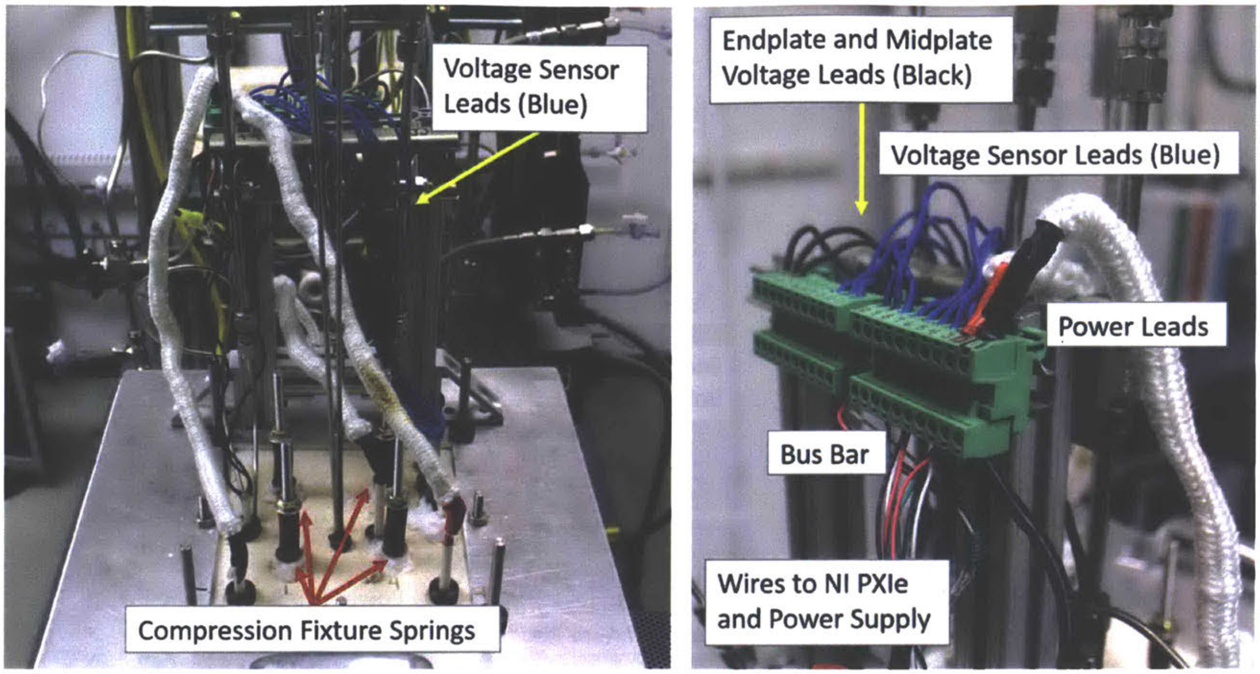

Figure 25 – Voltage lead and compression fixture locations (left) and bus bar detail (right)

Figure 26 below shows where the wires are connected to the SOXE stack. Ceramic tubing insulates all the wires. The wires on the left are the voltage leads for monitoring cell voltage. On the right, the current tabs for the top endplate, midplate, and bottom endplate are visible. The current leads are the lower wires with the large insulation and the additional voltage sensor leads are the small ceramic insulated wires above the current leads. Two of the current leads can also be seen with the red and blue paint on the ceramic tube that feeds them into the lid. The compression structure is visible as two metal plates connected compressed between four concentric metal rods. These experiments were conducted at ambient atmospheric pressure so the compression structure was not necessary. However, the structure was left in place to be similar to the compression applied to the stacks tested at JPL in a vacuum chamber at Mars atmospheric pressures. The SOXE stack in MOXIE will also be under compression by a similar type of fixture to counteract the pressure imbalance between the inside of the cell and the outside ambient pressure.

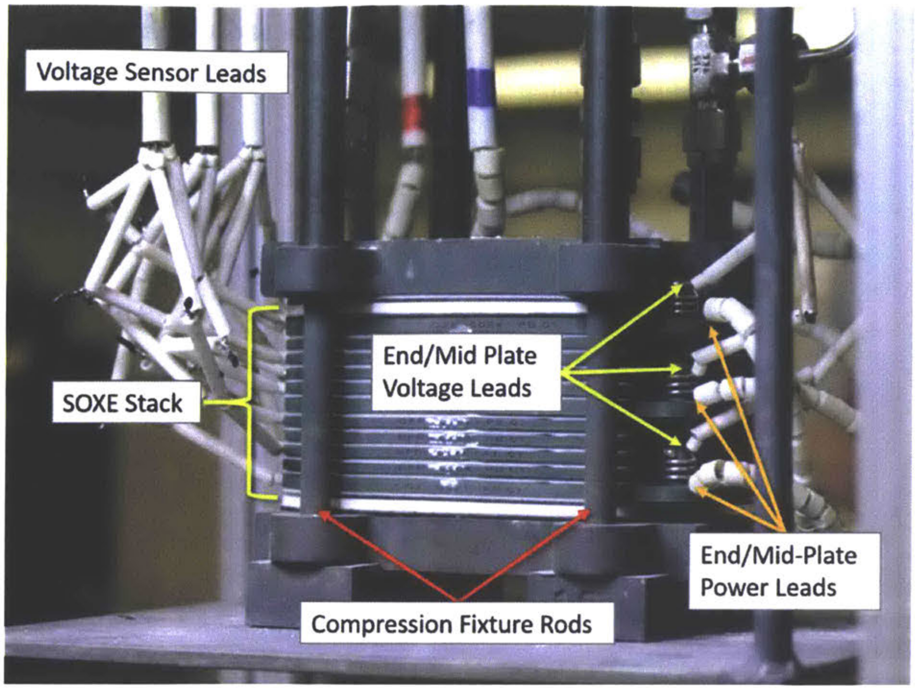

Figure 26 – SOXE mounted in compression fixture and wired for placement in the test rig kiln

National Instruments LabVIEW software was used to control experimental process parameters. LabVIEW controller settings were passed from the lab computer to a National Instruments PXIe Controller Bus. The NI PXIe interfaced with multiple Watlow EZ-ZONE panel mount controllers to control the furnace temperature and mass flow controllers. The Watlow controllers also recorded the inlet and outlet pressure on the CO_2/CO lines. A TDK-Lambda GENH30-25 750W DC Power Supply was controlled by the NI PXIe supplied SOXE current. Voltages are recorded by the NI PXIe for each cell, across the stack, and across the power supply to ground. The LabVIEW program samples data at 0.2 Hz. The data acquisition and control hardware are shown in Figure 27 below.

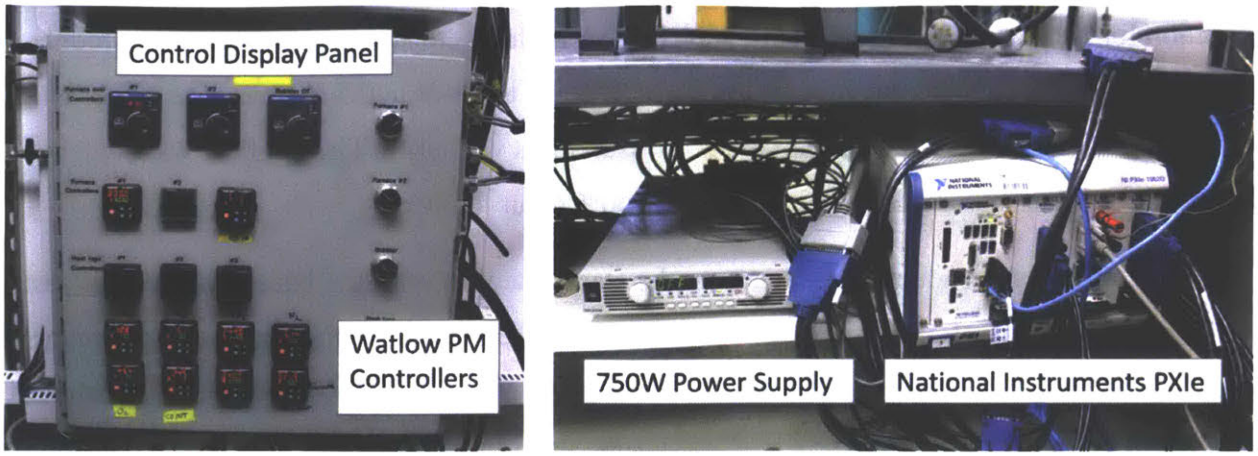

Figure 27 – Rig 1 control panel with Watlow Panel Mount Controllers (left) and the TDK-Lambda GENH30-25 power supply next to the National Instruments PXIe (right)

4.6 General methods for experiment 1, 2, and 3

4.6.1 Stack preparation and initial characterization

Each stack was prepared and characterized with a baseline test procedure prior to the operational window experiments (experiments 1, 2, and 3) and activation potential investigation (experiment 4). The pre-experimental steps were:

1. Stack reduction
2. Baseline characterization
3. Cold stack leak test

After installation into the SOXE test rig kiln, each stack was chemically reduced with H_2 gas for at least 24 hours. The reduction process ensures that the cathode is fully reduced before experimentation.

Next, the SOXE inlet gases were switched to a composition of 880 sccm CO_2 and 18 sccm CO (2% CO) for the baseline characterization step. A concentration of 2% CO was added to prevent oxidation of cathode at the stack inlet. The test rig kiln was held at 800°C for the duration of the test. The current response was recorded for a voltage controlled I-V sweep from 9.0 V (0.9 V/cell) to 12 V (1.2 V/cell) in 0.75 V increments. During the I-V sweep, the current was monitored and limited to a maximum of 4.0 amps. Once the stack voltage reached 12 V, the cell was held at that condition for 120 minutes. Gas chromatograph (GC) samples were taken at the beginning, middle, and end of this dwell. Next, the voltages were swept down to 9.0 V in 0.5 V steps. The power was then disconnected and an open circuit voltage measurement was taken. The gas flow was switched to N_2 and the kiln programed to cool at a rate of 100°C/hour to 30°C.

A cold leak test was conducted to determine the stack integrity after the baseline test. This test evaluated three types of stack leaks: anode leaks from the O_2 side to the outside of the stack, cathode leaks from the CO_2 side to the outside of the stack, and "crossover" leaks from the cathode to anode of the stack.

4.6.2 Operational window testing

The operational window experiments (Experiments 1, 2, and 3) for stacks CSA 003R, CSA 004, and CSA 005 all followed the same current set point progression in the operational window test matrix. Table 6 below shows the test matrix for mapping at 800°C.

Table 6 – Experimental test matrix for stack performance mapping

Pump g/h 100% CO2	30	35	40	45	50	55	60	65	70	75	80	100	
Total SCCM	254.5	296.9	339.3	381.7	424.2	466.6	509.0	551.4	593.8	636.2	678.6	848.3	
CO2 SCCM @ 2% CO	249	291	333	374	416	457	499	540	582	624	665	831	
2% CO SCCM flow	5.1	5.9	6.8	7.6	8.5	9.3	10.2	11.0	11.9	12.7	13.6	17.0	
100% Utilization Current	3.58	4.18	4.77	5.37	5.97	6.56	7.16	7.76	8.36	8.95	9.55	11.94	
CO2 Utilization	Stack Current, Amps												CO Nernst V
30%	1.07	1.25	1.43	1.61	1.79	1.97	2.15	2.33	2.51	2.69	2.86	3.58	1.123
32%	1.15	1.34	1.53	1.72	1.91	2.10	2.29	2.48	2.67	2.86	3.06	3.82	1.120
34%	1.22	1.42	1.62	1.83	2.03	2.23	2.43	2.64	2.84	3.04	3.25	4.06	1.117
36%	1.29	1.50	1.72	1.93	2.15	2.36	2.58	2.79	3.01	3.22	3.44	4.30	1.115
38%	1.36	1.59	1.81	2.04	2.27	2.49	2.72	2.95	3.18	3.40	3.63	4.54	1.112
40%	1.43	1.67	1.91	2.15	2.39	2.63	2.86	3.10	3.34	3.58	3.82	4.77	1.110
42%	1.50	1.75	2.01	2.26	2.51	2.76	3.01	3.26	3.51	3.76	4.01	5.01	1.107
44%	1.58	1.84	2.10	2.36	2.63	2.89	3.15	3.41	3.68	3.94	4.20	5.25	1.105
46%	1.65	1.92	2.20	2.47	2.75	3.02	3.29	3.57	3.84	4.12	4.39	5.49	1.103
48%	1.72	2.01	2.29	2.58	2.86	3.15	3.44	3.72	4.01	4.30	4.58	5.73	1.101
50%	1.79	2.09	2.39	2.69	2.98	3.28	3.58	3.88	4.18	4.48	4.77	5.97	1.099
52%	1.86	2.17	2.48	2.79	3.10	3.41	3.72	4.03	4.34	4.66	4.97	6.21	1.098
54%	1.93	2.26	2.58	2.90	3.22	3.55	3.87	4.19	4.51	4.83	5.16	6.45	1.096
56%	2.01	2.34	2.67	3.01	3.34	3.68	4.01	4.34	4.68	5.01	5.35	6.68	1.094
58%	2.08	2.42	2.77	3.12	3.46	3.81	4.15	4.50	4.85	5.19	5.54	6.92	1.093
60%	2.15	2.51	2.86	3.22	3.58	3.94	4.30	4.66	5.01	5.37	5.73	7.16	1.091
62%	2.22	2.59	2.96	3.33	3.70	4.07	4.44	4.81	5.18	5.55	5.92	7.40	1.089
64%	2.29	2.67	3.06	3.44	3.82	4.20	4.58	4.97	5.35	5.73	6.11	7.64	1.088
66%	2.36	2.76	3.15	3.55	3.94	4.33	4.73	5.12	5.51	5.91	6.30	7.88	1.087
68%	2.43	2.84	3.25	3.65	4.06	4.46	4.87	5.28	5.68	6.09	6.49	8.12	1.085
70%	2.51	2.92	3.34	3.76	4.18	4.60	5.01	5.43	5.85	6.27	6.68	8.36	1.084

The test is matrix organized into 12 columns. Each column is a different mass flow rate that the SOXE cells may experience in flight. The flows range from 30 to 80 g/hr in 5 g/hr increments, with an additional characterization point at 100 g/hr. Each flow condition is defined by standard cubic centimeters per minute, the units used for the test rig mass flow controllers. At each flow rate, 2% of the total flow is CO and 98% of the flow is CO_2. This inlet composition is used to reduce the risk of cathode oxidation so that the only degradation mechanism observed is coking.

On the left hand side of the matrix, the rows are labeled by utilization. Under each flow condition, the stack CO_2 utilization begins at 30% and steps up by 2% until reaching either 70%, a current limit of 4A (highlighted in red), or an indication of coking. The 4A current limit is an artifact of the limitations of the flight power supply for MOXIE and is not an electrochemical limitation. The percent utilization operation points are achieved by commanding stack current set points that are calculated based on the flow conditions. The calculated current values comprise the body of the table.

Each experiment began at 30% utilization at a specified flow and temperature condition and held that current level for 5 minutes (shorter when indicated below) to achieve steady state operation. Then the current was increased and held at the next point for 5 minutes. After the current and utilization limit for a column was reached, the stack was set to open circuit conditions with no current flow. The stack was left at open circuit conditions until the voltages of any cells that had climbed above the previously measured open circuit voltage (possibly due to degradation) returned to that previous open circuit voltage. The current value was then returned to 30% utilization for the recently characterized flow conditions, and then the CO_2 and CO flows were increased to the level required for the next flow condition.

The primary difference in these experiments is how the maximum current set point for any given flow and temperature combination is determined. The maximum current for CSA 003R was determined after the measured voltage of the stack began to drift upward during a 5-minute run. The maximum current for CSA 004 was determined as soon as the voltage drifted upwards in any cell or the ASR appeared to deviate. For CSA 005, the maximum current at a particular flow rate was determined to be the point when the voltage of a single cell rose above the CO-C Nernst potential. The CO-C Nernst potential is the lowest cell potential where CO reduction to carbon is possible. This potential is listed in the right most column of Table 6 above.

The expected voltage at each step can be calculated by assuming an ASR value and using Equation (4.6) to relate ASR and current to voltage. Table 7 shows the expected voltages based on an assumed ASR_{app} of 1.60.

Table 7 –Estimated cell voltage at target current

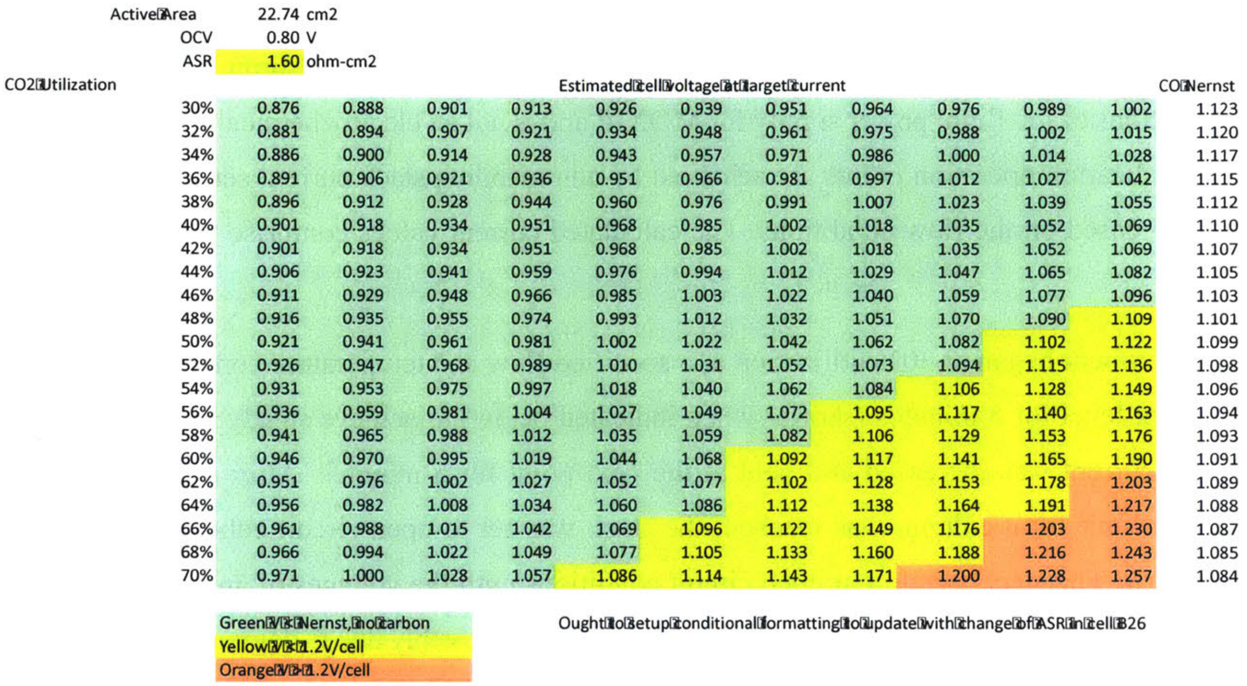

Active Area 22.74 cm2
OCV 0.80 V
ASR 1.60 ohm-cm2

CO2 Utilization					Estimated cell voltage at target current							CO Nernst
30%	0.876	0.888	0.901	0.913	0.926	0.939	0.951	0.964	0.976	0.989	1.002	1.123
32%	0.881	0.894	0.907	0.921	0.934	0.948	0.961	0.975	0.988	1.002	1.015	1.120
34%	0.886	0.900	0.914	0.928	0.943	0.957	0.971	0.986	1.000	1.014	1.028	1.117
36%	0.891	0.906	0.921	0.936	0.951	0.966	0.981	0.997	1.012	1.027	1.042	1.115
38%	0.896	0.912	0.928	0.944	0.960	0.976	0.991	1.007	1.023	1.039	1.055	1.112
40%	0.901	0.918	0.934	0.951	0.968	0.985	1.002	1.018	1.035	1.052	1.069	1.110
42%	0.901	0.918	0.934	0.951	0.968	0.985	1.002	1.018	1.035	1.052	1.069	1.107
44%	0.906	0.923	0.941	0.959	0.976	0.994	1.012	1.029	1.047	1.065	1.082	1.105
46%	0.911	0.929	0.948	0.966	0.985	1.003	1.022	1.040	1.059	1.077	1.096	1.103
48%	0.916	0.935	0.955	0.974	0.993	1.012	1.032	1.051	1.070	1.090	1.109	1.101
50%	0.921	0.941	0.961	0.981	1.002	1.022	1.042	1.062	1.082	1.102	1.122	1.099
52%	0.926	0.947	0.968	0.989	1.010	1.031	1.052	1.073	1.094	1.115	1.136	1.098
54%	0.931	0.953	0.975	0.997	1.018	1.040	1.062	1.084	1.106	1.128	1.149	1.096
56%	0.936	0.959	0.981	1.004	1.027	1.049	1.072	1.095	1.117	1.140	1.163	1.094
58%	0.941	0.965	0.988	1.012	1.035	1.059	1.082	1.106	1.129	1.153	1.176	1.093
60%	0.946	0.970	0.995	1.019	1.044	1.068	1.092	1.117	1.141	1.165	1.190	1.091
62%	0.951	0.976	1.002	1.027	1.052	1.077	1.102	1.128	1.153	1.178	1.203	1.089
64%	0.956	0.982	1.008	1.034	1.060	1.086	1.112	1.138	1.164	1.191	1.217	1.088
66%	0.961	0.988	1.015	1.042	1.069	1.096	1.122	1.149	1.176	1.203	1.230	1.087
68%	0.966	0.994	1.022	1.049	1.077	1.105	1.133	1.160	1.188	1.216	1.243	1.085
70%	0.971	1.000	1.028	1.057	1.086	1.114	1.143	1.171	1.200	1.228	1.257	1.084

Green V < Nernst, no carbon
Yellow V < 1.2V/cell
Orange V > 1.2V/cell

Ought to setup conditional formatting to update with change of ASR in cell B26

The green region in Table 7 shows voltages where the predicted operating voltage is below the CO-C Nernst potential. This area is considered safe for a cell with a 1.60 Ω-cm^2 ASR where coking is not thermodynamically favorable. The chart predicts a trend that the higher the flow rate, the lower the maximum CO_2 utilization before coking occurs.

4.7 Experiment 1, CSA 003R

4.7.1 Stack description and baseline characterization

CSA 003R was a 10-cell SOXE stack. One midplate separated the cells into two, 5-cell groups that can be independently powered. During this experiment, the cells were operated as a single 10-cell group. The stack was held in a compression fixture and tested in test rig 1. CSA 003R is shown in Figure 28.

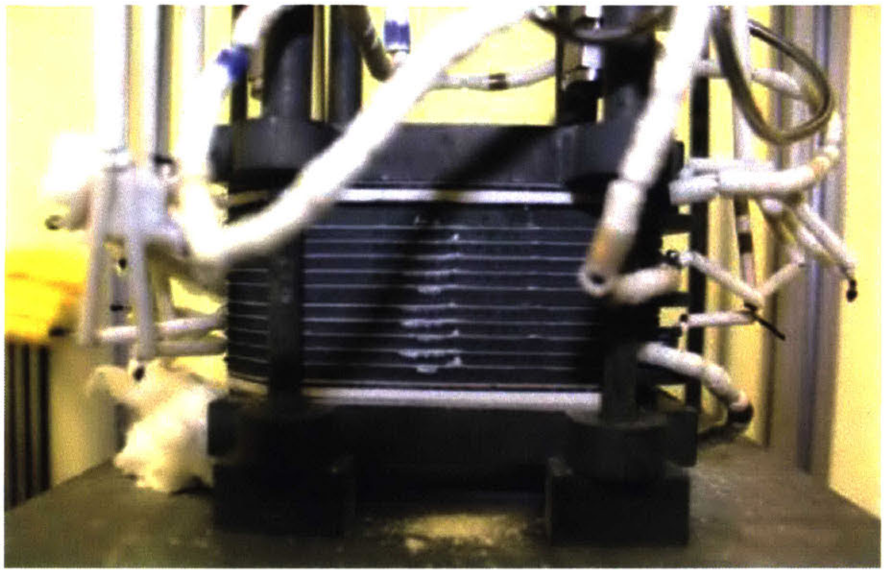

Figure 28 – CSA 003R in compression fixture

The stack underwent baseline characterization as described in Section 4.6.1. The stack had a baseline ASR_{app} of 1.42 Ω-cm^2. It reached a current of 3.992A at 1.050V equating to a baseline utilization of 33.4% and an O_2 production rate of 11.92 g/hr. The O_2 effluent was 99.29% pure, indicating a small cross-cell leak. A leak test conducted by Ceramatec Inc. at 1 psid indicated a leak rate of 0.43 g/hr of CO_2.

4.7.2 Experiment specific methods

SOXE stack CSA 003R was the first stack to undergo the operational window testing. The experiment followed the same general procedure described in Section 4.6.2. The current-controlled I-V sweeps began at a flow of 30 g/hr and temperature of 800°C. Each current step was incremented by a current step equivalent to 2% increase in utilization and held for 5 minutes to reach steady state. The current was stepped upward until evidence of coking was observed. For this experiment, a coking indication was defined as a steady upward drift in any cell voltage over the 5-minute period. Figure 29 is an I-V plot showing an example of this voltage climb characteristic of a coking event.

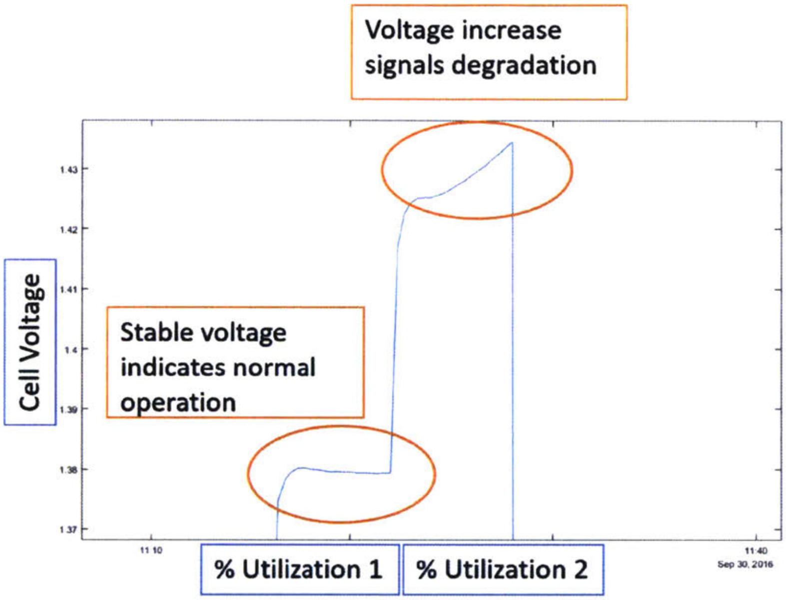

Figure 29 – A voltage spike is used as an indication of coking

After observing the characteristic voltage climb, the current was set back to the 30% utilization level and the flow was increased by 5 g/hr. This process continued up to a flow rate of 80 g/hr. After reaching 80 g/hr the flow conditions were adjusted to 100 g/hr for a baseline flow sweep. Next, I-V sweeps were performed at 100 g/hr at temperatures of 770°C, 790°C, 810°C, and 830°C.

4.7.3 Results

4.7.3.1 CSA 003R overview and initial observations

The maximum utilization boundary for CSA 005 is highest at low flow rates, with the boundary reaching 70% for a flow rate of 35 g/hr. The boundary slopes downward to 42% at a flow rate of 80 g/hr. The opposite trend is true for current and oxygen production. At 35 g/hr a maximum current of 2.91A and O_2 production of 7.48 g/hr were recorded. At the higher flow rate of 80 g/hr, CSA005 reached a current of 4.00A and an O_2 production of 11.934 g/hr. Figure 30 shows the data for the maximum utilization and current reached before voltage indicated degradation was observed.

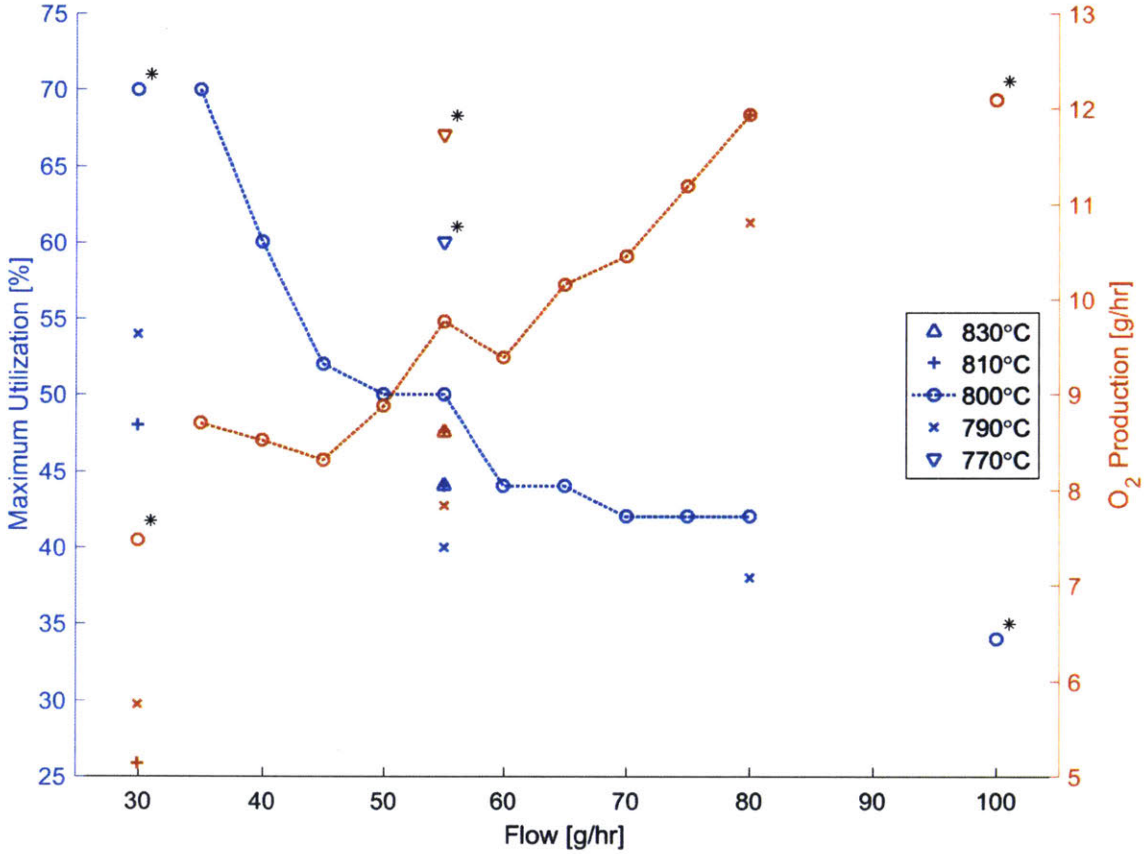

Figure 30 – CSA 003R maximum utilization % and O_2 production at different flow rates

The blue dashed line plots the maximum utilization boundary for the stack. The orange line shows the maximum O_2 production for the stack in g/hr. The 800°C, 30 g/hr data points are excluded from the trends because voltage drift was not detected in the 30 g/hr case even at the maximum test matrix utilization of 70%. The points excluded at 100 g/hr, indicated by the black star, were limited by the 4A maximum current allowed by the test matrix. No true utilization or current limit was determined for this stack at 100 g/hr.

The coking boundary experiment for CSA 003R was intentionally aggressive. The goal was to find the coking limit by observing voltage increases indicative of degradation. This methodology caused some degradation in the cell as the experiment progressed. Progressive degradation may be what caused the unexpected results where the maximum utilization of CSA 003R is higher at 55 g/hr and 770°C (60%) than at 55 g/hr and 830°C (44%). Theory predicts that a higher temperature should have a higher allowable utilization because overall resistance decreases with temperature. The test at 830°C was conducted later in the cycle. The results from CSA 005 using a method designed to avoid degradation show improved performance at higher temperatures.

Stacks often have a cell that has a higher resistance than other cells. In CSA 003R, the high resistance cell was Cell 8. For reference, the cells of the stack are numbered 1-10, with Cell 1 being the bottom cell of the stack and Cell 10 as the top cell near the CO_2 inlet. Cell 8 became the leading indicator of the onset of coking because it operated at the highest voltage and exhibited the first sustained rise in voltage for a fixed current at the limits of any flow and temperature combination. Figure 31 shows the results of CSA 003R Cell 8 plotted as current density vs. voltage.

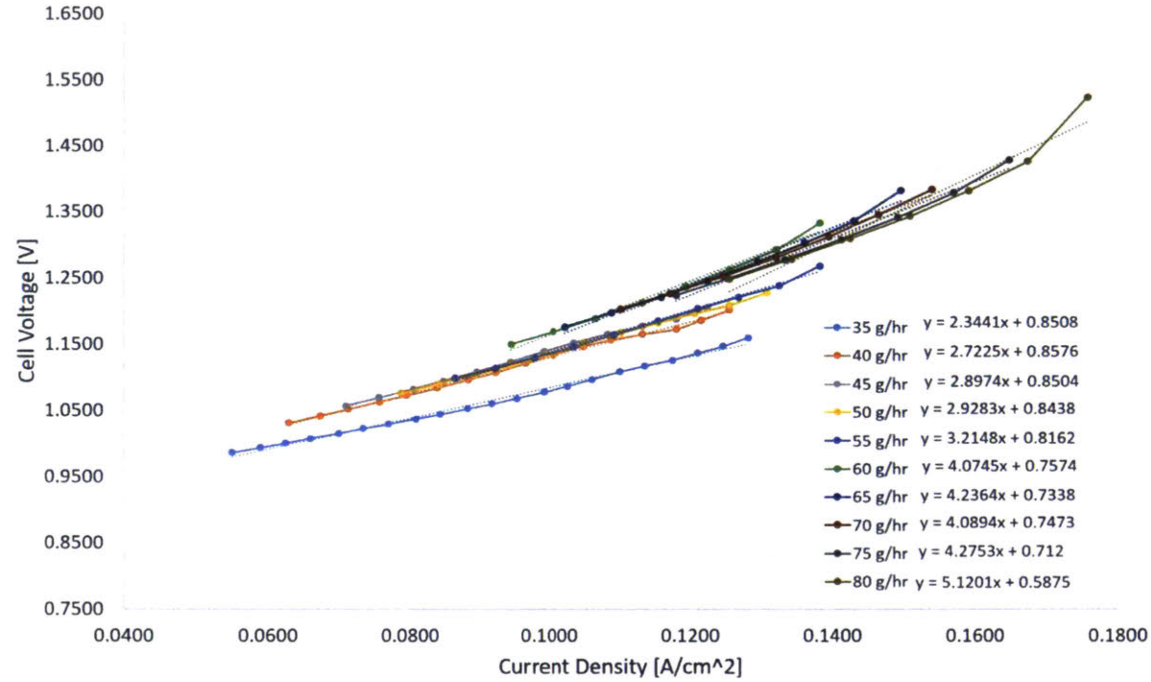

Figure 31 – i-V relation of Cell 8 performance mapping

The i-V curves were generally linear with an increasing slope towards the end of the curve. This slope increase is the result of upward voltage drift from degradation at the endpoint. The performance of the i-V curves shows an apparent clustering in three distinct groups.

At 40 g/hr and 55 g/hr the test utilization was increased 2% after the first sign of upward voltage drift. This was done because it appeared that the voltage drift was stabilizing at the lower level. The decision to push the cell harder appears to have caused noticeable damage to the cell that manifests itself in separation between the i-V groups. The linear fits in this example are an estimation of cell specific ASR. However, they include the non-linear region at the end of the cell that skew the slope and intercept. The best performing cells avoided voltage conditions favorable to coking and provide better linear fits.

The lowest resistance cell of stack CSA 003R was Cell 6. This cell exhibited linear behavior as shown in Figure 32 below.

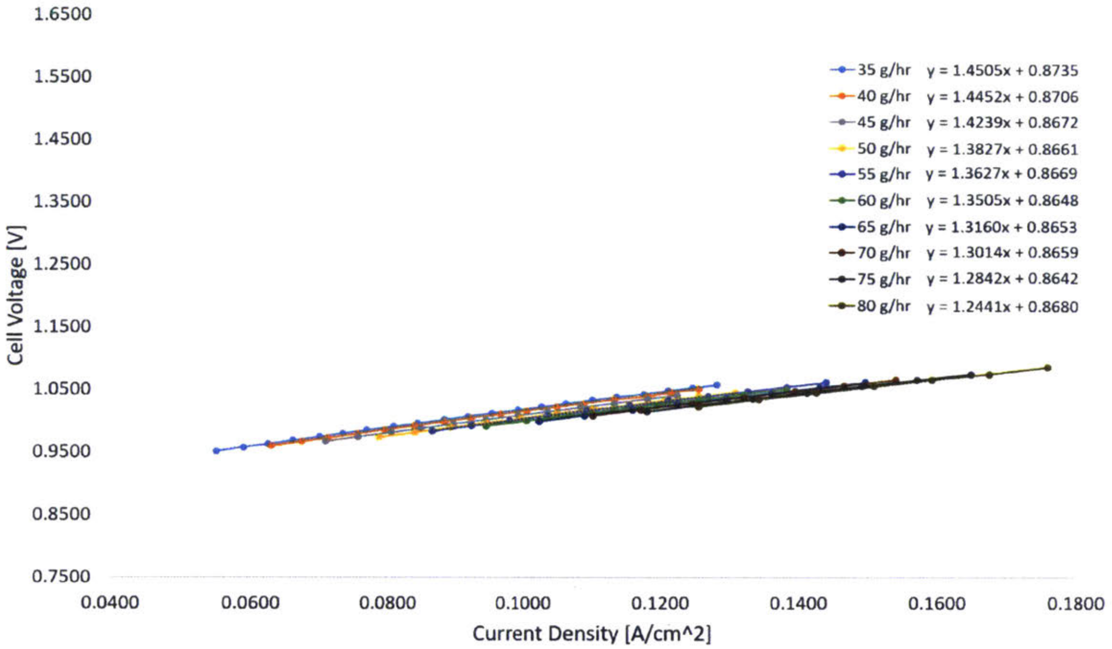

Figure 32 – CSA 003R Cell 6 i-V response

The Cell 6 data for Figure 32 is plotted on the same axis as Figure 31. The voltages stay well below the CO Nernst potential throughout operation. Unlike the data for Cell 8, which showed an increase in resistance at higher flow rates, the resistance of Cell 6 decreased at higher flow conditions. The linearity of the i-V curves means that the slope is a relatively good fit for ASR in this cell. The ASR begins at 1.45 Ω-cm^2 and decreases with increasing flows to 1.23 Ω-cm^2. Since the test matrix began at low flow and worked up to higher flow rates, the trend observed in Cell 8 is indicative of cumulative degradation.

4.7.3.2 Investigation of rates of coking

It is important to understand whether coking events can be detected by a climb in voltage so that a control response can be designed to avoid significant cell damage. The purpose of the MOXIE control system is to enable the plant to produce oxygen at the greatest rate and avoid hazards that could damage the instrument or the Mars 2020 rover. The standard operation mode for the stack will be a constant current mode. In this mode, total stack and 5-cell group voltages can be monitored. If carbon deposition results in a significant increase in voltage due to an increased ASR, this increase may be able to be detected by the control system. If implemented in the MOXIE control system, corrective action may then be taken by lowering the commanded stack current or by switching to voltage control mode and commanding a lower voltage. Figure 33 below shows the voltage increases over time for CSA 003R Cell 8 during operation at the degradation boundary.

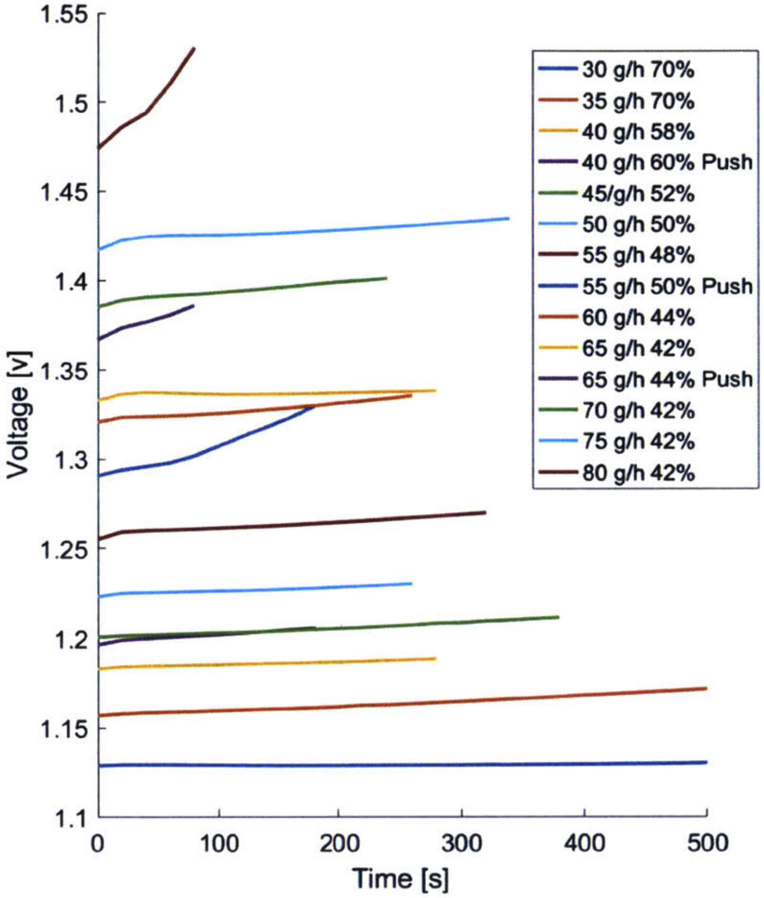

Figure 33 – Cell 8 voltage increases observed during degradation boundary operation

At 40 g/hr, 55 g/hr, and 60 g/hr the utilization was incremented an additional 2% after initial degradation was suspected, to confirm that the limit was reached. This is indicated on the plot legend by the tag “push”, signifying when the utilization was pushed past the initial voltage drift. The length held at each condition varies depending on operator judgement. As a cell nears a degradation limit, there is a trend for the voltages to climb slightly at first and then settle to a stable trend. The stack was removed from the degradation condition sooner when a rapid voltage climb was detected. The condition was held longer when a slow voltage climb was observed to see if the cell would stabilize.

The observed voltage rate increase was 0.0125 to 0.750 mV/s as seen in Table 8 below.

Table 8 – Voltage degradation rates for Cell 8

Flow Rate [g/hr]	% U	Voltage	Rate (V/s)*10^{-5}	95% CI (+/-)	R square
30	70%		1.253	0.221	0.9970
35	70%	1.1605	4.426	0.192	0.9994
40	58%	1.1866	2.212	0.190	0.9978
40P	60%	1.2025	4.550	0.143	0.9997
45	52%	1.2068	3.595	0.446	0.9955
50	50%	1.2286	3.066	0.174	0.9990
55	48%	1.2689	4.609	0.173	0.9996
55P	50%	1.3317	27.770	2.330	0.9979
60	44%	1.3334	6.754	0.308	0.9994
65	42%	1.3336	1.432	0.172	0.9958
65P	44%	1.3833	20.790	7.130	0.9812
70	42%	1.3844	5.508	0.522	0.9965
75	42%	1.4299	5.004	0.329	0.9987
80	42%	1.5253	74.900	41.685	0.9676

When the utilization was pushed an additional 2% above first onset, the voltage climb increased by 2.05, 6.02, and 14.5 times the initial rate observed at 40, 55, and 65 g/hr, respectively. It appears that early detection is the key. The process accelerates rapidly with just a small increase in utilization above the limit. Excluding the points that pushed past the degradation threshold and the last point, the average rate of voltage increase at first observation was 0.0379 mV/s. It should be noted that as shown in Section 4.7.3.1, permanent degradation occurred throughout the experiment, so some of the later rates observed here occurred in an already damaged cell.

4.7.3.3 Potential for coking recovery

It is important to understand coke recovery when designing a fault tolerant control system for MOXIE. MOXIE will typically operate far away from the coking threshold but degradation is still possible due to uncertainty in individual cell voltages, startup and shutdown transients, unforeseen environmental variation, and component failure. In the event that a coking event is detected, it may be possible to place the SOXE into a recovery state that would enable some of the carbon to oxidize and form CO, removing some of the carbon fouling from the SOXE cathode as shown in Equation (4.8):

$$C(S) + CO_2 \rightarrow 2CO \tag{4.8}$$

During the operational mapping of CSA 003R, the stack utilization was increased until an increase in voltage indicative of a coking event was observed. The stack was then placed in an OCV "parking" state with no current flow, and GC (Gas Chromatograph) samples were taken during the recovery period. During this period, the flow rate was constant and the feed gas still consisted of 2% CO to avoid the risk of oxidation. The GC data after returning to OCV at flow rates of 40 g/hr, 45 g/hr, and 50 g/hr is shown in Table 9.

Table 9 – GC Data taken during recovery at open circuit voltage

	40 g/hr		45 g/hr		50 g/hr	
Date	28-Sep	28-Sep	28-Sep	28-Sep	28-Sep	28-Sep
Time	10:41	10:47	15:18	15:23	16:49	16:53
CO_2 %	94.90	97.90	95.40	96.56	94.10	96.64
CO %	**5.05**	**2.07**	**4.58**	**3.40**	**5.84**	**3.32**
N_2 %	0.04	0.03	0.03	0.03	0.04	0.03
O_2 %	0.01	0.00	0.00	0.01	0.02	0.01
Cell 8 V	0.8324V	0.7083V	0.8286V	0.7637V	0.8509V	0.7570V

The first data point taken after returning to OCV in each case, shows elevated levels of CO when compared to the sample taken 4 to 6 minutes later. Over the recovery period, the open circuit voltage of Cell 8 also dropped to a level comparable with the other cells in the stack. It is hypothesized that the elevated CO levels are the result of the oxidation of small amounts of deposited carbon in the cell cathode under these flow conditions.

It was considered that the elevated levels of CO were from residual gas in the system from electrolysis. However, the OCVs of the other cells were lower, indicating that the heightened OCV levels of Cell 8 were due to increased CO levels in the degraded cell and not the healthy cells that showed no evidence of carbon deposition.

Returning to OCV upon detection of an upward voltage drift is a potential mitigation strategy in a laboratory but is not ideal for MOXIE. The reason is that in the laboratory, the cathode oxidation risk is mitigated by supplying a stream of CO to the feed gas. MOXIE relies on recirculation to feed CO effluent back into the inlet stream of the SOXE. The CO source of MOXIE relies on active electrolysis. In order to understand a potential mitigation strategy for MOXIE, the cell was operated at a low utilization of 30% and flow of 30 g/hr after operation at a degradation limit. Under such a condition, the MOXIE recirculation stream would still be providing a supply of CO to the cell. The cell voltage response over time is shown in Figure 34.

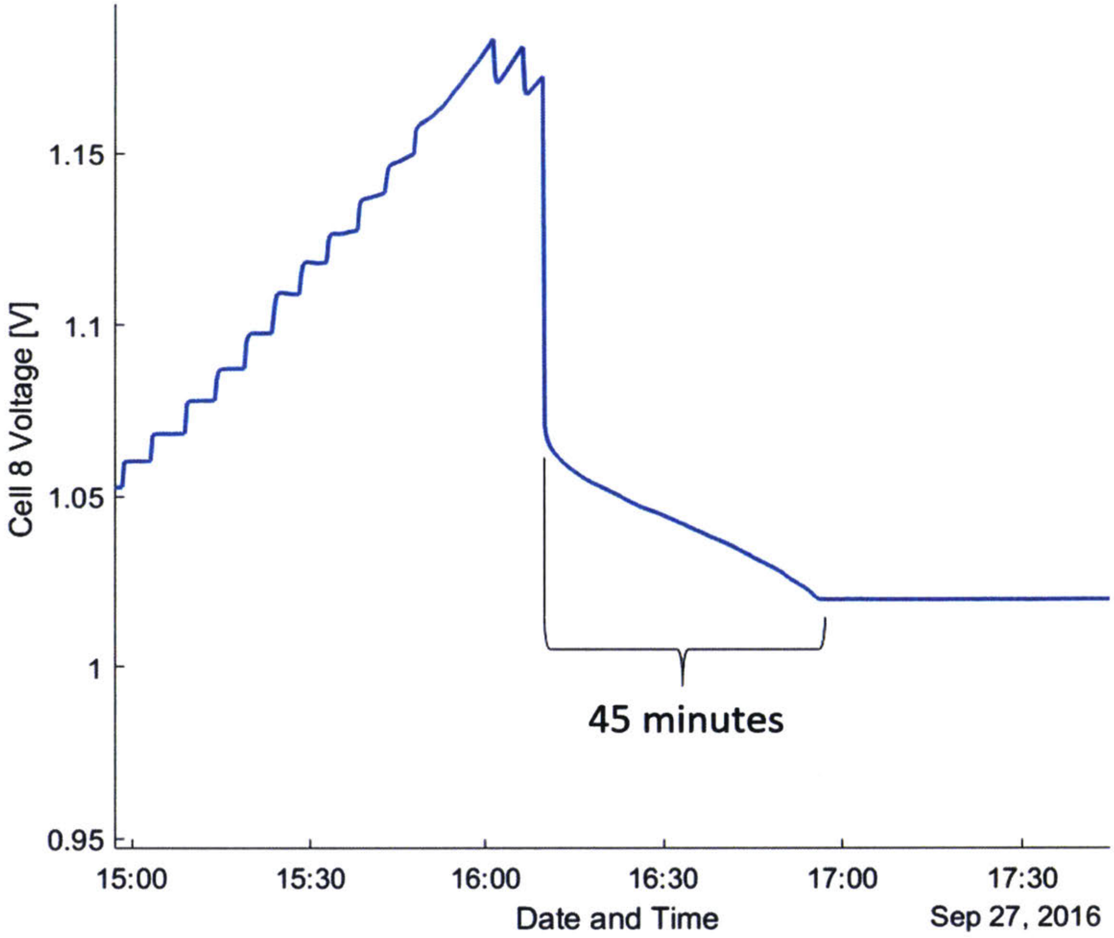

Figure 34 – Cell 8 voltage recovery over time at 30 g/hr, 30% utilization

The voltage recovery period lasted nearly 45 minutes before stabilizing. During this time, heightened CO levels were recorded in the stack effluent. Table 10 shows the GC data taken during recovery and two samples after the recovery period.

Table 10 – GC Data During and after recovery

	30 g/hr		
Date	**27-Sep**	**27-Sep**	**28-Sep**
Time	**16:20**	**18:02**	**8:46**
CO2 %	**65.19**	**66.81**	**66.65**
CO %	**34.74**	**33.14**	**33.28**
N2 %	**0.05**	**0.03**	**0.05**
O2 %	**0.02**	**0.01**	**0.02**
Voltage	**1.052 V**	**1.020 V**	**1.022V**

The results of this experiment indicate that some recovery occurred without returning completely to OCV, confirming its potential as a degradation reduction strategy for MOXIE. Over the recovery period, the voltage and ASR of the damaged cell decreased and elevated CO levels were observed. The implications for the control system are that if degradation is detected, the current control loop should be reduced to a low current such as 1 A while maintaining constant flow until the end of the trial. The current MOXIE baseline is to default to shut down. Additional experimentation is needed to know if coke recovery is possible after a MOXIE shutdown. A concern is that a direct shutdown will alter the carbon bonds or allotrope to a form that is less readily oxidized. The shutdown cycles of the SOXE have already shown to be hard on the cell resulting in some degradation after each cycle. Better cell condition before a shutdown may help preserve its function.

4.7.3.4 Observations relating to ASR and activation potential

The ASR was tracked during the operational mapping of CSA 003R using Equation (3.22) for approximate ASR and assumed no observable activation potential. The equation is re-written here.

$$ASR_{app} = \frac{(V_{op} - V_{ocv})/N_{cells}}{I/A} \tag{4.9}$$

The V_{OCV} is assumed to be 0.8 V per cell and 8 V per stack. The stack voltage is divided by the number of cells and the current reading by the cell area to get the ASR_{app} from the full stack numbers. Figure 35 describes the results.

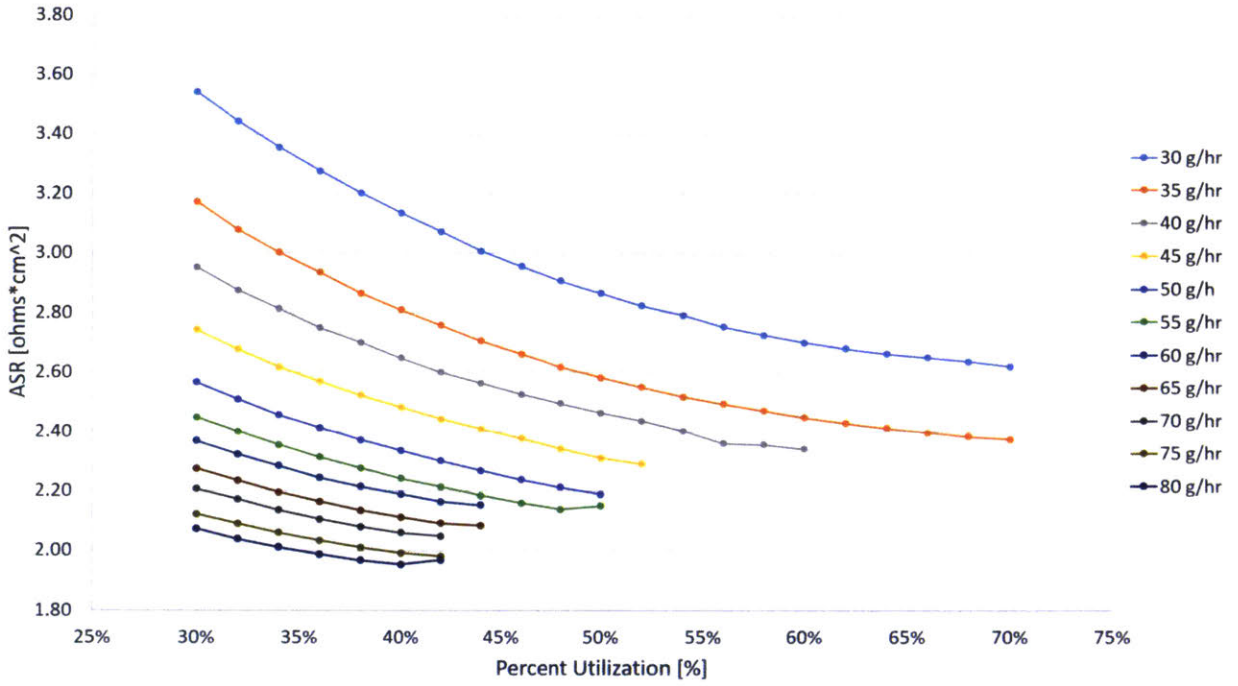

Figure 35 – CSA 003R ASR_{app} calculated from OCV of 0.8 vs. flow

The results show ASR values that seem to follow a smooth and predictable trend. The ASR_{app} decreases at higher utilizations and currents with only a slight increase observed near the degradation threshold. The expected behavior was that the ASR would be constant up the i-V curve with a slight increase when nearing the coking threshold. As stated in hypothesis 2, this ASR equation assumes that the i-V curve is linear and the intercept is at the V_{ocv} of 0.8V. To test this assumption, a linear fit was performed for the i-V curves from the undamaged Cell 6 for each flow condition (see Table 11). The average intercept observed was 0.867 V with a standard deviation of 0.0029 V.

Table 11 – Cell 6 slope and intercept data for i-V fits including approximated OCV

Flow Rate [g/hr]	Slope (ASR)	Intercept	OCV
35	1.451	0.874	0.8
40	1.445	0.871	0.8
45	1.424	0.867	0.8
50	1.383	0.866	0.8
55	1.363	0.867	0.8
60	1.351	0.865	0.8
65	1.316	0.865	0.8
70	1.301	0.866	0.8
75	1.284	0.864	0.8
80	1.244	0.868	0.8

The data in Table 11 indicates that the assumptions for the ASR_{app} equation are incorrect, and the actual intercept is slightly above V_{OCV} by 0.067V. A potential loss appears to be present in addition to the loss due to the OCV potential. In experiment 2, the characterization of CSA 004 was expanded to characterize this possible activation potential and its modeling implications. Some of this additional potential is attributed to the Nernst potential at observed conversion rate. Chapter 5 applies a CO_2-CO conversion correction to separate the contributions of the Nernst and activation potentials

The observation of an additional potential explains the decreasing behavior when the approximate ASR was calculated from point samples in Figure 35 above. Figure 36 shows how the approximate ASR equation, represented by the green dashed line, decreases in slope when it is derived from a point at the start and end of the i-V curve. This behavior is due to the discrepancy in the assumed and true intercept.

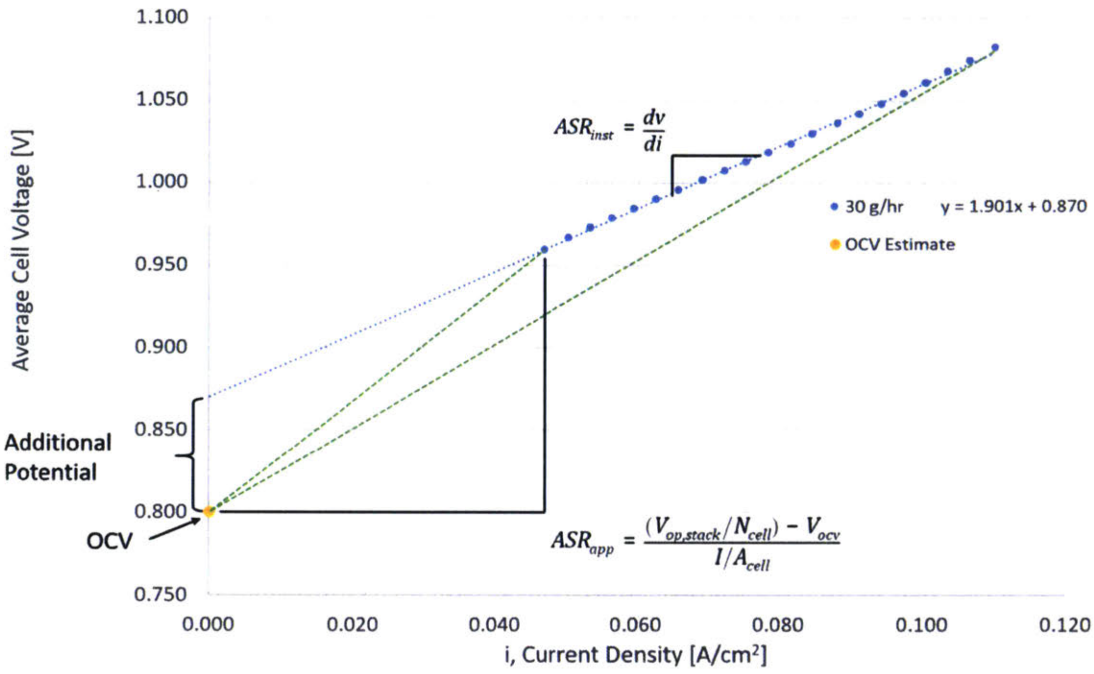

Figure 36 – The approximate ASR (green lines) calculated using different values of an i-V sweep. The ASR_{app} value depends on where the sample is taken. The slope of the blue line represents a more accurate ASR term.

Figure 36 illustrates the error in the approximate ASR equation. The activation potential estimate shown here and in Table 11 assumes a V_{OCV} of 0.8 when the actual value is slightly different. A portion of the slope of the line can also be attributed to changes in the CO_2-CO Nernst potential as the utilization changes through the current voltage sweep. The advanced electrochemical modeling in chapter 5 determines the activation potential is about 22 mV after correcting for CO_2 conversion.

4.8 Experiment 2, CSA 004

4.8.1 Stack description and baseline characterization

CSA 004 was a 10-cell stack. One midplate separated the cells into two, 5-cell groups that could be independently powered. During this experiment, the cells were operated as a single 10-cell group. The stack underwent baseline characterization as described in Section 4.6.1. CSA 004 had a baseline ASR_{app} of 1.51 Ω-cm^2. It reached a current of 3.988A at 1.064V equating to a baseline utilization of 33.4% and an O_2 production rate of 11.90 g/hr. The O_2 effluent was 99.60%, pure indicating a slight cross-cell leak. A leak test conducted by Ceramatec indicated a 0.31 g/hr of CO_2 cross-cell leak at 1 psid.

4.8.2 Experiment specific methods

Standard operational mapping was performed with CSA 004 using the methods and operational window test matrix described in the general procedures of Section 4.6. Additional i-V sweeps were conducted at 770°C, 790°C, 810°C, and 830°C. The operational limit was determined by the first noticeable climb in voltage from the worst performing cell of the SOXE. In addition to observing a voltage drift, the instantaneous ASR, or the center difference derivative of the i-V curve, was used to identify an ASR spike that may indicate coking.

The testing of CSA 004 included an additional procedure to investigate the discovery of the stack activation potential during the characterization of CSA 003R. The procedure included a low current density sweep of the cell to investigate the non-linear region of the i-V curve. The current set points were based upon utilization increments at the 30 g/hr flow condition. Table 12 below shows the test matrix for the activation potential characterization.

Table 12 – Current set point test matrix for characterizing the activation potential of CSA 004

		Flow Condition [g/hr]			
		30	55	80	100
Current Set Point	Current density	% Utilization	% Utilization	% Utilization	% Utilization
0	0	0.00%	0.00%	0.00%	0.00%
0.0179	0.0008	0.50%	0.27%	0.19%	0.15%
0.0358	0.0016	1.00%	0.55%	0.38%	0.30%

0.0716	0.0032	2.00%	1.09%	0.75%	0.60%
0.1433	0.0063	4.00%	2.18%	1.50%	1.20%
0.2149	0.0095	6.00%	3.27%	2.25%	1.80%
0.2865	0.0126	8.00%	4.36%	3.00%	2.40%
0.3582	0.0158	10.00%	5.45%	3.75%	3.00%
0.4298	0.0189	12.00%	6.55%	4.50%	3.60%
0.5014	0.0221	14.00%	7.64%	5.25%	4.20%
0.5730	0.0252	16.00%	8.73%	6.00%	4.80%
0.6447	0.0284	18.00%	9.82%	6.75%	5.40%
0.7163	0.0316	20.00%	10.91%	7.50%	6.00%
0.7879	0.0347	22.00%	12.00%	8.25%	6.60%
0.8596	0.0379	24.00%	13.09%	9.00%	7.20%
0.9312	0.0410	26.00%	14.18%	9.75%	7.80%
1.0028	0.0442	28.00%	15.27%	10.50%	8.40%

4.8.3 Results

Figure 37 below shows the results for the boundary mapping of CSA 004.

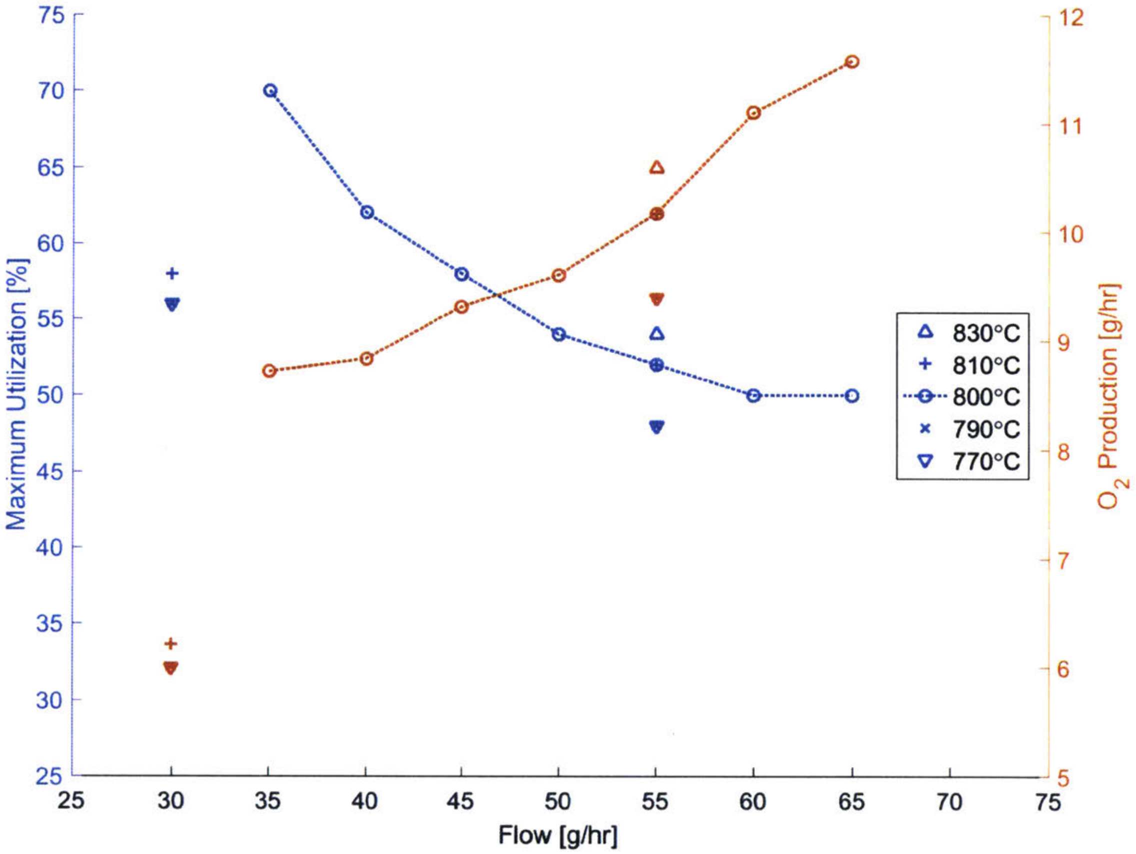

Figure 37 - CSA 004 maximum utilization % and O_2 production at different flow rates

A utilization limit was not found within the test matrix for the 30 g/hr flow rate, but at 35 g/hr the limit was 70%. At the high end of the flow range, a limit of 50% was observed for 65 g/hr flow. The complete data over a range of temperatures was characterized at 55 g/hr. The standard limit was 52% at 800°C, increasing to 54% at 830°C. The utilization limit decreased to 48% at both the 790°C and 770°C points. At 810°C and 30 g/hr some evidence of accumulated degradation was observed, with much lower limits appearing at 810°C for both maximum utilization and oxygen production. The plot data is displayed for reference in Table 20 of Appendix B. The data at 800°C is roughly described by the fits in Equations (4.10) and (4.11), valid over mass flow values from 35 – 65 g/hr.

$$O_2\ Production\ Limit = 0.1000\dot{m} + 4.906, \quad R^2 = 0.9565 \tag{4.10}$$

$$Utilization\ Limit = -0.02571\dot{m}^2 - 3.214\dot{m} + 150, \quad R^2 = 0.9947 \tag{4.11}$$

The most significant contribution of this experiment was the investigation of the additional potential, discovered during the analysis of CSA 003R. The goal was to investigate if this was attributed to an activation potential. Low current sweeps were conducted at 55, 80, and 100 g/hr at 800°C and additional 80 g/hr tests at 770°C and 830°C. A second 80 g/hr, 800°C test labeled V2 was conducted to test repeatability after a momentary loss of power. A final test at 770°C with 1.7% H_2 gas was conducted to explore if the addition of hydrogen would linearize an activation curve. The results are shown in Figure 38.

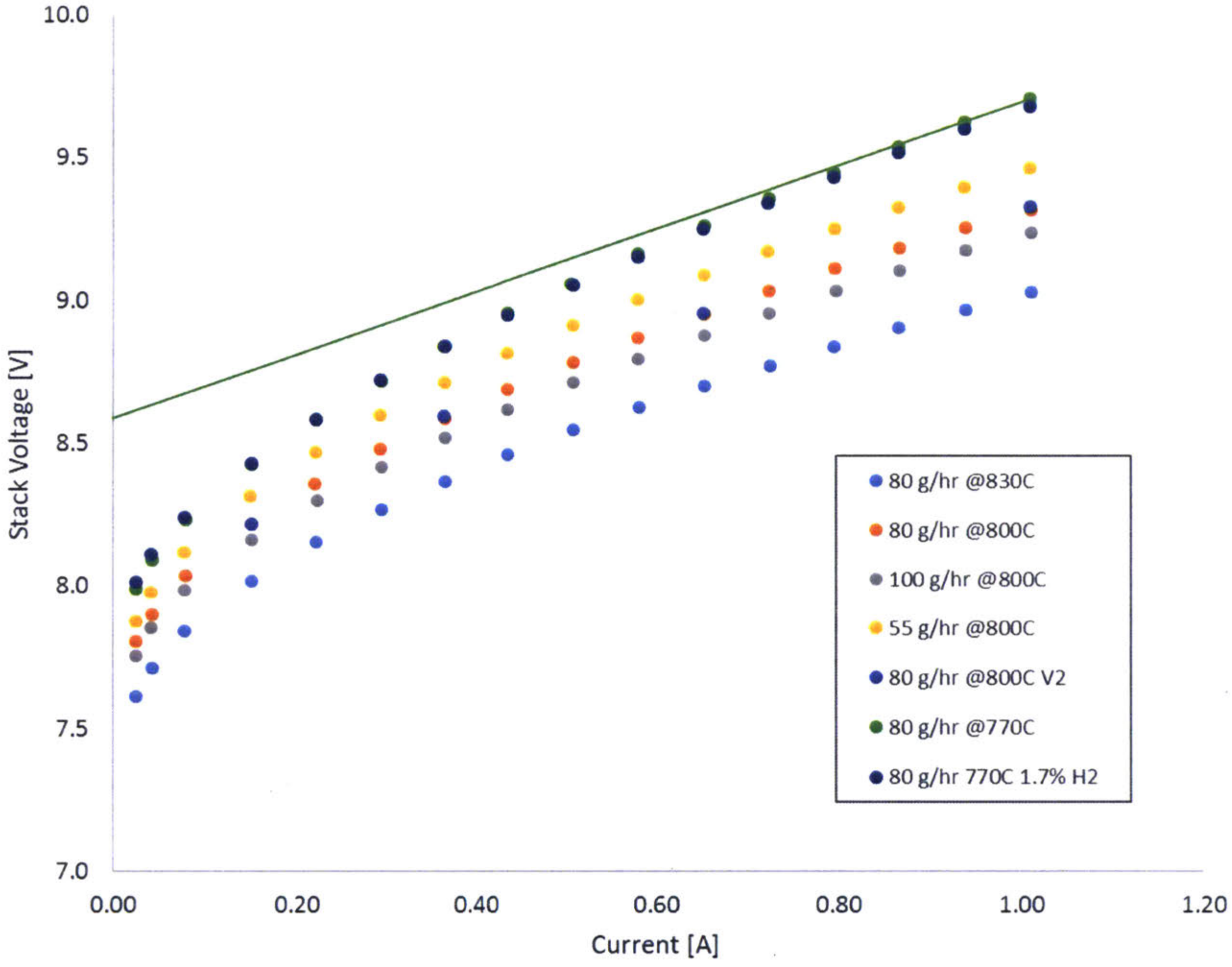

Figure 38 – Sloping curves demonstrating the activation potential

The green line represents a linear i-V trend with a constant ASR and intercept at 8.6 V (0.86 V/cell) similar to what was characterized in the higher current regions of CSA 005. The results clearly show non-linear i-V behavior characteristic of the activation potential region. The instantaneous ASR is defined as the derivative of voltage with respect to current density. At very low current densities, the ASR is much higher than during the linear range. Here, activation and Nernst potentials dominate ohmic losses. The ASR slowly decreases as it enters the linear region at around 1 A (0.044 A/cm^2 current density). Higher mass flow rates and higher temperatures decrease the additional losses while lower flows and lower temperatures increase it. The test points were shown to be repeatable with the second test at 80 g/hr and 800°C. When 1.7% H_2 gas was added, the curve showed only very minor improvements in linearlization. Higher amounts of H_2 gas would be required to significantly reduce the activation potential. Temperature changes of 30°C have over twice the impact than flow adjustments of 20-25 g/hr. This phenomena shows characteristics that could be modeled by the Tafel Fit shown in Equation (4.12):

$$\eta = \frac{RT}{\alpha F} \ln j_0 + \frac{RT}{\alpha F} \ln j \tag{4.12}$$

Where η is the activation potential, α is the charge transfer coefficient and j_o is the exchange current density. MOXIE will not operate at a CO_2 utilization of less than 11% which is in the linear region of the i-V curve. This minimum operating utilization is required to maintain a cathode inlet CO percentage of greater than 0.55% to avoid a thermodynamic risk of cathode inlet oxidation. In this operating region, the Tafel fit is no longer the best representation of the i-V curve and the activation potential loss can be modeled as constant for a fixed temperature. In Chapter 5, conversion correction for the utilization shows that the activation potential is a partial contributor to the additional potential, while some is attributed to the average CO_2-CO Nernst potential. The activation potential component it is approximately constant at 21.6 mV with a slight temperature dependence.

4.9 Experiment 3, CSA 005

4.9.1 Stack description and baseline characterization

CSA 005 was a 10-cell stack. One midplate separated the cells into two, 5-cell groups that could be independently powered. During this experiment, the cells were operated as a single 10-cell group. The cell was held in a compression fixture in the same manner of CSA 003R shown in Figure 28 above. The stack underwent baseline characterization as described in Section 4.6.1. CSA 005 had a baseline ASR_{app} of 1.40 Ω-cm^2. It reached a current of 4.006A at 1.046V, equating to a baseline utilization of 33.5% and an O_2 production rate of 11.96 g/hr. The O_2 effluent was 99.58% pure, indicating a slight cross-cell leak.

4.9.2 Experiment specific methods

CSA 005 closely followed the general procedures outlined in Section 4.6. The distinguishing method for this experiment was that the operational limit was determined by observing the voltage of any cell surpassing the CO-C Nernst potential. The goal was to map the greatest operational range without incurring any degradation from carbon deposition. The potential values used are listed in the right hand column of Table 6 and Table 7 in Section 4.6.2 above.

The raw data for CSA005 was averaged at each condition to produce the operational data map. Values at the beginning flow rate of each i-V sweep included points from adjusting the flow rate conditions for the new run. The stabilization values and other operational exceptions are flagged as outliers as shown in Figure 39.

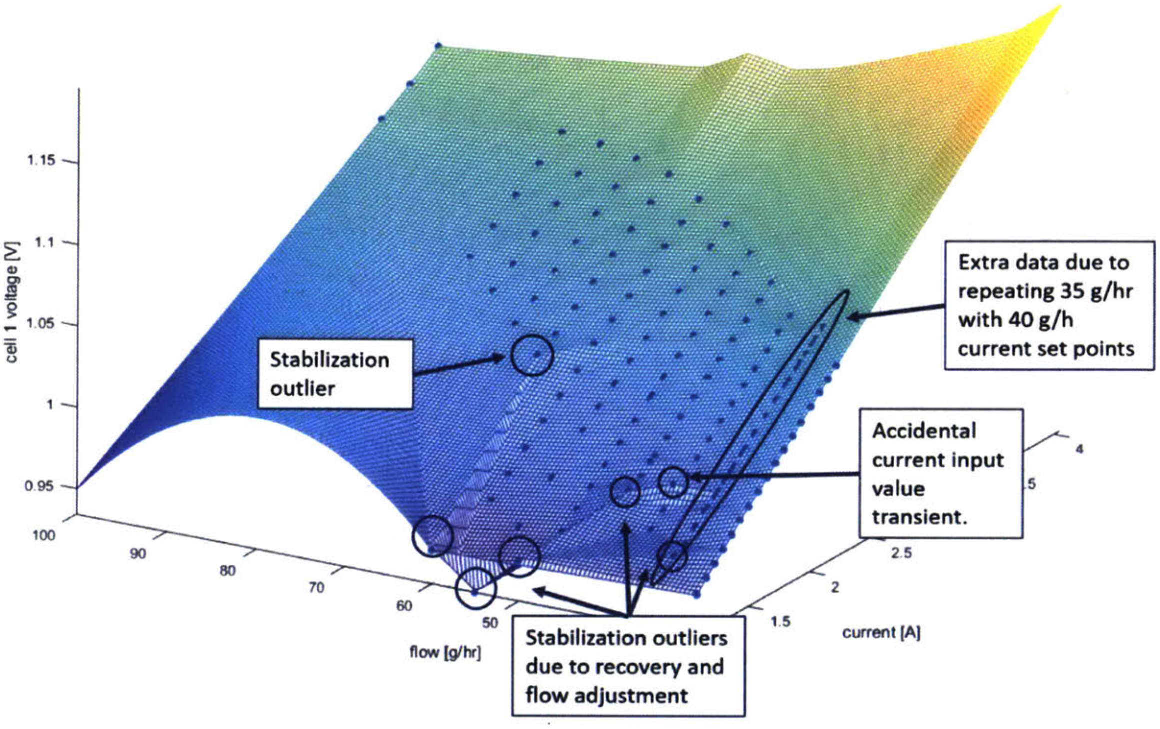

Extra data due to repeating 35 g/hr with 40 g/h current set points

Stabilization outlier

Accidental current input value transient.

Stabilization outliers due to recovery and flow adjustment

Figure 39 – CSA 005 800°C voltage, flow, and current data map with outliers indicated.

4.9.3 Results

CSA 005 performed the most predictably of the three stacks throughout its operational range because of the coke avoidance procedure. Due to the more conservative testing approach, some of the limits appear at lower values than for CSA 003R and CSA 004. The data shown in Figure 40 below is more representative of realistic boundaries for the SOXE operation.

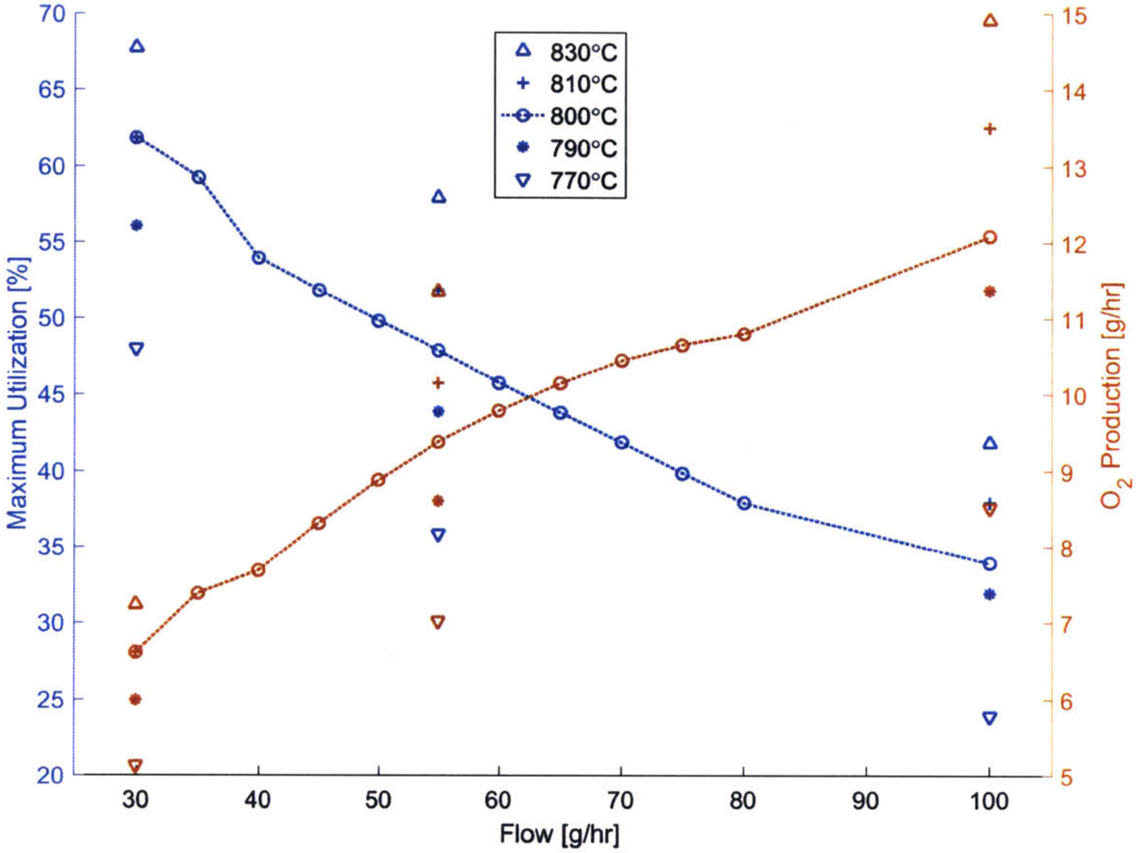

Figure 40 – CSA 005 safe utilization and maximum O_2 production boundaries

Here temperature is a major factor in the safe operational limits. The maximum utilization and maximum production boundaries at 800°C are described by Equations (4.13) and (4.14):

$$O_2\ Production\ Limit = 0.07754\dot{m} + 4.791, \quad R^2 = 0.9654 \tag{4.13}$$

$$Utilization\ Limit = -0.4061\dot{m} + 71.16, \quad R^2 = 0.9587 \tag{4.14}$$

These equations are for descriptive purposes. Margin will need to be added for MOXIE operation. The lower limits at possible cell temperatures such as 790°C must also be factored in to account for uncertainty on MOXIE thermal control. Higher temperature operation will enable higher operational limits for CO_2 utilization and O_2 production.

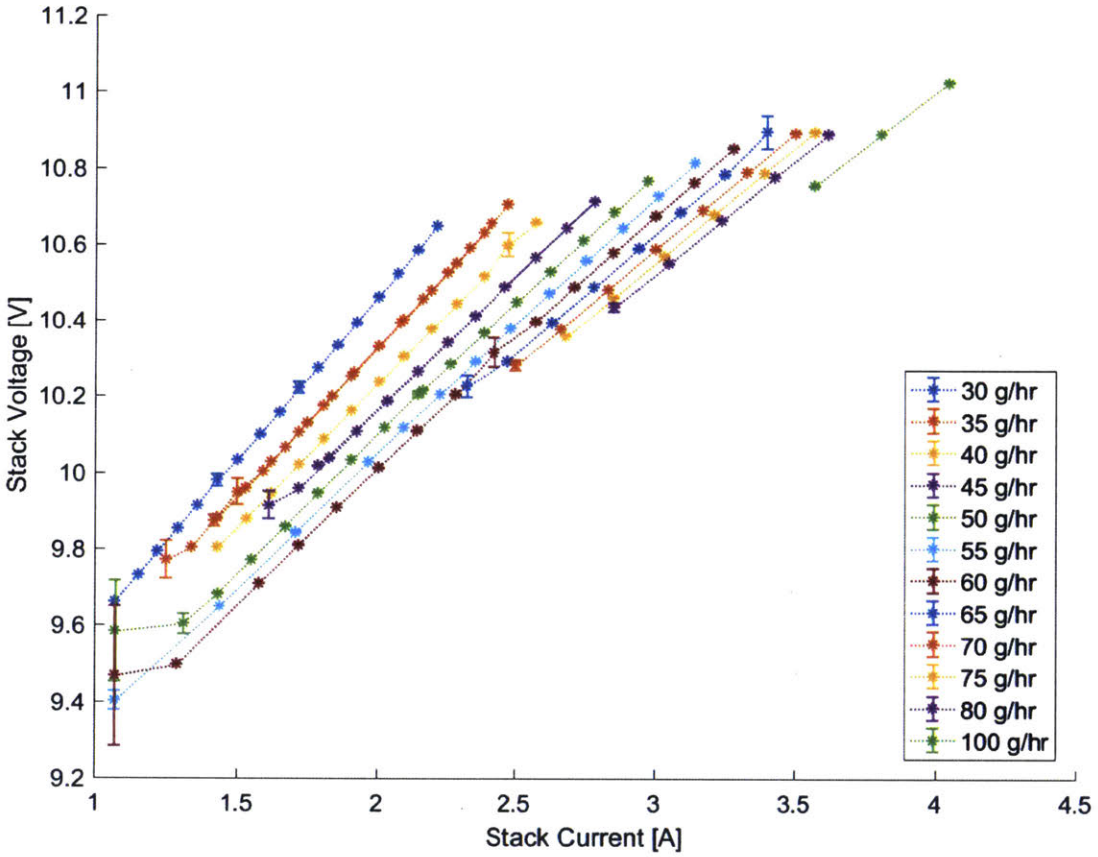

Figure 41 – CSA 005 I-V voltage distribution at 800°C

Figure 41 above shows the linear nature of the I-V curves for CSA 005. There was no departure from linearity at the maximum current as observed in stacks that were subjected to intentional coking. The large standard deviation bars for samples at 1.07 A were due to voltage shifts during flow composition adjustment.

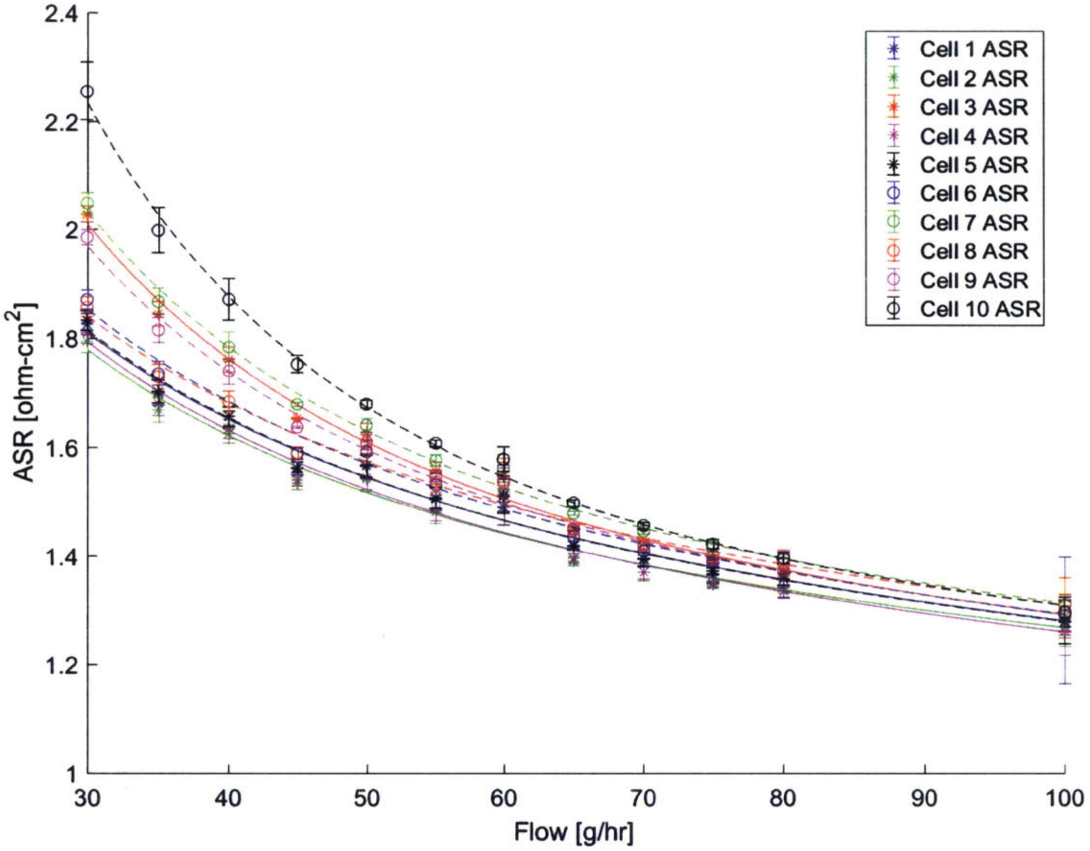

Figure 42 – ASR_{lin} flow dependence for CSA 005 with 95% confidence intervals

The ASR_{lin} values were calculated by first order polynomial fits of the linear region of the current voltage curve. The results for each cell are shown above in Figure 42. At a flow rate of 100 g/hr, there is no significant difference in performance between cells. As the flow rate begins to decrease, the ASR values diverge and the differences become significant. These results were unexpected as Hypothesis I assumed that the cell-to-cell variation was due to variability in cathode composition. These results support an alternative hypothesis that the variation is due to flow conditions. At lower flow conditions, it is possible that the flow into the cells is less equally distributed, resulting in greater ASR variation.

This has important implications for baseline characterization of the flight stack. In order to select a Mars flight stack with the least cell-to-cell variation, characterization should be done at 30 g/hr instead of 100 g/hr.

Figure 43 below shows the intercepts of the linear regions of the ASR.

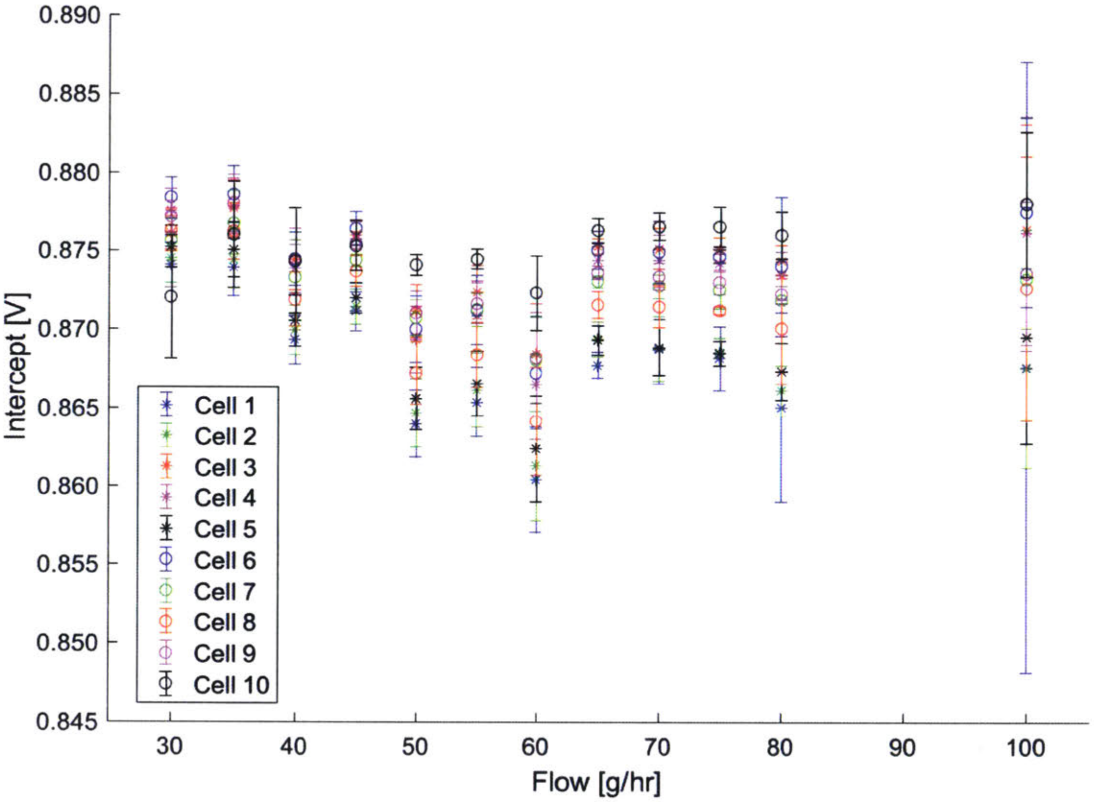

Figure 43 – Intercept values with 95% confidence bounds for all cells of CSA 005

Unlike the ASR data, the intercept data is relatively consistent throughout all flow conditions. There appears to be a small decrease in intercepts between 50 g/hr and 60 g/hr. The uncertainty in the intercepts is greatest at 100 g/hr in part because of the limited number of data steps taken at that flow rate. Of particular interest is that even though the variation in ASR is greatest at 30 g/hr, the intercepts are still tightly grouped. This suggests that the divergence in performance at low flows is unlikely to be related to factors that affect activation potential.

The V_{ocv} assumed for Hypothesis II was 0.8V. A significant difference is observed between this assumed value and these intercepts, further affirming that the original hypothesis was incorrect. A proper model for the i-V curve must include both the activation potential and OCV term.

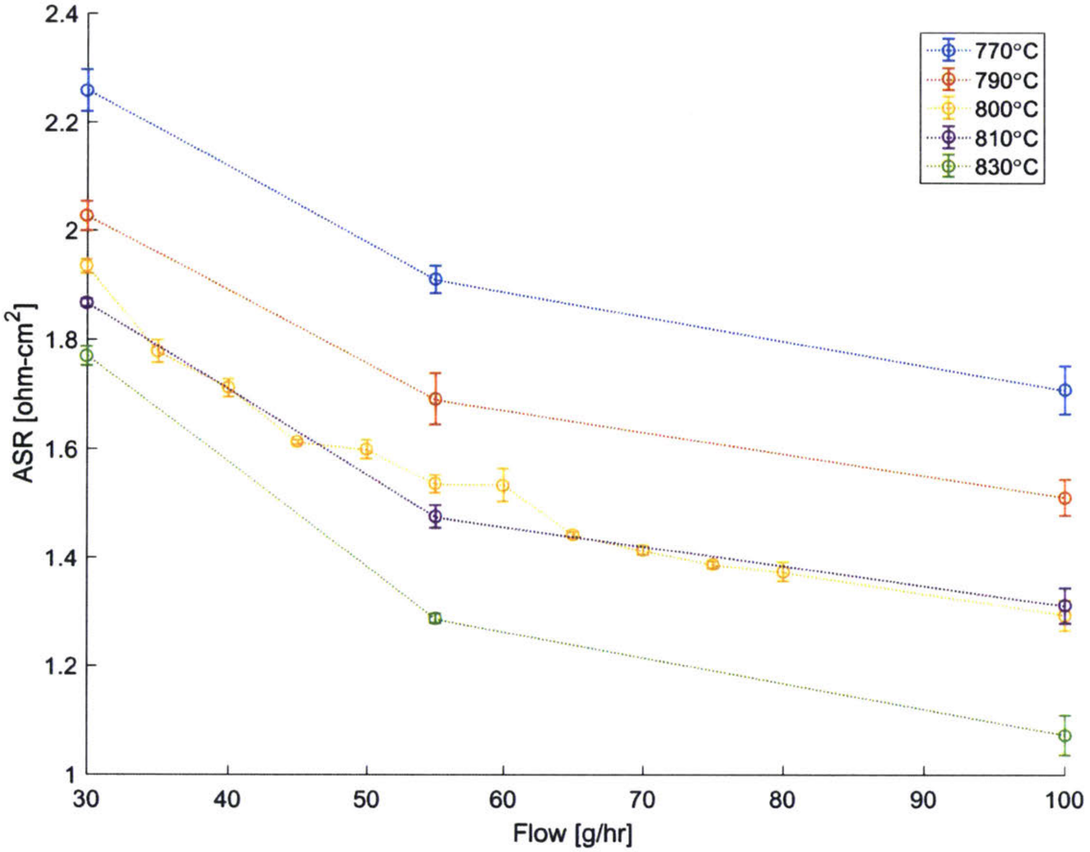

Figure 44 – CSA 005 ASR$_{lin}$ values with 95% confidence intervals at varying flow conditions and temperatures

The temperature dependence on ASR$_{lin}$ is shown in Figure 44 above. ASR is consistently lower at higher temperatures, with the exception of two ASR values observed to be slightly higher at 810°C than at 800°C. The separation between temperature samples is relatively consistent throughout the flow range. The overall increase in ASR with flow is consistent with observations in Figure 42.

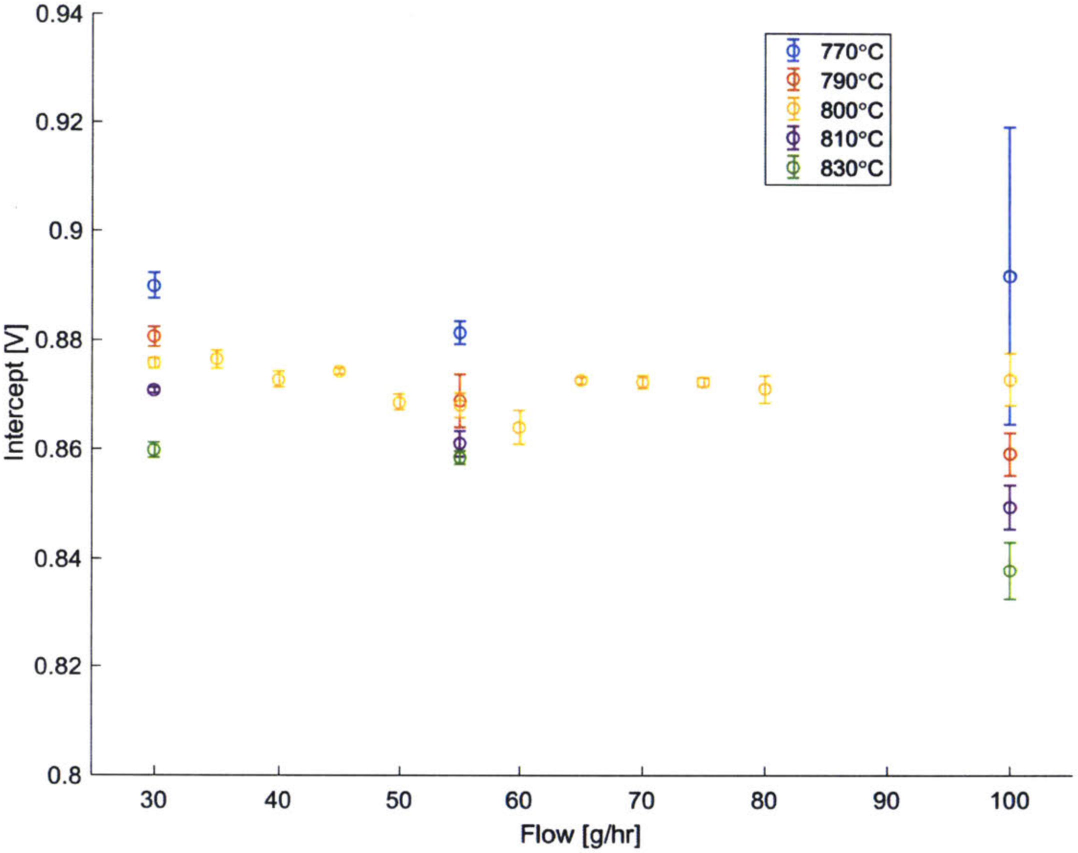

Figure 45 – CSA 005 i-V intercepts at varying flow conditions and voltages

The temperature dependent intercept values are shown in Figure 45 above. There is a slight reduction in potential observed for increased temperature. This is consistent with theory as the required activation potential decreases as temperature increases.

4.10 Hypotheses evaluation

4.10.1 Hypothesis I (cell to cell ASR variation)

Hypothesis I stated that the cell-to-cell variation observed in SOXE stacks is caused by variability in material processing, possibly due to local variations in the cathode material. It assumed that a modeling approach that characterizes current-voltage trends of a test stack and shifts these values with respect to a characterized ASR for each cell could be used to describe accurately the full envelope performance of a flight stack.

Such an approach assumed that cell-to-cell variation would look similar over the operational flow ranges as the temperature dependent shifts shown in Figure 44 above. Cell variation behavior as predicted would enable flight stack models to be accurately generated from a limited characterization sweep at 100 g/hr. However, during experimental characterization of CSA 005 it was observed that at 100 g/hr, there is no statistically significant difference observed between the ASR of the best and worst cells. Figure 46 shows ASR values and 95% confidence intervals of the best and worst performing cells of CSA 005.

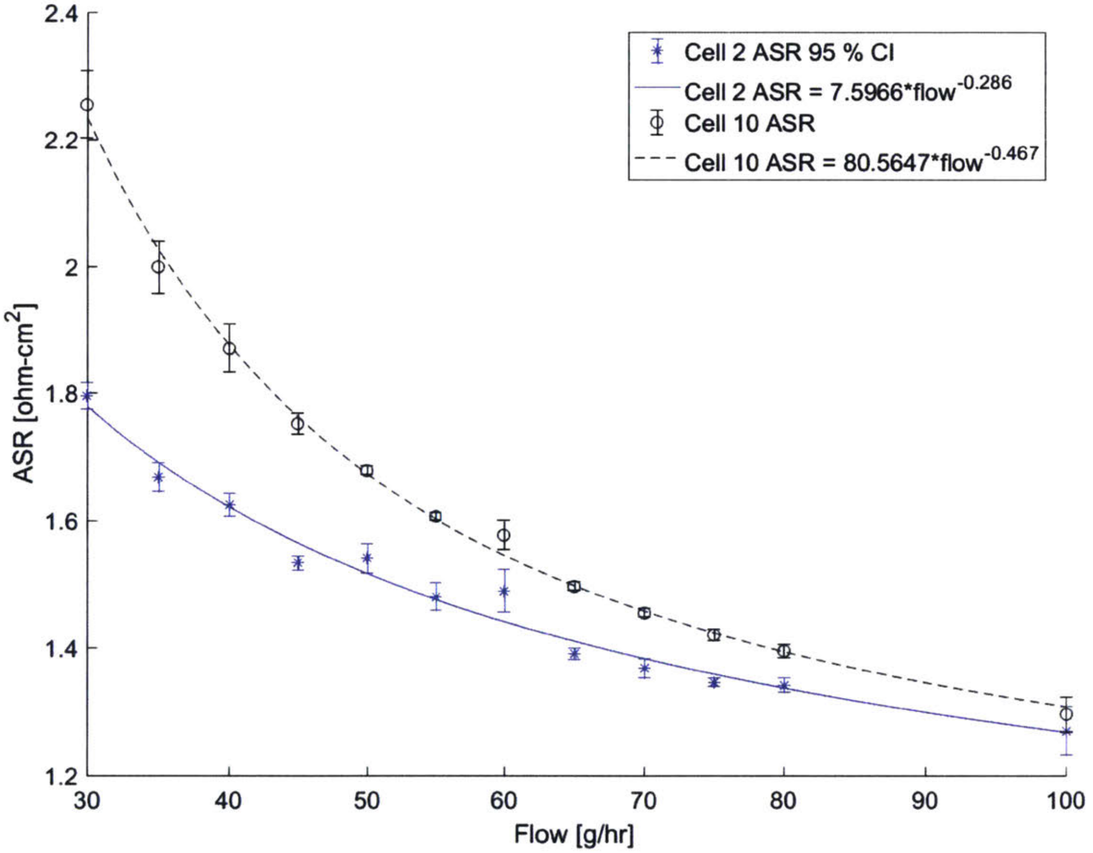

Figure 46 – Cell 10 and 2 ASR values at 800°C and varying flow conditions

Because minimal difference is observed at 100 g/hr, it is unlikely that the variation is due to the cathode composition itself. The greatest variation in ASRs occurs at 30 g/hr, implying that gas flow rates constitute the greatest source of ASR variation. If the equation fits for Cell 2 in Figure 46 can be assumed to represent an unobstructed flow of 3 g/hr (1/10 of the total 30 g/hr flow), the

ASR observed for cell 10 would be observed at an equivalent flow of 1.25 g/hr (equivalent to 12.5 g/hr stack flow).

From the observations in these experiments, it can be concluded that characterization at lower flow rates will provide the best opportunity to understand cell-to-cell variation when selecting flight stacks.

4.10.2 Hypothesis II (additional potential)

The results of this study rejected Hypothesis II stating that the approximate ASR equation with an assumed Vocv of 0.80 is an accurate representation of the SOXE i-V curve. Experiments 1, 2, and 3 all observed an ASR value with an intercept above the assumed V_{ocv} of 0.80. Additional characterization of the activation potential region was characterized by low current sweeps in experiment 2. This discovery has important implications to stack modeling, characterization, and control of the SOXE. Figure 47 demonstrates the difference between these two models.

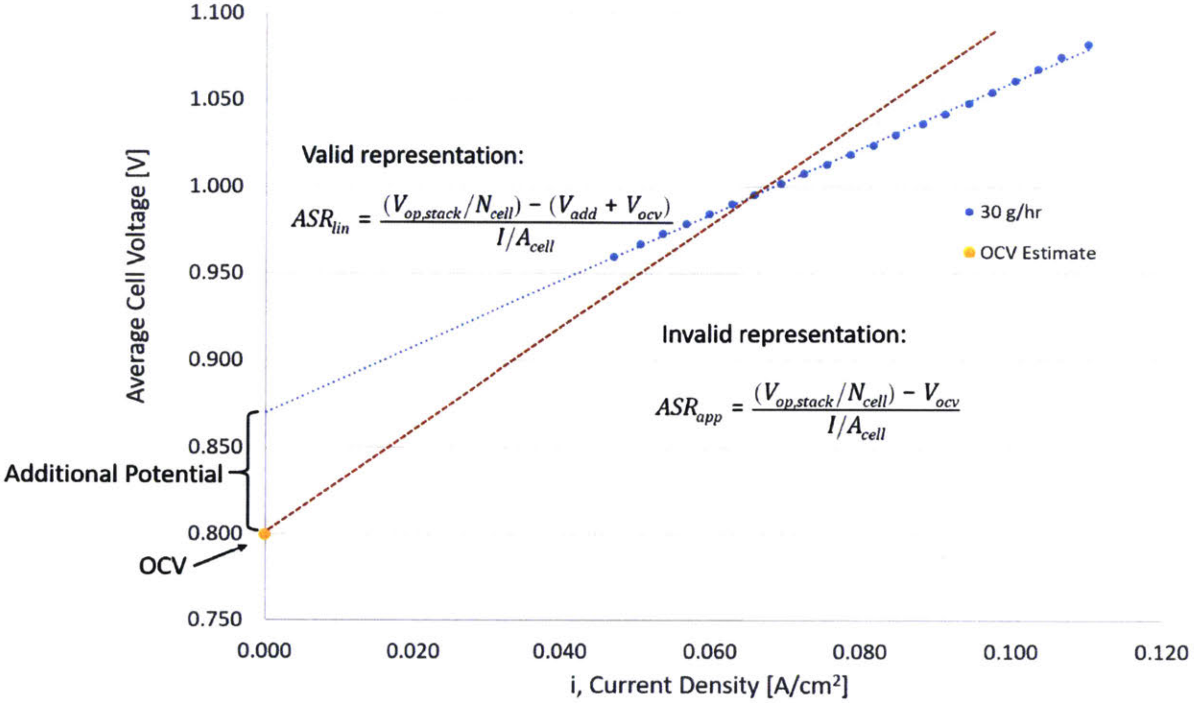

Figure 47 – Comparison of linear ASR and approximate ASR to a data sample from CSA 003R.

Because this phenomenon was not previously characterized for SOXE stacks during dry electrolysis, the approximate ASR model was implemented as the metric to test the baseline performance of the SOXE stacks for MOXIE. The ASR_{app} values are consistently higher than the true ASR. The ASR_{app} values are useful to compare historical data between stacks but should not be used for model and control design. The red line in Figure 47 is the i-V curve by the ASR_{app} equation derived from the middle current sample. Any current below the sample will predict lower than actual cell voltage and any current above will predict a higher voltage. The linear ASR equation (ASR_{lin}) corrects for this by accounting for the additional potential.

4.11 Chapter summary and conclusion

Chapter 4 covered the experimental characterization of three flight-like SOXE stacks. The motivation for these characterization tests was two-fold. First, stack performance data in varying flow, temperature, and I-V conditions was needed to develop models for the grey model of the SOXE system. Second, data on the limitations imposed by the coking risk was needed in order to avoid carbon deposition when operating MOXIE. SOXE stacks CSA 003R, CSA 004 and CSA 005 were characterized using slightly different procedures to obtain different characterization measurements. CSA 003R was used to investigate the effects of coking and was intentionally driven to coking regimes and held there for a period. CSA 004 was used to better understand where those coking limits were but was not held in coking regimes for extended periods. In addition, CSA 004 was used to characterize the additional potential discovered in experiment I. CSA 005 was used to characterize the operational envelope of a SOXE while avoiding any degradation. All cell voltages for CSA 005 were monitored and maintained below the CO-C Nernst potential, which is the voltage above which coking can thermodynamically occur. Cell-to-cell ASR variation was studied and it was concluded that a majority of the cell-to-cell variation was due to differences in flow distribution across the cells. The flow distribution improves and ASR variation decreases at higher flow rates. It was also discovered that the approximate ASR equation was underestimating the intercept of the linear portion of the i-V curve. The true ASR equation was derived to account for the activation potential of the reaction.

5. Physical System Modeling

5.1 Introduction

This chapter covers the grey SOXE model and the implementation of the multi-domain physical system model of MOXIE. This model has been named SimSitu, because it is designed to simulate the in-situ resource of MOXIE and is designed to be flexible to enable simulation of future ISRU designs. First, this chapter motivates the physical system modeling section with potential approaches to SOXE models. Next, the development and implementation of the tunable "grey" SOXE model is presented. The impact of temperature, flow, and initial ionic resistance are elaborated. The SOXE section of this chapter concludes with information on how to characterize a new SOXE stack to tune the multi-domain model to be representative of a particular stack. Section 5.4 covers the thermal domain of the SOXE model. Assumptions for each component are described and the model results are compared to the presently available MOXIE thermal characterization data. The thermal model is tied to the SOXE electrochemical model by defining the reaction temperatures. The heat generated or consumed by the electrochemical reaction is passed back to the thermal model. Simulations show the impact of system thermal variation and cell flow differences on SOXE performance. The framework for a gas flow model is also described. Finally, the control system is described and tested. The baseline cascaded current control operation, and alternate SOXE controls for voltage and utilization control are demonstrated.

5.2 Introduction to multi-domain physical system modeling

Multi-domain physical system models track bi-directional energy information flows between physical systems in different domains. These domains may include electric, thermal, fluid, and mechanical systems. This type of modeling enables the efficient development of modular models that can be quickly integrated to represent the full system. In this chapter, a multi-domain physical system model of MOXIE is implemented using the Simscape programming language by MathWorks. The bi-directional nature of physical system models has advantages over uni-directional models such as Simulink, because the models more closely represent real systems. Downstream model component changes of physical systems affect upstream system components.

One example is physical system models of circuit elements. For resistors connected in series (or equivalent circuit models of SOXE cells) operated under a constant voltage, an increase in resistance of the last resistive element will reduce the current through all resistors. An example of this type of system implemented for a simplified 5-Cell SOXE model is shown in Figure 48.

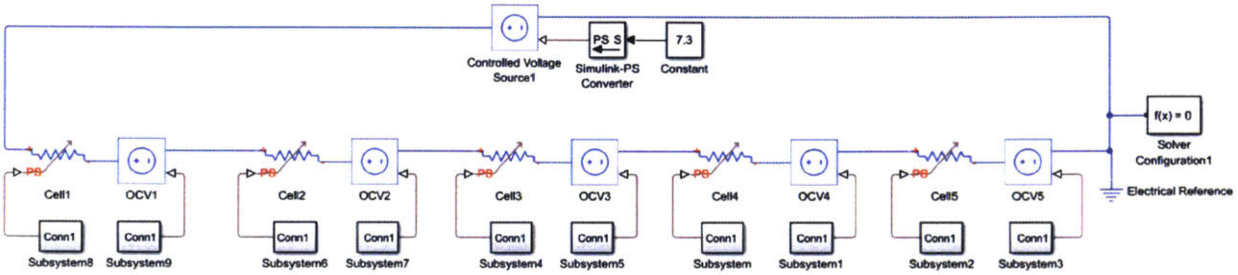

Figure 48 - Implementation simple, notional 5-cell variable ASR model in Simscape

Additional cells are added by connecting more equivalent circuit elements in series. Modeling a similar system in a unidirectional language such as Simulink requires feedback to calculate the system current. Figure 49 is an example of the implementation of the same 5-cell system as Figure 48 in Simulink. Unidirectional information flow complicates model design and reduces flexibility. Similar problems are encountered when modeling flow systems and thermal networks.

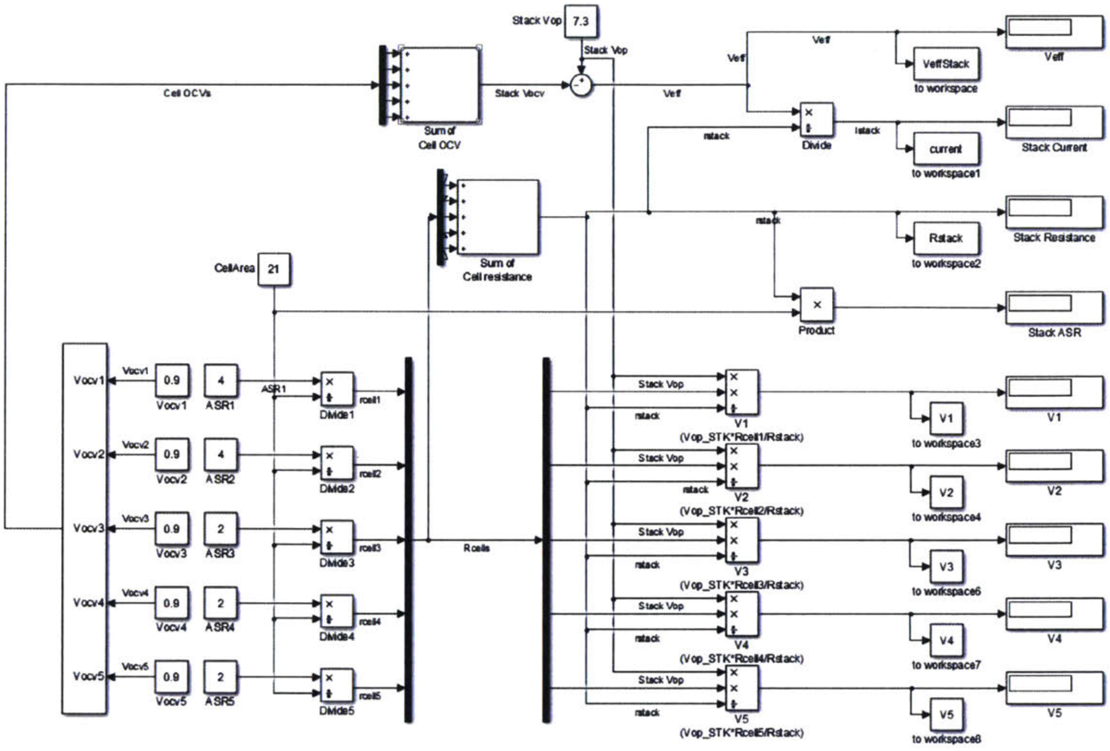

Figure 49 – Implementation simple 5-cell variable ASR model in Simulink.

An additional benefit of physical system models is that they track units of energy and mass, allowing transfer between compatible components, serving as a check during model construction. Simulink can interface with Simscape models for implementing control systems and modeling simplified system components.

5.3 Tunable grey SOXE model

The tunable grey model is developed so that it can be easily adjusted to match a particular SOXE stack. This feature is especially important for modeling specific test stacks as well as for creating an accurate representation of the MOXIE system. The experimental characterization in Chapter 4 facilitated the development of this model by testing key assumptions and identifying SOXE stack performance properties. The identification and characterization of an activation potential was one such property that enables the grey model to better match the i-V characteristics of actual cells. Cell-to-cell variability was discovered to be primarily a product of flow distribution variability and was most significant at the lowest flow conditions. Data on baseline ASR and temperature variation was also collected. This section describes the final conversion of these data and insights into a complete model.

5.3.1 Model structure

The tunable electrochemical model for each cell consists of three electrical components modified by unique subsystems. Voltage applied to the cell must overcome two significant potentials: an activation potential of approximately 21.6 mV and an average Nernst potential between 790-950 mV. The remaining voltage contributes to the production of oxygen by driving the oxygen ions across the YSZ electrolyte. The voltage drop due to this component is determined by the temperature-dependent ionic resistance of the electrolyte. The average Nernst potential and ionic resistive voltage losses increase as cell current increases. The average Nernst potential and ionic potential contribute to the total slope of the i-V curve, also known as the ASR (Area Specific Resistance). When combined with the activation potential, the three components form an equivalent circuit model. Each component may change in value depending on operating conditions such as temperature, pressures, and flow rates. Figure 50 shows how these model components are arranged in an electrical circuit to represent a SOXE cell.

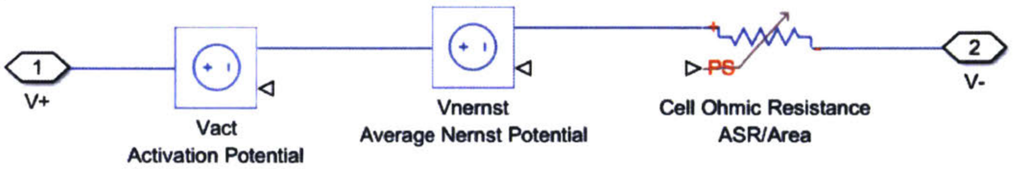

Figure 50 – Equivalent circuit SOXE cell model structure

The model may also be represented analytically by Equation (5.1):

$$V_{op} = V_{act} + V_{nernst} + I(ASR_{ohmic,temp}/A_{cell}) \tag{5.1}$$

The following sections describe the calculation of each component of the model.

5.3.2 Nernst potential contribution

The Nernst potential is the largest potential applied voltage that must be overcome during the electrolysis process. This potential depends on the partial pressures of the products and reactants, as well as the temperature of the reaction. The Nernst potential for dry CO_2 electrolysis is described in Chapter 3 and is displayed in Equation (5.2):

$$V_{Nernst} = \frac{-\Delta G_f}{4F} + \frac{RT}{4F} \ln \left[\frac{(P^0_{CO})^2 P^0_{O_2}}{(P^0_{CO_2})^2} \right] \tag{5.2}$$

Chapter 3 described how the Nernst potential changes as CO_2 is consumed across the stack. To account for this change across the cell, the integral average of the Nernst potential is calculated. The solution of this integral is shown in Equation (5.3) below:

$$\frac{1}{x_{co,out} - x_{co,in}} * \left[\frac{-\Delta G_f^o}{4F} x_{co} + \frac{RT}{4F} \left(x_{co} \ln \left(\frac{P_{O_2} * x_{co}^2}{(x_{co} - 1)^2} \right) + 2 \ln(1 - x_{co}) \right) \right]_{x_{co,in}}^{x_{co,out}} \tag{5.3}$$

The partial pressures of CO_2 and CO are expressed in terms of their mole fraction of total cathode pressure. X_{CO} represents the mole fraction of CO, and the mole fraction of CO_2 is replaced by 1-X_{CO} to reduce the number of variables. Under the test conditions of Chapter 4, the cathode gases were comprised of only CO_2 and CO without the 4-5% of inert gases that are also present in the Martian atmosphere. In this scenario, X_{CO} is also equivalent to molar utilization. When using Mars mixed gas, the X_{CO} term would be applied to the cathode partial pressure minus the partial pressure of the inert gases. In either gas composition scenario, the integral eliminates the pressure term on the cathode side of the equation. The only pressure term that affects the average Nernst potential across the cell is the partial pressure of the O_2 on the cell anode.

Equation (5.3) has extremely important implications for the operation and system design of MOXIE and extensible systems. Cathode pressure has nearly no influence on the oxygen production for a SOXE. From an electrochemical standpoint, there is no need to provide significant compression of the Mars atmosphere to feed a SOXE. This greatly reduces the compression ratio required of the feed pumps. The pumps should instead be optimized for maximum flow rates, and the tubing of MOXIE or an extensible system should be optimized to minimize any flow restrictions.

The limitations on minimum feed pressure become largely structural. There is a maximum pressure differential between cathode and anode before failure of the YSZ electrolyte or glass seal occurs. The anode pressure may also be lowered to match the cathode by reducing flow restrictions on the O_2 side. However, higher O_2 pressures are desirable for the O_2 liquefaction and storage stage after the SOXE on extensible systems. Additional experimentation on the highest, structurally sound cross-cell pressure differential is needed.

Substituting in thermally dependent fits for the reversible voltage ($-\Delta G_f/4F$), and $(R/4F)$ yields Equation (5.4):

$$\frac{1}{x_{co,out}-x_{co,in}}\left[1.4629 * x_{co} - 4.4924(10^{-4})T * x_{co} + 2.1543(10^{-5})T\left(x_{co}\ln\left(\frac{P_{O_2} * x_{co}^2}{(x_{co}-1)^2}\right) + 2\ln(1-x_{co})\right)\right]_{x_{co,in}}^{x_{co,out}} \tag{5.4}$$

This value is calculated for every operational point measured during the experimentation described in Chapter 4. The average Nernst potential is subtracted from the measured voltage at each point in the experiment. The remaining voltage should comprise only the activation potential, ohmic potential, and other minor potential losses such as diffusion effects through the cathode. Figure 51 shows the result of removing the average Nernst potential from the observed voltages of SOXE stack CSA 005 at all 800 °C flow conditions.

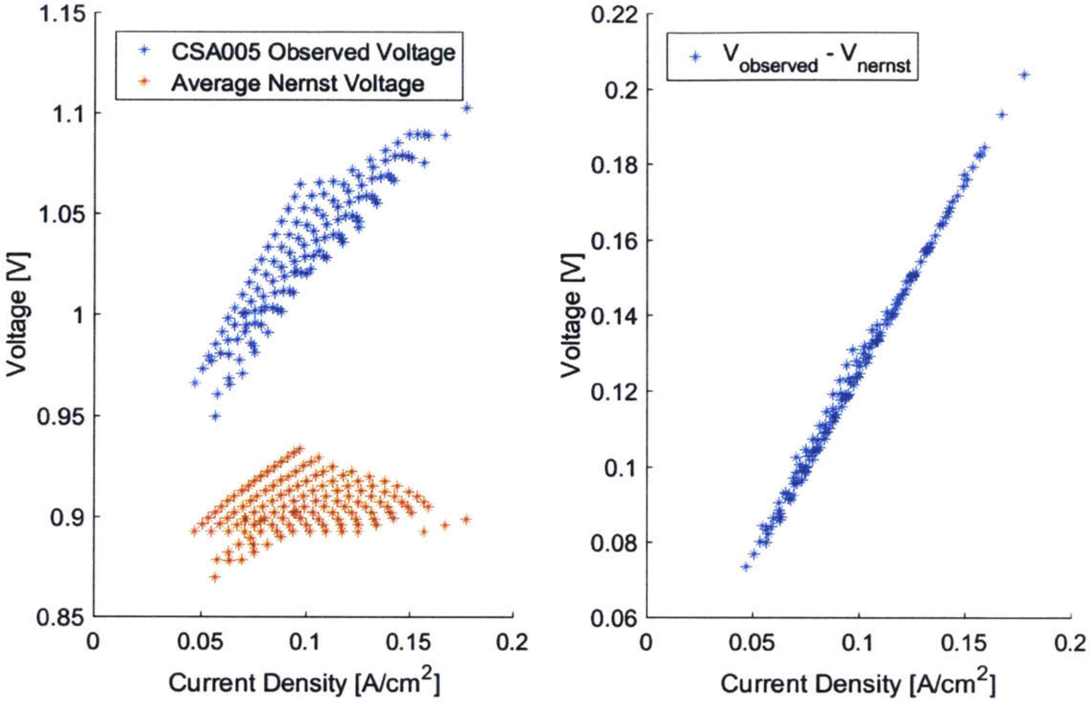

Figure 51 – Subtracting the average Nernst potential (orange, left) from the the average observed voltage (blue, left) at all flow conditions results in a linear, flow-independent i-V relation (right)

The results show that the average Nernst potential accounts for nearly all flow-dependent variation in ASR. The linear i-V relationship is consistent with all flow conditions, characteristic of potential loss due to ionic conduction through the YSZ electrolyte. For this reason, the slope of the data in Figure 51 (right) will be referred to as conversion corrected or intrinsic ASR (ASR_{int}). A slight increase in the slope can be observed at low flow rates such as 30 g/hr. This increase is likely due to increased flow variability at low flow rates, which increased the SOXE stack average of the average Nernst potential. Figure 52 shows the ASR_{int} for each cell assuming uniform cell-to-cell flow distribution.

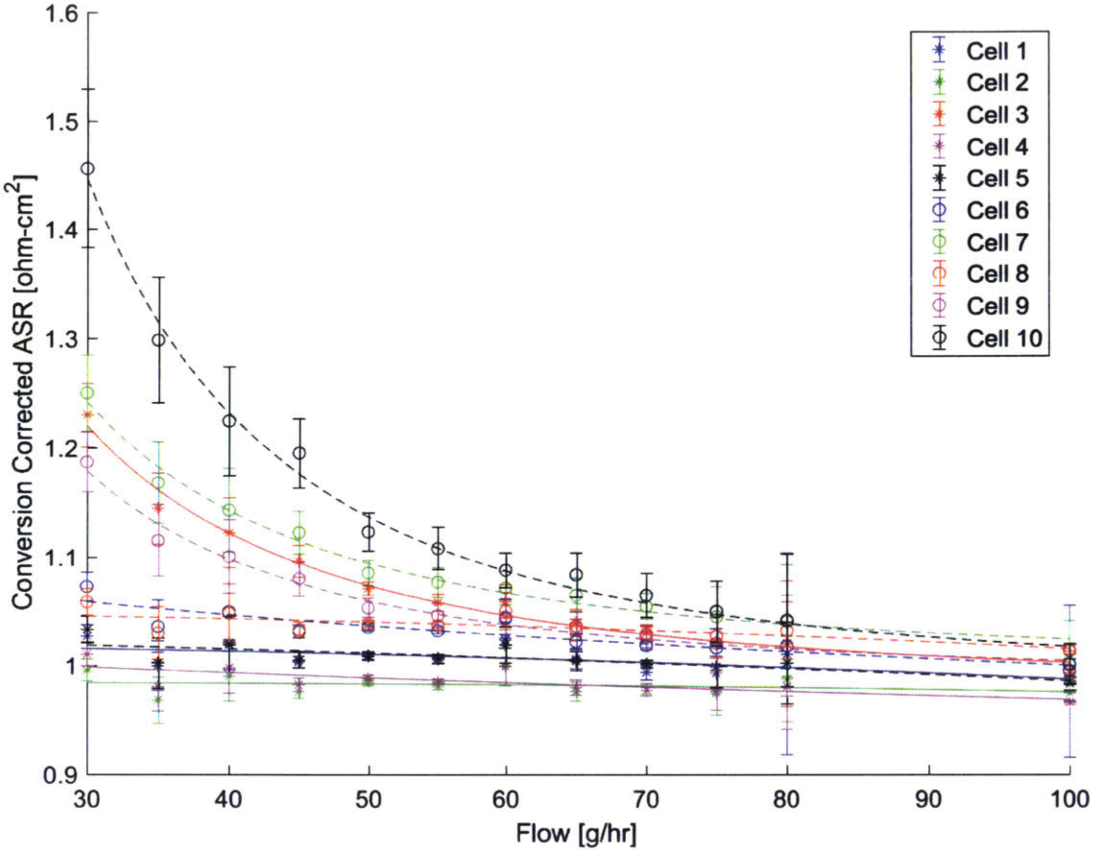

Figure 52 – Individual cell intrinsic (conversion corrected) ASR_{int} values across various flows

Cells 1, 2, 4, 5, 6, and 8 show constant ASR_{int} values across flow rates. Cells 3, 7, and 9 appear to have a slight reduction in their percentage of total flow. Cell 10 exhibits the greatest departure from constant ionic resistance, indicating that the flow rate to that cell is reduced the most with respect to other cells during low flow conditions. The average ASR_{int} of the 6 constant cells across all flow rates is 1.008 Ω-cm^2 with a standard deviation of 0.024 Ω-cm^2 which is nearly within one standard deviation of the average ASR_{int} of all cells at 100 g/hr ($ASR_{int} = 0.9922$ Ω-cm^2, $\sigma = 0.015$ Ω-cm^2.) Therefore, it is reasonable to characterize the ASR_{int} for a stack based only on characterization points at 100 g/hr. Corrections for cell-to-cell flow distribution can then be characterized by measuring the i-V response at 30 g/hr, and using the average Nernst equation to back calculate the flow distribution.

The integral average Nernst potential is used to account for flow effects in the system model. Figure 53 shows the high-level model structure for how Equation (5.4) is implemented to alter a Simscape variable voltage block.

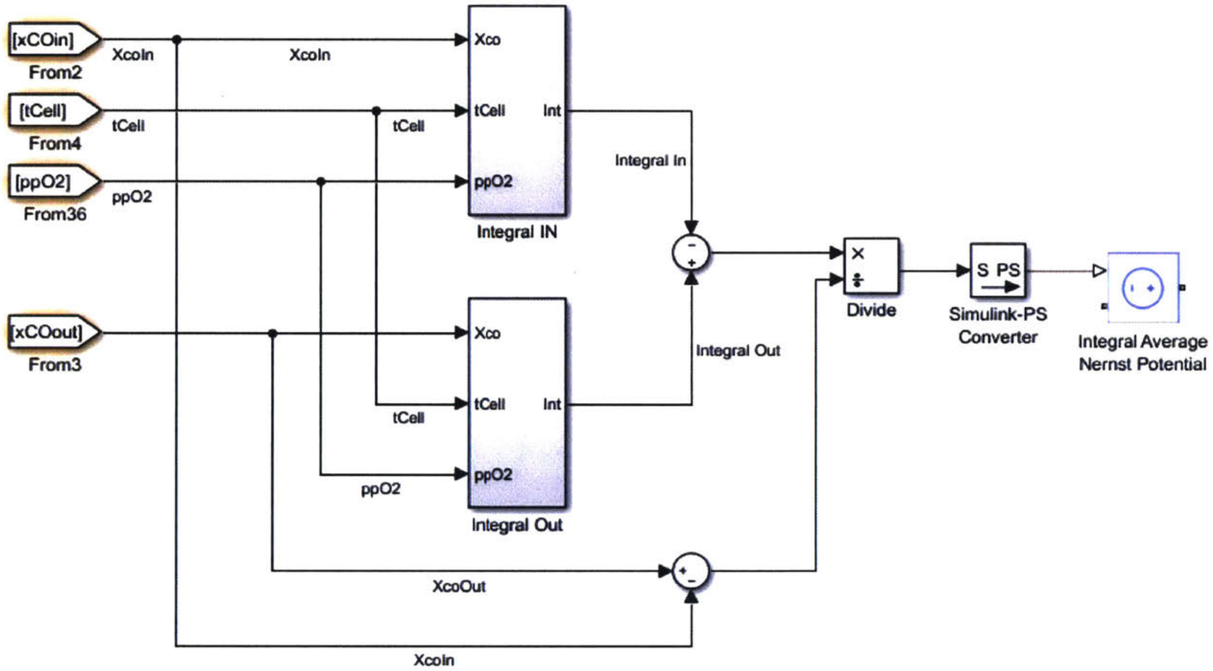

Figure 53 – High level block for calculating the integral average Nernst potential based on the dynamic system variables (highlighted in yellow)

The dynamic variables passed to the model are highlighted in yellow. These variables include the molar fraction of CO into the cell and out of the cell, the partial pressure of O_2 on the anode, and the cell temperature. This block defines the integral average Nernst potential, which helps define the cell production and the outlet molar fraction of CO. The result is an algebraic loop that is broken by a memory block with an initial condition of 0.5.

Simulink is used to calculate the value of the integral Nernst potential that is passed to a variable voltage source in the Simscape network (blue). The model structure for one of the integral blocks is shown in Figure 54 below.

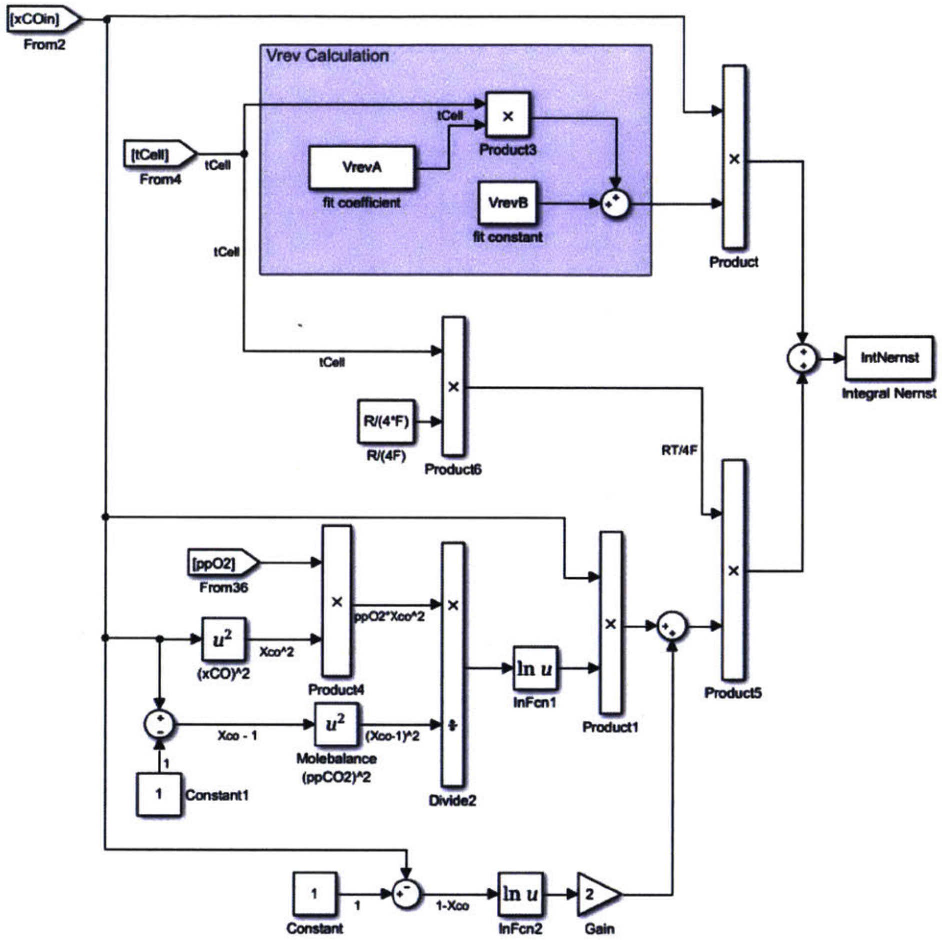

Figure 54 – Detail of the integral in block for the calculation of the Nernst potential

5.3.3 Arrhenius Derivation (ASR temperature dependence)

While ionic ASR is flow independent, conduction through the YSZ electrolyte is very temperature dependent. Higher temperatures result in lower ionic resistance. This concept was first introduced in Chapter 3. The average ionic ASR of the stack is shown in Figure 55.

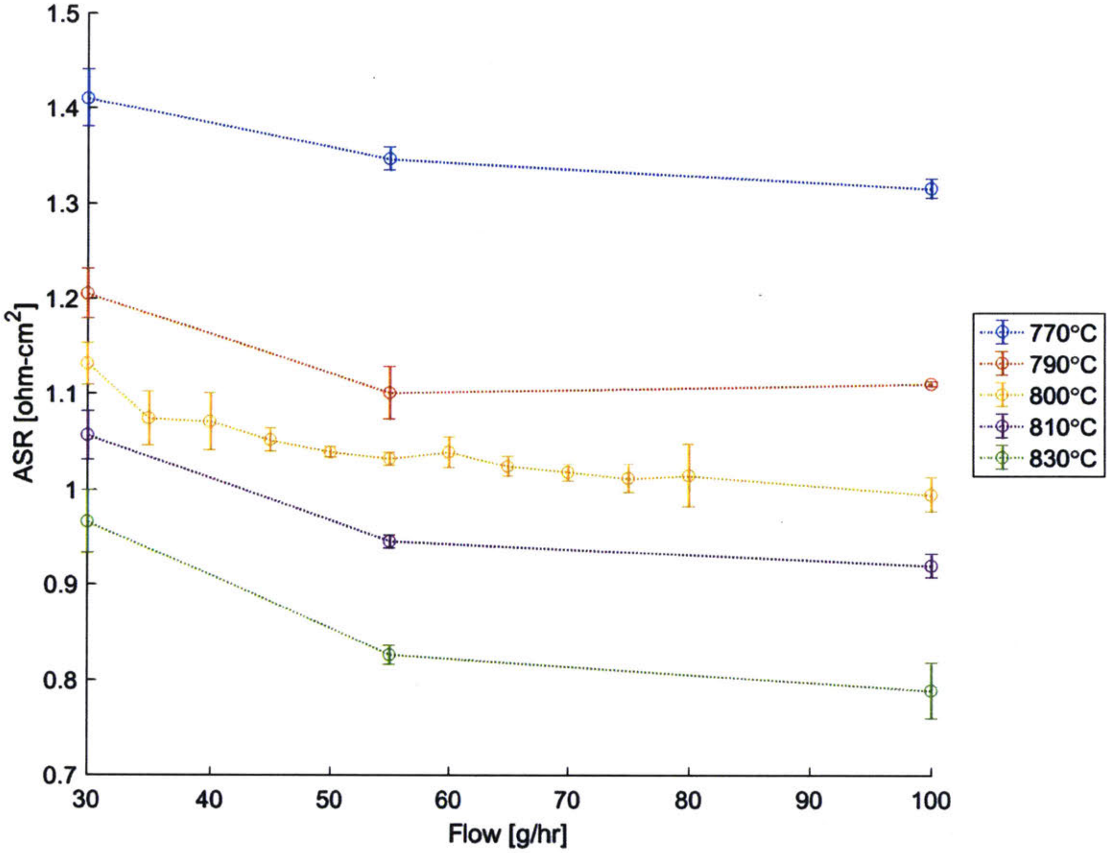

Figure 55 – CSA 005 conversion corrected ASR at all sampled temperatures.

Significant temperature effects are visible. The increase in resistance observed at lower flow rates is due to non-uniformity at low flow conditions. The results are presented in Table 13.

Table 13 – ASR_{int} values at different flow rates in Ω-cm^2

	770°C	790°C	800°C	810°C	830°C
100 g/hr	1.316	1.111	0.9951	0.9200	0.7886
55 g/hr	1.347	1.101	1.033	0.9457	0.826
30 g/hr	1.410	1.205	1.132	1.057	0.9664

The relationship is then fit to the Arrhenius relation shown in Equation (5.5) below:

$$\frac{k}{k_o} = Ae^{\frac{-E_A}{RT}} \tag{5.5}$$

Where k is the measured ionic conductivity per unit area (S/cm^2) at each flow condition and k_o is the reference conductivity measured at 800 °C. A is the pre-expoential term and intercept of the linear fit of the natural log of k/k_o vs $-1/T$. The activation energy, E_A, is calculated by multiplying the slope of that linear fit, E_A/R, by the universal gas constant. The fit for temperature dependence at 100 g/hr is shown in Figure 56.

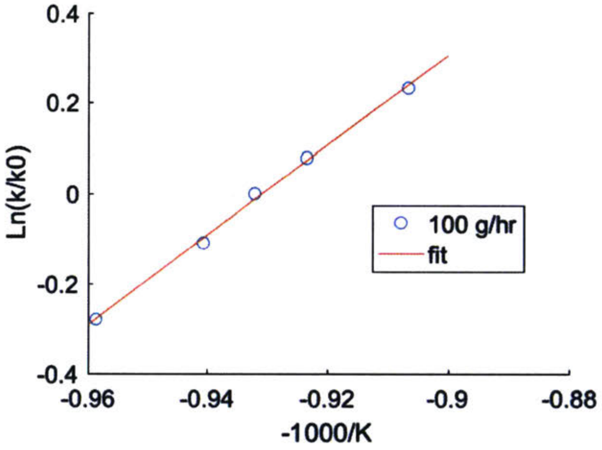

Figure 56 – Linear fit to derive the activation energy and pre-expoential terms

The activation energy of the SOXE cells is 82.6 kJ/mol with a pre-exponential term of 10300. The values derived for each flow rate are shown in Table 14. The results cannot be accurately derived at 55 and 30 g/hr because they are confounded by the cell-to-cell flow variation driving up the average Nernst potential.

Table 14 – Arrhenious terms intrinsic (conversion corrected) ASR

Flow [g/hr]	Pre-Exponential	Activation Energy [J/mol]	R^2 of Fit
100	10300	82557	0.9977

Substituting the in ASR for conductance, and including the terms solved for at 100 g/hr yields the following temperature dependent ASR correction:

$$ASR_{temp} = \frac{ASR_{cc@1073K}}{10300e^{\frac{-82557}{RT}}} \tag{5.6}$$

Where ASR_{temp} is the temperature corrected ASR calculated from the conversion corrected ASR characterized at 1073K, which for CSA 005 is 0.9922 Ω-cm^2. Figure 57 shows the activation energy and pre-exponential term modeled in Simulink to modify the ionic resistance term.

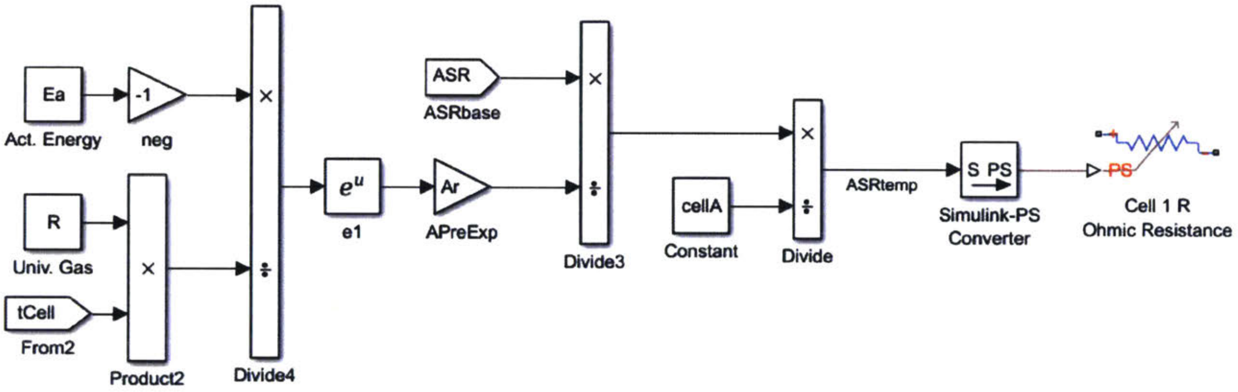

Figure 57 - The Simulink block modeling the temperature dependent corrections to the conversion corrected ASR

The combined temperature and conversion corrected resistance and average Nernst potential both contribute to the slope of the total ASR for a SOXE cell. The first contributes to a majority of the temperature dependence and the second contributes primarily to the flow dependence with a small temperature dependence contribution. The activation potential shifts the i-V curve upwards. The activation potential is the final term of the electrolysis model and is described in the following section.

5.3.4 Activation potential

The activation potential is defined as the difference between the intercept of the linear part of the i-V curve minus the contribution of the Nernst potential. The results from CSA 005 were used to calculate V_{act}. The averaged V_{act} values across all flows and temperatures are shown in Figure 58.

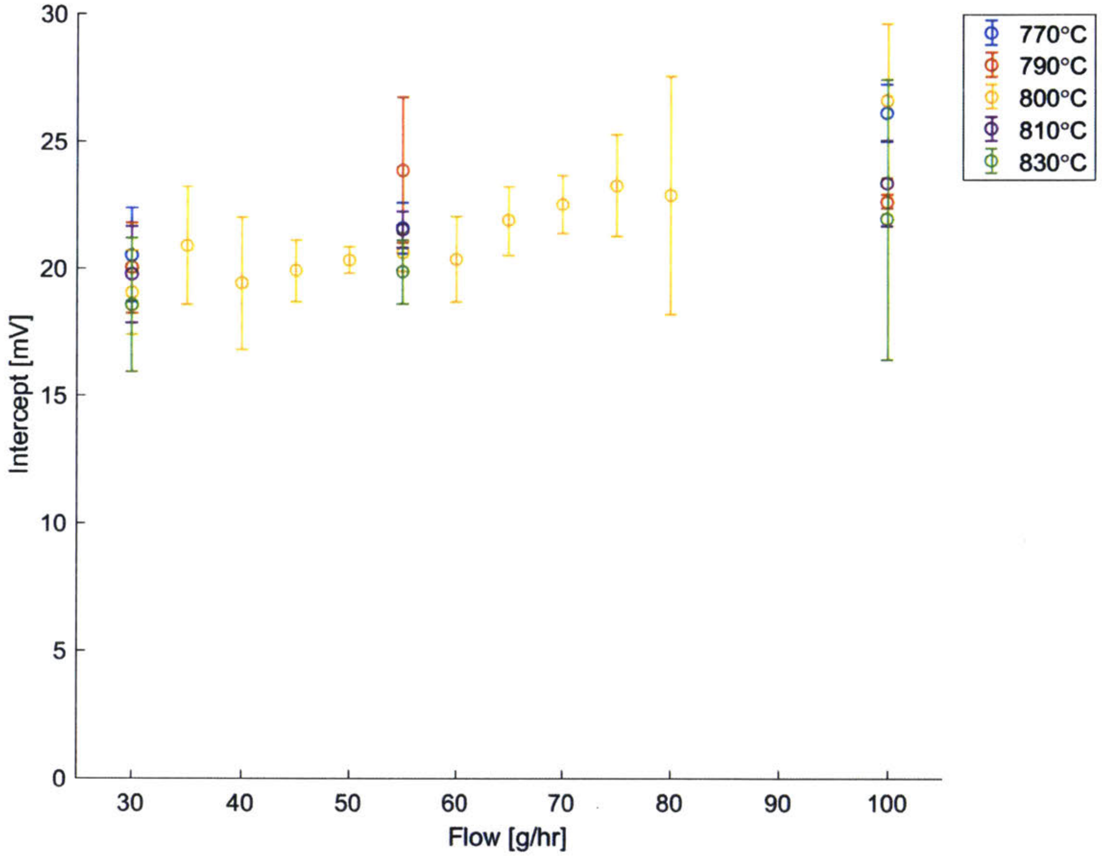

Figure 58 – CSA 005 activation potentials across all flows and temperatures with 95% CI

The average activation potential across all conditions is 21.55 mV. Due to the amount of overlap of the confidence intervals, it is reasonable to assume this value. For slightly improved accuracy, a temperature dependent fit can be made using the Arrhenius relation as shown in Equation (5.5) above.

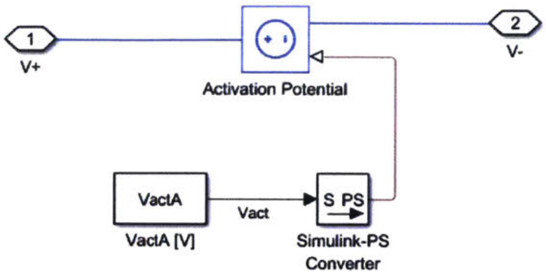

Figure 59 – Activation potential subsystem

The activation potential and open circuit voltage potentials account for the cell potential losses prior to electrolysis.

5.3.5 Converting flow to utilization

Mass flow controllers were used to target specific utilizations in the characterization experiments. The MOXIE baseline control system uses pressure control but will also have a flow meter. For these reasons, when building the system model, each cell will be passed a dynamic flow rate value based on the system variables. Utilization can then be calculated from flow and current values. This calculation was introduced in Chapter 3. Equation (5.7) is the calculation of final utilization using current and the combined inlet flow of $CO + CO_2$ on a per cell basis:

$$X_{co,out} = \frac{I}{(1 - X_{co,in})\dot{m}_{CO+CO_2,cell,in} * 1.2182} \tag{5.7}$$

This equation enables the model to convert individualized cell flow rates to specialized utilization value that is then used to calculate the integral average Nernst potential for that cell.

5.3.6 SOXE model validation

The SimSitu model developed in this chapter is validated by comparing model results to the test data of CSA 005. The results were also compared to the SOXE ASR definition model used to track the MOXIE figures of merit (FOM) which is also the same model proposed in Hypothesis 2 of Chapter 4. Figure 60 below shows a comparison of both models at both ends of the thermal operating range, 770 °C and 830 °C, during I-V sweeps at 30 g/hr, 55 g/hr, and 100 g/hr.

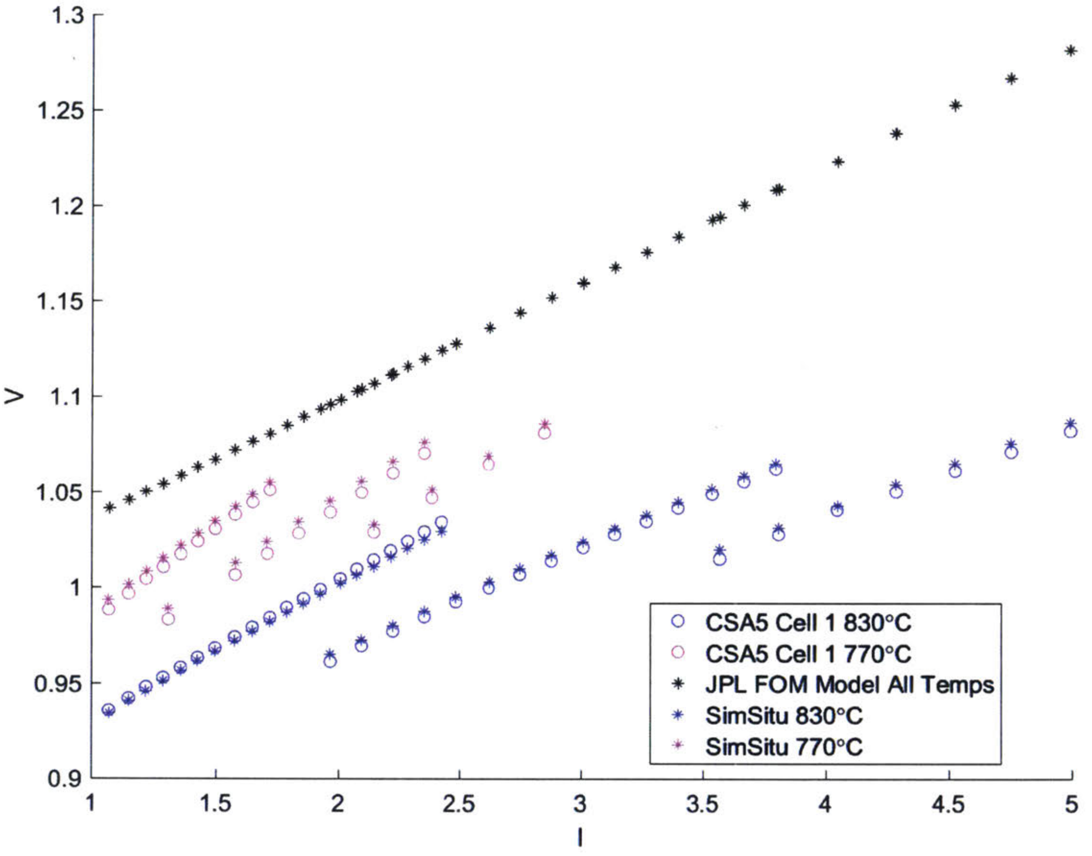

Figure 60 – Comparison of CSA5 Cell 1 results, SimSitu, the JPL Figure of Merit (FOM) model

The SimSitu grey model shows good correlation to the actual data across a wide temperature range and all flow rates. The root-mean-square error (RMSE) for all flow rates at 830°C is 3.1 mV and at 770°C is 5.1 mV. The RMSE for the FOM model is 131.8 mV at 830°C.

5.3.7 Stack characterization requirements for the tunable model

The SimSitu grey model is tunable to a characterized stack performance baseline. Three generalizable properties of the flight stacks were discovered during the experimentation of Chapter 4 and the model development of Chapter 5. First, the resistance of ionic conduction through the cells is constant at all flow conditions. Second, the increase in ASR observed at lower flows is attributed to an increase in the average Nernst potential resulting from higher steps in utilization at low flow compared to the same current steps at high flow. Third, cell-to-cell flow distribution variation is most pronounced in the low flow regimes.

Conversion corrected ASR will be determined as the value from which all other components of the model are referenced. The reference values for the tunable portion of the model should meet as many of the following requirements as possible:

1. Easily characterized
2. Data point collection unlikely to cause damage
3. Standard condition from which MOXIE has historically comparable test values
4. Cell-to-cell variability is minimized
5. Ideally a standard operating value for MOXIE

The point selected to characterize ASR_{int} is 100 g/hr at 800°C. This point satisfies 4 of the 5 requirements. This data point is easily collected, unlikely to damage the SOXE except at high currents, has been the standard for baselining all SOXE stacks throughout the project, and exhibits only minor flow variation between cells at standard operating temperature. The only downside of tuning the model at this point is that it is at a flow rate unlikely to be achieved by the flight MOXIE due to pump limitations. Fortunately, the flight stack will likely be characterized at this condition for experimental legacy comparison. For modeling average stack performance, only this primary value needs to be used.

Secondary baseline values can be used to further expand the accuracy of the model. Good secondary tuning points meet the following requirements:

1. Easily characterized
2. Accentuates cell-to-cell and stack variation

Chapter 4 demonstrated that characterization at 30 g/hr is the most sensitive to cell-to-cell variation. This variation was attributed to flow distribution. ASR values derived from I-V sweeps at low flows can then be used to back-calculate the estimated flow distribution based on the average Nernst potential equation. This enables potential flight stacks to be selected based on minimizing flow variability and identifies the worst performing cells. The flow distribution can then be entered into the grey, SimSitu model to tune the predicted voltages to the flight stack.

5.3.8 Electrochemical model summary

The final representation of the cell model as an equivalent circuit is shown in Figure 61 below.

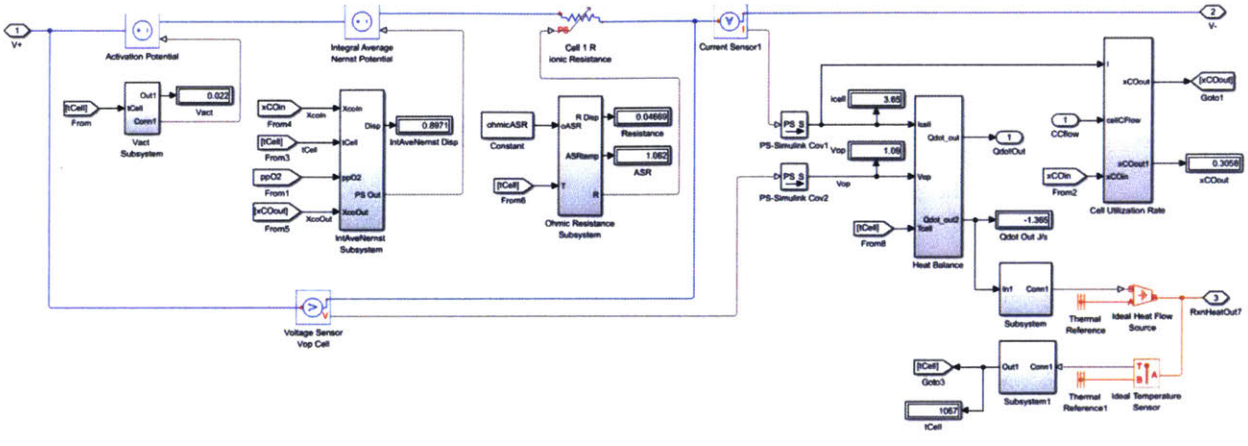

Figure 61 – Equivalent circuit model of a cell

The current flows from left to right. Two controlled voltage sources and a single variable resistance blocks define the voltage drop across the cell. On the right of the image are blocks for calculating the reaction heat generation from the current, temperature, and operating voltage, as well as a block to calculate individual cell utilization. The heat transfer out and temperature are passed in and out of the system though the orange signals in the bottom right.

Figure 62 below shows each of these cells connected in series to reflect the arrangement of the SOXE stack. Two independent current sources power the cells in 5-cell groups. Lead resistances to connect to these cells are modeled and all cells are individually instrumented to measure voltage. Current through each 5-cell group and through the SOXE midplate is measured. The temperature of each cell is defined by the thermal domain described in the next section.

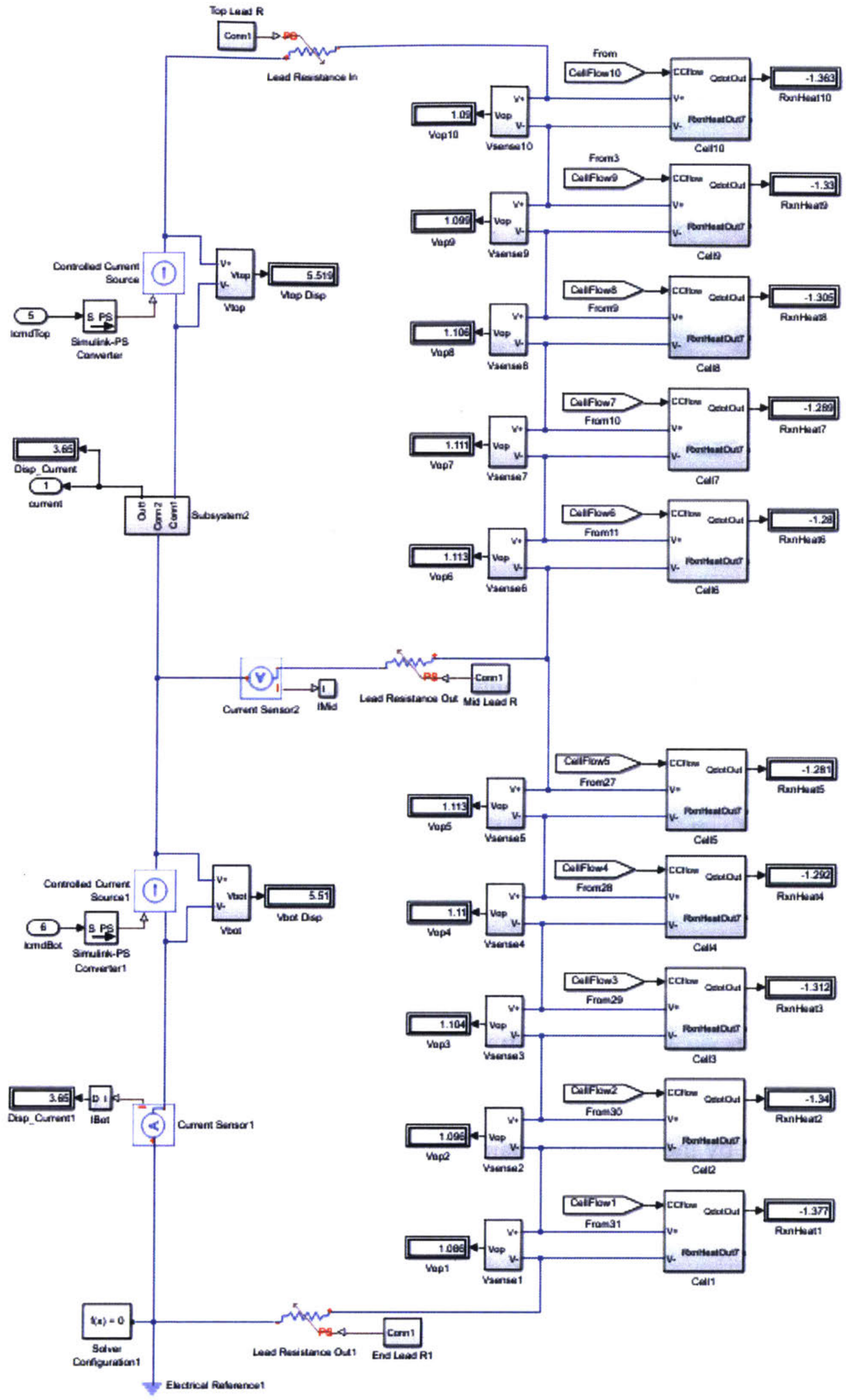

Figure 62 – SimSitu electrochemical model of the entire SOXE stack with two 5-cell groups

5.4 Thermal domain

The thermal domain is one of the most important domains for predicting the performance of the SOXE stack. The ionic conductance of the SOXE, the Nernst potential, and degradation processes are thermally dependent. Higher temperatures result in more efficient oxygen ion transport across the yttria-stabilized zirconia (YSZ) electrolyte, but also lead to greater degradation rates and heater power requirements (Wachsman and Lee 2011). The standard target temperature for a MOXIE cell is 800°C. Great effort is put into insulating the SOXE cell from the Mars 2020 Rover Avionics Mounting Panel (RAMP) in order to reduce the power consumption required to keep the cells heated during operation and to protect MOXIE and rover components from overheating. This is accomplished by securing the SOXE in the insulating enclosure shown in Figure 63.

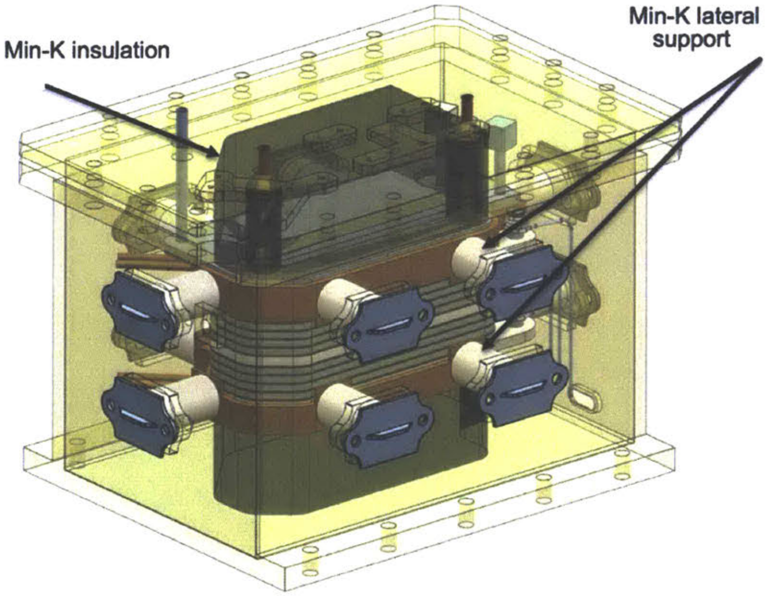

Figure 63 – The SOXE assembly in its insulating enclosure

The SOXE is held in place by Min-K insulation on the top and bottom of the stack. A compression system transfers load to the stack through the insulation. The gap between the SOXE and the enclosure is filled with non-load bearing aerogel insulation. Additional Min-K lateral supports shown in Figure 63 were included in the design to prevent lateral movement of the stack during launch.

5.4.1 Thermal model development

The thermal domain is implemented in the Simscape thermal domain language. Each component is modeled as a thermal mass defined by the mass and specific heat. These masses are placed in a thermal network. The cells in a stack are represented by the CFY interconnect and YSZ cell properties. The thermal network for a cell is shown in Figure 64 below:

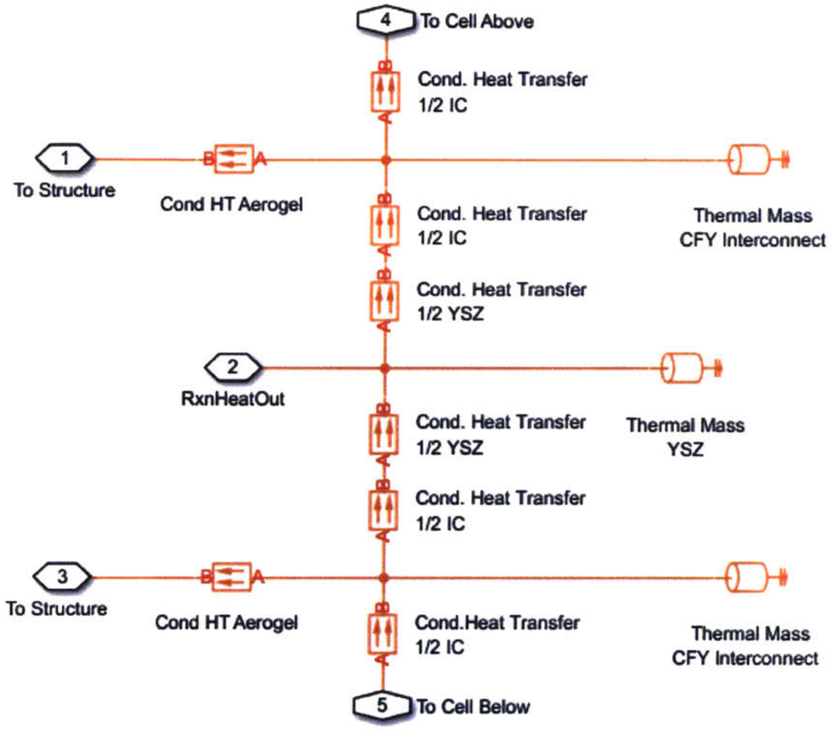

Figure 64 – Thermal network for SOXE cell and CFY interconnects

Thermal energy is passed between the cell and its surroundings through conduction from the top and bottom interconnects. Conduction from the perimeter of the stack is arranged through conduction to the aerogel insulation touching the perimeter of the cell interconnects. The cell itself is relatively thin and does not have significant area perpendicular to the perimeter so conduction from the cell directly to the aerogel is ignored. Energy consumed or generated during the reaction leaves the thermal network via the HeatRxnOut port. The temperature of each cell is passed to the electrochemical model from Section 5.3 to define the temperatures for the electrolysis reaction. The thermal networks are connected in series to model an entire 10-cell SOXE stack. The larger size of the midplate and end-plate interconnects is accounted for by increased thermal mass, thickness, and side conduction area for those components.

The stack thermal model is coupled to the SOXE Box and RAMP with an expansive lumped parameter thermal network. Figure 65 depicts the location of the other significant thermal components that surround the SOXE.

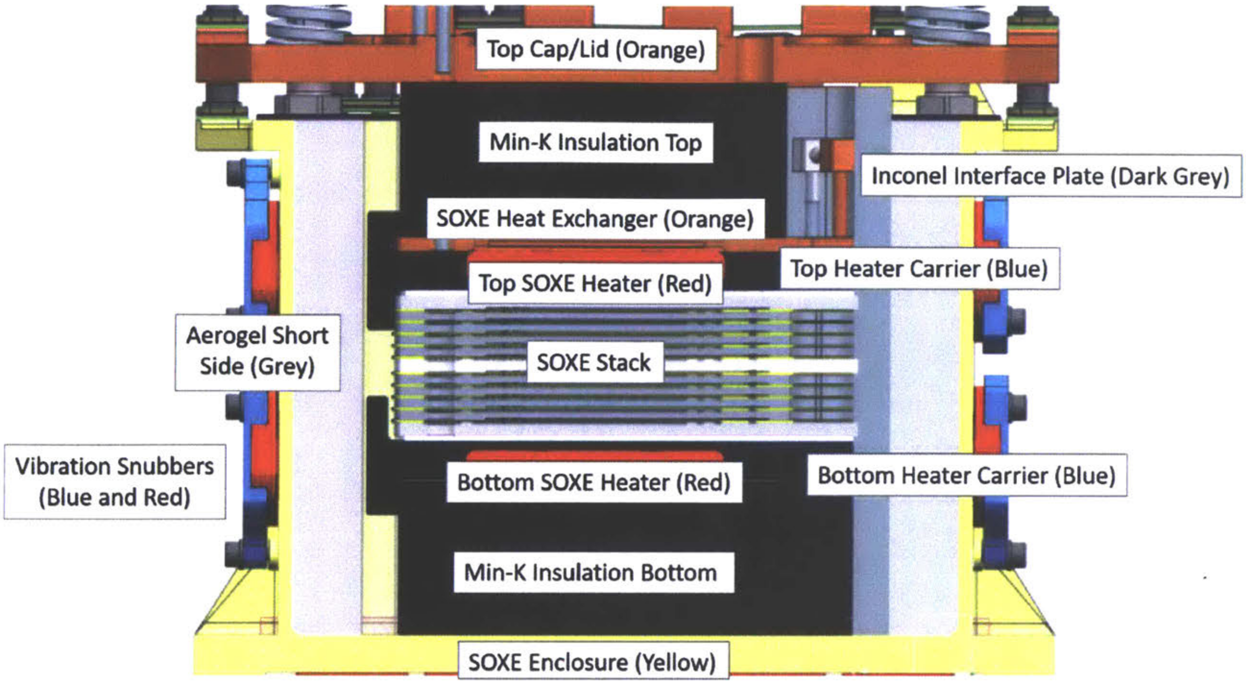

Figure 65 – Components within the hot zone of the SOXE assembly

The assumed properties for each of these components are listed in Table 15.

Table 15 – Poperties of SOXE box thermal network

Component	CBE Mass [g]	Material	k [W/m-K]	ρ [kg/m^3]	c [J/kg-K]
SOXE Box Lid	905	Al 6061T6	167	2770	961
Min-K top	43	Min-K 1800	0.045	592	990
Interface Plate	16	Inconel 600	14.9	8300	460.8
Inlet Heat Exchanger	95	Inconel 600	14.9	8300	460.8
Heater Carrier Top	154	SiC	158.8	3210	680.79
SOXE Heaters 2X	113	Inconel 600	14.9	8300	460.8
SOXE Stack Total	778	CFY	50	7220	620
SOXE Cell	8	YSZ	2	5938	600
SOXE Interconnect	50	CFY	50	7220	620
SOXE Endplates	100	CFY	50	7220	620
Heater Carrier Bottom	156	SiC	158.8	3210	680.79
Min-K bottom	43	Min-K 1800	0.045	592	990
SOXE Enclosure	1692	Al 6061T6	167	2770	961
Aerogel Short Side	67	JPL Aerogel	0.004368	239	704.7
Aerogel Long Side	155	JPL Aerogel	0.004368	239	704.7

Thermal conductivity values vary with temperature so as a simplifying assumption values near operating temperature were used when necessary. The components are modeled in the thermal network in Figure 66. The cell network is grouped into the stack thermal subsystem. The stack is linked to the thermal masses of components above and below the stack. The top and bottom heaters deliver thermal power to the heater mass elements. Heat conducted to the top of the aluminum enclosure follows a conduction path down the sides and to the base. Heat can also conduct to the enclosure walls through aerogel insulating the sides of the stack. The model is anchored to a fixed temperature at the base of the SOXE enclosure, assumed to be in equilibrium with the RAMP temperature.

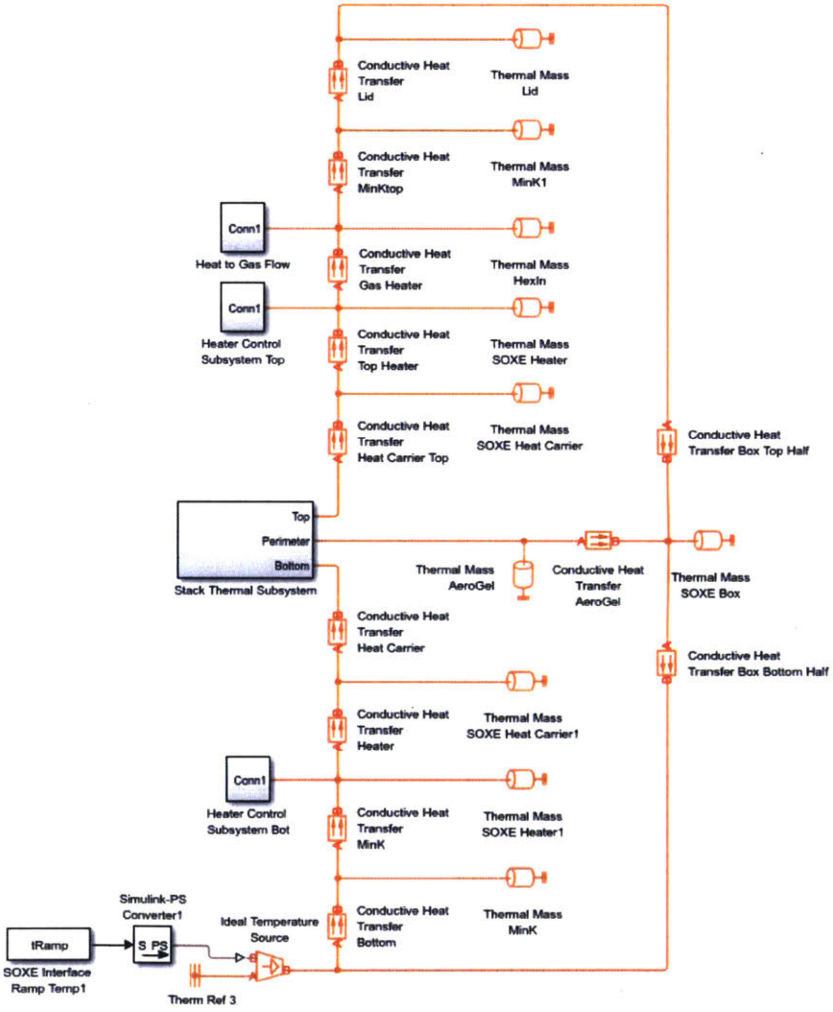

Figure 66 – Thermal network surrounding SOXE stack

Heat loss to the SOXE inlet heat exchange is calculated using the average specific heat at constant pressure of CO_2 and the temperature difference between the RAMP temperature and heater temperature. It is assumed that conductive heat transfer between components is dominant and radiative heat transfer is neglected as a simplifying assumption. The model can accept radiative heat loss between the SOXE Box and the surroundings, as well as between internal components as part of future enhancements. Another model assumption is that before start-up, all thermal masses are assumed to begin in thermal equilibrium with the RAMP. The RAMP temperature has been modeled as an ideal temperature source. It is assumed that MOXIE does not affect the ramp temperature, but the temperature may change based on rover operations as a whole or Martian environmental conditions for a range of -45°C to 50°C (Hua 2017). The RAMP temperature value can be specified at the start of a simulation.

The top and bottom SOXE heaters are modeled as an ideal heat source that flows into the thermal mass of the heater. The heater profile can be controlled through a PID controller with feedback from the top and bottom SOXE cells. The heater subsystem as configured for the model validation run is in Figure 67.

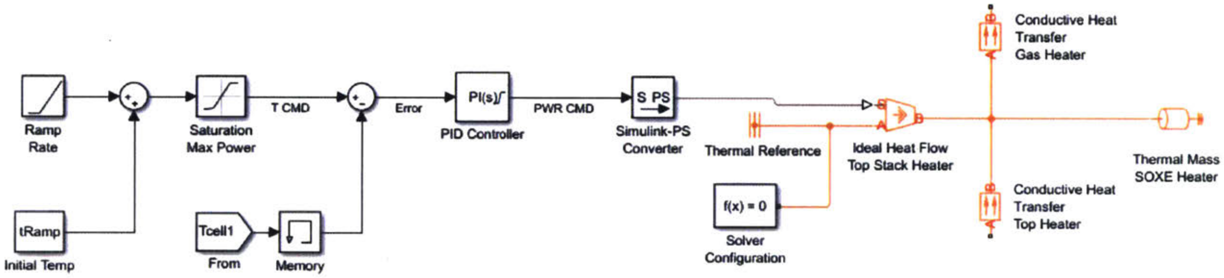

Figure 67 – Heater model and PI control architecture for validation testing

5.4.2 Thermal model validation and tuning

The thermal model was validated using experimental data collected by the MOXIE thermal team at JPL. The experiment tested SOXE STK-002 in a bell jar vacuum chamber. The insulation was flight-like with Min-K on the top and bottom of the stack and JPL aerogel on the stack sides. The heater carriers were brass instead of SiC, and cartridge heaters with a total available power of 175W were used in place of flight models. The stack was instrumented with thermocouples to measure variation in pressure. The SOXE assembly was enclosed in an aluminum casing similar to the flight stack (Aboobaker, Smith et al. 2016). The test setup is shown in Figure 68 below.

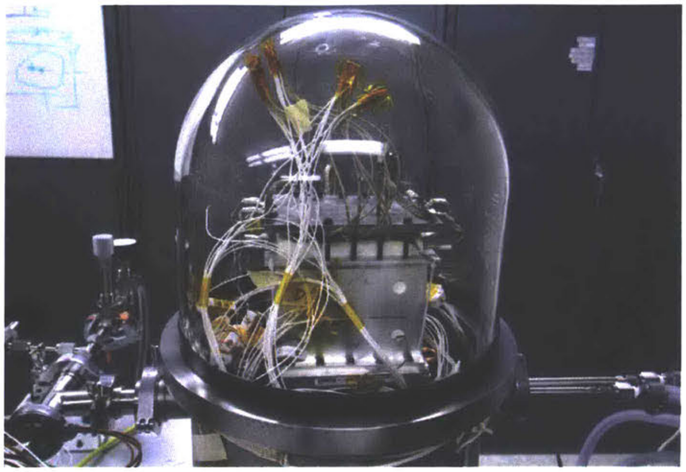

Figure 68 – Vacuum enclosure and test SOXE stack used for thermal characterization (Aboobaker, Smith et al. 2016)

Flight-like heating profiles were conducted and the variation in temperature of the internal cells was recorded. All tests began with a CO_2 pressure of 7 Torr. The SimSitu thermal model was tuned using experimental results from a heating profile with a 5°C per min ramp from 25°C to 800°C. The experimental profile and stack response is shown in Figure 69.

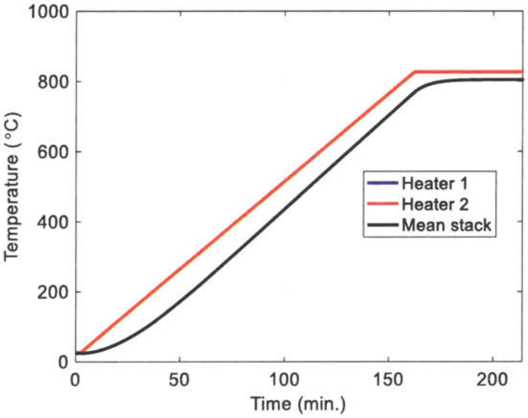

Figure 69 – Heater temperature profiles (heater 1 and 2 overlap) and mean stack response (Aboobaker, Smith et al. 2016)

The experimental results show cell-to-cell temperature differences of up to 17°C during heating, with steading state temperature differences of about 5°C. The middle of the stack is the coldest, and the top and bottom cells are the warmest. The experimental cell-to-cell variation and SimSitu tuned model results are shown in Figure 70.

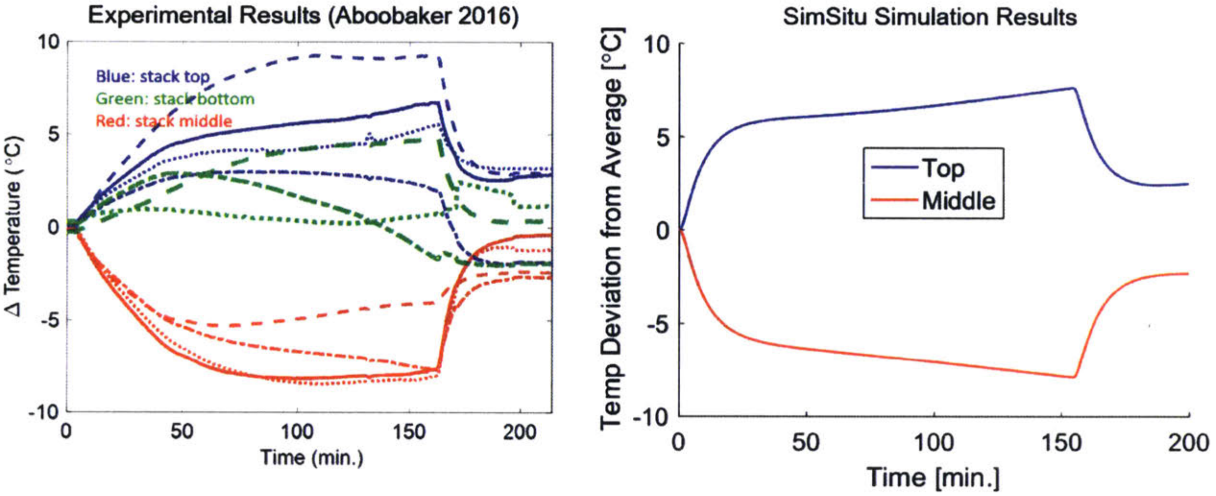

Figure 70 – Experimental SOXE cell temperature variation (left) and SimSitu results (right)

The un-tuned SimSitu results showed less cell-to-cell variation. To tune the model to show similar characteristics of the test data, grey modeling factors were included to enhance or reduce heat transfer between some thermal elements. Conduction area between cell interconnects was reduced 84% to increase the model's transient cell-to-cell variation. This adjustment has conceptual validity because much of the planar surface area of the cell interconnects do not touch the adjacent cell due to flow channel gaps. The conduction through the aerogel to the sides was increased to match the observed steady state variation. This is reasonable because the stack midplate has additional exposed surface area at the electrical connection bus that was not modeled. This area may act as a heat fin in the middle of the cell. Additional thermal resistance was added at the top and bottom of the Min-K insulation to match the observed heater power consumption. The heater power results are shown in Figure 71 below.

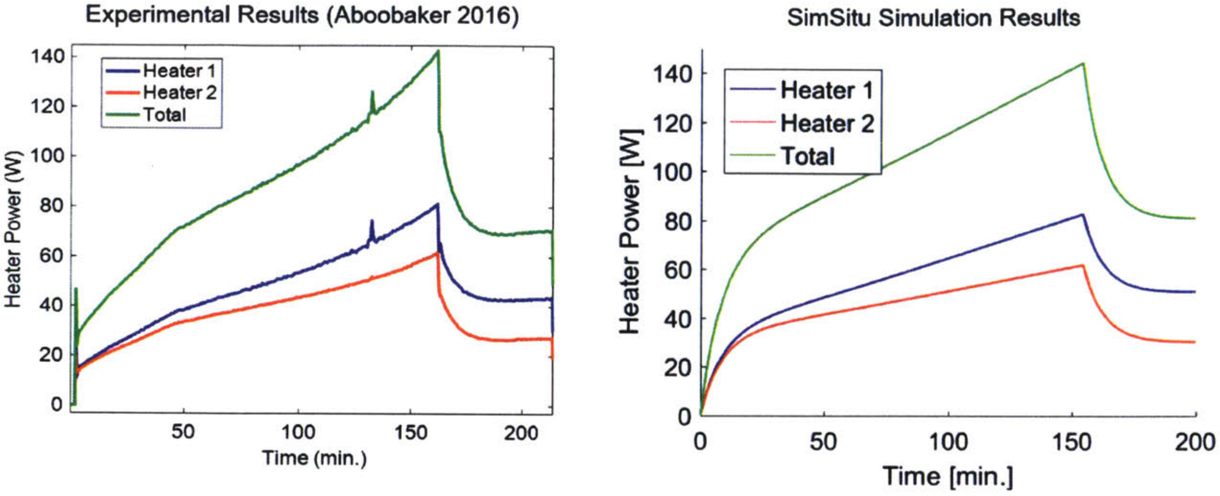
Experimental Results (Aboobaker 2016)

SimSitu Simulation Results

Figure 71 – Experimental heater power (left) and SimSitu results (right)

The thermal domain model improves the understanding of the SOXE and the MOXIE system. In this scenario, the peak heater powers observed were 80W for the top of the stack and 60W for the bottom of the stack. The model predicts that the steady state heat leak from the side of the SOXE is approximately 19.4 W. The steady state heat leak through the top and bottom of the stack is 42.6 W and 20.5 W respectively. The gas preheat consumes 22.4 W of the top heater's power. Figure 72 shows the heat loss to different thermal paths for a whole MOXIE run.

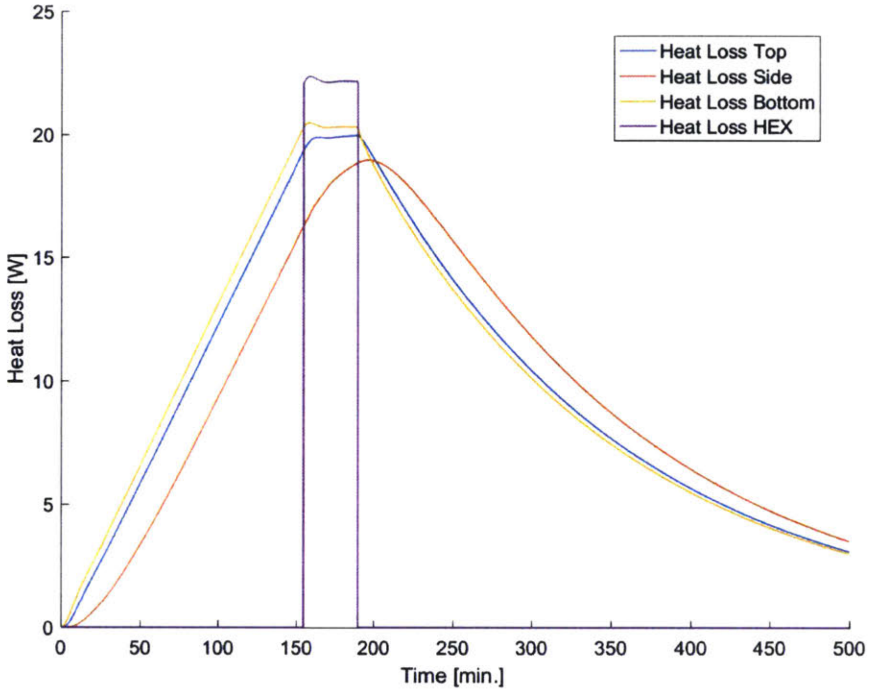

Figure 72 – SOXE heat loss paths over a full MOXE run

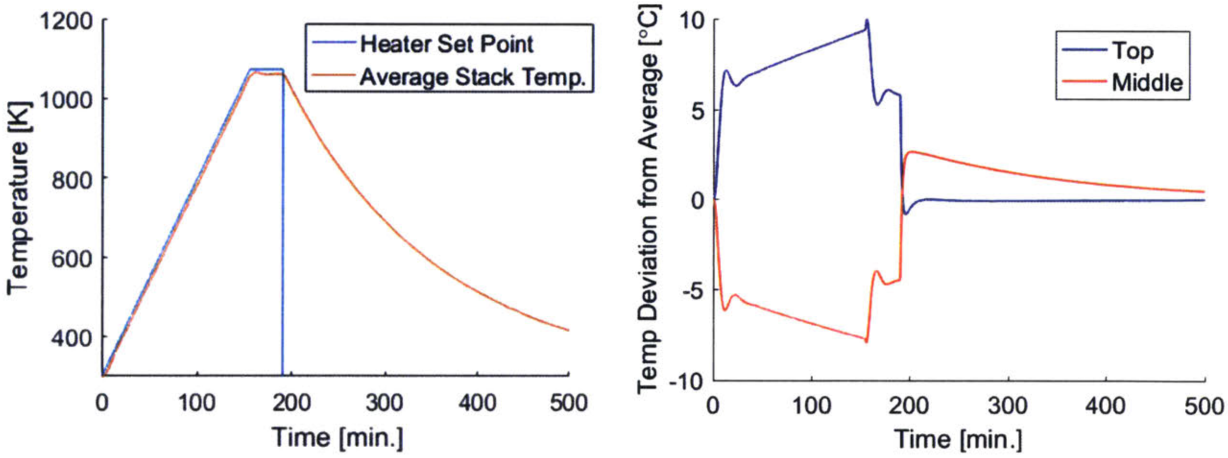

Figure 73 – Simulated average stack temperature and cell variation during a full MOXIE run

By connecting the thermal domain to the electrochemical model, SimSitu can also model the interactions between these two systems. The voltage losses in the electrochemical domain are influenced by temperatures defined by the thermal domain. The electrochemical domain alters the thermal system by consuming heat during a typically endothermic reaction.

5.5 Pneumatic domain

The pneumatic domain includes the scroll pump, flow system, and gas heat exchangers. It is modeled as a compressible pneumatic fluid in Simscape. There is a separate pneumatic system for the CO_2/CO line and the O_2 line. All pressure sensors are mapped to the same locations as on the MOXIE system. Figure 74 below shows the pneumatic domain for the CO_2/CO and O_2 lines.

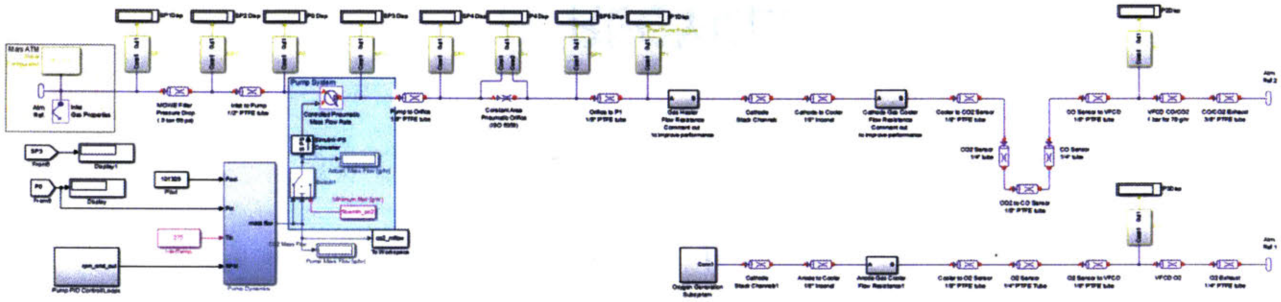

Figure 74 – Pneumatic domain system

The source gas composition is defined by the inlet gas specific heat at constant pressure, specific heat at constant volume, dynamic viscosity, ambient pressure of Mars, and ambient temperature. The Reynolds number for the upper bounds of laminar flow is assumed to be 2000. In laminar flow conditions, the pressure drop through a section of pipe is calculated using the Hagen-Poiseuille equation. The viscous flow control devices (VFCDs) are also modeled using the Hagen-Poiseuille equation with additional resistance added as additional equivalent length to match the empirical flow resistance of these devices.

The scroll pump (Figure 75) is the heart of the pneumatic domain. This device volumetrically compresses inlet air through a series of involutes.

Figure 75 – Rendering of the MOXIE scroll pump

An ideal mass flow source drives atmospheric gases through the pneumatic domain. The mass flow rate is calculated as a function of inlet gas density, scroll volume, scroll speed (RPM), and scroll volumetric efficiency. Volumetric efficiency is defined as the ratio of the volume of the scroll to the volume of gas delivered to the pump outlet. Volumetric efficiency has a relationship to the differential pressure across the scroll. The pressure at the inlet of the scroll pump is determined by the flow rate and flow resistances of the filter and the inlet tube. The filter drop is estimated to be a 0.5 torr drop at a flow rate of 70 g/hr, although recent experiments suggest it may be lower. The pressure on the outlet of the pump is determined by the flow resistances of the entire MOXIE system. Figure 76 shows the system that calculates the mass flow rate based on pump RPM.

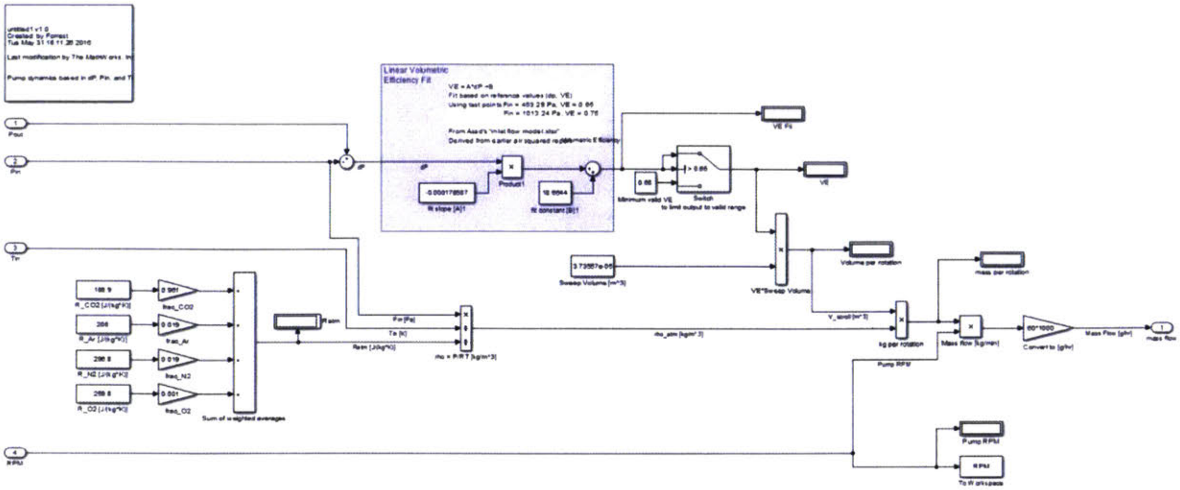

Figure 76 – Scroll pump domain system

5.6 Combined thermal electrochemical domain

The key advantage of the SimSitu multi-domain physical system model is the ability to pass energy between domains with bi-directional connections. Figure 77 below shows how the thermal and electrochemical systems are linked to create a unified model.

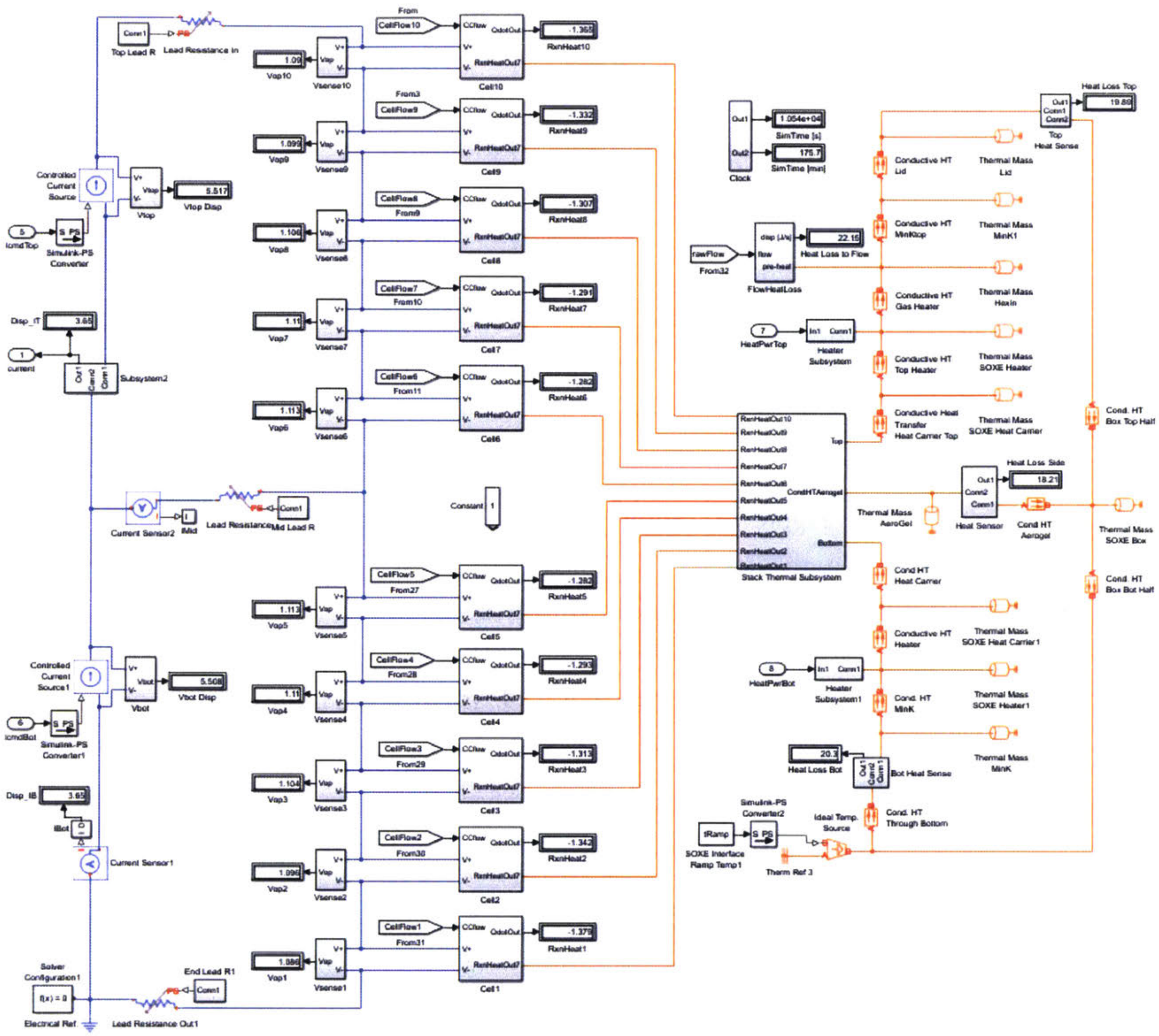

Figure 77 – Multi-domain electrochemical (blue lines) and thermal (orange lines) system

The model can now demonstrate individual cell voltages by factoring in cell-to-cell thermal and flow variation as defined by the MOXIE system model. The right image of Figure 78 shows individual cell voltages for a current controlled MOXIE. The left image of Figure 78 shows the voltage response including temperature variation and a maximum cell-to-cell flow variation of up to 60%.

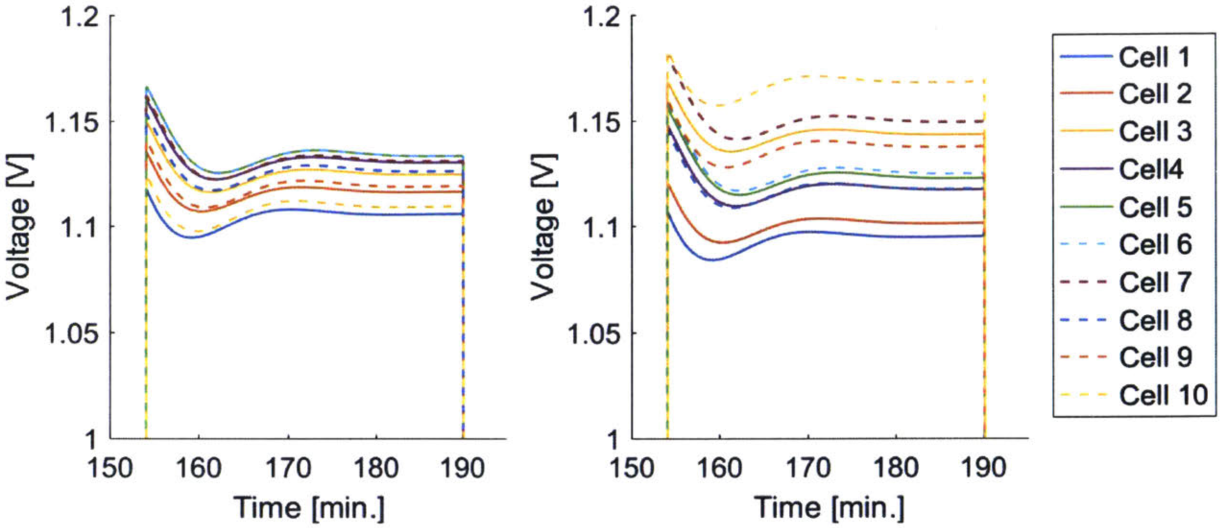

Figure 78 – Standard run voltage response with temperature variation (left) and including flow variation (right)

These variations in cell voltages are important to model when testing control systems that are designed to avoid degredation conditions such as coking. The experimental work in Chapter 4 discovered that these limits are best avoided by limiting voltage of the worst performing cell to below the threshold where it is thermodynamically possible to form carbon. The flight stack will only have voltage monitoring on 5-cell groups so the SimSitu model will be needed to make up that gap in knowledge during operation. Several potential control strategies are demonstrated in the following section.

5.7 Control system analysis and demonstration

5.7.1 MOXIE System Theoretic Process (STPA) analysis

System Theoretic Process Analysis (STPA) is a system safety methodology developed by Leveson (2011). The methodology was applied to MOXIE to study the system at various stages, but the analysis is outside of the scope of this thesis. Below is a partial STPA analysis of four SOXE control methodologies. The goal of this analysis is to identify high level recommendations for the control system. The following section will demonstrate these controllers using the SimSitu program.

5.7.1.1 STPA Step 1 analysis of SOXE production controller scenario

The high-level SOXE control structure, including the controller, actuator, possible sensors, and process of the SOXE system is shown in Figure 79.

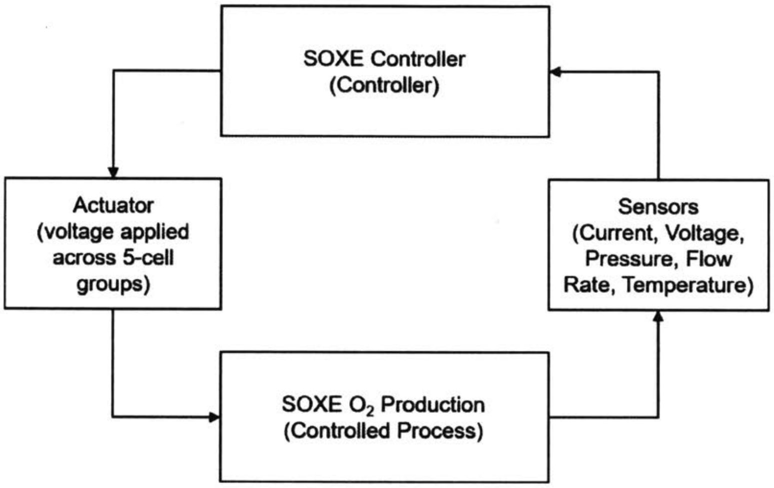

Figure 79 – High level control structure of SOXE production control

The SOXE production process is directly acted upon by voltage controllers. A cascaded control strategy is used to alter the voltage set point to achieve SOXE control by different parameters. The baseline control for O_2 production on MOXIE is a cascaded current control strategy. A current set point is specified and the voltage output from a PI controller is adjusted in order to reduce the error between the current set point and the current measurement sensor. Other potential control methods investigated in this chapter include: direct voltage control, cascaded utilization control, and the novel Safe Margin Active Reduction Tracking (SMART) control, which actively calculates a control set point to maintain the stack at a constant voltage margin below the hazardous CO-C Nernst potential. Table 16 examines the hazards of these types of controls when implemented on the SOXE.

Table 16 – Hazardous system behavior relating to the SOXE control type

Control Action	Not Providing Causes Hazard	Providing Causes Hazard	Wrong Timing or Order	Stopped Too Soon or Applied Too Long

Cascaded current control	Hazardous if flow is on and SOXE is hot	Hazardous if: 1. cell-to-cell variability is greater than expected 2. cell resistance is higher than expected from • Degradation • Low stack temperature 3. coking threshold is lower than expended from • High pressure • Low stack temperature	--	Too long: Hazardous if operation time degradation leads to voltage increase and further degradation
Direct voltage control	Hazardous if flow is on and SOXE is hot	Hazardous if: 1. cell-to-cell variability is greater than expected 2. coking threshold is lower than expended from • High pressure • Low stack temperature	--	Too long: Not Hazardous Operation time degradation would decrease current production, as voltage is constant
Utilization control	Hazardous if flow is on and SOXE is hot	Hazardous if: 1. cell-to-cell variability is greater than expected 2. flow is higher than expected	--	Too long: Hazardous if operation time degradation leads to voltage increase to maintain utilization, leading to further degradation
CO-C Nernst potential control	Hazardous if flow is on and SOXE is hot	Hazardous if: 1. cell-to-cell variability is greater than expected	--	Too long: Not Hazardous Operation time degradation would decrease current production, as voltage is held constant

The results of this analysis show that all control modes have a risk of oxidation if the control mode never initializes. Current control has the most potentially hazardous states because this control mode does not actively adapt to hazardous, voltage-determined coking risks. If degradation occurs, a current controller will increase the command voltage to maintain a steady current, which may result in voltages reaching the region where coking is possible. Utilization control uses flow rate and current to calculate utilization, which gives it some robustness to flow variations and start/stop cycles but may still encounter problems if cell resistance increases and total voltage climbs. Direct voltage control maintains voltage so that if performance declines, current and O_2 production declines with it. This helps prevent a positive feedback loop seen in current control that can increase degradation. CO-C Nernst voltage control (SMART) is a voltage control mode that maintains the voltage below a margin based on the calculated CO-C Nernst potential that is believed to represent the boundary for coking. This calculation factors in pressure, flow, and temperature effects and is the most robust to hazards.

The following control modes are hazardous under these conditions:

1. Any type of SOXE control not powering SOXE under hot flow conditions
    - Oxidation hazard due to flowing CO_2 without CO over a hot SOXE
2. Current, voltage, utilization, or CO-C Nernst control if cell-to-cell variability is greater than expected
    - Coking hazard due to voltage of a single cell exceeding CO-C Nernst
3. Current or voltage control if coking threshold (CO-C Nernst) is lower than expected due to
    a. High pressure
    b. Low stack temperature
        - Coking hazard due to voltage exceeding CO-C Nernst
4. Current or utilization control too long if voltage creep occurs due to operation time degradation
    - Coking hazard due to high voltage
5. Current control if cell resistance is higher than expected due to degradation
    a. Cycle-to-cycle degradation
    b. Low stack temperature
    - Coking hazard due to high voltage

Safety constraints (requirements) that can be derived from this analysis include:

1. SOXE power must be on during hot flow conditions

2. Cell-to-cell voltages and variability should be monitored to avoid uncertainty
3. Current and voltage control should respond to pressure and temperature effects that alter the CO-C Nernst potential
4. Current and utilization control should be stopped or set points lowered if voltage rise is detected
5. Current control mode should not be activated when stack temperature is below planned temperature or temperature is uncertain.
6. Control strategy should account for increased cell resistance at low temperatures and have either appropriate margin, or actively adjust to the lower coking threshold at low temperatures

5.7.2 Control system demonstration

The baseline SOXE control strategy is a cascaded current controller. The outer current loop sets a current command and compares it to the current measurement of the SOXE stack. The error term is a discrete signal passed to a PI controller. The output of the current PI controller is a voltage set point that is summed to an initial voltage offset value. The output of the current PI controller is limited by a saturation block, and back calculation is implemented to reduce integrator wind-up. The inner loop is a controller that applies voltage across 5-cells of the stack. Figure 80 is an example of this control layout.

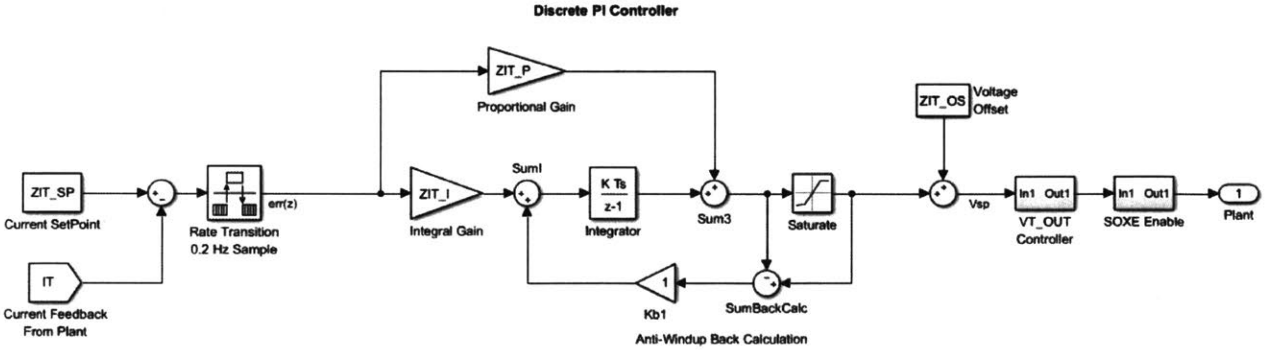

Figure 80 – Cascaded current control system

The cascaded controller includes a lower sample rate for the outer current control loop. The MOXIE control system operates at a frequency of 1 Hz. In the example shown here, the outer loop samples and executes at a slower rate of 0.2 Hz. The stack current response, as it steps to a set point of 3.65 A, is shown in Figure 81.

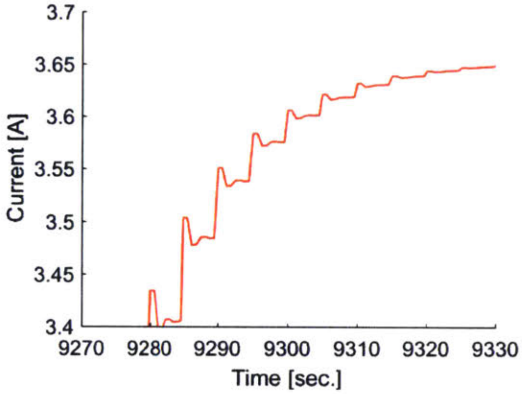

Figure 81 – Simulated stack current response to descrete steps of cascaded current controller

A full MOXIE run was simulated with 155-minute pre-heat and a 35-minute electrolysis run. To simulate the controller response to thermal transients, the current was switched on early, when the heater temperature reached 797 °C. Figure 82 shows the response of the cascaded current controller as the temperature stabilizes to 800 °C and adjusts to the thermal transients at the start of the reaction.

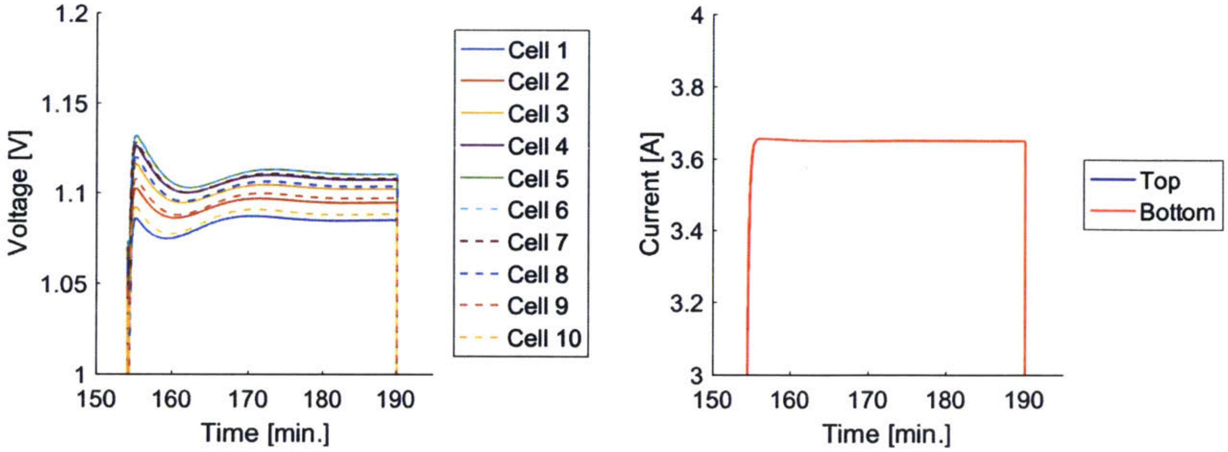

Figure 82 – Response to cascaded current control

In current control mode, the cell voltages reflect the thermal transients. The spike from turning on the stack slightly early highlights a risk of current control for MOXIE. If electrolysis begins before temperatures have stabilized, it may be possible for voltages to spike into a region that may cause damage due to coking. Other thermal or flow transients that occur during operation may also cause voltage fluctuation into regions where degradation is likely. To safely implement a current control scheme, an increased safety margin, over what is required for a voltage control scheme, would be needed.

Direct voltage control is an alternative control scheme discussed in the STPA analysis of chapter 5. Figure 83 shows the control schematic of a continuous PID voltage controller for MOXIE.

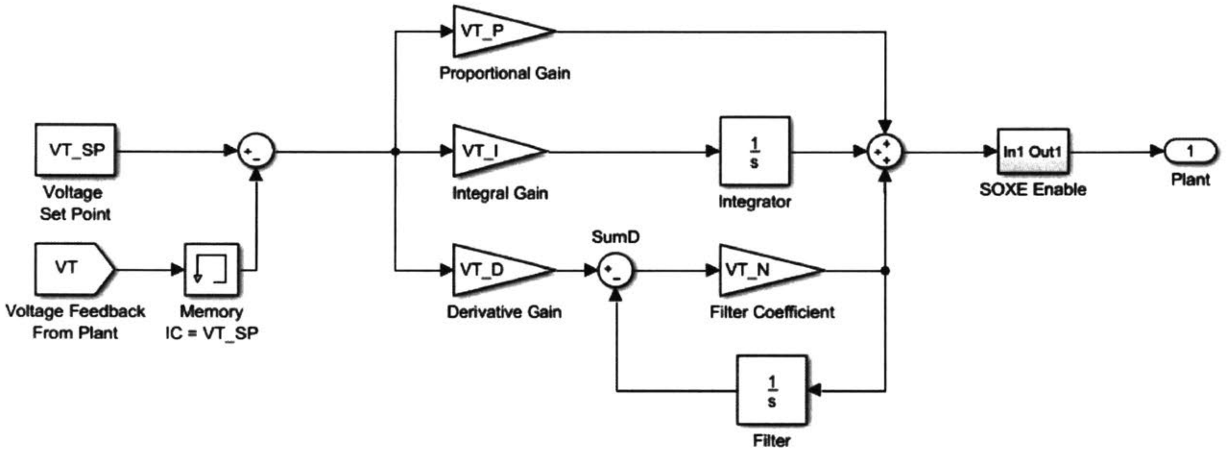

Figure 83 – Voltage controller

The voltage controller was simulated under the same conditions as the cascaded current controller. The voltage set point was 5.5 V (1.1 V per cell) for the top and bottom voltage controllers. The response is shown in Figure 84.

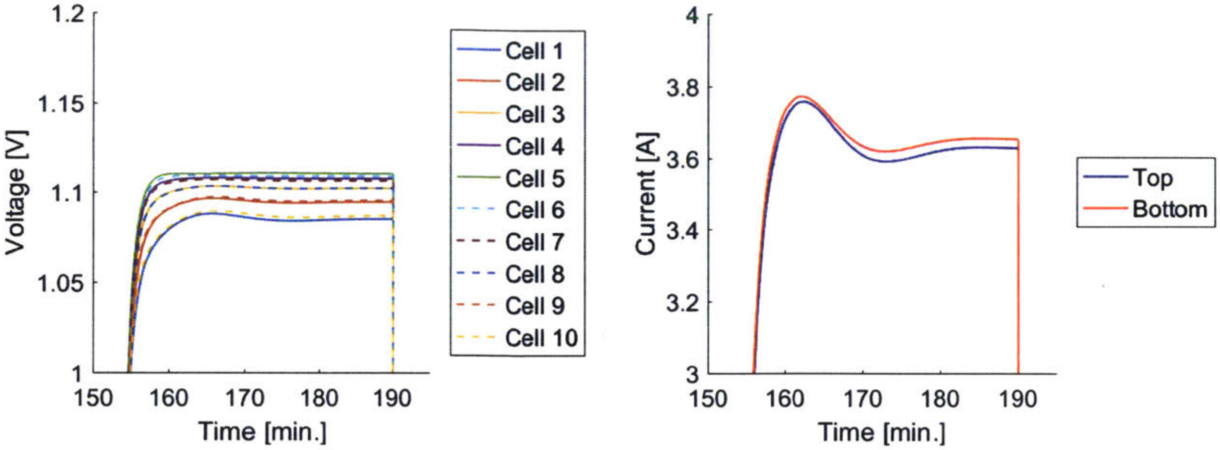

Figure 84 – Voltage control response

The advantage of this type of controller is that there are no voltage spikes due to thermal transients. Some individual voltages reach steady state conditions above 1.1 V due to cell-to-cell temperature variation but there are no upward spikes. Instead, the current fluctuates as the temperature varies cell resistance. An interesting effect of this control mode is that the top and bottom 5-cell stack currents vary slightly due to the slight differences in net resistance of the top and bottom cell groups. Most of the current flows from the top 5-cell stack grouping through the bottom resulting in low currents through the midplate leads. Figure 85 shows the current variation through the midplate over time in response to resistance differences in the top and bottom stacks.

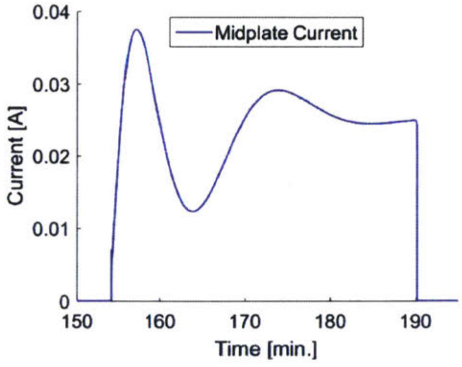

Figure 85 – Midplate current response

SimSitu provides utility for testing alternative control modes. Utilization control was proposed in the STPA analysis of Chapter 5, because it reduces some hazards associated with flow variation and unexpectedly low cell resistance. This type of controller adjusts the voltage set point based on the calculated average utilization of the stack. The utilization can be calculated using feedback from the current and flow sensors of MOXIE and the analytical relationships established in Chapter 3. If we assume the example of a current control scenario where a stack is operating at 3.82 A, with a flow of 80 g/hr. The corresponding utilization is 40% and the CO-C Nernst potential is 1.11 V per cell. Assume that a voltage saturation is used to limit the voltage to 1.09 V per cell for margin. If the flow of the system decreases to 50 g/hr, at constant current operation (3.82 A), the utilization would then be 64% with a corresponding CO-C Nernst of 1.088 V. The voltage controller would now allow the cells to exceed the limit. Under a utilization control scenario, the CO-C Nernst potential would be constant and voltage saturations would not need to be changed for a run, regardless of changes in flow condition.

The design of this controller, as tested in the model, is shown in Figure 86.

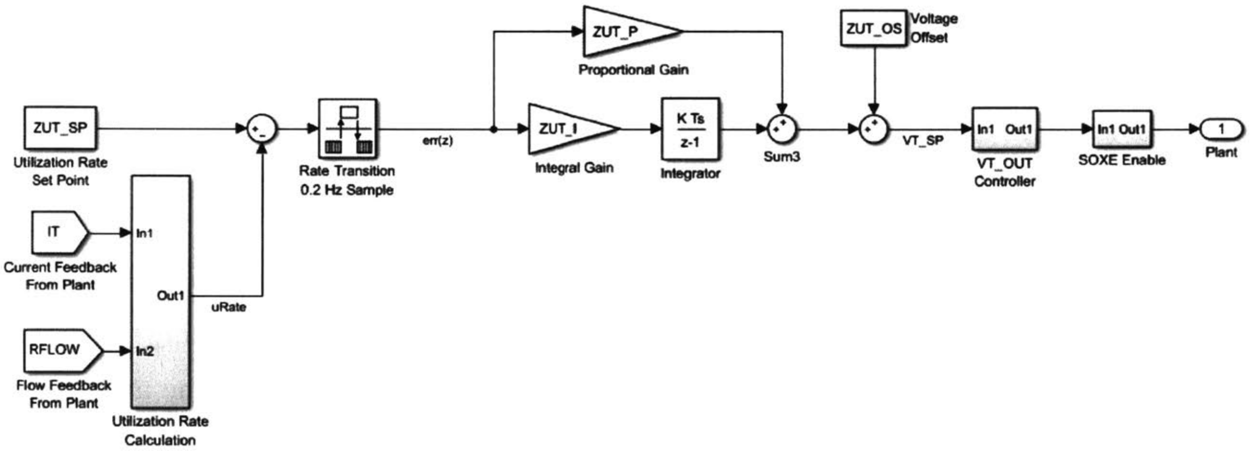

Figure 86 - Cascaded utilization control scheme

This controller was tested for the same MOXIE run profile as the previous two. The utilization was set to 30%. The sample frequency for the outer loop is 0.2 Hz. The controller response is shown in Figure 87.

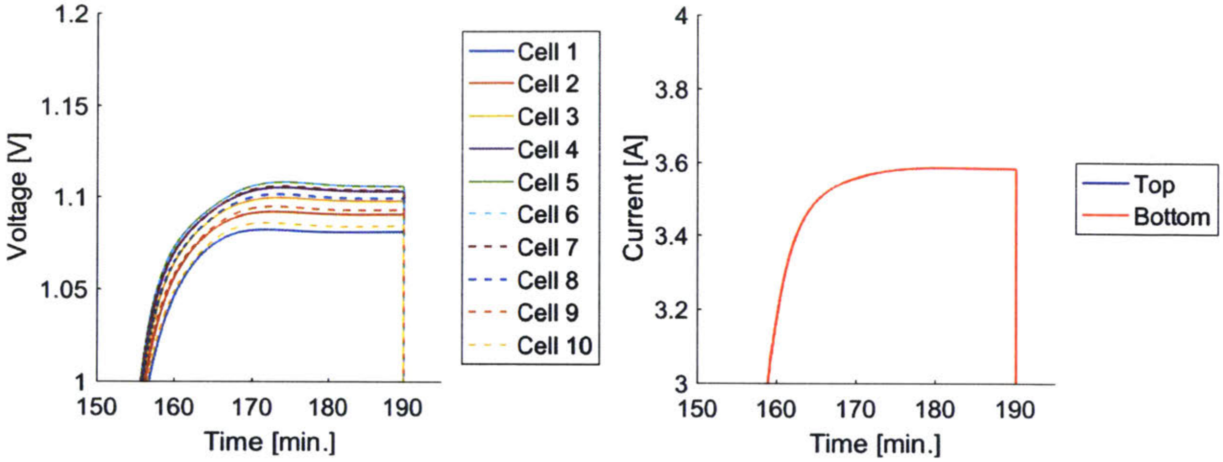

Figure 87 – Utilization control

The cascaded utilization control tested here demonstrates a slower rise time but also a more stable response in voltage and current. Because the CO-C Nernst potential is constant across a given utilization, a utilization control combined with a voltage saturation limits may be a robust strategy to operate the SOXE when thermal and flow fluctuations are present.

5.8 Safe Margin Active Reduction Tracking (SMART) controller

The Safe Margin Active Reduction Tracking (SMART) control algorithm was conceived based on lessons learned mapping the coking threshold of SOXE stacks in Chapter 4. The coking threshold was observed to follow the CO-C Nernst potential. The strategy employed to map the maximum performance by never exceeding the potential required to reduce CO to carbon. Chapter 5 explored this type of control using STPA and determined that it was the least hazardous method to control the SOXE. The SMART controller was designed and tested in the SimSitu model of MOXIE. The control design is shown in Figure 88.

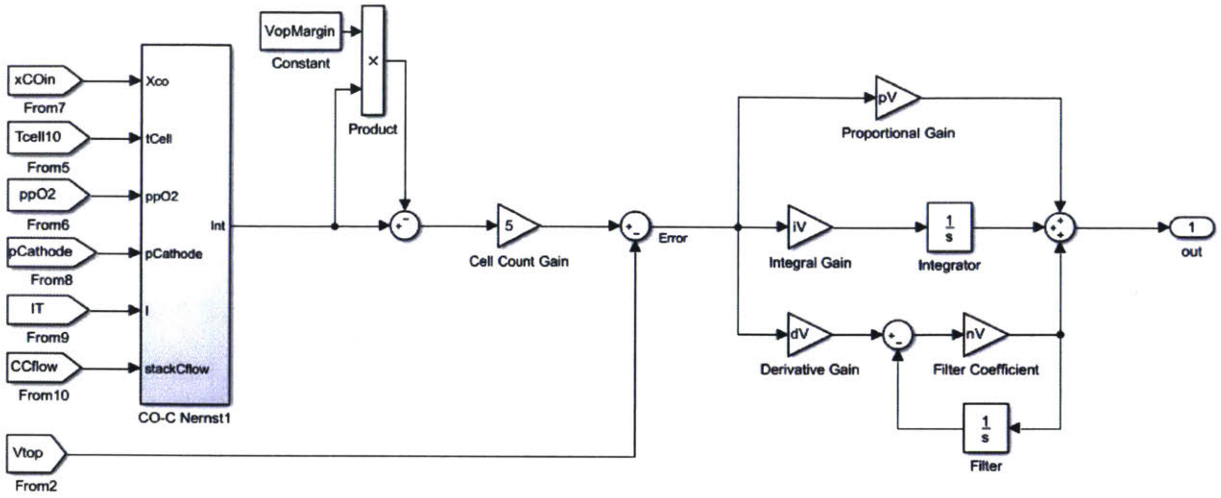

Figure 88 – Safe margin active reduction tracking (SMART) control design

The SMART controller incorporates an actively adapted set point that a margin below the CO-C Nernst potential. It uses sensors available on MOXIE to calculate the CO-C Nernst potential at any condition. The set point calculator is shown in Figure 89.

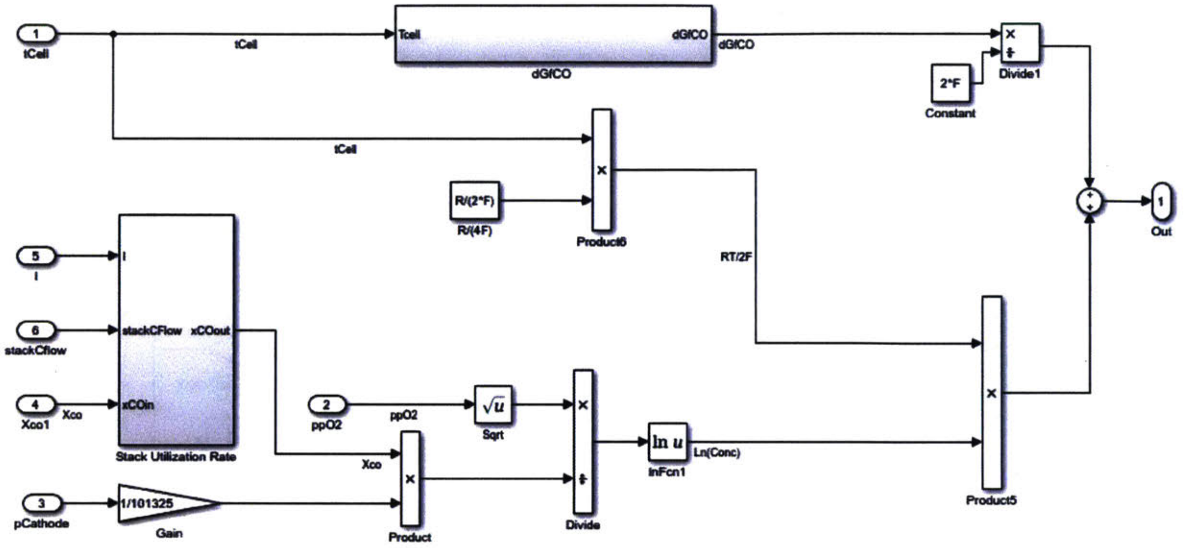

Figure 89 – CO-C Nernst potential calculator for SMART controller

The result is a controller that actively avoids coking by maintaining a margin of separation between the operating voltage and the coking potential. In addition to providing safe operation, this controller enables higher oxygen production rates because there is less uncertainty between the operating point and the threshold for cell degradation. Figure 90 shows the response of this controller to the same conditions as the previous controllers.

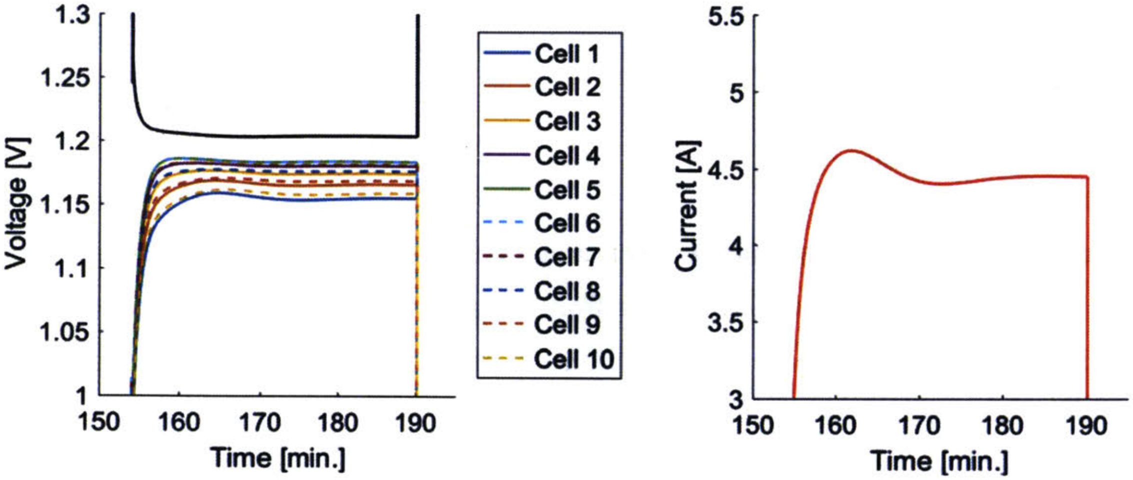

Figure 90 – Cell voltage and current response to the SMART controller

The baseline cascaded current control method and the SMART controller were run in a dynamic simulation with a flow of 45 g/hr with a 20% anode pressure fluctuation. The controllers were started when the top cell temperature reached 797 °C to simulate an early turn on due to a slow heating cycle. The results are shown in Figure 91.

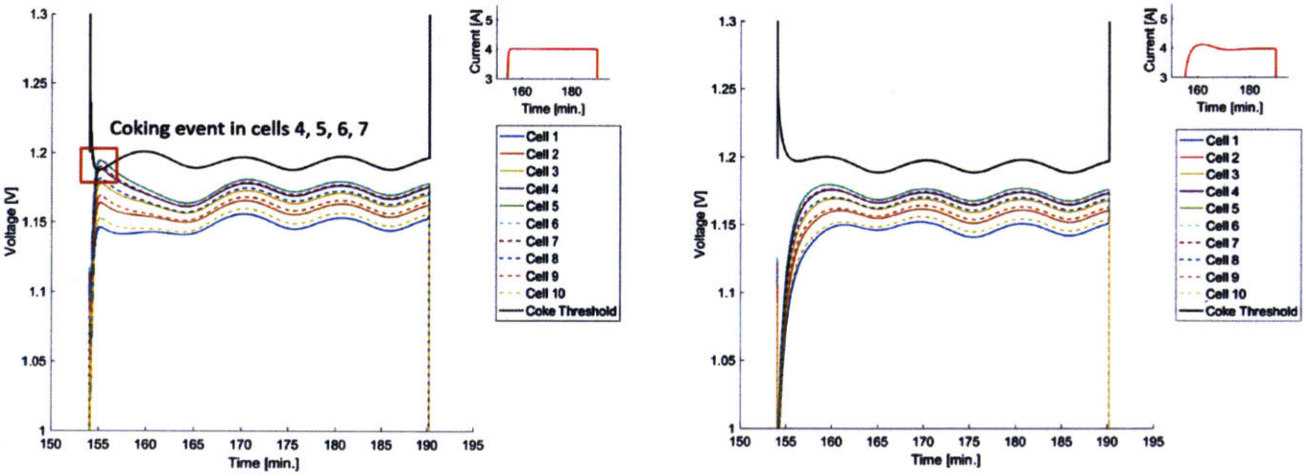

Figure 91 – Cascaded current control (Left) and SMART controller (Right)

During the simulation 4 cells of the cascaded current controller experienced a coking event. The SMART controller maintained a safe margin for the cell voltages during the whole simulation.

This is just one of many examples the MOXIE control improvements that are gained by implementing the SMART controller.

5.8.1 Recommendations

Implement a soft fault recovery mode when a sudden intrinsic ASR (conversion corrected ASR) increase is detected. Characterization from Chapter 4 indicated that some performance recovery is possible in the event of degradation due to coking. When a degradation event is detected that may be the result of carbon formation, the system should be placed into low utilization operating mode until the end of the run instead of defaulting directly to the idle (pump off, SOXE off, heat off) mode. It has yet to be characterized whether any recovery is possible after shutting off the SOXE, and such characterization is recommended as the next experimental step.

Implement voltage control that ideally tracks the CO-C Nernst potential. Current control was identified as one of the highest risk control strategies based on the potential for voltage to reach unsafe values. Current control also feeds degradation after onset by increasing voltage to maintain a constant current. The voltages can be limited through use of a saturation on the cascaded current-voltage controller; however, safe voltages vary significantly depending on operating pressures, temperatures, flows, and currents (utilizations). For this reason, extremely restrictive voltage limits would be needed. A CO-C Nernst potential tracking voltage controller that maintains separation between the operating voltage and the CO-C Nernst potential would help maintain safety while maximizing production. This controller is designed and implemented in Chapter 5 and is called the Safe Margin Active Reduction Tracking (SMART) controller because it tracks the reduction potential of CO to C and maintains the voltage set points below that level with some margin.

5.9 Chapter summary and conclusion

Chapter 5 presented the tunable, grey SOXE model, including the thermal and control domains that comprise SimSitu, the multi-domain physical model of MOXIE. Major system discoveries were described as part of the development of the electrochemical model. In Chapter 4 ASR variation in SOXE ASR was discovered to only be significant at low flow rates. For this reason, cell-to-cell performance differences in Chapter 4 testing were attributed to flow distribution. The electrochemical model in Chapter 5 showed that cells that received less flow operated at a higher utilization than other cells in the series, resulting in a higher integral average Nernst potential. The Nernst potential conversion correction accounted for the differences in ASR at different flow rates. The Arrhenius equation was used to derive the temperature dependence of the cell ionic resistance. The activation potential was also characterized. The electrochemical model was then compared to real data for varying flow rates and temperatures and was shown to be superior to the project Figure of Merit model assumed for the SOXE stack. A lumped parameter thermal network model was developed and tuned to the characterization results from SOXE thermal characterization. The pneumatic system was described. Chapter 5 elaborated upon the control domain of the model and baseline controls demonstrated. The utility of the model was also demonstrated with voltage and utilization control methods. The SMART control system was developed to actively keep the average stack voltage a safe margin below the CO-C Nernst potential. This control method is proposed for MOXIE operation as well as for operation of extensible systems. Chapter 7 applies this control method to determine the maximum production and mass requirements of a solid oxide electrolysis system for human mission scale Mars ISRU.

6. MOXIE Extensibility to Support Crewed Mars Missions

Extensibility is a property of an engineering design that enables it to be implemented on a larger scale. From the perspective of the development of MOXIE, extensibility refers to scaling the technology to support a crewed mission to Mars. Most MOXIE design decisions were made with the goal of designing the most extensible atmospheric ISRU system possible. However, some Mars 2020 mission constraints lead to differences between MOXIE and a crewed mission ISRU system. Differences between MOXIE and a full-scale system include that a full-scale system will:

1. Have few on/off cycles resulting in reduced SOXE cycling degradation
2. Be thermally coupled primarily to the Mars environment or a nuclear reactor instead of a rover system
3. Endure a significantly longer total operation time which may result in additional degradation of filters, pumps, and long term SOXE degradation modes
4. Have increased computational and sensor capability for system control
5. Prioritize total oxygen production over peak rate

These differences influence final system design but are only a minor impact on what we can learn from MOXIE. Most of the implementation challenges become easier as MOXIE is scaled up. MOXIE is volume limited. As MOXIE is scaled up, the ratio between SOXE mass and insulation packaging is expected to improve. The mass and volume of the control system and computer will scale slower than the electrolysis system mass. Options for atmospheric acquisition also improve as the system is scaled. One area that may become more challenging as the system scales is ensuring that the full-scale system is robust against long-term degradation. However, some mitigation strategies that are unavailable to MOXIE due to its mass and volume constraints may become available at a larger scale. These strategies may include the use of self-cleaning dust filters, hydrogen for cell regeneration, stored CO to reduce start-up oxidation, H_2O co-electrolysis, spare pump capacity and advanced autonomy.

6.1 Introduction

This chapter applies the contributions of the previous chapters of this thesis to develop new insights and recommendations for developing a full-scale atmospheric ISRU system to support a crewed

Mars mission. This chapter addresses the system scaling based on the electrochemical component of the SimSitu MOXIE model and the SMART control system developed in Chapter 5. The primary design trade is between supplied flow rate and minimum SOXE cell count required to produce a minimum oxygen production rate of 2 kg/hr. This design trade is introduced with a pressure and temperature sensitivity analysis, followed by trades based on potential improvements in SOXE cell technology. Next, the effects of some of these values on system mass and power are explored.

6.2 Requirements development and general scaling laws

6.2.1 Oxygen production rate

The O_2 production rate used for scaling MOXIE for a crewed mission is based on the NASA Mars mission from Design Reference Mission 5 (DRM 5) authored by Drake (2009) and the subsequent addendums (Mars Architecture Steering Group 2009, Drake and Watts 2014). In DRM 5, an atmospheric ISRU system is to be sent a Mars launch opportunity ahead of the crew, approximately 26 months. After the ISRU spacecraft completes transit and lands, it begins oxygen production at a rate necessary to fill the Mars Ascent Vehicle (MAV) with liquid oxygen (LOX). Only after the MAV is confirmed to be full of oxygen, would a crew leave Earth. See Chapter 2 for an elaborated description of DRM 5. The time available for oxygen production is based on assumed values by Kleinhenz and Paz (2017). Their trade study allocated a maximum of 9 months for transit and 1 month for transit margin and system setup, leaving 16 months (480 days) available for oxygen production to complete production before the crew leaves Earth. It would also be possible to send a smaller system with a lower production rate 2 launch opportunities before the crewed launch and still achieve the mission goals but this option has yet to be thoroughly examined. Table 17 describes the propellant requirement for three mission architectures, and the production rate requirement given 480 days of production.

Table 17 – MAV Oxygen ISRU total production and rate requirements

	Total Propellant [kg]	O2 Req. [kg]	Rate Req. [kg/hr]
4 Crew Member MAV with 250 lb Payload (Drake and Watts 2014)			
1st Stage Propellant	18861	14670	
2nd Stage Propellant	4106	3194	
Total	22967	17863	**1.55**
6 Crew Members MAV (Drake and Watts 2014)			
1st Stage Propellant	18119	13906	
2nd Stage Propellant	12544	9627	
Total	30663	23532	**2.04**
4 Crew Member MAV (Polsgrove, Thomas et al. 2015)			
1st Stage Propellant	20278	15681	
2nd Stage Propellant	9377	7036	
Total	29655	22717	**1.97**

The requirements for the MAV architectures above assume a LOX/LCH$_4$ powered, two phase to orbit (TPTO) rocket design. Crew size varies between 4-6 crewmembers. The calculated required O$_2$ production rate ranged between 1.55 and 2.04 kg/hr. Due to uncertainty in the final MAV design, the system scaling in this chapter assumes a 2 kg/hr production rate. Additional oxygen may be required due to O$_2$ boil off. The following trades do not include added margin for oxygen loss or system inefficiencies.

6.2.2 Solid oxide electrolysis cell size

A solid oxide electrolysis cell with an active area of 100 cm^2 was selected. The largest available externally cell interconnect size with an external manifold has a 127 cm^2 active area and is manufactured by Plansee (Megel, Kusnezoff et al. 2011). The 100 cm^2 area assumes that an internal manifold would reduce the active area from what is currently available with external manifolds. A rendering of a notional cell interconnect designed to illustrate this chapter's crewed mission scale system is the left interconnect depicted in Figure 92 below.

Figure 92 – A notional crewed mission scale SOXE interconnect with an active area of 100 cm^2 (left) compared to a MOXIE cell with an active area of 22.74 cm^2 (right)

The 100 cm^2 extensible reference cell is over four times the area of the 22.74 cm^2 active area of a cell in MOXIE. Larger cells are desirable over smaller cells because they have a reduced mass per unit area by increasing the active area to perimeter ratio. The cell perimeter is heavier due to seals and extra material and does not contribute to production. Larger cells also require less voltage to drive the same current through a stack. Some limitations on cell size include variations in the flatness of the cells and interconnect and size limitations for manufacturing interconnects that are comprised of a material that is heat resistant and has a coefficient of thermal expansion matched to the electrolyte.

6.3 Sensitivity analysis and impact on system design

The solid oxide electrolysis technology developed for MOXIE has been demonstrated to be readily scalable by adjusting the cell area, number of cells, and cell groupings (stacks). The electrochemical portion of the SimSitu model was incorporated into a scaling spreadsheet in Microsoft Excel. The model assumes the performance of SOXE stack CSA 005 as characterized in Chapter 4. A cell area of 100 cm^2 was assumed along with an O_2 production rate requirement of 2.0 kg/hr. The model also assumes a 2% molar flow of CO in the inlet stream from recirculated gas to avoid oxidation of the cathode. A GRG Nonlinear Solver was used to minimize the number of cells needed to meet the production requirement by increasing cell current, subject to the constraint that the operation voltage would not exceed the CO-C Nernst potential. The results show the minimum stack cell count needed to achieve the production required while operating under a control system like the SMART control strategy proposed in Chapter 5 (except with zero margin between the operating voltage and coke threshold). System designers may add additional margin to the results of the trade study as necessary. Table 18 shows the primary variables used in in the model.

Table 18 – Primary variables used in electrolysis system scaling program

Independent Variables	Units	Dependent Variables	Units
Fixed Independent Variables:		Cost Function:	
Oxygen Production Rate	kg/hr	Number of Cells	1
Cell Area	cm^2	Constraint: $V_{op} <= V_{CO\text{-}C,\ Nernst}$	
Other Independent Variables		V_{op}	V
Cell Current	A	$V_{CO\text{-}C,\ Nernst}$	V
Mars Atmosphere flow in	kg/hr	Other Dependent Variables	
Cathode Pressure	atm	$V_{CO2\text{-}Co,\ Ave.\ Nernst}$	V
Anode Pressure	atm	V_{act}	V
Operating Temperature	K	V_{ohmic}	V
Cell Sensitivity Terms:		V_{tn}	V
-Activation Potential	%	CO_2 Utilization	%
-Electrolyte Ohmic Resistance	%	Stack Power	W
-Activation Energy	%	Stack Power with Make-up heat	W
		SOXE System Mass	kg

6.3.1 Feed gas flow rate and pressure effects

Mars atmosphere mass flow rate was varied to calculate the minimum cell count needed to achieve an oxygen production rate of 2 kg/hr. The CO_2 utilization that the extensible model must achieve is calculated by the CO_2 flow rate delivered to the electrolysis system and the required percentage of CO_2 that must be electrolyzed to achieve minimum production. Lower current densities can safely achieve the higher utilizations because lower currents induce less ohmic potential drop across the cell electrolyte. Current is directly proportional to oxygen production; therefore, more cells are needed to produce the same amount of oxygen at a lower stack current. Figure 93 shows the relationship between Mars atmospheric supply flow, the utilization to meet production requirements, and the maximum safe current. Higher supply flow rates consume more energy and required larger equipment, while lower flow rates require higher utilizations to meet the oxygen production goals.

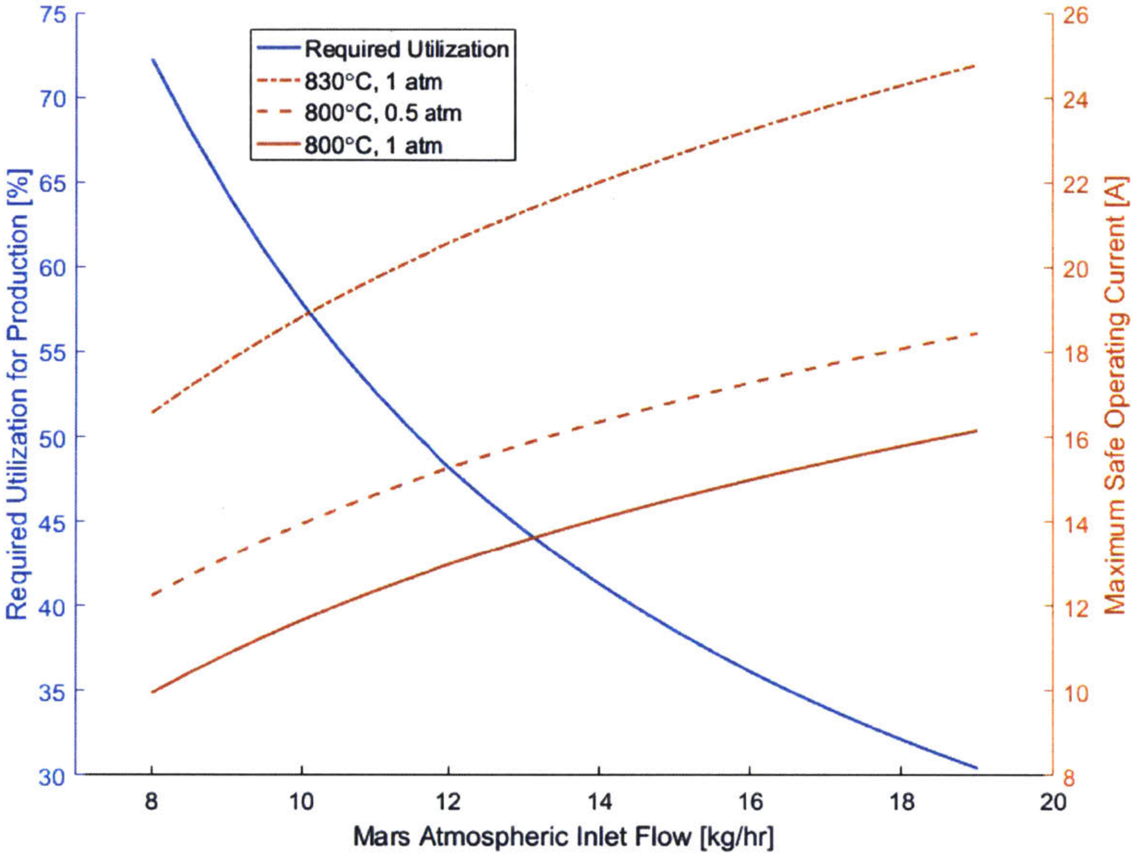

Figure 93 – Required utilization and maximum safe cell current for different supply flow rates

In Figure 93, the simulation assumed three different operating conditions: a standard run at temperature of 800 °C and pressure of 1 atm, an elevated temperature run at 830 °C and 1 atm, and a reduced pressure run at 800 °C and 0.5 atm. The maximum safe operating current increases as the required target utilization decreases. It also improves as temperature increases and as operating pressure decreases.

Figure 94 illustrates the effect of operating pressure on the minimum cell count requirements. The CO_2 electrolysis process does not require Earth atmospheric pressure to operate. An Earth atmosphere is typically specified as the baseline operating pressure for the cathode because of the ease of testing on Earth. However, testing of the cells at Ceramatec Inc. was conducted at the local ambient pressure of about 0.87 atm. The lowest pressure achievable for the full system would likely be limited by the pressure drop required to drive the desired mass flow rate through the system. The interplay between gas density, minimum mass flow rate, the gas velocity required to achieve that flow rate, and the pressure drop required to drive it though a system is a study of importance beyond the scope of this thesis. This thesis assumes 0.1 bar as a reasonable lower limit for pressure of an extensible system.

The pressure effects are significant. As the operating pressure is decreased, the CO-C Nernst potential, that is a boundary for possible carbon formation, increases. This additional voltage headroom result in higher safe operating currents. Fewer cells are needed as the safe operating current is increased. At an atmospheric gas flow rate of 8 kg/hr and standard operating conditions, 674 cells are required at a total mass of 221 kg. If the operating pressure is halved, only 548 cells are required at a mass of 180 kg. The minimum cell count at 0.1 atm is 382 with a mass of 125 kg.

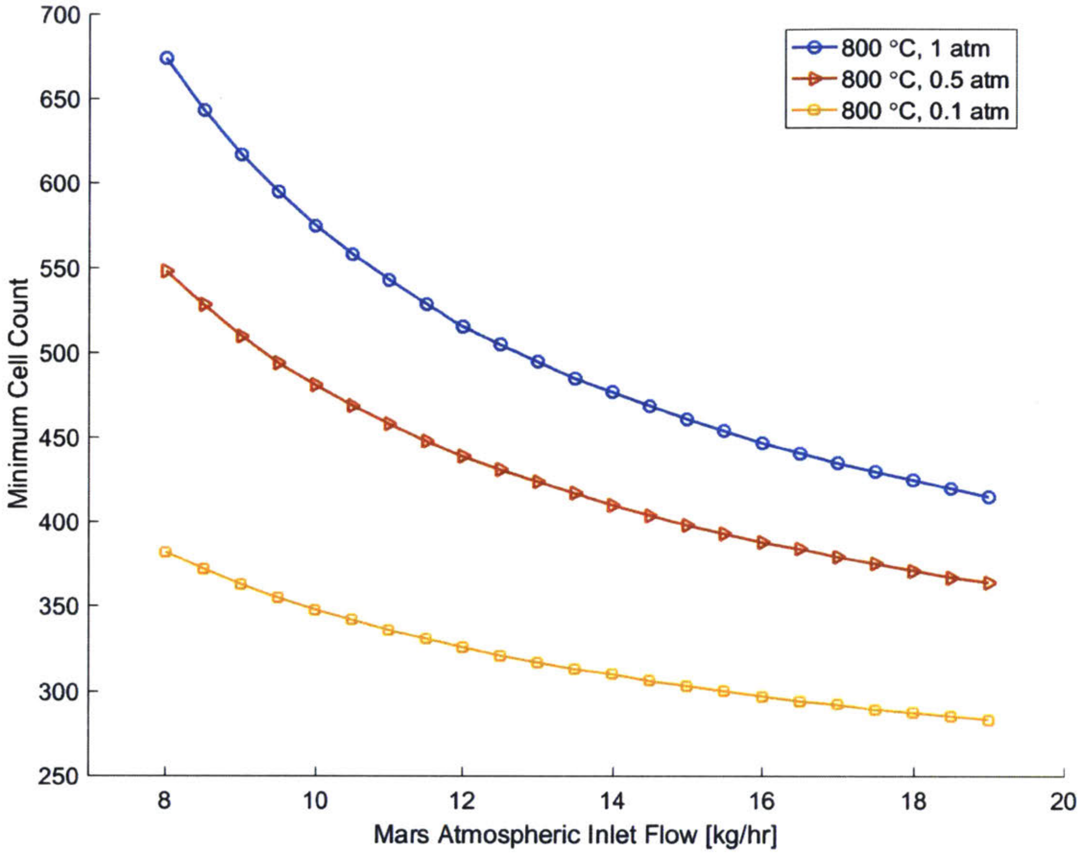

Figure 94 – The effect of operating pressure and flow rate on minimum required cell count

Operating at lower pressure saves energy that would go into compression of the Mars atmospheric gases. Additionally, it is unlikely that low-pressure cathode operation significantly lowers the pressure to which oxygen can be electrochemically compressed by the SOXE. The SOXE electrolyte can withstand a two bar pressure differential. The likely limit to anode pressures is the strength of the glass seals and compression system. The mass of the feed gases will be 4-10 times the oxygen mass. Avoiding excessive compression of feed gasses and using the SOXE for oxygen electrochemical compression has the potential to enhance system power efficiency.

6.3.2 SOE operating temperature

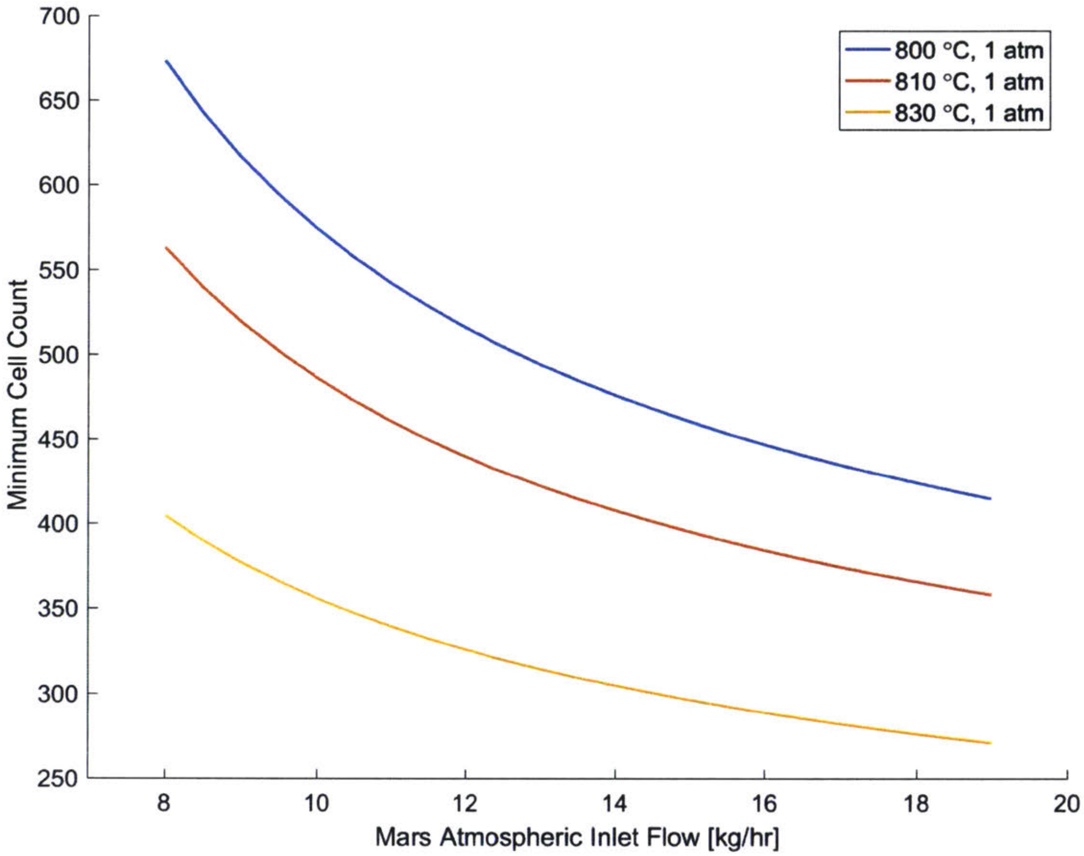

Figure 95 – Sensitivity of minimum cell count to operating temperature

It is easy to see how planned operating parameters significantly alter the requirements for the electrolysis system. Electrolysis system mass is most sensitive to many of these parameters, while total power including make-up heat for the endothermic reaction remain stable at 9.8 kW total with only a very slight sensitivity to operating temperature. For this reason, the following sensitivity analysis continues to focus on stack cell sizing based on various electrochemical performance improvements. Improvements in material properties may also lead to enhancements that can reduce the number of cells and mass required for the system. If achieved, these improvements will translate directly to increased savings in propellant to send the system to Mars.

6.3.3 SOE cell sensitivity parameters

SOE cell sensitivity parameters are incorporated into the model to predict improvements due to future advances in cell design or materials. The first parameter investigated was to increase and decrease the electrolyte thickness by 20%. Figure 96 displays the result of this trade.

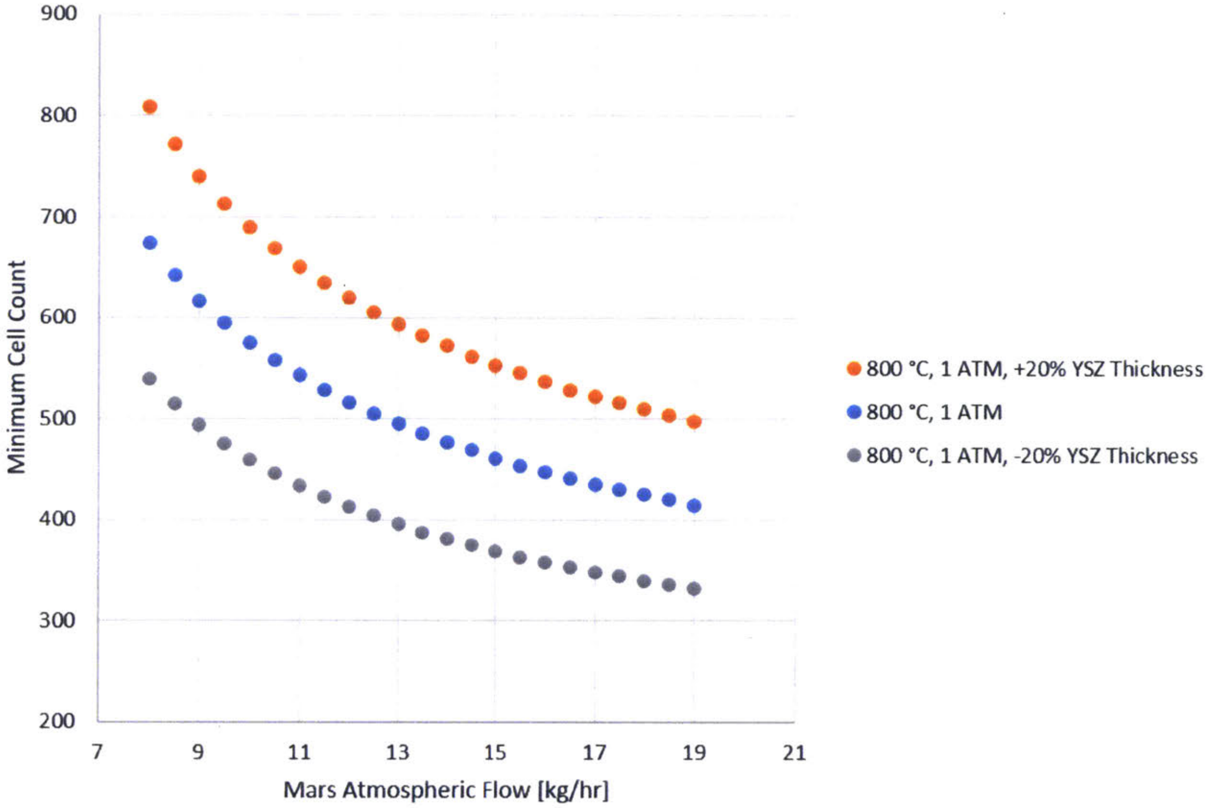

Figure 96 – Electrolyte thickness conductivity

A decrease in electrolyte thickness results in lower ohmic voltage losses due to transporting oxygen ions through the electrolyte. The result is a lower total cell voltage, which allows the control system to operate at a higher voltage (and current) before exceeding the CO-C Nernst potential. When more current can be safely achieved per cell, less cell are needed in the system design. At a Mars atmospheric flow rate of 8 kg/hr, a 20% decrease in electrolyte thickness results in a decrease in cell count from 674 to 539. The trend appears as a linear decrease throughout the flow region because the ohmic voltage drop has a linear relationship with respect to current. In electrolyte-supported cells such as those used for SOXE, the cell is also a structural component that separates the anode and cathode. Reductions in thickness are limited due to structural constraints, manufacturability, and cracking risks. It is important to note that electrolyte for MOXIE is formed through a tape casting process which currently has a batch variability of approximately +/- 10%.

Another electrochemical term modeled is the activation potential. The activation potential was characterized as the intercept of the linear i-V relationship after the contributions of the Nernst potential are subtracted. The activation potential may be reduced by adding steam or hydrogen to the inlet steam. Figure 97 shows how major reductions in this potential have little effect on minimum cell count. Strategies to reduce activation potential are unlikely to yield major returns.

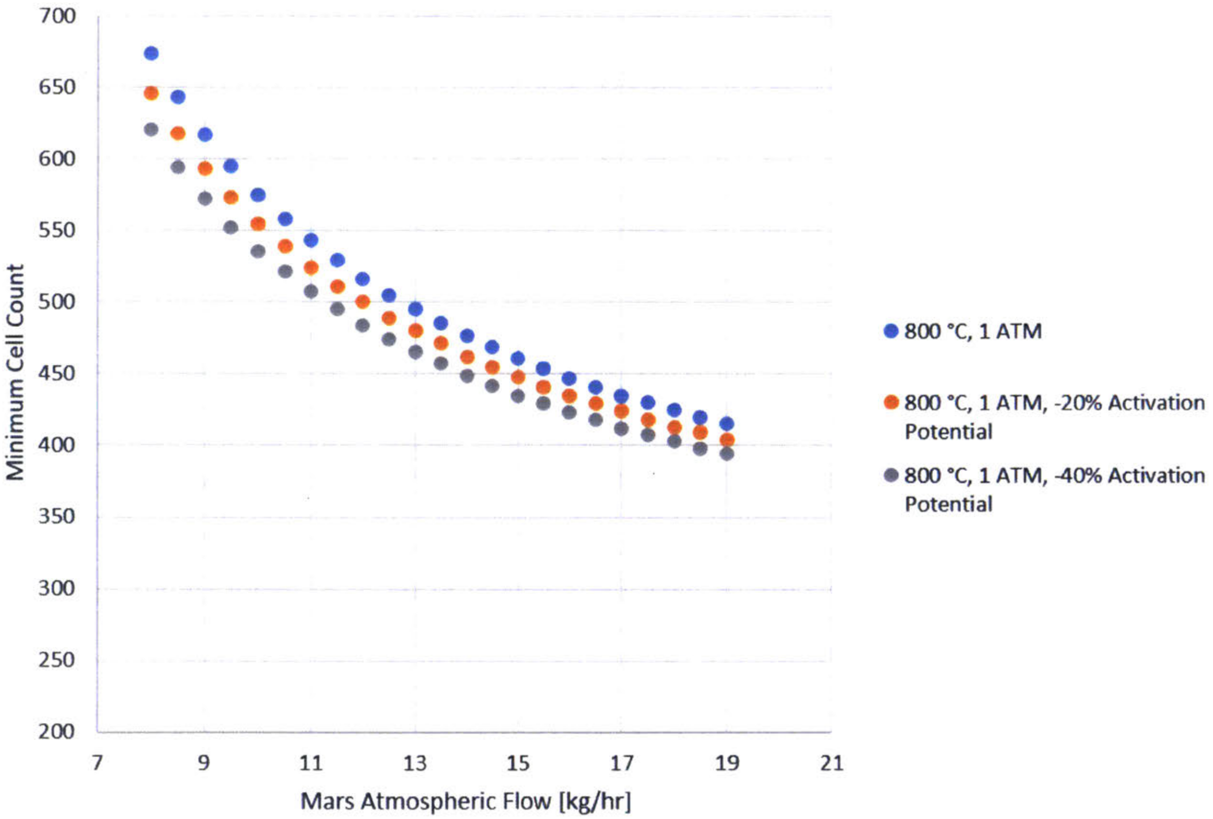

Figure 97 – Activation potential reduction and the effect on minimum cell count

A term more sensitive to change is activation energy. The activation energy term is from the Arrhenius relation that models the temperature sensitivity of the electrolyte to the conduction of oxygen ions. Figure 98 shows the effect of a 2.5% and 5% decrease in this term.

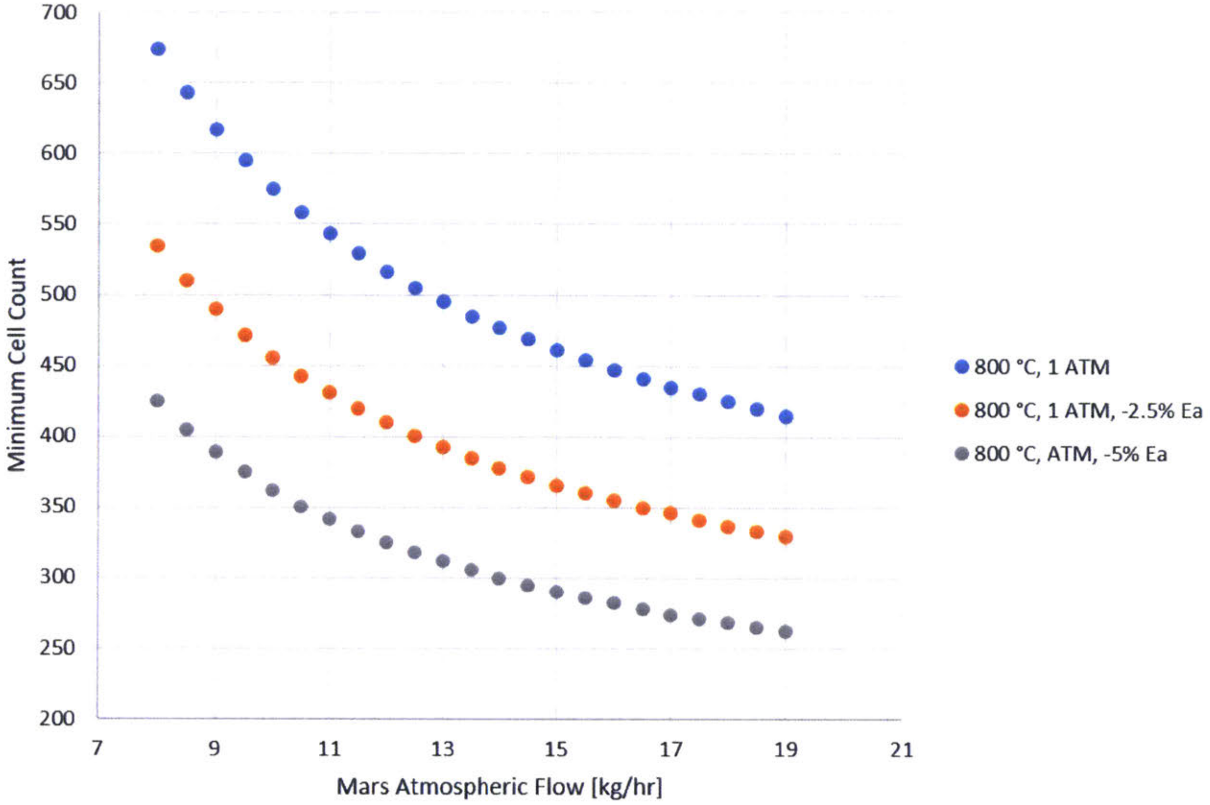

Figure 98 – Activation energy reduction and the effect on minimum cell count

Even a modest 2.5% decrease in activation energy results in a minimum cell count decrease of over 20% at 8 kg/hr Mars atmosphere flow. Small changes in the material properties and temperature sensitivity of the electrolyte have the potential to result in major improvements to electrolysis system size.

6.3.4 Power scaling

Power scaling was modeled for a 2 kg/hr production requirement. The SOE system power requirement was calculated from the thermal neutral voltage (described in Chapter 3) and by multiplying it by the number of cells and current. The thermal neutral voltage is based on the enthalpy of formation for the electrolysis reaction so it does not change with operating voltage. When the operating voltage is below the thermal neutral voltage, the reaction is endothermic and additional make-up heat must be supplied from the heaters to keep the system temperature constant. The enthalpy of formation determines the combined electrolysis + make up heat power requirement is 9.81 kW for a 2 kg/hr production rate.

The gas compression and heating power was calculated for 80% isentropic compression. For simplicity, the gas was assumed pure CO_2. The starting temperature, 212 K, and pressure , 700 Pa, was based on the average temperature and pressure for the Jezero landing site 5 meters above the surface, as calculated by the Mars Climate Database (Lewis, Collins et al. 1999). This design assumes that a recuperator is implemented to pre-heat the compressed gas using the waste heat from the SOXE effluent. It is assumed that the recuperator warms the SOXE inlet gas to within 50 K of the SOXE operating temperature. Additional energy is consumed at steady state to warm the gas the final 50 K. The results are shown in Figure 99 below.

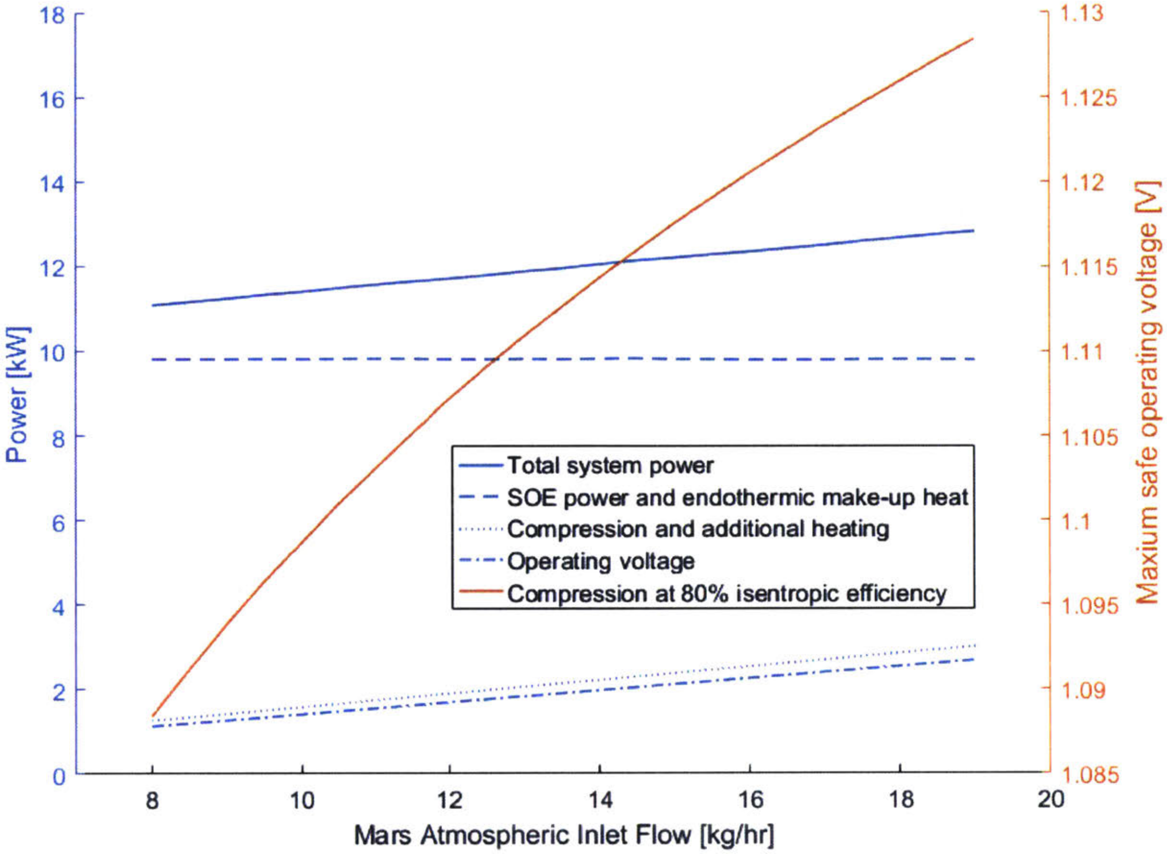

Figure 99 – Power for electrolysis and atmosphere acquisition (left) cell operating voltage (right)

The energy of CO_2 acquisition is calculated to be 0.1415 kW/kg-hr. An additional 0.0173 kW/kg-hr is used to heat the gas to operating temperature. This means that at 12 kg/hr, the energy of compression is about 1.70 kW. The SOE power is a constant 9.81 kW to satisfy the production requirements. The total system power to produce 2 kg/hr of O_2 (SOXE, compression and heating) varies from 11.8 kW at a CO_2 supply flow of 8 kg/hr to 12.83 kW at a flow of 19 kg/hr. These numbers represent minimum values for SOXE power and a best estimate of pump efficiency assuming a dynamic compressor or a highly efficient scroll. Other losses such as heat leak to the surrounding environment or power losses over current leads are not considered.

6.3.5 System level mass trades

System level mass and power trades for a crewed mission ISRU plant depend heavily on operating conditions and the method of carbon dioxide acquisition and compression. The results in Figure 100 are based on a mass scaling law for a scroll pump of the design type used for MOXIE (Wilson 2017).

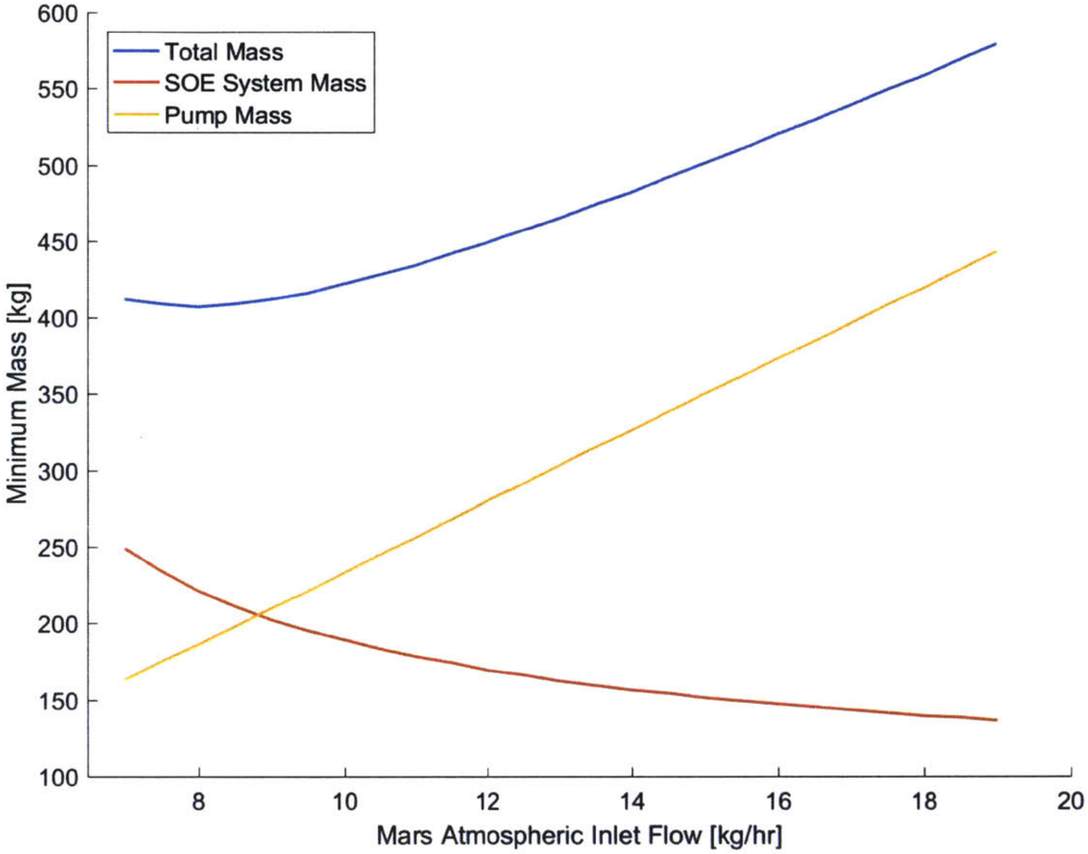

Figure 100 – Pump, SOE system, and total mass estimates

From a mass optimization perspective, it appears that operating at lower flow rates is ideal as pump mass quickly dominates system mass at higher flow rates. Figure 101, above, illustrates the trade when the estimated total mass is decreased by 10% and 20%, respectively.

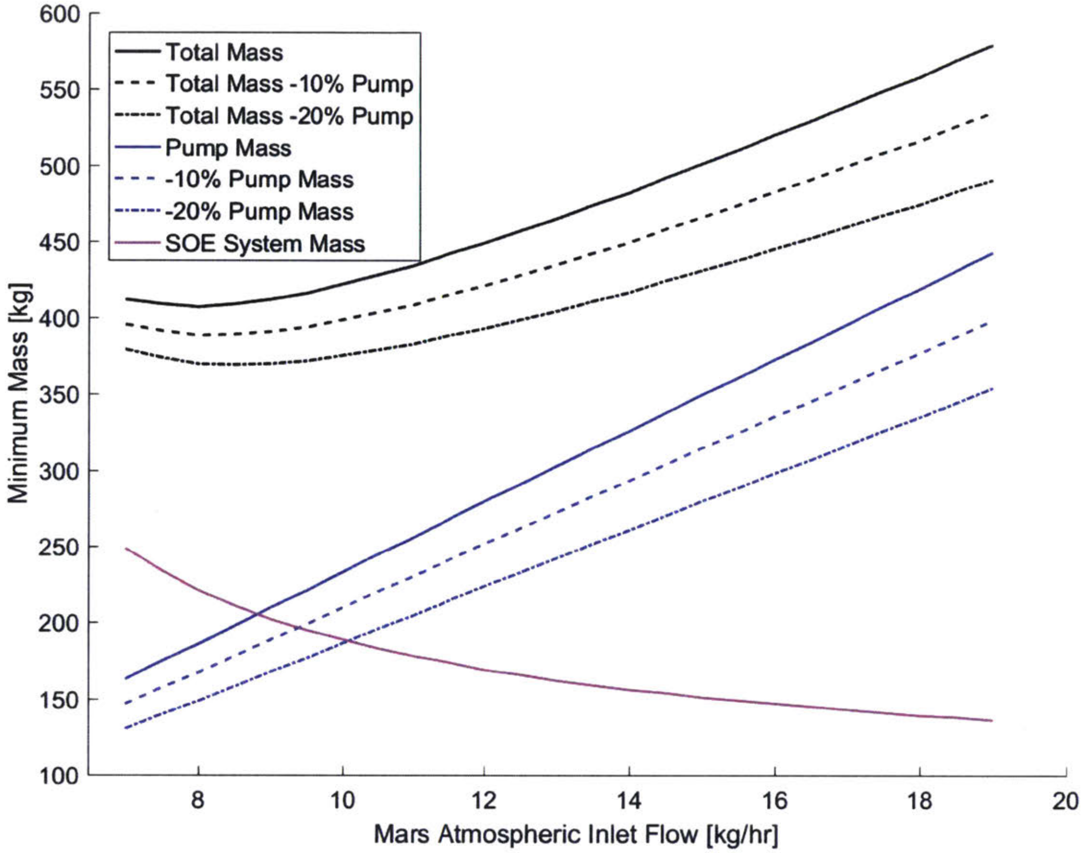

Figure 101 – Sensitivity of pump mass scaling to optimal operation to minimize mass

A minimum mass appears at 8 kg/hr for the standard mass scaling. At a 10% decrease, flow for minimal mass is about 8.25 kg/hr. With a 20% decrease in pump mass scaling, the minimum mass design flow is about 8.5 kg/hr. When selecting system flow rates, mass cannot be considered alone. Consider Figure 93 which shows the required minimum utilization vs. flow rate. At 8 kg/hr a utilization of 72.3% is required, a utilization where individual cells may have a higher risk of surpassing the Boudouard boundary for coking (87% utilization in these conditions). By operating at 10 kg/hr, the system mass only increases 15 kg (422 vs. 407 kg) yet a minimum utilization of 57.8% is required, gaining significant margin for that mechanism of coke formation. As pump technology improves in mass and efficiency, the best flow supply rate may increase more. A 12 kg/hr supply flow results in a required utilization of 48.2% with a base mass increase of 42 kg. 10 – 12 kg/hr of supply flow appears to be the ideal given the current technology. A 12 kg/hr system would have a combined pump and stack mass (before insulation and additional structure) of 449 kg. Increasing operating temperature will lower cell count and reduce mass. Using the current performance of MOXE derived SOXE cells with an area of 100 cm^2 per cell and operating at a minimum of 810 °C, it is estimated the system would need a minimum of 440 cells grouped in 8-12 stacks.

6.4 Chapter summary and conclusion

This chapter combined the SimSitu electrochemical model with scaling parameters to solve for the mass and power of the electrolysis and CO_2 acquisition components for a crewed mission scale SOE plant. The electrolysis system size greatly decreases as operating pressure is lowered and operating temperature increases. Minimum stack size is achieved at higher flow rates but the additional mass and power of operating at higher atmospheric mass flows likely outweighs the benefits from a system perspective. Future improvements in material properties and cell design have the potential to reduce SOE system mass. The SOE system was most sensitive to changes in activation energy (which is difficult to change and would require different cell materials) and least sensitive to changes in activation potential. Reductions in system size can also be achieved with reductions in electrolyte thickness or improvements in electrolyte ionic conductivity. Total electrolysis power required to produce 2 kg/hr of O_2, including any endothermic reaction that make up heat, is not sensitive to most parameters except for slight temperature dependence. System wide reductions in power can be achieved by reducing the required flow rate. This can be accomplished with a high cell count design that will reduce the required current in conjunction with lower flow density to increase the maximum safe utilization of Martian supply gas. If a system is designed for lower flow densities, attention must be made to create a design that ensures even flow distribution between cells in a stack. Uneven flow distribution could reduce the maximum safe current. Electrochemical analysis of MOXIE indicated that cell to cell flow distribution appears less uniform at lower flow densities. The most promising system enhancements is low pressure operation (0.1 to 0.5 bar). Low pressure operation has the potential to significantly reduce the cost of CO_2 acquisition and increases the maximum safe current density by increasing the CO-C Nernst potential. This would significantly alter trades between CO_2 acquisition pump types since many trades currently assume that the Mars atmosphere needs to be compressed to 1 Earth atmosphere.

Therefore, the effects of low cathode pressure for CO_2 acquisition and electrolysis is highly recommended for future studies.

7. Conclusion

This thesis makes significant contributions to ISRU technologies for Mars: specifically, solid oxide electrolysis modeling, control, and extensibility. Chapter 1 motivates this thesis by introducing ISRU, MOXIE, and the potential that ISRU has for unlocking new destinations in space by using extraterrestrial resources. It also outlines the primary research questions and hypotheses that guided the research. Chapter 2 describes the history of Mars ISRU and different approaches to ISRU. MOXIE was introduced in depth and relevant research in solid oxide electrolysis for ISRU is detailed. A thermodynamic model of the MOXIE electrolysis process is developed in Chapter 3. Chapter 4 then describes three electrochemical characterization experiments of the SOXE that were conducted to answer the modeling hypotheses introduced in Chapter 1. Chapter 5 combines the results from Chapter 3, and 4 to create a multi-domain physical system model of MOXIE. That chapter concludes with a demonstration of the model and testing of some relevant control methodologies. Chapter 6 extends the model to explore trades for an atmospheric ISRU for a crewed Mars mission.

7.1 Discoveries and implications

Discovery 1: Cell-to-cell performance variation observed in the SOXE cells was primarily the result of variations in flow distributions of the SOXE cells.

This discovery was made during the analysis to assess Hypothesis 1, which speculated that the performance variation was primarily due to variations in cell manufacturing and that the separation between each cell would be constant across operational conditions. The results, which are discussed in detail in Chapter 4, show that cell performance is statistically indistinguishable at high flow rates, but varies greatly at lower flow rate.

Implications for MOXIE:

- Operation at high flow rates will tighten cell voltage groupings and result in safer operation.
- When selecting stacks for flight, characterization should be conducted during low flow operation of 30 g/hr to observe the maximum deviation of cell-to-cell voltages and select the flight stack with the smallest deviation.

Implications for crewed mission ISRU systems:

- It is important to design stack feed tubes and cell flow manifolds that evenly distribute flow across a stack. If the flow distribution is uneven, higher utilizations will vary among the stack cells, resulting in variation of cell potentials due to the composition dependent CO_2 - CO Nernst potential. The highest cell potential limits the safe operating current of the stack so non-uniform flow ultimately reduces the total safe production rate for a stack.

Discovery 2: Cell current-voltage performance does not follow the approximate ASR relations assumed in the early MOXIE model. This discovery disproved Hypothesis 2. The i-V curve has an intercept above the open circuit voltage due to the contribution of a Nernst and activation potential. The slope of the i-V curve in the linear region of the curve is the ASR in that region. The ASR increases as flow rate decreases, an effect that was primarily attributed to the effects of the CO_2-CO Nernst potential. A new ASR term was derived to represent the intrinsic performance of the cells by subtracting the Nernst potential from observed potentials. The slope of the remaining potentials in the linear region of the i-V sweep is fitted to calculate a conversion corrected Nernst potential. The conversion corrected Nernst potential is nearly the same across all flow conditions. The intercept of this line is used to estimate of the activation potential.

Implications for MOXIE:

- The approximate ASR calculations used for comparing the performance of SOXE cells predict worse than actual performance. Intrinsic (conversion corrected) ASR should be used for cell performance comparison.
- All system models predicting performance should be enhanced with this updated modeling methodology.

Implications for crewed mission ISRU systems:

- Flow effects are important for the performance of the electrolysis system. Flow density over cell area must be considered as a part of the trade space for a full scale ISRU system.

Discovery 3: Cathode pressure is irrelevant to the integral average CO_2 – CO Nernst potential. The cathode pressure is mathematically eliminated from the Nernst equation for this reaction. Limits to low pressure operation include factors beyond the Nernst potential and are likely dominated by the pressure required to achieve required mass flow rates. Feed gas flow rate remains extremely important due to the implications of the model listed above. However, for the MOXIE design which generates pressure by compressing air against a flow restriction, pressure can be used in for a stand in for flow except for off nominal situations such as flow system leaks or obstructions:

Implications for MOXIE:

- Cathode operating pressure does not affect the voltage required to achieve oxygen production.
- When possible, the system design should be optimized to enhance gas flow rate at the expense of operating pressure. This may mean selecting a flow restrictor (viscous flow control device) that provides less back pressure.
- The pump system should be controlled by flow rate feedback instead of pressure, as this is the most direct measurement of a critical system parameter.

Implications for crewed mission ISRU systems:

- Carbon dioxide acquisition systems should be optimized for flow rates, not compression.
- Dynamic compressors, such as axial and radial compressors become feasible and energetically preferable.
- Lower pressure systems should have a lower energy cost than previous ISRU studies predicted for the system operating at Earth pressure.
- Flow restrictions in the system should be minimized.
    - Dust mitigation and filter methods are critical to minimizing these flow restrictions.

<u>Additional observations</u>

- Lower operating pressure also improves operating margin to maintain voltage below the CO-C Nernst potential
- Lower current densities can safely achieve the higher utilizations because lower currents induce less ohmic potential drop across the cell electrolyte. Current is directly proportional to oxygen production; therefore, more cells are needed to produce the same amount of oxygen at a lower stack current. This is the basis of the extensibility trades on stack size.

7.2 Summary of contributions

A novel tunable grey SOXE model to predict oxygen production performance

A novel, tunable grey SOXE model was developed to predict the oxygen production performance of MOXIE. The model was developed with a range of stack operating parameters. The methodology to tune the model for a different SOXE stack only requires a limited characterization data set at 100 g/hr and 30 g/hr flow rates. This allows modeling of a MOXIE flight stack without putting it through a week of operation as previously required when mapping the performance of the three SOXE stacks tested as part of the thesis.

SimSitu, the first multi-domain physical model of a solid oxide electrolysis system using Simscape

SimSitu was implemented in the Simscape language developed by MathWorks. It enables rapid prototyping of system simulations with multiple energy domains. SimSitu was used to model the interactions of the electrochemical model with a thermal mass representation of MOXIE. Alternative control modes were also demonstrated through the implementation of a Simulink control domain.

A strategy for characterizing and selecting flight SOXE stacks for the flight to Mars

The original characterization plan included baselining the performance of each stack at the maximum pump flow rate. A flow of 100 g/hr was used as an early estimate for maximum pump capability. Experimental characterization and modeling proved that testing at maximum pump flow is the least effective condition for screening out stacks with the greatest cell-to-cell performance variability. The lowest flow rate tested (30 g/hr) showed the greatest variability and should be used for selecting flight stacks. A higher flow rate of 100 g/hr is best suited for calculating the intrinsic (conversion corrected) ASR of the stack to compare intrinsic cell properties.

The creation of the Safe Margin Active Reduction Tracking (SMART) control algorithm

A method for controlling a solid oxide electrolysis process to achieve maximum production while avoiding hazards in dynamic operating environments. This controller integrates sensor data on pressure, temperature, current, and flow to calculate the CO-C Nernst potential and control to a safe margin below the hazardous level.

The first atmospheric ISRU electrolysis system mass and power trades based on data derived from the development of MOXIE that incorporates an electrochemical model of the operational limits.

Trades were developed by maximizing the performance of the ISRU system for a crewed mission to Mars. Maximum cell current densities were calculated based on an equivalent circuit voltage model and a model of the coking Nernst potential. The results show the importance of minimizing supply flow rate at the expense of electrolysis system mass to achieve total system reduction in mass and power. Insights from this model can be used by ISRU system engineers when weighing trades for future ISRU systems.

7.3 Limitations

The methodologies in this thesis have several limitations

- Experimental characterization limitations
    - Stack characterization was limited to ambient operational pressure.
    - Cell voltage increase under constant current conditions was used as a proxy for degradation. Carbon was found in the post cell destruction but it is difficult to tell for what reason.
- Multi-domain system limitations
    - Thermal model was based on data collected from a pre-CDR MOXIE thermal system design.
    - Cell-to-cell temperature variation was not measured while the stack was being operated.
    - Some final MOXIE dimensions were uncertain at that point in development.
- Extensibility trade limitations
    - The mass and power trades for the scale model are based on limited characterization for the MOXIE scroll pump and estimations for compressor performance. Thermodynamic work is calculated and mechanical losses are assumed to be minimal.
    - The scale of MOXIE and its design constraints make some parts unlike a full-scale system; some of these components, such as electronics mass and heat leak were not extrapolated.

7.4 Future work

- Experimental investigation of SOXE coking limits in a low cathode pressure environment.
- Experimental investigation of the minimum inlet CO concentration to avoid SOXE oxidation degradation and the effects of start-up and shout down methods on CO recirculation concentration.
- Experimental investigation comparing SOXE performance recovery after a coking event and a fault to idle versus a fault to a lower utilization recovery state.
- Pursue enhancements to SimSitu multi-domain physical system model.
    - Mechanical system domain model of MOXIE scroll pump based on verified pump data.
    - Tuning of the system to model to engineering hardware model.
    - Integration of experimentally verified degradation rates when cell voltages cross coking thresholds.
- Apply SimSitu to atmospheric ISRU systems for Mars sample return missions and human scale missions.
- Implementation of control strategies on engineering hardware model.
- Expanded STPA analysis of other MOXIE subsystems and crewed mission ISRU system implementation.
- Extensibility study of oxygen liquefaction methods for Mars and upstream requirements.

7.5 Final thoughts

The work described in this thesis made significant contributions to the planning, design, and understanding of the Mars Oxygen In-Situ Resource Utilization Experiment. MOXIE is part of the Mars 2020 mission and will be the first demonstration of ISRU on another planet. The successful production of oxygen on Mars by solid oxide electrolysis of the Martian atmosphere will signal the dawn of a new age in planetary exploration. Mars may someday become a fueling depot used to provide rockets with the oxygen needed to transport explorers back to Earth, and potentially to other parts of the solar system. This research takes us one step closer to a remarkable future.

References

Aboobaker, A., C. Smith and J. Hua (2016). SOXE Thermal Testing, NASA Jet Propulsion Laboratory.

Ash, R., W. Dowler and G. Varsi (1978). "Feasibility of rocket propellant production on Mars." Acta Astronautica **5**(9): 705-724.

Bove, R. and S. Ubertini (2008). Modeling Solid Oxide Fuel Cells, Springer.

Cohen, A. (1989). "Report of the 90-day study on human exploration of the Moon and Mars." NASA, Nov: 1518-1560.

Colvin, J., P. Schallhorn and K. Ramohalli (1992). "Full system engineering design and operation of an oxygen plant." Journal of Propulsion and Power **8**(5): 1103-1108.

Drake, B. G. (2009). Human exploration of Mars: Design Reference Architecture 5.0. N. J. S. Center. Washington, D.C., NASA.

Drake, B. G., S. J. Hoffman and D. W. Beaty (2010). Human exploration of Mars, design reference architecture 5.0. Aerospace Conference, 2010 IEEE, IEEE.

Drake, B. G. and K. Watts (2014). Human Exploration of Mars Design Reference Architecture 5.0 Addendum #2. Houston, TX, NASA Johnson Space Center: 598.

Ebbesen, S. D. and M. Mogensen (2009). "Electrolysis of carbon dioxide in solid oxide electrolysis cells." Journal of Power Sources **193**(1): 349-358.

Frisbee, R. H., J. R. French Jr and E. A. Lawton (1987). "A new look at oxygen production on Mars-In situ propellant production (ISPP)."

Gemmen, R. S. and C. D. Johnson (2005). "Effect of load transients on SOFC operation—current reversal on loss of load." Journal of Power Sources **144**(1): 152-164.

Hartvigsen, J. (2016). Solid oxide electrolysis stack development update. MOXIE Science Team Meeting. Salt Lake City, UT, Ceramatec Inc.

Hartvigsen, J., S. Elangovan, D. Larson, M. Elwell, M. Bokil, L. Frost and L. M. Clark (2015). Challenges of Solid Oxide Electrolysis for Production of Fuel and Oxygen from Mars Atmospheric CO2. ECS Conference on Electrochemical Energy Conversion & Storage, Glasgow, Scotland, Ecs.

Hoffman, S. J. and D. I. Kaplan (1997). Human Exploration of Mars: The Reference Mission of the NASA Mars Exploration Study Team. Exploration of Mars. Houston, Texas, Lyndon B. Johnson Space Center.

Hua, J. (2017). MOXIE Thermal iCDR, NASA JPL: 61.

Johnson, J. (2017). MOXIE iCDR 1-02: Systems Engineering, NASA JPL.

Kaplan, D., R. Baird, H. Flynn, J. Ratliff, C. Baraona, P. Jenkins, G. Landis, D. Scheiman, K. Johnson, P. Karlmann and e. al (2000). The 2001 Mars In-situ-propellant-production Precursor (MIP) Flight Demonstration - Project objectives and qualification test results. Space 2000 Conference and Exposition, American Institute of Aeronautics and Astronautics.

Kleinhenz, J. E. and A. Paz (2017). An ISRU propellant production system for a fully fueled Mars Ascent Vehicle. 10th Symposium on Space Resource Utilization.

Leighton, R. B. and B. C. Murray (1966). "Behavior of carbon dioxide and other volatiles on Mars." Science **153**(3732): 136-144.

Leveson, N. (2011). Engineering a safer world: Systems thinking applied to safety, Mit Press.

Lewis, S. R., M. Collins, P. L. Read, F. Forget, F. Hourdin, R. Fournier, C. Hourdin, O. Talagrand and J.-P. Huot (1999). "A climate database for Mars." Journal of Geophysical Research **104**(E10): 24,177-124,194.

Mahaffy, P. R., C. R. Webster, S. K. Atreya, H. Franz, M. Wong, P. G. Conrad, D. Harpold, J. J. Jones, L. A. Leshin and H. Manning (2013). "Abundance and isotopic composition of gases in the martian atmosphere from the Curiosity rover." Science **341**(6143): 263-266.

Mars Architecture Steering Group (2009). Design Refernce Architecture 5.0 Addendum. Human Exploration of Mars. B. G. Drake. Houston, Texas, NASA Johnson Space Center.

Megel, S., M. Kusnezoff, N. Trofimenko, V. Sauchuk, A. Michaelis, A. Venskutonis, K. Rissbacher, W. Kraussler, M. Brandner and C. Bienert (2011). "High efficiency CFY-stack for high power applications." ECS Transactions **35**(1): 269-277.

Meyen, F., J. Hoffman and M. Hecht (2015). Thermodynamic Model of Mars Oxygen ISRU Experiment (MOXIE). The 66th International Astronautical Congress. Jerusalem, Israel.

Meyen, F. E., M. H. Hecht, J. A. Hoffman and M. Team (2016). "Thermodynamic model of Mars Oxygen ISRU Experiment (MOXIE)." Acta Astronautica **129**: 82-87.

Nehrir, M. H. and C. Wang (2009). Modeling and control of fuel cells: distributed generation applications, John Wiley & Sons.

Nernst, W. (1899). "On the electrolytic conduction of solid bodies at high temperatures." Z. Electrochem **6**(2): 41-43.

Ni, M. (2010). "Modeling of a solid oxide electrolysis cell for carbon dioxide electrolysis." Chemical Engineering Journal **164**(1): 246-254.

Ni, M., M. K. Leung and D. Y. Leung (2006). "A modeling study on concentration overpotentials of a reversible solid oxide fuel cell." Journal of Power Sources **163**(1): 460-466.

Nier, A. and M. B. McElroy (1977). "Composition and structure of Mars' upper atmosphere: Results from the neutral mass spectrometers on Viking 1 and 2." Journal of Geophysical Research **82**(28): 4341-4349.

Paine, T. (1986). "Pioneering the space frontier: The report of the National Commission on Space." Bantam, New York.

Polsgrove, T., H. D. Thomas, W. Stephens and M. A. Rucker (2015). Mars Ascent Vehicle Design for Human Exploration. AIAA SPACE 2015 Conference and Exposition.

Ramohalli, K., W. Dowler, J. French and R. Ash (1987). "Novel extraterrestrial processing for space propulsion." Acta Astronautica **15**(5): 259-273.

Ramohalli, K., E. Lawton and R. Ash (1989). "Recent concepts in missions to Mars-Extraterrestrial processes." Journal of Propulsion and Power **5**(2): 181-187.

Rapp, D., J. A. Hoffman, F. Meyen and M. H. Hecht (2015). The Mars Oxygen ISRU Experiment (MOXIE) on the Mars 2020 Rover. AIAA Space 2015 Conference and Exposition. Pasadena, California, AIAA. **2015-4561**.

Richter, R. (1981). "Basic Investigation Oxygen in a Solid Electrolyte Process."

Sanders, G. B. and W. E. Larson (2011). "Integration of In-Situ Resource Utilization into lunar/Mars exploration through field analogs." Advances in Space Research **47**(1): 20-29.

Sanders, G. B., A. Paz, L. Oryshchyn, K. Araghi, A. Muscatello, D. L. Linne, J. E. Kleinhenz and T. Peters (2015). "Mars ISRU for Production of Mission Critical Consumables–Options, Recent Studies, and Current State of the Art." AIAA Space 2015.

Skafte, T. (2015). Carbon Deposition during CO 2 Electrolysis in Ni-Based Solid-Oxide-Cell Electrodes. ECS Conference on Electrochemical Energy Conversion & Storage with SOFC-XIV (July 26-31, 2015), Ecs.

Soffen, G. A. (1977). "The Viking project." Journal of Geophysical Research **82**(28): 3959-3970.

Sridhar, K. (1995). "Mars sample return mission with in-situ resource utilization." Journal of Propulsion and Power **11**(6): 1356-1362.

Sridhar, K., C. S. Iacomini and J. E. Finn (2004). "Combined H2O/CO2 solid oxide electrolysis for mars in situ resource utilization." Journal of propulsion and power **20**(5): 892-901.

Sridhar, K. R., J. E. Finn and M. H. Kliss (2000). "In-situ resource utilization technologies for Mars life support systems." Advances in Space Research **25**(2): 249-255.

Sridhar, K. R. and B. T. Vaniman (1997). "Oxygen production on Mars using solid oxide electrolysis." Solid State Ionics **93**(3–4): 321-328.

Stoots, C. M., J. E. O'Brien, J. S. Herring, K. G. Condie and J. J. Hartvigsen (2008). Idaho National Laboratory experimental research in high temperature electrolysis for hydrogen and syngas production. Fourth International Topical Meeting on High Temperature Reactor Technology, American Society of Mechanical Engineers.

Strickland, J. (2013). Revisiting SLS/Orion launch costs. The Space Review, The Space Review.

Strickler, D. and W. Carlson (1965). "Electrical Conductivity in the ZrO2-Rich Region of Several M2O3—ZrO2 Systems." Journal of the American Ceramic Society **48**(6): 286-289.

United States Senate (2010). NASA Authorization Act of 2010. Washington, DC, USA.

Wachsman, E. D. and K. T. Lee (2011). "Lowering the Temperature of Solid Oxide Fuel Cells." Science **334**(6058): 935-939.

Weaver, D. B., M. B. Duke and B. B. Roberts (1993). Mars exploration strategies- A reference design mission. IAF, International Astronautical Congress, 44 th, Graz, Austria.

Williams, D. R. (2015). "Mars Fact Sheet." 2015, from http://nssdc.gsfc.nasa.gov/planetary/factsheet/marsfact.html.

Wilson, J. (2017). MOXE Scroll Pump Scaling. M. Nasr and F. Meyen, Air Squared.

Zubrin, R., D. Baker and O. Gwynne (1991). Mars direct: a simple, robust, and cost effective architecture for the space exploration initiative. 29th Aerospace Sciences Meeting, AIAA.

Appendix A – Additional Data Plots and Results for CSA 003R

Table 19 – Utilization Boundary of CSA 003R

Temp [C]	Flow [g/hr]	Current [A]	Stack Voltage [V]	Utilization [%]	O2 Production [g/hr]	Boundary Not Found (BNF)
770	55	3.930	13.06	60	11.73	BNF
790	30	1.928	10.88	54	5.75	
790	55	2.624	11.48	40	7.83	
790	80	3.620	11.51	38	10.80	
800	30	2.505	10.82	70	7.48	
800	35	2.914	10.97	70	8.70	
800	40	2.854	10.86	60	8.52	
800	45	2.785	10.73	52	8.31	
800	50	2.975	10.79	50	8.88	
800	55	3.274	11.02	50	9.77	
800	60	3.144	10.90	44	9.39	
800	65	3.403	11.05	44	10.16	
800	70	3.502	11.08	42	10.45	
800	75	3.750	11.19	42	11.19	
800	80	3.999	11.39	42	11.94	
800	100	4.049	11.21	34	12.09	BNF
810	30	1.720	10.32	48	5.13	
810	55	2.883	10.91	44	8.61	
810	80	3.999	11.81	42	11.94	BNF
830	55	2.883	10.67	44	8.61	

Appendix B – Additional Data Plots and Results for CSA 004

Table 20 – Utilization and production boundary for CSA 004

Temp [C]	Flow [g/hr]	Current [A]	Utilization [%]	O_2 Production [g/hr]
770	30	2.01	56	6.00
770	55	3.15	48	9.40
790	30	2.01	56	6.00
790	55	3.15	48	9.40
800	35	2.92	70	8.72
800	40	2.96	62	8.84
800	45	3.12	58	9.31
800	50	3.22	54	9.61
800	55	3.41	52	10.18
800	60	3.72	50	11.10
800	65	3.88	50	11.58
810	30	2.08	58	6.21
810	55	3.41	52	10.18
830	55	3.55	54	10.60

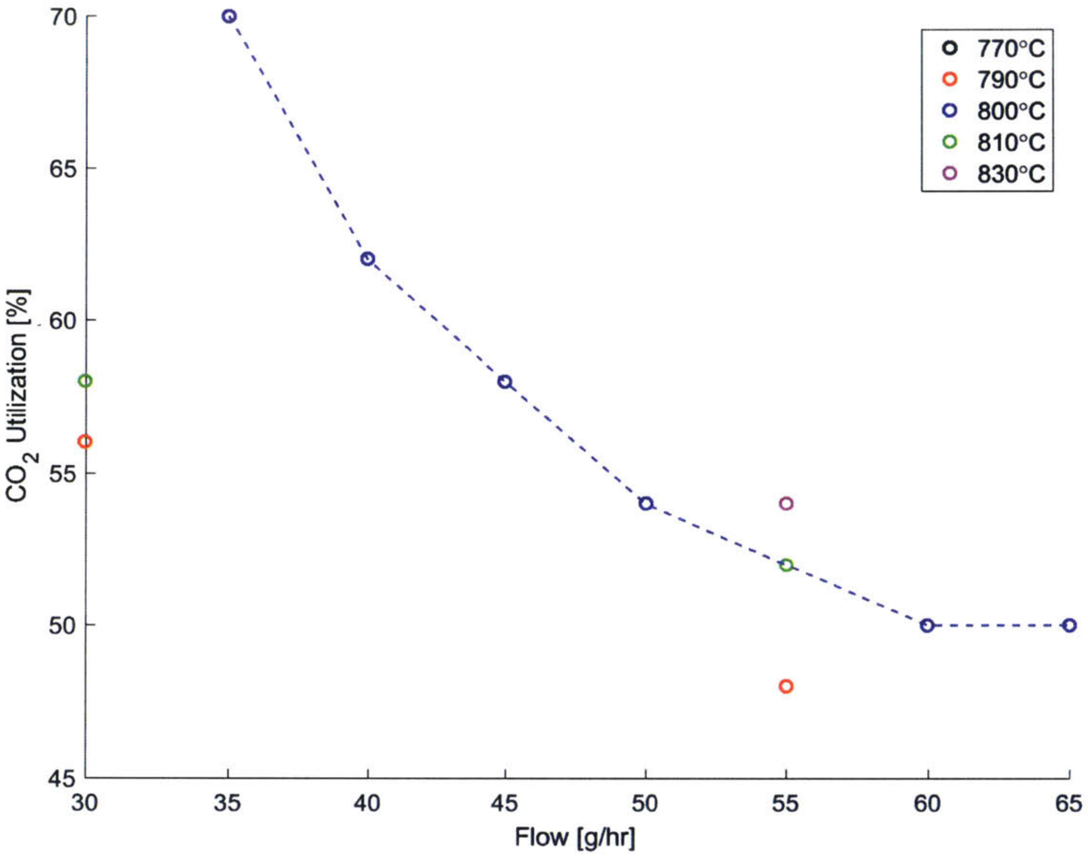

Figure 102 CSA 004 CO$_2$ utilization boundary at various flows and temperatures

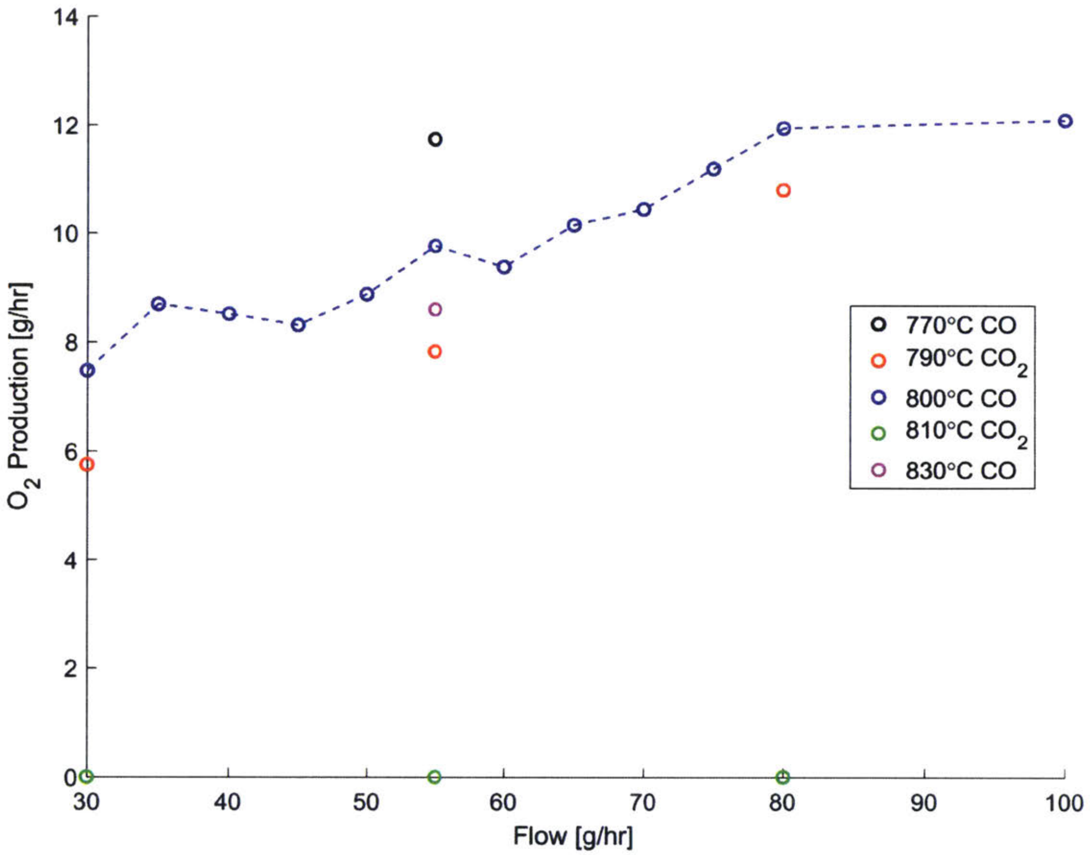

Figure 103 - CSA 004 maximum O_2 production boundary at various flows and temperatures

Appendix C – Additional Data Plots and Results for CSA 005

Table 21 – Operational Limits of CSA 005

Temp [C]	Flow [g/hr]	Current [A]	Stack Voltage [V]	Utilization [%]	O2 Production [g/hr]
770	30	1.718	10.60	48.0	5.13
770	55	2.354	10.79	35.9	7.03
770	100	2.853	10.90	23.9	8.51
790	30	2.006	10.59	56.0	5.99
790	55	2.882	10.82	43.9	8.60
790	100	3.808	11.10	31.9	11.37
800	30	2.215	10.65	61.8	6.61
800	35	2.475	10.70	59.2	7.39
800	40	2.575	10.66	53.9	7.68
800	45	2.784	10.71	51.8	8.31
800	50	2.974	10.77	49.8	8.88
800	55	3.143	10.81	47.9	9.38
800	60	3.279	10.85	45.8	9.79
800	65	3.400	10.90	43.8	10.15
800	70	3.499	10.89	41.9	10.44
800	75	3.569	10.90	39.9	10.65
800	80	3.618	10.89	37.9	10.80
800	100	4.046	11.03	33.9	12.08
810	30	2.215	10.53	61.8	6.61
810	55	3.399	10.81	51.8	10.15
810	100	4.525	11.06	37.9	13.51
830	30	2.425	10.51	67.7	7.24
830	55	3.799	10.73	57.9	11.34
830	100	4.995	10.90	41.8	14.91

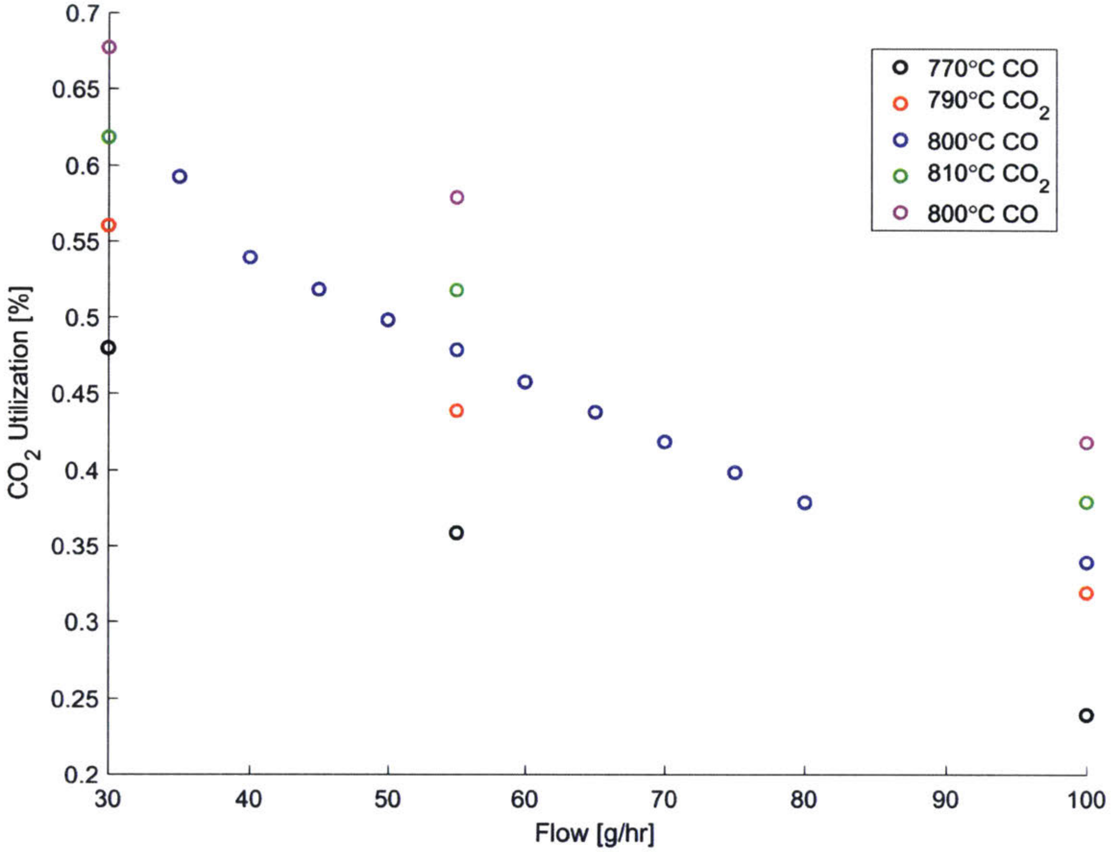

Figure 104 – CSA 005 CO$_2$ utilization boundary at various flows and temperatures

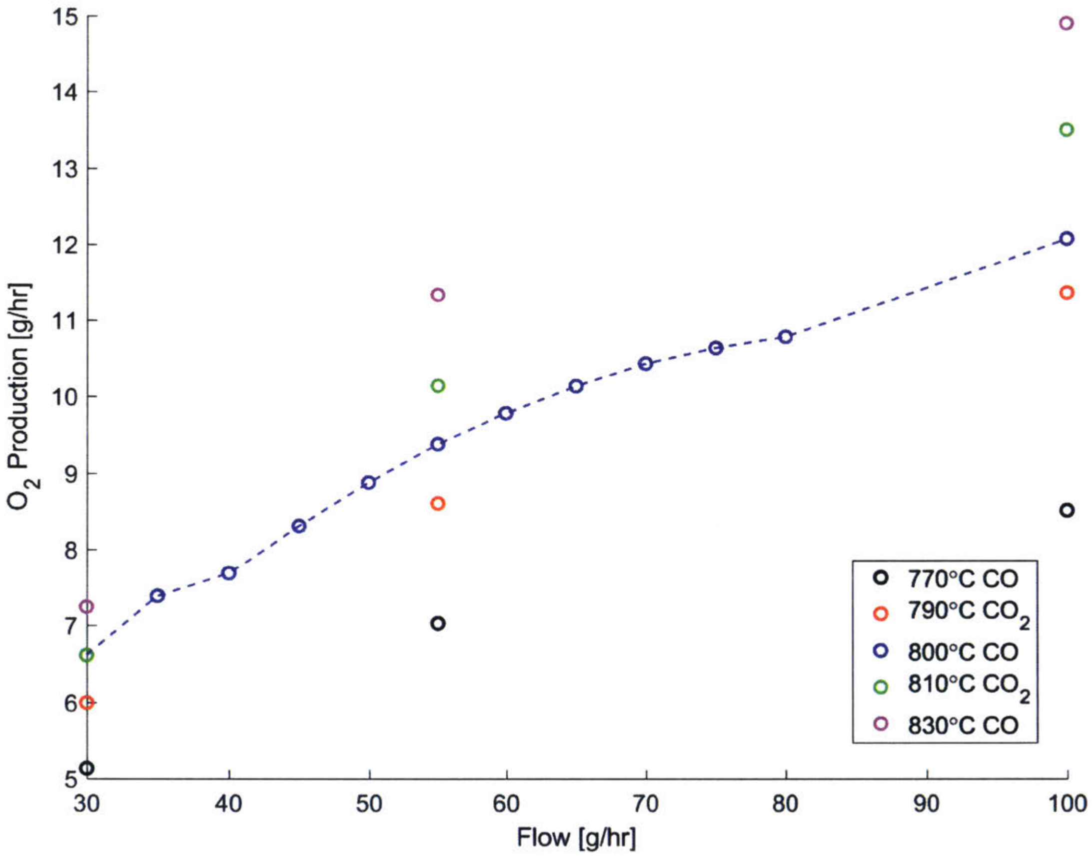

Figure 105 – CSA 005 maximum O_2 production boundary at various flows and temperatures

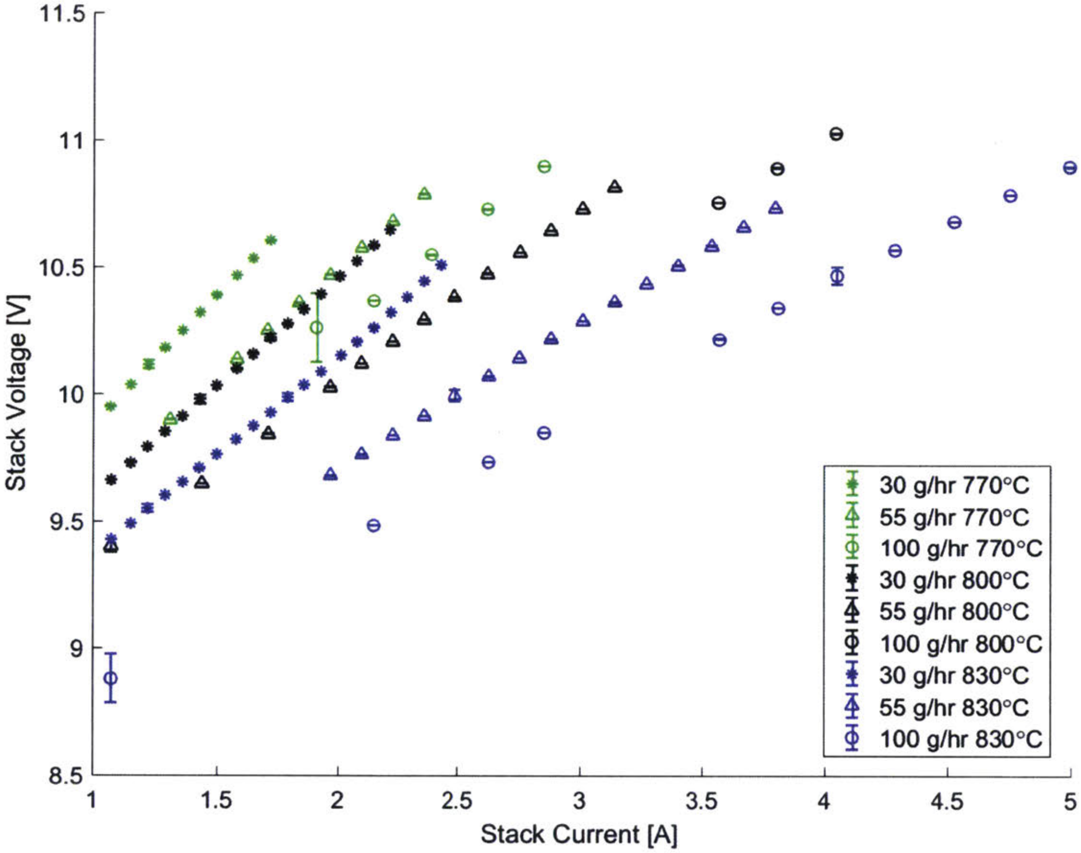

Figure 106 – CSA 005 total stack I-V curves for varying flow and temperatures

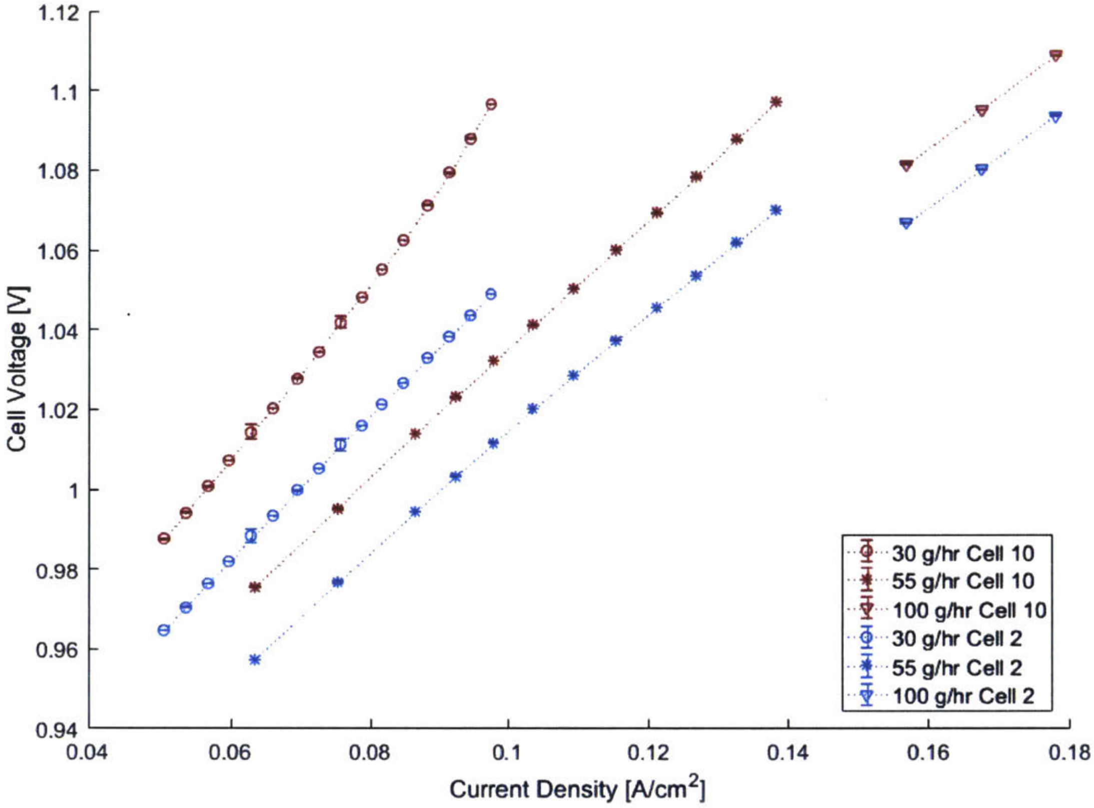

Figure 107 – Comparison of i-V curves for CSA 005 best and worst performing cells

Table 22 – CSA 005 800°C ASR Values with 95% Confidence Intervals

Flow [g/hr]	ASR 1	95% CI	ASR 2	95% CI	ASR 3	95% CI	ASR 4	95% CI	ASR 5	95% CI
30	1.8290	0.0385	1.7981	0.0422	2.0321	0.0291	1.8131	0.0388	1.8351	0.0362
35	1.7028	0.0444	1.6714	0.0452	1.8475	0.0447	1.6835	0.0440	1.7051	0.0426
40	1.6613	0.0289	1.6308	0.0300	1.7626	0.0366	1.6384	0.0294	1.6601	0.0305
45	1.5633	0.0245	1.5363	0.0220	1.6556	0.0044	1.5427	0.0215	1.5655	0.0194
50	1.5725	0.0391	1.5474	0.0400	1.6318	0.0302	1.5509	0.0386	1.5697	0.0355
55	1.5279	0.0517	1.5049	0.0548	1.5775	0.0428	1.5079	0.0518	1.5275	0.0470
60	1.5355	0.0657	1.5120	0.0692	1.5709	0.0642	1.5126	0.0686	1.5307	0.0654
65	1.4224	0.0130	1.3927	0.0173	1.4555	0.0076	1.3966	0.0173	1.4205	0.0149
70	1.3869	0.0325	1.3705	0.0311	1.4234	0.0199	1.3710	0.0252	1.3948	0.0269
75	1.3661	0.0293	1.3483	0.0130	1.3955	0.0116	1.3499	0.0085	1.3726	0.0112
80	1.3669	0.0846	1.3438	0.0225	1.3761	0.0147	1.3368	0.0218	1.3588	0.0253
100	1.2825	0.2322	1.2719	0.0758	1.2902	0.0810	1.2632	0.0892	1.2803	0.0811

Flow [g/hr]	ASR 6	95% CI	ASR 7	95% CI	ASR 8	95% CI	ASR 9	95% CI	ASR 10	95% CI
30	1.8747	0.0353	2.0528	0.0361	1.8606	0.0370	1.9894	0.0275	2.2587	0.1066
35	1.7387	0.0440	1.8710	0.0490	1.7328	0.0440	1.8178	0.0447	2.0019	0.0827
40	1.6899	0.0312	1.7836	0.0444	1.6885	0.0321	1.7407	0.0395	1.8652	0.0658
45	1.5911	0.0210	1.6823	0.0078	1.5929	0.0193	1.6396	0.0034	1.7551	0.0318
50	1.5966	0.0379	1.6425	0.0204	1.5985	0.0353	1.6111	0.0246	1.6781	0.0150
55	1.5540	0.0504	1.5904	0.0277	1.5578	0.0477	1.5620	0.0334	1.6180	0.0183
60	1.5560	0.0698	1.5784	0.0518	1.5614	0.0660	1.5530	0.0557	1.5932	0.0459
65	1.4385	0.0192	1.4809	0.0058	1.4494	0.0137	1.4526	0.0067	1.4996	0.0127
70	1.4116	0.0301	1.4477	0.0114	1.4225	0.0206	1.4205	0.0125	1.4577	0.0132
75	1.3899	0.0066	1.4184	0.0180	1.4006	0.0036	1.3939	0.0114	1.4234	0.0183
80	1.3739	0.0623	1.3968	0.0019	1.3882	0.0490	1.3745	0.0080	1.3977	0.0212
100	1.2925	0.0720	1.3102	0.0376	1.3109	0.1005	1.2913	0.0546	1.2983	0.0550

Table 23 - CSA 005 800°C Intercept Values with 95% Confidence Intervals

Flow [g/hr]	C1 Int	95% CI	C2 Int	95% CI	C3 Int	95% CI	C4 Int	95% CI	C5 Int	95% CI
30	0.8741	0.0028	0.8745	0.0031	0.8761	0.0021	0.8775	0.0029	0.8753	0.0027
35	0.8739	0.0036	0.8744	0.0037	0.8776	0.0037	0.8778	0.0036	0.8750	0.0035
40	0.8691	0.0025	0.8697	0.0026	0.8745	0.0032	0.8736	0.0026	0.8704	0.0027
45	0.8711	0.0025	0.8714	0.0022	0.8759	0.0004	0.8757	0.0022	0.8720	0.0019
50	0.8636	0.0037	0.8643	0.0038	0.8709	0.0028	0.8690	0.0036	0.8654	0.0033
55	0.8630	0.0054	0.8637	0.0057	0.8704	0.0045	0.8685	0.0054	0.8645	0.0049
60	0.8583	0.0068	0.8590	0.0071	0.8662	0.0066	0.8642	0.0071	0.8603	0.0067
65	0.8677	0.0016	0.8693	0.0022	0.8753	0.0010	0.8744	0.0022	0.8693	0.0019
70	0.8687	0.0043	0.8688	0.0041	0.8751	0.0026	0.8744	0.0033	0.8689	0.0036
75	0.8681	0.0040	0.8686	0.0018	0.8750	0.0016	0.8742	0.0012	0.8684	0.0015
80	0.8650	0.0121	0.8661	0.0032	0.8743	0.0021	0.8734	0.0031	0.8673	0.0036
100	0.8676	0.0389	0.8675	0.0127	0.8763	0.0136	0.8761	0.0150	0.8695	0.0136
Flow [g/hr]	C6 Int	95% CI	C7 Int	95% CI	C8 Int	95% CI	C9 Int	95% CI	10 Int	95% CI
30	0.8784	0.0026	0.8757	0.0027	0.8763	0.0027	0.8771	0.0020	0.8720	0.0079
35	0.8786	0.0036	0.8768	0.0040	0.8762	0.0036	0.8780	0.0037	0.8760	0.0068
40	0.8743	0.0027	0.8737	0.0039	0.8717	0.0028	0.8744	0.0034	0.8752	0.0057
45	0.8764	0.0021	0.8744	0.0008	0.8737	0.0019	0.8754	0.0003	0.8753	0.0032
50	0.8697	0.0036	0.8708	0.0019	0.8671	0.0033	0.8711	0.0023	0.8745	0.0014
55	0.8690	0.0053	0.8699	0.0029	0.8663	0.0050	0.8701	0.0035	0.8736	0.0019
60	0.8650	0.0072	0.8664	0.0053	0.8620	0.0068	0.8664	0.0057	0.8709	0.0047
65	0.8751	0.0024	0.8730	0.0007	0.8715	0.0017	0.8736	0.0008	0.8763	0.0016
70	0.8749	0.0040	0.8727	0.0015	0.8714	0.0027	0.8734	0.0017	0.8766	0.0017
75	0.8747	0.0009	0.8725	0.0025	0.8712	0.0005	0.8730	0.0016	0.8766	0.0025
80	0.8740	0.0089	0.8718	0.0003	0.8700	0.0070	0.8722	0.0011	0.8760	0.0030
100	0.8774	0.0121	0.8732	0.0063	0.8726	0.0169	0.8736	0.0092	0.8780	0.0092

Table 24 – CSA 005 Stack ASR with 95% Confidence Interval

Temp [C]	Flow [g/hr]	Stack ASR	95% CI
770	30	2.2586	0.0768
770	55	1.9105	0.0509
770	100	1.5662	0.5175
790	30	2.0274	0.0547
790	55	1.6911	0.0943
790	100	1.5100	0.0650
800	30	1.9346	0.0252
800	35	1.7778	0.0418
800	40	1.7119	0.0334
800	45	1.6122	0.0093
800	50	1.6015	0.0312
800	55	1.5526	0.0430
800	60	1.5505	0.0618
800	65	1.4413	0.0102
800	70	1.4120	0.0183
800	75	1.3860	0.0121
800	80	1.3714	0.0352
800	100	1.2923	0.0566
810	30	1.8673	0.0150
810	55	1.4856	0.0452
810	100	1.3033	0.0595
830	30	1.7698	0.0347
830	55	1.2865	0.0185
830	100	1.1621	0.0648

Table 25 CSA 005 Stack Intercepts with 95% Confidence Interval

Temp [C]	Flow [g/hr]	Stack Int [V]	95% CI
770	30	0.8900	0.0048
770	55	0.8813	0.0043
770	100	0.8918	0.0548
790	30	0.8806	0.0037
790	55	0.8688	0.0098
790	100	0.8590	0.0078
800	30	0.8757	0.0019
800	35	0.8764	0.0034
800	40	0.8727	0.0029
800	45	0.8742	0.0009
800	50	0.8685	0.0029
800	55	0.8679	0.0045
800	60	0.8639	0.0064
800	65	0.8725	0.0013
800	70	0.8723	0.0024
800	75	0.8722	0.0017
800	80	0.8710	0.0050
800	100	0.8727	0.0095
810	30	0.8707	0.0011
810	55	0.8609	0.0046
810	100	0.8492	0.0080
830	30	0.8597	0.0027
830	55	0.8583	0.0024
830	100	0.8375	0.0106

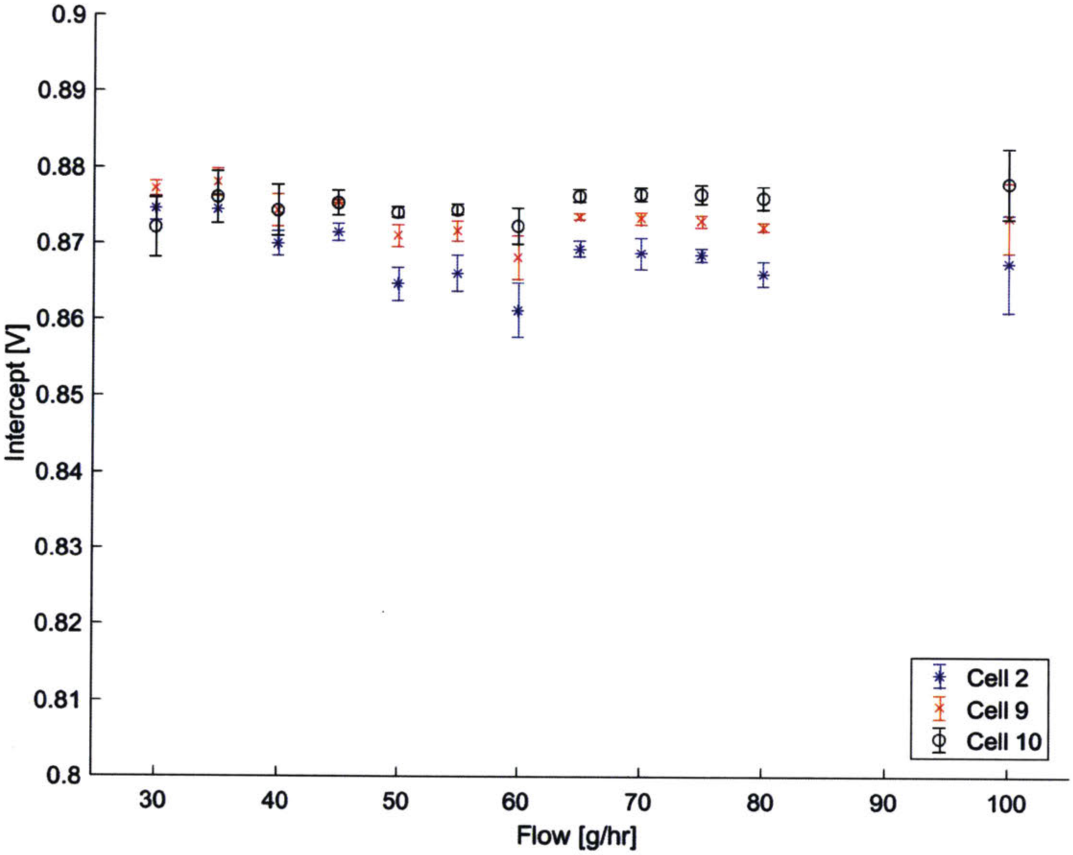

Figure 108 – Intercept variation between the best (Cell 2), median (Cell 9), and lowest (Cell 10) performing cells of CSA 005